THREE-DIMENSIONAL ANALYSIS OF TWO-LAYERED MICROCHANNEL HEAT SINKS IN PARALLEL AND COUNTER-FLOW ARRANGEMENTS

BY

MARC LEVAC

A Thesis
Presented to the Faculty of Graduate Studies
In Partial Fulfilment of the Requirements for the Degree of

MASTER OF SCIENCE

Department of Mechanical and Manufacturing Engineering
University of Manitoba
Winnipeg, Manitoba, Canada

THE UNIVERSITY OF MANITOBA

FACULTY OF GRADUATE STUDIES

*****

COPYRIGHT PERMISSION

THREE-DIMENSIONAL ANALYSIS OF TWO-LAYERED MICROCHANNEL HEAT SINKS IN PARALLEL AND COUNTER-FLOW ARRANGEMENTS

BY

Marc Levac

A Thesis/Practicum submitted to the Faculty of Graduate Studies of The University of Manitoba in partial fulfillment of the requirement of the degree

MASTER OF SCIENCE

ABSTRACT

Microchannel heat sinks, using various flow arrangements, were considered in this thesis, with the goal of exploring the possibility of using multiple rows of channels, instead of the conventional single-row designs. This possibility has not been studied extensively up to this point. The various arrangements examined included two single-row designs, and two two-row arrangements. The two-row arrangements were the parallel-flow arrangement, where the flow in both channels was in the same direction, and the counter-flow arrangement, where the flow in both channels was in opposite directions. The analyses were performed using both the fully-developed inlet velocity assumption, and the more realistic uniform inlet velocity assumption, to assess the impact of making the fully-developed inlet velocity assumption on the solution accuracy. Both high and low Reynolds numbers, with the laminar flow regime, were considered.

The arrangements were compared on the basis of two thermal parameters, and the pumping power. The thermal parameters were the thermal resistance, with a lower value being more desirable, and the maximum temperature difference along the heated surface, which is a measure of the uniformity of temperature along the heated surface. A temperature distribution that is as uniform as possible along the heated surface is desirable.

It was found that making the assumption of fully-developed flow in the inlet has a negligible impact on the prediction of the thermal resistance (at low and high Reynolds numbers). However, predicting the other two parameters to reasonable accuracy requires uniform inlet velocity assumption. This is particularly true at high Reynolds numbers.

In terms of thermal parameters, it was found that both two-row designs offer significant improvement over the conventional single-row design. Among the two-row designs, the counter-flow arrangement offers a lower thermal resistance than the parallel-flow arrangement, but, the difference is not overwhelming. In terms of the temperature variation along the heated surface, the counter-flow arrangement offers significant improvements over all other cases considered. However, in terms of heat dissipation per unit pumping power, for fixed mass flowrate and overall temperature difference across the heat sink, the single-channel arrangement is better.

Detailed descriptions of the fluid flow and heat transfer phenomena occurring in the various design alternatives were also performed, in order to obtain a good understanding of the physics occurring during the fluid flow and heat transfer processes.

ACKNOWLEDGEMENTS

I would like to thank Dr. S. J. Ormiston and Dr. H. M. Soliman for their continuous and consistently thorough supervision throughout this work. Their expertise in fluid mechanics, and the guidance that they provided to me based on their experience in technical writing, have been much appreciated.

I would also like to thank the Academic Computing and Networking department here at the University of Manitoba, for maintaining a wonderful Unix network that I used over the course of my research. Additionally, I would like to thank Guy Durocher, from the Physics department, who maintained the Linux machine that I made use of throughout this work.

My family and friends also deserve many thanks. While they did not help me with the technical aspects of this work, they provided constant support and encouragement throughout this work. Also, their patience and understanding when I had to either decline, or limit my involvement in, various social commitments in order to work on this thesis, were also much appreciated.

Finally, I would like to hereby gratefully acknowledge the financial support provided by the Natural Sciences and Engineering Research Council of Canada (NSERC).

TABLE OF CONTENTS

LIST OF FIGURES

LIST OF TABLES

NOMENCLATURE

A_{ch}	channel cross-sectional area, [m^2]
AF	area fraction, defined in Eq. (5.11)
B	width, or horizontal separation distance, [m]
b	dimensionless width, or dimensionless horizontal separation distance
C_p	constant pressure specific heat, [J/(kg K)]
D_h	hydraulic diameter, [m^2]
$D_h\|_{Vafai\ and\ Zhu}$	alternative hydraulic diameter definition, defined in Eq. (3.125c), [m^2]
f	friction factor
f_{app}	apparent friction factor
H	height, [m]
h	dimensionless height
HF	heat fraction, defined in Eq. (5.12)
H_f	height of "fin", [m]
h_f	dimensionless height of "fin"
h_Z	axially local heat transfer coefficient, [W/(m^2 K)]
k	thermal conductivity, [W/(m K)]
L	axial length of heat sink, [m]
l	dimensionless axial length of heat sink
$\dot{m}$	mass flowrate, [kg/s]
N	number of channels
Nu	local nusselt number
Nu_m	mean nusselt number
nx, ny, ...	number of nodal spacings
P	pressure, [Pa]
p	dimensionless pressure
PP	pumping power, [W]
pp	pimensionless pumping power

Pr	Prandtl number
P_{wetted}	wetted perimeter, [m]
q''	heat flux, [W/m^2]
R_{th}	thermal resistance, [K/W]
r_{th}	dimensionless thermal resistance
Re	Reynolds number
r_X, r_Y, ...	geometric expansion factors
T	temperature, [K]
T_{in}	specified inlet temperature, [K]
T_{wall}	specified wall temperature, [K]
U	X-component of velocity, [m/s]
u	x-component of dimensionless velocity
V	Y-component of velocity, [m/s]
v	y-component of dimensionless velocity
W	Z-component of velocity, [m/s]
w	z-component of dimensionless velocity
W_{in}	specified inlet velocity, [m/s]
w_{in}	specified dimensionless inlet velocity
$W_{in\ \text{large}}$	specified inlet velocity for the single channel (large) arrangement, [m/s]
$w_{in\ \text{large}}$	specified dimensionless inlet velocity for the single channel (large) arrangement
X, Y, Z	co-ordinate directions, [m]
x, y, z	dimensionless co-ordinate directions
Z^+	dimensionless Z co-ordinate, defined in Eq. (4.7)
Z^*	dimensionless Z co-ordinate, defined in Eq. (4.15)

Greek Symbols

α	thermal diffusivity, [m^2/s]
β	parameter defined in Eq. (5.9), [1/(m^2 K)]
ΔX	X-direction nodal spacing, [m]

ΔY	Y-direction nodal spacing, [m]
ΔZ	Z-direction nodal spacing, [m]
ρ	density, [kg/m^3]
μ	dynamic viscosity, [kg/(m s)]
θ	dimensionless temperature

Superscripts

$\bar{}$	cross-section average

Subscripts

bulk	cross-section, momentum-weighted average
c	channel
cent	centerline
cs	in the solid and the channel
D_h	based on hydraulic diameter (sometimes omitted)
f	fluid
heated	along heated surface
in	inlet
max	maximum value
max,*Y*=0	maximum value in $Y = 0$ plane
min,*Y*=0	minimum value in $Y = 0$ plane
out	outlet
s	solid
T	total, or overall

CHAPTER 1
INTRODUCTION

1.1 Background

The topic under consideration in this thesis is that of microchannel heat sinks. A generic microchannel heat sink arrangement is shown in Figure 1.1 in a three-dimensional view, and in Figure 1.2 in a cross-sectional view. Some heat-producing component (typically a computer chip) generates an appreciable amount of heat, which is to be dissipated. To remove this heat, a heat sink is placed above this heat producing component. This heat sink consists of a block made of a highly conductive solid material, into which several holes, or channels, are located. Some coolant fluid flows through these channels. The heat generated by the heat-producing component is absorbed by the fluid flowing in the channels. Because the dimensions of the channels are usually small (on the order of micrometers or smaller), they are referred to as *micro*channels. Microchannels are effective because, with their small sizes, the ratio of surface area to volume is quite large, enabling large heat transfer coefficient values to be obtained.

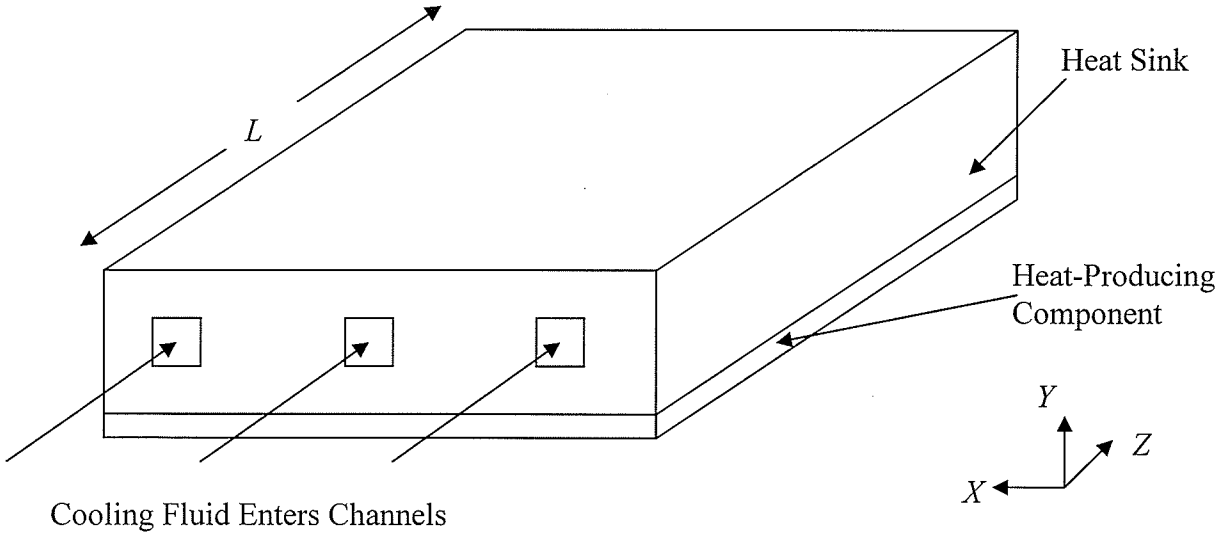

Figure 1.1: Schematic Representation of a Generic Microchannel Heat Sink, Three-Dimensional View

For the purposes of analysis, the heat-producing component is assumed to produce a uniform heat flux, q'', over the bottom surface of the heat sink. The sides and top of the solid material are usually assumed to be insulated. The overall width, height and length of the heat sink are B_T, H and L, respectively. The channels have a width of $2B_c$ and height of H_c, and are separated by a distance of $2B$ in the horizontal (X) direction. The coolant enters the channels with an average velocity W_{in}.

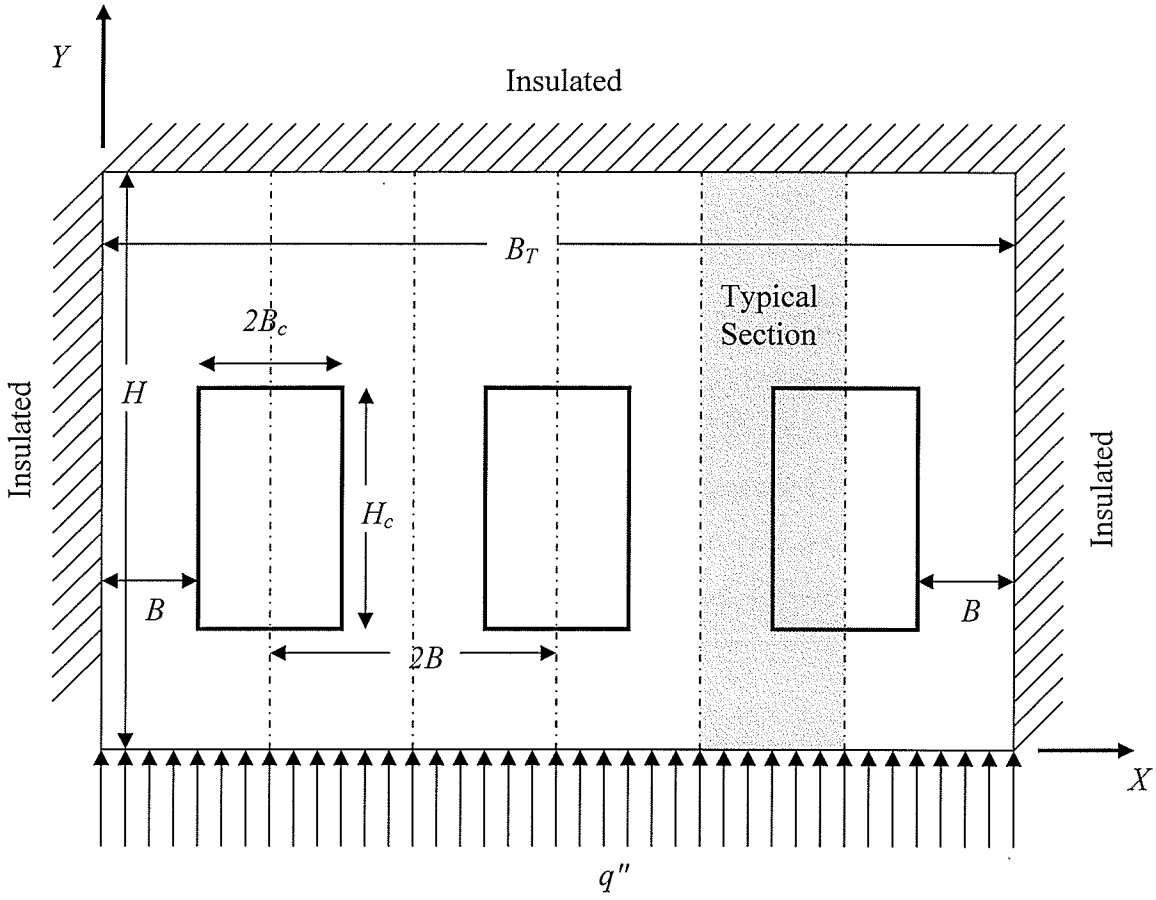

Figure 1.2: Schematic Representation of a Generic Microchannel Heat Sink, Two-Dimensional View

Because of the symmetry in the geometry and boundary conditions, it is possible to simplify the analysis by considering only one typical section, which is $\frac{1}{2N}$ the size of the total domain, where N is the number of channels.

It should be noted that a number of characteristics of the heat sink arrangement

shown in Figures 1.1 and 1.2 can be varied. For example, while three channels are shown in these figures, any number of channels, within the limits of manufacturability, is possible. Furthermore, while rectangular channels are shown, other shapes are possible (for example, circular channels). Theoretically, the channels do not even need to be of the same size and shape. The arrangement of the channels can also be varied. For example, instead of positioning the channels in a single row, it is possible to use two or more rows of channels.

1.2 Purpose and Scope

To the best knowledge of the author, few studies have considered the possibility of using multiple rows of channels (these studies will be discussed in greater detail in Chapter 2). Therefore, exploring the possibility of using multiple rows of channels is the main purpose of this thesis. This work will be limited in scope to considering two-row arrangements only. That is, multi-row designs with three or more rows will be excluded from study in this work. This would be a possible topic for further study.

1.3 Layout of Thesis

A review of existing literature in the area of microchannel heat sinks is presented in Chapter 2. The following chapter, Chapter 3, presents the solution approach. This includes a description of the cases to be considered, the assumptions made in the analysis, a few definitions, the governing equations, and a description of the software used to perform the analysis. Chapter 4 presents various validations and mesh independence tests, used to ensure that the present model is reliable. Results and discussions are presented in Chapter 5, with emphasis on understanding the physical phenomena occurring. Finally, a few closing remarks are presented in Chapter 6.

CHAPTER 2
LITERATURE REVIEW

Microchannel heat sinks are an important technological means of removing large amounts of heat from small spaces. They are effective because, with the channels being so small, a large surface-area-to-fluid-volume ratio is possible, which allows large heat transfer coefficients to be obtained. With the trend that computer chips are needing to dissipate increasing amounts of heat, and the simultaneous trend that these chips are getting smaller and smaller, the importance of microchannel heat sinks has increased in recent years. As a result, much research has been devoted to the topic of microchannel heat sinks. This chapter presents a sampling of some of these studies, with an emphasis on numerical studies.

2.1 Previous Work

Weisberg et al. (1992) examined microchannels of rectangular cross-section. They employed a two-dimensional numerical approach that consisted of simultaneously solving for the temperature distributions in the heat sink material and in the fluid (that is, they solved the *conjugate* heat transfer problem). They also presented a design algorithm that can be used to select the optimum dimensions of the heat exchanger.

Adams et al. (1998) performed an experimental investigation that examined the turbulent, forced-convection flow of water in circular microchannels. Using their own data, as well as other data available at the time, Adams et al. (1998) developed a correlation giving the Nusselt number for turbulent, single-phase forced convection in circular microchannels. Their correlation was based on the following ranges of data: diameters ranging from 0.102 [mm] to 1.09 [mm], Reynolds numbers ranging from 2.6×10^3 and 2.3×10^4, and Prandtl numbers ranging from 1.53 to 6.43. They obtained Nusselt numbers that are higher than those that would be predicted with conventional large channel correlations.

Fedorov and Viskanta (2000) developed a three-dimensional theoretical model that used the laminar incompressible Navier-Stokes equations to investigate the fluid flow and heat transfer in heat sinks with rectangular microchannels used for electronic packaging. They then validated their model by comparing their results (thermal resistance and friction coefficient) with

experimental data. They presented and discussed detailed temperature and heat flux distributions.

Tunc and Bayazitoglu (2002) also investigated heat transfer in rectangular microchannels. Their analysis was simplified by assuming that the flow is fully-developed, both hydrodynamically and thermally. However, they account for the so-called *velocity slip* that occurs for low channel sizes, resulting from the non-applicability of the continuum assumption for sufficiently small channels. Nusselt numbers for varying aspect ratios were reported.

Qu and Mudawar (2002) performed a three-dimensional numerical study of fluid flow and heat transfer in rectangular channels. They used a computer code based on the finite difference method and the SIMPLE algorithm. They validated their model by comparing their results with both analytical solutions and experimental data. It was found that the temperature rise of the heat sink can be approximated as linear along its length.

Owhaib and Palm (2004) performed experiments on circular microchannels with inner diameters of 0.8 [mm], 1.2 [mm] and 1.7 [mm]. The fluid was R134a. They compared their data with correlations suggested for microscale geometries, and classical (macroscale) correlations. Interestingly, the large scale correlations performed well, while none of the small scale correlations agreed well with their data. It was also found that, in the laminar regime, the heat transfer coefficients for all three diameters were nearly identical.

Kroeker et al. (2004) performed a three-dimensional numerical analysis of microchannel heat sinks with circular channels. The pressure drop and thermal characteristics of the heat sinks were investigated. Good agreement was obtained by Kroeker et al. (2004) between their results and existing experimental data. The effects of various geometrical parameters, material properties, and Reynolds number on the thermal performance of the heat sink were investigated. Kroeker et al. (2004) also compared circular channels to rectangular channels, finding that at the same Reynolds number and hydraulic diameter, rectangular channels have a lower thermal resistance. However, circular channels dissipate more heat per unit pumping power.

Li and Peterson (2007) have developed a full three-dimensional conjugate heat transfer model to study the heat transfer performance of silicon-based microchannel heat sinks. A simplified three-dimensional model, which they called the "semi-normalized 3-dimensional heat transfer model", was also developed. This simplified model was validated using the full three-

dimensional model. Using the simplified model, the geometric structure of the microchannel heat sink was optimized, and the optimized geometric parameters were presented.

The studies discussed so far have dealt with channels of rectangular and circular geometry, and have been performed experimentally and using analyses of varying degrees of complexity. However, none of them explored the design alternative of "stacking" more than one row of channels.

To the best knowledge of the present author, the first study to begin exploring this possibility of employing more than one row of channels in the design of microchannel heat sinks was conducted by Vafai and Zhu (1999). They selected one geometry and a set of operating conditions, and solved for the temperature distributions, assuming fully-developed inlet velocity conditions in their analysis. They presented the temperature distributions thus-obtained. Furthermore, they presented a technique to determine the optimal set of geometric design parameters. They found that the two-layered design is a substantial improvement, in terms of thermal resistance and uniformity of temperatures over the heated surface, over the conventional one-layered design. Their study only considered counter-flow (that is, the flow in the upper layer is in the opposite direction to the flow in the lower layer).

Ng and Poh (2001) developed a code, using the finite volume method, to simultaneously solve for the temperature distributions in the solid and fluid regions of a double-layer microchannel heat sink with rectangular channels. Fully-developed velocity conditions were assumed in the inlet. When accounting for the electric double layer effects, there was a source term in the momentum equation. It was found that the electric double layer effects were significant, particularly for hydraulic diameters of 40 [μm] or less. Ng and Poh (2001) found lower thermal resistances when using the double-layer configuration as compared to the single-layer configuration.

Chong et al. (2002) performed optimizations on a single-layer counter-flow microchannel heat exchanger with rectangular channels, and on a double-layer counter-flow heat exchanger with rectangular channels (similar to the one presented by Vafai and Zhu(1999)). Their analysis was somewhat rudimentary, using a thermal resistance network to analyze the heat transfer. They performed some calculations using the FLUENT computer program, and used these to validate their simplified approach based on the thermal resistance network. Their optimization

results showed that, for both types of heat exchangers analyzed, operation in the laminar flow regime outperforms operation in the turbulent flow regime, in terms of both heat transfer and fluid flow considerations.

Wei and Joshi (2004) numerically studied microchannel heat sinks with multiple rows of rectangular channels. They performed their analysis using both a simplified thermal resistance network method, and by writing a FORTRAN program which made use of the symmetrically coupled Gauss-Seidel (SCGS) multigrid method. They studied the effect of channel aspect ratio, and the number of layers (up to 5 layers). They found that for a given pumping power and heat removal, the necessary overall mass flow rate was lower for cases of multiple rows of channels.

Skandakumaran et al. (2004) performed an experimental investigation of multi-layered SiC microchannel heat sinks, fabricated using an extrusion freeform fabrication (EFF) technique. Their experimental data, which were gathered for cases of one, two and four rows of channels, were compared to the results of closed-form analytical solutions, derived based on thermal resistance network analyses. They found that multi-layered heat sinks have lower thermal resistances than single-row heat sinks, and that, for the same overall flow rate, the overall pressure drop was reduced for greater number of layers.

Cheng (2007) presented a three-dimensional numerical investigation of a two-layered microchannel heat sink with counter-flow, similar to that studied by Vafai and Zhu (1999), but with one important difference: the inclusion, along the length of the channels, of several rectangular embedded structures, designed to promote mixing of the flow within the channels. The ratio of the height of these embedded structures over the total microchannel height was varied from 0.13 to 0.26. Only one Reynolds number was considered, namely 14.8. It was found that the thermal resistance obtained using the embedded structures was lower than that obtained without using these embedded structures.

2.2 Contributions of this Thesis

There have been relatively few studies that examined the possibility of employing more than one row of channels in microchannel heat sink designs. The work of Vafai and Zhu (1999) was, to the best knowledge of the author, the first work to explore this possibility. While it was indeed an important contribution to the field of microchannel heat sinks, their work was

somewhat limited in scope. The analysis made the assumption of fully-developed flow conditions throughout the channels. In the present work, the computations were performed using the more realistic condition of having a uniform velocity in the inlet, and allowing the flow to develop. Vafai and Zhu (1999) used only one, low value of Reynolds number. In this thesis, high and low Reynolds numbers, within the laminar flow regime, were investigated. The purpose performing the present computations for both high and low Reynolds number was to explore the validity of the assumption of fully-developed inlet velocity. It was thought that this assumption may be valid only at low Reynolds numbers where the developing length occupies a small portion of the total flow channel. In terms of two-row designs, Vafai and Zhu (1999) only considered the case of counter-flow, while this work examined both the counter-flow and parallel-flow designs. Finally, in the work of Vafai and Zhu (1999), a comparison was made between the single-row design and the two-row design whereby their two-row design was compared to a single-row design that had half the mass flowrate and occupied half the space as this two-row design. In the present work, a more interesting comparison was made, whereby the two-row design was compared to a single-row design that used the same overall mass flowrate and occupied the same overall dimensions as the two-row design.

In this work, the main thermal criteria used to judge the various heat sink designs were that the temperature on the heated surface be as low as possible, and as uniform as possible. Electronics perform better at lower temperatures, and a temperature distribution on the heated surface that is as uniform as possible was important because this avoids complications due to thermal stresses that can occur due to mis-matches in the coefficient of thermal expansion.

CHAPTER 3
SOLUTION APPROACH

In order to explore two-row microchannels, especially in relation to their single-row counterparts, a number of cases were examined in this work. These cases are presented and described next.

3.1 Cases Considered

Each case examined in this work can be characterized by a set of three specifications: the flow arrangement (including the geometry, and the direction of fluid flow), the inlet velocity profile assumption (uniform or fully-developed), and the Reynolds number (high or low). More details on these specifications, and the reasons for their choice, follow.

Vafai and Zhu's (1999) arrangement (termed, in this work, the *counter-flow* arrangement) is shown schematically, in cross-section view, in Figure 3.1. The bottom surface receives a uniform heat flux, q''. The top and left surfaces are insulated, while the right surface is a symmetry plane. The overall height is H, and the width of this repeat-unit is B. The length, perpendicular to the plane of this cross-section, is L. The two channels, which have their vertical mid-planes aligned to the right hand side of the domain, each have a height of H_c and a width of 2 B_c (the portion of the channels within the typical section is only half of this, however). The bottom of the bottom channel is located a distance of H_f above the bottom of the domain, and, the bottom of the top channel is located a distance of H_f above the top of the bottom channel. The flow in the top channel occurs in the positive Z-direction, while that in the bottom channel is in the negative Z-direction. The values of the geometric parameters are as follows:
H = 240 [μm], B = 60 [μm], L = 8000 [μm], H_c = 100 [μm], B_c = 30 [μm], and
H_f = 20 [μm].

It should be noted that Vafai and Zhu (1999) set up their Z axis in the opposite direction as is done in the present work. But, in order to obtain a right-handed coordinate system, it was necessary to reverse the direction of the Z axis. This is mentioned for the benefit of the reader who is consulting both this work and Vafai and Zhu (1999).

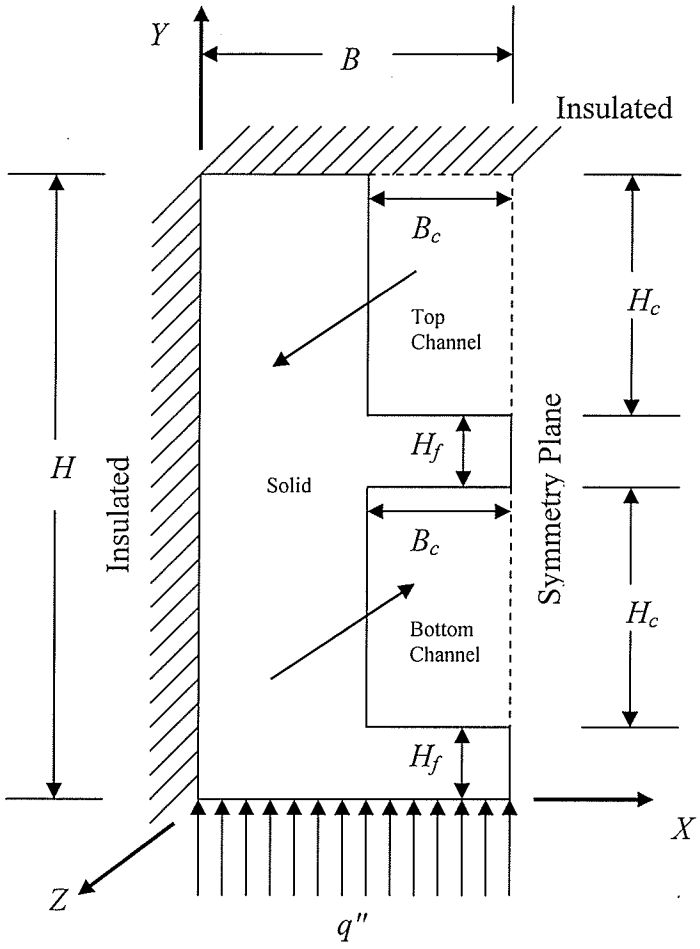

Figure 3.1: Schematic Representation of One Typical Section for the Counter-Flow Arrangement

The second arrangement, the *parallel-flow* arrangement, is shown in Figure 3.2. It is identical to the counter-flow arrangement in all respects but one: whereas in the counter-flow arrangement, the flow in the bottom channel is in the negative Z-direction, in the parallel-flow arrangement, it is in the positive Z-direction. Thus, for this arrangement, the flow in both channels is in the same direction, which explains the name. The geometry itself is identical to that of the counter-flow arrangement.

A typical section for the third arrangement, the *single channel (large)* arrangement, is shown schematically, in cross-section view, in Figure 3.3. This case can be thought of as a parallel-flow case, but where the solid between the top of the bottom channel, and bottom of the channel (that is, the shaded portion in Figure 3.3), is removed.

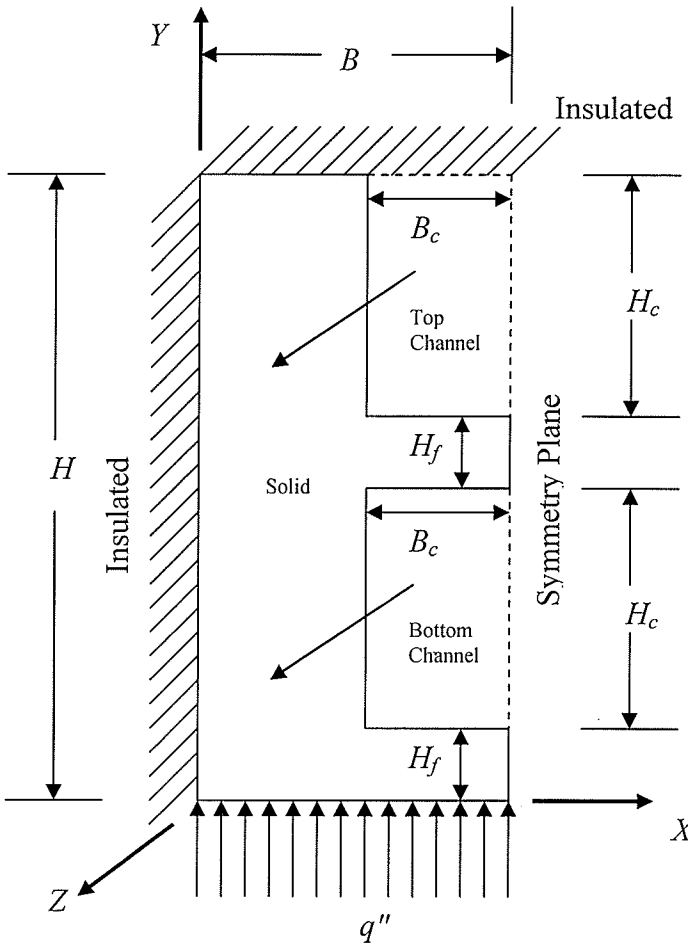

Figure 3.2: Schematic Representation of One Typical Section for the Parallel-Flow Arrangement

This results in a channel with a width of 2 B_c (only B_c inside the typical section) and a height of (2 H_c + H_f). While many choices were possible, the choice that was made in the present work was to put, in the channel, the total of what flowed in the parallel-flow arrangement in both channels. Thus, this single channel (large) arrangement is exactly like a parallel-flow arrangement, where the solid has been removed.

The fourth and final arrangement to be considered is the *single channel (small)* arrangement. It is shown, in cross-section view, in Figure 3.4. Here, there is only one single channel, of dimensions 2 B_c by H_c, which has the same dimensions as the individual channels on the two-row arrangements (counter-flow and parallel-flow). The mass flow rate in this channel is the same as what is in each individual channel in the

two-row cases.

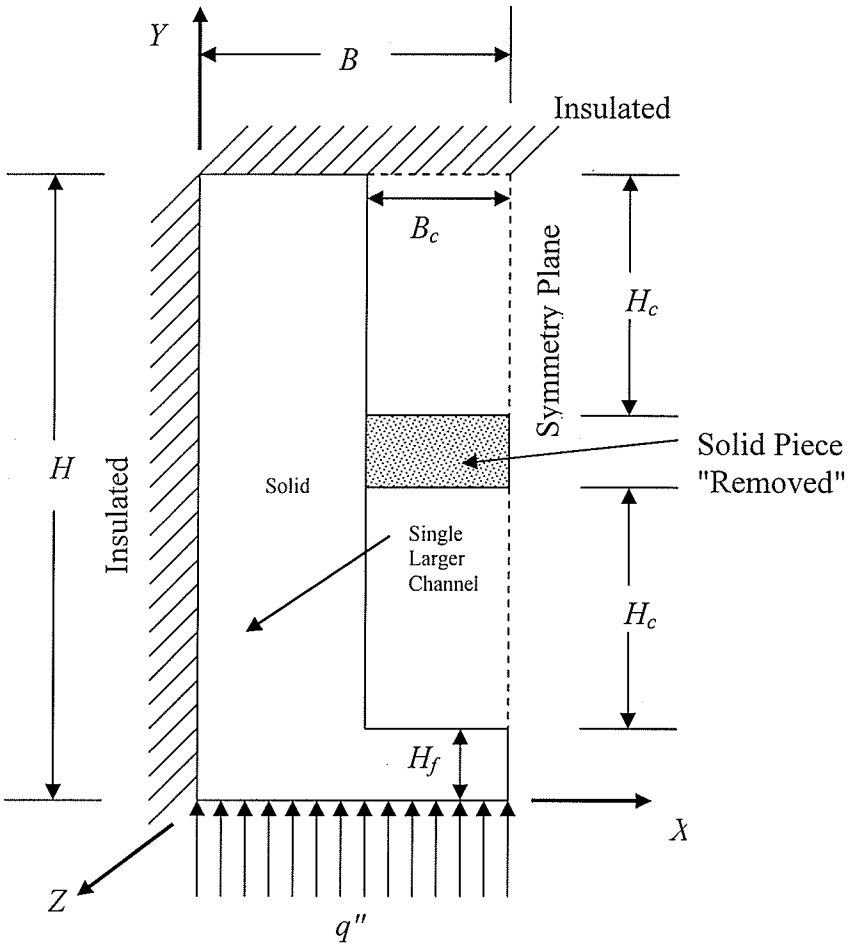

Figure 3.3: Schematic Representation of One Typical Section for the Single Channel (Large) Arrangement

This case is included for two reasons. First, Vafai and Zhu (1999) used this, and so, for comparison and consistency, it is examined here as well. The other reason is that this arrangement gives a good comparison with the two-row cases. It allows an answer to the question: given a single row of channels, what is the effect of adding another *identical* row, or "stack", on top of the first one?

The arrangements listed and described above are one of the characteristics that are necessary to specify the cases examined in this thesis. The other two characteristics to be specified are the Reynolds number and the inlet assumption.

Two different Reynolds numbers are examined in this thesis. The first,

designated in this work the "low Reynolds number", or "low Re", is the same Reynolds

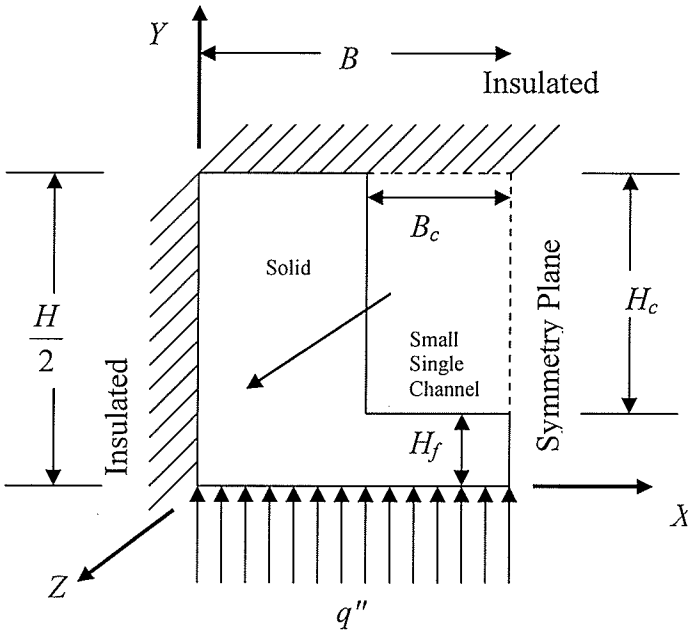

Figure 3.4: Schematic Representation of One Typical Section for the Single Channel (Small) Arrangement

number used by Vafai and Zhu (1999). This Reynolds number has a value of 115.96. Vafai and Zhu (1999) quoted this Reynolds number as 143.6. This is not incorrect per se, but, they arrived at this Reynolds number by employing a different definition for the hydraulic diameter. If one employs the standard hydraulic diameter definition, one arrives at a Reynolds of 115.96. But, to be clear, the low Re case in this case corresponds exactly to the velocity conditions used by Vafai and Zhu (1999). The second Reynolds number to be studied, called the "high Reynolds number", or "high Re" is 1159.6, or ten times the low Re. For the low Re cases, a heat flux, q'', of 3×10^5 [W/m^2] was used, to match what was used by Vafai and Zhu (1999). For the cases using a high Re, the heat flux was increased tenfold to 3×10^6 [W/m^2]. This was done to avoid small temperature differences, which can be problematic in the numerical computations.

The final characteristic that needs to be specified is the inlet velocity assumption. Two cases were explored. The first is a uniform inlet velocity assumption, where it is assumed that the flow enters the channel(s) uniformly in the Z-direction (or the negative

Z-direction, as applicable). The other case, which was the case studied by Vafai and Zhu (1999), is the fully-developed inlet velocity assumption. Here, the known fully-developed inlet velocity profile was fed into the inlets as a boundary condition, which simplified the analysis considerably.

In summary, the cases that will be examined in this thesis can be specified by three characteristics: the arrangement (counter-flow, parallel-flow, single channel (large) or single channel (small)), the Reynolds number (high (1159.6) or low (115.96)), and the inlet profile assumption (uniform, or fully-developed). Table 3.1 gives a summary of the cases examined in this thesis, as well as the numbering scheme used to designate the various cases. It should be noted that the case that matches Vafai and Zhu's (1999) work is Case number 2.

Table 3.1: Summary of Cases Examined in this Work

Case Number	Arrangement	Reynolds Number	Inlet Assumption
1	Counter-Flow	Low	Uniform
2	Counter-Flow	Low	Fully-Developed
3	Counter-Flow	High	Uniform
4	Counter-Flow	High	Fully-Developed
5	Parallel-Flow	Low	Uniform
6	Parallel-Flow	Low	Fully-Developed
7	Parallel-Flow	High	Uniform
8	Parallel-Flow	High	Fully-Developed
9	Single Channel (large)	Low	Uniform
10	Single Channel (large)	Low	Fully-Developed
11	Single Channel (large)	High	Uniform
12	Single Channel (large)	High	Fully-Developed
13	Single Channel (small)	Low	Uniform
14	Single Channel (small)	High	Uniform

What follows is the rationale for the choice of test cases.

Case 2 was chosen as a starting point, since, it matches the work of Vafai and Zhu (1999). Whereas Vafai and Zhu (1999) claimed, on the basis of a simple calculation, that

the fully-developed inlet velocity profile assumption would be adequate, it was desired to confirm (or possibly deny) this. Thus, Case 1 was chosen to see the effect of this assumption. Similarly, the remaining cases that employ the fully-developed inlet velocity assumption (that is, Cases 4, 6, 8, 10 and 12) were chosen for the same purpose: to see if the fully-developed inlet velocity assumption has any impact on the accuracy of the solution.

The decision to use two different Reynolds numbers was made to assess how the impact of making the fully-developed inlet velocity assumption on the solution accuracy might vary with Reynolds number. For example, even if it turns out that the fully-developed inlet velocity assumption can be made in certain cases, it was desired to find out if this assumption can be made generally, or only in certain conditions (for example, only at lower Reynolds number).

An important point should be mentioned. The discussion above implicitly assumes that the uniform inlet assumption is the "correct" inlet velocity assumption. This is necessarily the case. In reality, determining the velocity in the inlet requires a precise knowledge of the header arrangement. Since this arrangement is not specified in this work, it is not possible to know exactly what the inlet velocity will be. However, it is deemed on physical grounds that the uniform inlet velocity assumption, while not exact, is closer to reality than the fully-developed inlet flow assumption.

The choice of the four arrangements (counter-flow, parallel-flow, single channel (large) and single channel (small)) was made for a variety of reasons. The cases using the counter-flow arrangement were chosen simply because that is the arrangement that Vafai and Zhu (1999) chose. But, Vafai and Zhu (1999) simply used the counter-flow arrangement, claiming from the outset that this would be superior to the parallel-flow arrangement. Thus, it was desired in the present work to investigate to see if this holds true, and if so, to what extent. It should also be mentioned that the parallel-flow arrangement is much simpler to construct. If the performance is only slightly inferior to the counter-flow arrangement (assuming that it even is inferior in the first place), then, the parallel-flow arrangement might still be a better design. Additionally, it was desired to observe what differences exist, in terms of numerical solution requirements, between the parallel-flow and counter-flow arrangements.

Now, in order to assess the merits of two-row designs as compared to the single-row designs, it is necessary to explore single-row designs. That is why the single channel (large) and single channel (small) cases are included. The single channel (large) arrangement seems to be the more logical type to compare with the two-row designs, when the heat sink has the same overall dimensions and the same total mass flow rates as the two-row arrangements. This is because the single channel (large) arrangement, when compared to the two-row arrangements, addresses the question: which is better: one row of deep channels, or two rows of shallow channels? The single channel (small) arrangement, on the other hand, allows for an answer to the question: given a single-row of channels, if another identical row is added to the top (with, for the counter-flow arrangement, the flow in the opposite direction, and, for the parallel-flow, flow in the same direction), what is the effect? While this is not an ideal comparison, it is included for completeness, and to compare to what Vafai and Zhu (1999) studied. It should be noted that, for the single channel (small) arrangement, the runs were performed with uniform inlet assumption only. This is because these runs are of lesser importance, and, by the time these runs were to be performed, it was already known that the fully-developed inlet assumption would give excellent agreement with the uniform inlet.

With all of these runs, it is desired not only to assess the relative merits of each of the arrangements, but, it is also desired to obtain a detailed qualitative understanding of the heat transfer and fluid flow phenomena taking place.

3.2 Assumptions

In order to bring the analysis to a manageable level, a number of assumptions were made in this work. These are:

- Properties of the fluid and solid are constant and uniform.
- The flow is laminar (valid because only Reynolds numbers below 2300 are considered).
- Buoyancy effects are negligible (valid because the ratio of the Grashof number over the square of the Reynolds number is always significantly inferior to unity; a simple calculation reveals that this quantity is always of the order of 10^{-6} or smaller for every case examined in this work).

- The fluid flow and heat transfer processes are steady-state.
- Classical fluid mechanics are valid. That is, the continuum assumption remains valid.
- The fluid is incompressible, and behaves as a Newtonian fluid.

3.3 Governing Equations

The physical phenomena (heat transfer and fluid flow) taking place within the microchannel heat sinks obey a small set of well-established differential equations. Solving the problem consists of solving a fluid flow problem (in the fluid region(s) only), and a heat transfer problem (solved in the fluid region(s) and the solid region simultaneously). In the fluid region(s), the flow is governed by the conservation of mass equation, and, the momentum balance (Navier-Stokes) equation. The conservation of mass equation is, for steady-state conditions with constant properties,

$$\frac{\partial U}{\partial X}+\frac{\partial V}{\partial Y}+\frac{\partial W}{\partial Z}=0 \tag{3.1}$$

where U, V and W are the X-, Y- and Z-components of the fluid's velocity, respectively, and where X, Y and Z are the coordinate directions. The momentum equation is one vector equation in three components. For steady-state conditions and constant properties, in the absence of any body forces (such as gravity), the three components of the momentum equation are:

$$\rho_f U\frac{\partial U}{\partial X}+\rho_f V\frac{\partial U}{\partial Y}+\rho_f W\frac{\partial U}{\partial Z}=-\frac{\partial P}{\partial X}+\mu_f\left(\frac{\partial^2 U}{\partial X^2}+\frac{\partial^2 U}{\partial Y^2}+\frac{\partial^2 U}{\partial Z^2}\right) \tag{3.2a}$$

$$\rho_f U\frac{\partial V}{\partial X}+\rho_f V\frac{\partial V}{\partial Y}+\rho_f W\frac{\partial V}{\partial Z}=-\frac{\partial P}{\partial Y}+\mu_f\left(\frac{\partial^2 V}{\partial X^2}+\frac{\partial^2 V}{\partial Y^2}+\frac{\partial^2 V}{\partial Z^2}\right) \tag{3.2b}$$

$$\rho_f U\frac{\partial W}{\partial X}+\rho_f V\frac{\partial W}{\partial Y}+\rho_f W\frac{\partial W}{\partial Z}=-\frac{\partial P}{\partial Z}+\mu_f\left(\frac{\partial^2 W}{\partial X^2}+\frac{\partial^2 W}{\partial Y^2}+\frac{\partial^2 W}{\partial Z^2}\right) \tag{3.2c}$$

where ρ_f is the fluid's density, P is the fluid's pressure, and μ_f is the fluid's dynamic viscosity.

Together, Eqs. (3.1) and (3.2), along with appropriate boundary conditions (discussed later), form the set of equations that needs to be solved to obtain the velocity field. Once this velocity field is obtained, it can be used to solve the heat transfer

problem.

In the solid region, the heat transfer is governed by the well-known Laplace equation:

$$\nabla^2 T_s = \frac{\partial^2 T_s}{\partial X^2} + \frac{\partial^2 T_s}{\partial Y^2} + \frac{\partial^2 T_s}{\partial Z^2} = 0 \tag{3.3}$$

where T_s is the temperature field in the solid, and ∇^2 is the Laplacian operator. In the fluid region, for steady-state conditions with constant properties, and neglecting viscous dissipation, the temperature distribution is governed by

$$U\frac{\partial T_f}{\partial X} + V\frac{\partial T_f}{\partial Y} + W\frac{\partial T_f}{\partial Z} = \alpha_f\left(\frac{\partial^2 T_f}{\partial X^2} + \frac{\partial^2 T_f}{\partial Y^2} + \frac{\partial^2 T_f}{\partial Z^2}\right) \tag{3.4}$$

where T_f is the temperature of the fluid, and α_f is the thermal diffusivity of the fluid, which is defined as

$$\alpha_f = \frac{k_f}{\rho_f C_{p,f}} \tag{3.5}$$

where k_f is the thermal conductivity of the fluid, and $C_{p,f}$ is the constant pressure specific heat of the fluid.

Thus, to obtain the temperature distributions in the fluid and the solid (T_f and T_s, respectively), it is necessary to execute the following steps:

- Solve Eqs. (3.1) and (3.2), to obtain the pressure field, P, as well as the three components of the velocity field, U, V and W.
- Using the U, V and W fields obtained in the previous step, solve Eqs. (3.3) and (3.4) to yield the temperature fields T_f and T_s.

It should be noted that T_f and T_s cannot be calculated separately; they must be calculated simultaneously. Because of this, it is said that the heat transfer problem is a *conjugate* heat transfer problem. The details of how the two fields are "connected" together are presented below.

It should also be noted that the heat transfer and fluid flow problems are *de-coupled*. This means that it is possible to solve the fluid flow problem independently of the heat transfer problem, and then, to simply use the resulting velocity field as input to the heat transfer problem. This is a desirable feature, which arises in part because the effect of temperature on the properties, as well as buoyancy effects, are neglected.

The governing equations themselves are the same for every arrangement considered in this thesis (counter-flow, parallel-flow, single channel (large) and single channel (small)). However, the problems differ, for each of the arrangements, by the regions over which the governing equations are to be solved (which are specified by the sizes and shapes of the domains), and by the boundary conditions. What follows is a detailed listing, for each arrangement, of the regions over which the governing equations are to be solved, the boundary conditions, and mathematical expressions of the equations used to "connect" the temperature field in the solid region to that in the fluid region(s).

For the counter-flow arrangement, Eqs. (3.1), (3.2) and (3.4) are to be solved in the following regions: $(B-B_c) \le X \le B$, $H_f \le Y \le (H_f + H_c)$, $0 \le Z \le L$ (the bottom channel), and on $(B-B_c) \le X \le B$, $(2H_f + H_c) \le Y \le H$, $0 \le Z \le L$ (the top channel). Eq. (3.3) is to be solved at every point in the solid region, which is given by the sum of the following three sub-regions: the sub-region $0 \le X \le (B-B_c)$, $0 \le Y \le H$, $0 \le Z \le L$, the sub-region $(B-B_c) \le X \le B$, $0 \le Y \le H_f$, $0 \le Z \le L$ and the sub-region $(B-B_c) \le X \le B$, $(H_f + H_c) \le Y \le (2H_f + H_c)$, $0 \le Z \le L$. For the solid region, for the counter-flow arrangement, the relevant boundary conditions are as follows:

$$\left.\frac{\partial T_s}{\partial Z}\right|_{\substack{Z=0,0\le X\le(B-B_c),0\le Y\le H;\\ Z=0,(B-B_c)\le X\le B,0\le Y\le H_f;\\ Z=0,(B-B_c)\le X\le B,(H_f+H_c)\le Y\le(2H_f+H_c)}} = 0 \tag{3.6}$$

$$\left.\frac{\partial T_s}{\partial Z}\right|_{\substack{Z=L,0\le X\le(B-B_c),0\le Y\le H;\\ Z=L,(B-B_c)\le X\le B,0\le Y\le H_f;\\ Z=L,(B-B_c)\le X\le B,(H_f+H_c)\le Y\le(2H_f+H_c)}} = 0 \tag{3.7}$$

$$\left.\frac{\partial T_s}{\partial X}\right|_{X=0,0\le Y\le H,0\le Z\le L} = 0 \tag{3.8}$$

$$\left.\frac{\partial T_s}{\partial X}\right|_{\substack{X=B,0\le Y\le H_f,0\le Z\le L;\\ X=B,(H_f+H_c)\le Y\le(2H_f+H_c),0\le Z\le L}} = 0 \tag{3.9}$$

$$\left.\frac{\partial T_s}{\partial Y}\right|_{Y=H,0\le X\le(B-B_c),0\le Z\le L} = 0 \tag{3.10}$$

$$-k_s \left.\frac{\partial T_s}{\partial Y}\right|_{Y=0,0\le X\le B,0\le Z\le L} = q'' \tag{3.11}$$

where k_s is the thermal conductivity of the solid.

For the bottom channel, again looking at the counter-flow arrangement, the hydrodynamic boundary conditions are as follows:

$$U\big|_{Z=L,(B-B_c)\le X\le B,H_f\le Y\le(H_f+H_c)} = 0 \tag{3.12a}$$

$$V\big|_{Z=L,(B-B_c)\le X\le B,H_f\le Y\le(H_f+H_c)} = 0 \tag{3.12b}$$

$$W\big|_{Z=L,(B-B_c)\le X\le B,H_f\le Y\le(H_f+H_c)} = -W_{in} \tag{3.12c}$$

$$\overline{P}\big|_{Z=0,(B-B_c)\le X\le B,H_f\le Y\le(H_f+H_c)} = 0 \tag{3.13}$$

$$U\big|_{X=(B-B_c),H_f\le Y\le(H_f+H_c),0\le Z\le L} = 0 \tag{3.14a}$$

$$V\big|_{X=(B-B_c),H_f\le Y\le(H_f+H_c),0\le Z\le L} = 0 \tag{3.14b}$$

$$W\big|_{X=(B-B_c),H_f\le Y\le(H_f+H_c),0\le Z\le L} = 0 \tag{3.14c}$$

$$U\big|_{Y=H_f,(B-B_c)\le X\le B,0\le Z\le L} = 0 \tag{3.15a}$$

$$V\big|_{Y=H_f,(B-B_c)\le X\le B,0\le Z\le L} = 0 \tag{3.15b}$$

$$W\big|_{Y=H_f,(B-B_c)\le X\le B,0\le Z\le L} = 0 \tag{3.15c}$$

$$U\big|_{Y=(H_f+H_c),(B-B_c)\le X\le B,0\le Z\le L} = 0 \tag{3.16a}$$

$$V\big|_{Y=(H_f+H_c),(B-B_c)\le X\le B,0\le Z\le L} = 0 \tag{3.16b}$$

$$W\big|_{Y=(H_f+H_c),(B-B_c)\le X\le B,0\le Z\le L} = 0 \tag{3.16c}$$

$$U\big|_{X=B,H_f\le Y\le(H_f+H_c),0\le Z\le L} = 0 \tag{3.17a}$$

$$\left.\frac{\partial V}{\partial X}\right|_{X=B,H_f\le Y\le(H_f+H_c),0\le Z\le L} = 0 \tag{3.17b}$$

$$\left.\frac{\partial W}{\partial X}\right|_{X=B,H_f\le Y\le(H_f+H_c),0\le Z\le L} = 0 \tag{3.17c}$$

where W_{in} is the *magnitude* of the inlet velocity and $\overline{P}\big|_{Z=0,(B-B_c)\le X\le B,H_f\le Y\le(H_f+H_c)}$ is the average pressure at the bottom channel outlet. Eqs. (3.14) - (3.16) are called the *no-slip* boundary conditions, while Eqs. (3.17) express a *symmetry* boundary condition. It should

be noted that, since the bottom channel has six boundaries, it has six hydrodynamic boundary conditions. The thermal boundary conditions of the bottom channel are as follows:

$$T_f\Big|_{Z=L,(B-B_c)\le X\le B,H_f\le Y\le(H_f+H_c)} = T_{in} \tag{3.18}$$

$$\left.\frac{\partial T_f}{\partial Z}\right|_{Z=0,(B-B_c)\le X\le B,H_f\le Y\le(H_f+H_c)} = 0 \tag{3.19}$$

$$\left.\frac{\partial T_f}{\partial X}\right|_{X=B,H_f\le Y\le(H_f+H_c),0\le Z\le L} = 0 \tag{3.20}$$

where T_{in} is the uniform inlet temperature of the channels. It should be noted that Eq. (3.19) is an approximation, since, the slope of the temperature profile at the outlet is not known. It should be noted that there are only three thermal boundary conditions presented above, because the remaining three boundaries do not have thermal boundary conditions per se. They have, instead, equations that "connect" the temperature field in the bottom channel to that in the solid. Mathematically, these conditions can be expressed as follows:

$$T_f\Big|_{X=(B-B_c),H_f\le Y\le(H_f+H_c),0\le Z\le L} = T_s\Big|_{X=(B-B_c),H_f\le Y\le(H_f+H_c),0\le Z\le L} \tag{3.21}$$

$$k_f\left.\frac{\partial T_f}{\partial X}\right|_{X=(B-B_c),H_f\le Y\le(H_f+H_c),0\le Z\le L} = k_s\left.\frac{\partial T_s}{\partial X}\right|_{X=(B-B_c),H_f\le Y\le(H_f+H_c),0\le Z\le L} \tag{3.22}$$

$$T_f\Big|_{Y=H_f,(B-B_c)\le X\le B,0\le Z\le L} = T_s\Big|_{Y=H_f,(B-B_c)\le X\le B,0\le Z\le L} \tag{3.23}$$

$$k_f\left.\frac{\partial T_f}{\partial Y}\right|_{Y=H_f,(B-B_c)\le X\le B,0\le Z\le L} = k_s\left.\frac{\partial T_s}{\partial Y}\right|_{Y=H_f,(B-B_c)\le X\le B,0\le Z\le L} \tag{3.24}$$

$$T_f\Big|_{Y=(H_f+H_c),(B-B_c)\le X\le B,0\le Z\le L} = T_s\Big|_{Y=(H_f+H_c),(B-B_c)\le X\le B,0\le Z\le L} \tag{3.25}$$

$$k_f\left.\frac{\partial T_f}{\partial Y}\right|_{Y=(H_f+H_c),(B-B_c)\le X\le B,0\le Z\le L} = k_s\left.\frac{\partial T_s}{\partial Y}\right|_{Y=(H_f+H_c),(B-B_c)\le X\le B,0\le Z\le L} \tag{3.26}$$

These conditions enforce the physical requirements that no discontinuity in temperature, and no discontinuity in heat flux, occur across any of the solid-fluid interfaces of the bottom channel and the solid region.

For the top channel (still looking at the counter-flow arrangement), the hydrodynamic boundary conditions are

$$U\big|_{Z=0,(B-B_c)\le X\le B,(2H_f+H_c)\le Y\le H} = 0 \tag{3.27a}$$

$$V\big|_{Z=0,(B-B_c)\le X\le B,(2H_f+H_c)\le Y\le H} = 0 \tag{3.27b}$$

$$W\big|_{Z=0,(B-B_c)\le X\le B,(2H_f+H_c)\le Y\le H} = W_{in} \tag{3.27c}$$

$$\overline{P}\big|_{Z=L,(B-B_c)\le X\le B,(2H_f+H_c)\le Y\le H} = 0 \tag{3.28}$$

$$U\big|_{X=(B-B_c),(2H_f+H_c)\le Y\le H,0\le Z\le L} = 0 \tag{3.29a}$$

$$V\big|_{X=(B-B_c),(2H_f+H_c)\le Y\le H,0\le Z\le L} = 0 \tag{3.29b}$$

$$W\big|_{X=(B-B_c),(2H_f+H_c)\le Y\le H,0\le Z\le L} = 0 \tag{3.29c}$$

$$U\big|_{Y=(2H_f+H_c),(B-B_c)\le X\le B,0\le Z\le L} = 0 \tag{3.30a}$$

$$V\big|_{Y=(2H_f+H_c),(B-B_c)\le X\le B,0\le Z\le L} = 0 \tag{3.30b}$$

$$W\big|_{Y=(2H_f+H_c),(B-B_c)\le X\le B,0\le Z\le L} = 0 \tag{3.30c}$$

$$U\big|_{Y=H,(B-B_c)\le X\le B,0\le Z\le L} = 0 \tag{3.31a}$$

$$V\big|_{Y=H,(B-B_c)\le X\le B,0\le Z\le L} = 0 \tag{3.31b}$$

$$W\big|_{Y=H,(B-B_c)\le X\le B,0\le Z\le L} = 0 \tag{3.31c}$$

$$U\big|_{X=B,(2H_f+H_c)\le Y\le H,0\le Z\le L} = 0 \tag{3.32a}$$

$$\left.\frac{\partial V}{\partial X}\right|_{X=B,(2H_f+H_c)\le Y\le H,0\le Z\le L} = 0 \tag{3.32b}$$

$$\left.\frac{\partial W}{\partial X}\right|_{X=B,(2H_f+H_c)\le Y\le H,0\le Z\le L} = 0 \tag{3.32c}$$

and the thermal boundary conditions are

$$T_f\big|_{Z=0,(B-B_c)\le X\le B,(2H_f+H_c)\le Y\le H} = T_{in} \tag{3.33}$$

$$\left.\frac{\partial T_f}{\partial Z}\right|_{Z=L,(B-B_c)\le X\le B,(2H_f+H_c)\le Y\le H} = 0 \tag{3.34}$$

$$\left.\frac{\partial T_f}{\partial X}\right|_{X=B,(2H_f+H_c)\le Y\le H,0\le Z\le L} = 0 \tag{3.35}$$

$$\left.\frac{\partial T_f}{\partial Y}\right|_{Y=H,(B-B_c)\le X\le B,0\le Z\le L} = 0 \tag{3.36}$$

Because the top channel has no solid material above it, it has four proper boundary conditions, and only two fluid-solid interfaces with the solid region. The conditions imposed on these solid-fluid interfaces can be expressed as

$$T_f\big|_{X=(B-B_c),(2H_f+H_c)\le Y\le H,0\le Z\le L} = T_s\big|_{X=(B-B_c),(2H_f+H_c)\le Y\le H,0\le Z\le L} \tag{3.37}$$

$$k_f\left.\frac{\partial T_f}{\partial X}\right|_{X=(B-B_c),(2H_f+H_c)\le Y\le H,0\le Z\le L} = k_s\left.\frac{\partial T_s}{\partial X}\right|_{X=(B-B_c),(2H_f+H_c)\le Y\le H,0\le Z\le L} \tag{3.38}$$

$$T_f\big|_{Y=(2H_f+H_c),(B-B_c)\le X\le B,0\le Z\le L} = T_s\big|_{Y=(2H_f+H_c),(B-B_c)\le X\le B,0\le Z\le L} \tag{3.39}$$

$$k_f\left.\frac{\partial T_f}{\partial Y}\right|_{Y=(2H_f+H_c),(B-B_c)\le X\le B,0\le Z\le L} = k_s\left.\frac{\partial T_s}{\partial Y}\right|_{Y=(2H_f+H_c),(B-B_c)\le X\le B,0\le Z\le L} \tag{3.40}$$

Thus, the governing equations expressed by Eqs. (3.1) - (3.4), solved on the appropriate regions (identified above), subject to the boundary conditions and interface conditions expressed by Eqs. (3.6) - (3.40), comprise the complete mathematical formulation for the counter-flow arrangement.

Now, attention is focused on the parallel-flow arrangement. For the parallel-flow arrangement, Eqs. (3.1), (3.2) and (3.4) are to be solved on the following regions: $(B-B_c)\le X\le B$, $H_f\le Y\le(H_f+H_c)$, $0\le Z\le L$ (the bottom channel), and on $(B-B_c)\le X\le B$, $(2H_f+H_c)\le Y\le H$, $0\le Z\le L$ (the top channel). Eq. (3.3) is to be solved at every point in the solid region, which is given by the sum of the following three sub-regions: the sub-region $0\le X\le(B-B_c)$, $0\le Y\le H$, $0\le Z\le L$, the sub-region $(B-B_c)\le X\le B$, $0\le Y\le H_f$, $0\le Z\le L$ and the sub-region $(B-B_c)\le X\le B$, $(H_f+H_c)\le Y\le(2H_f+H_c)$, $0\le Z\le L$. For the solid region, for the parallel-flow arrangement, the relevant boundary conditions are

$$\left.\frac{\partial T_s}{\partial Z}\right|_{\substack{Z=0,0\le X\le(B-B_c),0\le Y\le H;\\ Z=0,(B-B_c)\le X\le B,0\le Y\le H_f;\\ Z=0,(B-B_c)\le X\le B,(H_f+H_c)\le Y\le(2H_f+H_c)}} = 0 \tag{3.41}$$

$$\left.\frac{\partial T_s}{\partial Z}\right|_{\substack{Z=L,0\le X\le(B-B_c),0\le Y\le H;\\ Z=L,(B-B_c)\le X\le B,0\le Y\le H_f;\\ Z=L,(B-B_c)\le X\le B,(H_f+H_c)\le Y\le(2H_f+H_c)}} = 0 \tag{3.42}$$

$$\left.\frac{\partial T_s}{\partial X}\right|_{X=0,0\le Y\le H,0\le Z\le L} = 0 \tag{3.43}$$

$$\left.\frac{\partial T_s}{\partial X}\right|_{\substack{X=B,0<Y<H_f,0<Z<L;\\ X=B,(H_f+H_c)<Y<(2H_f+H_c),0<Z<L}} = 0 \tag{3.44}$$

$$\left.\frac{\partial T_s}{\partial Y}\right|_{Y=H,0<X<(B-B_c),0<Z<L} = 0 \tag{3.45}$$

$$-k_s\left.\frac{\partial T_s}{\partial Y}\right|_{Y=0,0\le X\le B,0\le Z\le L} = q'' \tag{3.46}$$

For the bottom channel, for the parallel-flow arrangement, the hydrodynamic boundary conditions are as follows:

$$U\big|_{Z=0,(B-B_c)\le X\le B,H_f\le Y\le(H_f+H_c)} = 0 \tag{3.47a}$$

$$V\big|_{Z=0,(B-B_c)\le X\le B,H_f\le Y\le(H_f+H_c)} = 0 \tag{3.47b}$$

$$W\big|_{Z=0,(B-B_c)\le X\le B,H_f\le Y\le(H_f+H_c)} = 0 \tag{3.47c}$$

$$\overline{P}\big|_{Z=L,(B-B_c)\le X\le B,H_f\le Y\le(H_f+H_c)} = 0 \tag{3.48}$$

$$U\big|_{X=(B-B_c),H_f\le Y\le(H_f+H_c),0\le Z\le L} = 0 \tag{3.49a}$$

$$V\big|_{X=(B-B_c),H_f\le Y\le(H_f+H_c),0\le Z\le L} = 0 \tag{3.49b}$$

$$W\big|_{X=(B-B_c),H_f\le Y\le(H_f+H_c),0\le Z\le L} = 0 \tag{3.49c}$$

$$U\big|_{Y=H_f,(B-B_c)\le X\le B,0\le Z\le L} = 0 \tag{3.50a}$$

$$V\big|_{Y=H_f,(B-B_c)\le X\le B,0\le Z\le L} = 0 \tag{3.50b}$$

$$W\big|_{Y=H_f,(B-B_c)\le X\le B,0\le Z\le L} = 0 \tag{3.50c}$$

$$U\big|_{Y=(H_f+H_c),(B-B_c)\le X\le B,0\le Z\le L}=0 \tag{3.51a}$$

$$V\big|_{Y=(H_f+H_c),(B-B_c)\le X\le B,0\le Z\le L}=0 \tag{3.51b}$$

$$W\big|_{Y=(H_f+H_c),(B-B_c)\le X\le B,0\le Z\le L}=0 \tag{3.51c}$$

$$U\big|_{X=B,H_f\le Y\le(H_f+H_c),0\le Z\le L}=0 \tag{3.52a}$$

$$\left.\frac{\partial V}{\partial X}\right|_{X=B,H_f\le Y\le(H_f+H_c),0\le Z\le L}=0 \tag{3.52b}$$

$$\left.\frac{\partial W}{\partial X}\right|_{X=B,H_f\le Y\le(H_f+H_c),0\le Z\le L}=0 \tag{3.52c}$$

Eqs. (3.49) - (3.51) are the no-slip boundary conditions, while Eqs. (3.52) express a symmetry boundary condition. The thermal boundary conditions of the bottom channel, for the parallel-flow arrangement, are as follows:

$$T_f\big|_{Z=0,(B-B_c)\le X\le B,H_f\le Y\le(H_f+H_c)}=T_{in} \tag{3.53}$$

$$\left.\frac{\partial T_f}{\partial Z}\right|_{Z=L,(B-B_c)\le X\le B,H_f\le Y\le(H_f+H_c)}=0 \tag{3.54}$$

$$\left.\frac{\partial T_f}{\partial X}\right|_{X=B,H_f\le Y\le(H_f+H_c),0\le Z\le L}=0 \tag{3.55}$$

As was the case in the counter-flow arrangement, Eq. (3.54) is an approximation. The mathematical expressions ensuring continuity of temperature and heat flux at the solid-fluid interfaces between the solid region and the bottom channel are as follows:

$$T_f\big|_{X=(B-B_c),H_f\le Y\le(H_f+H_c),0\le Z\le L}=T_s\big|_{X=(B-B_c),H_f\le Y\le(H_f+H_c),0\le Z\le L} \tag{3.56}$$

$$k_f\left.\frac{\partial T_f}{\partial X}\right|_{X=(B-B_c),H_f\le Y\le(H_f+H_c),0\le Z\le L}=k_s\left.\frac{\partial T_s}{\partial X}\right|_{X=(B-B_c),H_f\le Y\le(H_f+H_c),0\le Z\le L} \tag{3.57}$$

$$T_f\big|_{Y=H_f,(B-B_c)\le X\le B,0\le Z\le L}=T_s\big|_{Y=H_f,(B-B_c)\le X\le B,0\le Z\le L} \tag{3.58}$$

$$k_f\left.\frac{\partial T_f}{\partial Y}\right|_{Y=H_f,(B-B_c)\le X\le B,0\le Z\le L}=k_s\left.\frac{\partial T_s}{\partial Y}\right|_{Y=H_f,(B-B_c)\le X\le B,0\le Z\le L} \tag{3.59}$$

$$T_f\big|_{Y=(H_f+H_c),(B-B_c)\le X\le B,0\le Z\le L}=T_s\big|_{Y=(H_f+H_c),(B-B_c)\le X\le B,0\le Z\le L} \tag{3.60}$$

$$k_f \left.\frac{\partial T_f}{\partial Y}\right|_{Y=(H_f+H_c),(B-B_c)\le X\le B,0\le Z\le L} = k_s \left.\frac{\partial T_s}{\partial Y}\right|_{Y=(H_f+H_c),(B-B_c)\le X\le B,0\le Z\le L} \tag{3.61}$$

Looking now at the top channel, for the parallel-flow case, the hydrodynamic boundary conditions are

$$U\big|_{Z=0,(B-B_c)\le X\le B,(2H_f+H_c)\le Y\le H} = 0 \tag{3.62a}$$

$$V\big|_{Z=0,(B-B_c)\le X\le B,(2H_f+H_c)\le Y\le H} = 0 \tag{3.62b}$$

$$W\big|_{Z=0,(B-B_c)\le X\le B,(2H_f+H_c)\le Y\le H} = 0 \tag{3.62c}$$

$$\overline{P}\big|_{Z=L,(B-B_c)\le X\le B,(2H_f+H_c)\le Y\le H} = 0 \tag{3.63}$$

$$U\big|_{X=(B-B_c),(2H_f+H_c)\le Y\le H,0\le Z\le L} = 0 \tag{3.64a}$$

$$V\big|_{X=(B-B_c),(2H_f+H_c)\le Y\le H,0\le Z\le L} = 0 \tag{3.64b}$$

$$W\big|_{X=(B-B_c),(2H_f+H_c)\le Y\le H,0\le Z\le L} = 0 \tag{3.64c}$$

$$U\big|_{Y=(2H_f+H_c),(B-B_c)\le X\le B,0\le Z\le L} = 0 \tag{3.65a}$$

$$V\big|_{Y=(2H_f+H_c),(B-B_c)\le X\le B,0\le Z\le L} = 0 \tag{3.65b}$$

$$W\big|_{Y=(2H_f+H_c),(B-B_c)\le X\le B,0\le Z\le L} = 0 \tag{3.65c}$$

$$U\big|_{Y=H,(B-B_c)\le X\le B,0\le Z\le L} = 0 \tag{3.66a}$$

$$V\big|_{Y=H,(B-B_c)\le X\le B,0\le Z\le L} = 0 \tag{3.66b}$$

$$W\big|_{Y=H,(B-B_c)\le X\le B,0\le Z\le L} = 0 \tag{3.66c}$$

$$U\big|_{X=B,(2H_f+H_c)\le Y\le H,0\le Z\le L} = 0 \tag{3.67a}$$

$$\left.\frac{\partial V}{\partial X}\right|_{X=B,(2H_f+H_c)\le Y\le H,0\le Z\le L} = 0 \tag{3.67b}$$

$$\left.\frac{\partial W}{\partial X}\right|_{X=B,(2H_f+H_c)\le Y\le H,0\le Z\le L} = 0 \tag{3.67c}$$

and the thermal boundary conditions are

$$T_f\big|_{Z=0,(B-B_c)\le X\le B,(2H_f+H_c)\le Y\le H} = T_{in} \tag{3.68}$$

$$\left.\frac{\partial T_f}{\partial Z}\right|_{Z=L,(B-B_c)\le X\le B,(2H_f+H_c)\le Y\le H} = 0 \tag{3.69}$$

$$\left.\frac{\partial T_f}{\partial X}\right|_{X=B,(2H_f+H_c)\le Y\le H,0\le Z\le L} = 0 \tag{3.70}$$

$$\left.\frac{\partial T_f}{\partial Y}\right|_{Y=H,(B-B_c)\le X\le B,0\le Z\le L} = 0 \tag{3.71}$$

The mathematical expressions ensuring continuity of temperature and heat flux at the solid-fluid interfaces between the solid region and the top channel are as follows:

$$T_f\Big|_{X=(B-B_c),(2H_f+H_c)\le Y\le H,0\le Z\le L} = T_s\Big|_{X=(B-B_c),(2H_f+H_c)\le Y\le H,0\le Z\le L} \tag{3.72}$$

$$k_f\left.\frac{\partial T_f}{\partial X}\right|_{X=(B-B_c),(2H_f+H_c)\le Y\le H,0\le Z\le L} = k_s\left.\frac{\partial T_s}{\partial X}\right|_{X=(B-B_c),(2H_f+H_c)\le Y\le H,0\le Z\le L} \tag{3.73}$$

$$T_f\Big|_{Y=(2H_f+H_c),(B-B_c)\le X\le B,0\le Z\le L} = T_s\Big|_{Y=(2H_f+H_c),(B-B_c)\le X\le B,0\le Z\le L} \tag{3.74}$$

$$k_f\left.\frac{\partial T_f}{\partial Y}\right|_{Y=(2H_f+H_c),(B-B_c)\le X\le B,0\le Z\le L} = k_s\left.\frac{\partial T_s}{\partial Y}\right|_{Y=(2H_f+H_c),(B-B_c)\le X\le B,0\le Z\le L} \tag{3.75}$$

Thus, the governing equations expressed by Eqs. (3.1) - (3.4), solved on the appropriate regions (identified above), subject to the boundary conditions and interface conditions expressed by Eqs. (3.41) - (3.75), comprise the complete mathematical formulation for the parallel-flow arrangement.

Next, the single channel (large) arrangement is considered. For the single channel (large) arrangement, Eqs. (3.1), (3.2) and (3.4) are to be solved on only one region, namely, inside the channel, or on $(B-B_c)\le X\le B$, $H_f\le Y\le H$, $0\le Z\le L$. Eq. (3.3) is to be solved on the solid region, which is the sum of the following two sub-regions: the sub-region $0\le X\le(B-B_c)$, $0\le Y\le H$, $0\le Z\le L$ and the sub-region $(B-B_c)\le X\le B$, $0\le Y\le H_f$, $0\le Z\le L$. For the solid region, for the single channel (large) arrangement, the relevant boundary conditions are

$$\left.\frac{\partial T_s}{\partial Z}\right|_{\substack{Z=0,0\le X\le(B-B_c),0\le Y\le H;\\ Z=0,(B-B_c)\le X\le B,0\le Y\le H_f}} = 0 \tag{3.76}$$

$$\left.\frac{\partial T_s}{\partial Z}\right|_{\substack{Z=L,0\le X\le(B-B_c),0\le Y\le H;\\ Z=L,(B-B_c)\le X\le B,0\le Y\le H_f}} = 0 \tag{3.77}$$

$$\left.\frac{\partial T_s}{\partial X}\right|_{X=0,0\le Y\le H,0\le Z\le L} = 0 \tag{3.78}$$

$$\left.\frac{\partial T_s}{\partial X}\right|_{X=B,0<Y<H_f,0<Z<L} = 0 \tag{3.79}$$

$$\left.\frac{\partial T_s}{\partial Y}\right|_{Y=H,0<X<(B-B_c),0<Z<L} = 0 \tag{3.80}$$

$$-k_s\left.\frac{\partial T_s}{\partial Y}\right|_{Y=0,0\le X\le B,0\le Z\le L} = q'' \tag{3.81}$$

For the channel region, for the single channel (large) arrangement, the hydrodynamic boundary conditions are as follows:

$$U\big|_{Z=0,(B-B_c)\le X\le B,H_f\le Y\le H} = 0 \tag{3.82a}$$

$$V\big|_{Z=0,(B-B_c)\le X\le B,H_f\le Y\le H} = 0 \tag{3.82b}$$

$$W\big|_{Z=0,(B-B_c)\le X\le B,H_f\le Y\le H} = W_{in,\,\text{large}} \tag{3.82c}$$

$$\overline{P}\big|_{Z=L,(B-B_c)\le X\le B,H_f\le Y\le H} = 0 \tag{3.83}$$

$$U\big|_{X=(B-B_c),H_f\le Y\le H,0\le Z\le L} = 0 \tag{3.84a}$$

$$V\big|_{X=(B-B_c),H_f\le Y\le H,0\le Z\le L} = 0 \tag{3.84b}$$

$$W\big|_{X=(B-B_c),H_f\le Y\le H,0\le Z\le L} = 0 \tag{3.84c}$$

$$U\big|_{Y=H_f,(B-B_c)\le X\le B,0\le Z\le L} = 0 \tag{3.85a}$$

$$V\big|_{Y=H_f,(B-B_c)\le X\le B,0\le Z\le L} = 0 \tag{3.85b}$$

$$W\big|_{Y=H_f,(B-B_c)\le X\le B,0\le Z\le L} = 0 \tag{3.85c}$$

$$U\big|_{Y=H,(B-B_c)\le X\le B,0\le Z\le L} = 0 \tag{3.86a}$$

$$V\big|_{Y=H,(B-B_c)\le X\le B,0\le Z\le L} = 0 \tag{3.86b}$$

$$W\big|_{Y=H,(B-B_c)\le X\le B,0\le Z\le L} = 0 \tag{3.86c}$$

$$U\big|_{X=B,H_f\le Y\le H,0\le Z\le L}=0 \tag{3.87a}$$

$$\left.\frac{\partial V}{\partial X}\right|_{X=B,H_f\le Y\le H,0\le Z\le L}=0 \tag{3.87b}$$

$$\left.\frac{\partial W}{\partial X}\right|_{X=B,H_f\le Y\le H,0\le Z\le L}=0 \tag{3.87c}$$

where $W_{in,\ large}$ is the inlet velocity to the large channel. It is calculated in such a way that, for the single channel (large) arrangement, the mass flow rate is the same as what flows in both rows of channels in the parallel-flow arrangement.

For the channel, again in the single channel (large) arrangement, the thermal boundary conditions are

$$T_f\big|_{Z=0,(B-B_c)\le X\le B,H_f\le Y\le H}=T_{in} \tag{3.88}$$

$$\left.\frac{\partial T_f}{\partial Z}\right|_{Z=L,(B-B_c)\le X\le B,H_f\le Y\le H}=0 \tag{3.89}$$

$$\left.\frac{\partial T_f}{\partial X}\right|_{X=B,H_f\le Y\le H,0\le Z\le L}=0 \tag{3.90}$$

$$\left.\frac{\partial T_f}{\partial Y}\right|_{Y=H,(B-B_c)\le X\le B,0\le Z\le L}=0 \tag{3.91}$$

The mathematical expressions ensuring continuity of temperature and heat flux at the solid-fluid interfaces between the solid region and the channel for the single channel (large) arrangement are as follows:

$$T_f\big|_{X=(B-B_c),H_f\le Y\le H,0\le Z\le L}=T_s\big|_{X=(B-B_c),H_f\le Y\le H,0\le Z\le L} \tag{3.92}$$

$$k_f\left.\frac{\partial T_f}{\partial X}\right|_{X=(B-B_c),H_f\le Y\le H,0\le Z\le L}=k_s\left.\frac{\partial T_s}{\partial X}\right|_{X=(B-B_c),H_f\le Y\le H,0\le Z\le L} \tag{3.93}$$

$$T_f\big|_{Y=H_f,(B-B_c)\le X\le B,0\le Z\le L}=T_s\big|_{Y=H_f,(B-B_c)\le X\le B,0\le Z\le L} \tag{3.94}$$

$$k_f\left.\frac{\partial T_f}{\partial Y}\right|_{Y=H_f,(B-B_c)\le X\le B,0\le Z\le L}=k_s\left.\frac{\partial T_s}{\partial Y}\right|_{Y=H_f,(B-B_c)\le X\le B,0\le Z\le L} \tag{3.95}$$

Thus, the governing equations expressed by Eqs. (3.1) - (3.4), solved on the

appropriate regions (identified above), subject to the boundary conditions and interface conditions expressed by Eqs. (3.76) - (3.95), comprise the complete mathematical formulation for the single channel (large) arrangement.

Finally, the single channel (small) arrangement is considered. For the single channel (small) arrangement, Eqs. (3.1), (3.2) and (3.4) are to be solved on only one region, namely, inside the channel, or in $(B-B_c)\le X\le B$, $H_f\le Y\le\frac{H}{2}$, $0\le Z\le L$. Eq. (3.3) is to be solved on the solid region, which is the sum of the following two sub-regions: the sub-region $0\le X\le(B-B_c)$, $0\le Y\le\frac{H}{2}$, $0\le Z\le L$ and the sub-region $(B-B_c)\le X\le B$, $0\le Y\le H_f$, $0\le Z\le L$.

For the solid region, for the single channel (small) arrangement, the boundary conditions are

$$\left.\frac{\partial T_s}{\partial Z}\right|_{\substack{Z=0,0\le X\le(B-B_c),0\le Y\le(H/2);\\ Z=0,(B-B_c)\le X\le B,0\le Y\le H_f}}=0 \tag{3.96}$$

$$\left.\frac{\partial T_s}{\partial Z}\right|_{\substack{Z=L,0\le X\le(B-B_c),0\le Y\le(H/2);\\ Z=L,(B-B_c)\le X\le B,0\le Y\le H_f}}=0 \tag{3.97}$$

$$\left.\frac{\partial T_s}{\partial X}\right|_{X=0,0\le Y\le(H/2),0\le Z\le L}=0 \tag{3.98}$$

$$\left.\frac{\partial T_s}{\partial X}\right|_{X=B,0<Y<H_f,0<Z<L}=0 \tag{3.99}$$

$$\left.\frac{\partial T_s}{\partial Y}\right|_{Y=(H/2),0<X<(B-B_c),0<Z<L}=0 \tag{3.100}$$

$$-k_s\left.\frac{\partial T_s}{\partial Y}\right|_{Y=0,0\le X\le B,0\le Z\le L}=q'' \tag{3.101}$$

For the channel region, for the single channel (small) arrangement, the hydrodynamic boundary conditions are as follows:

$$U|_{Z=0,(B-B_c)\le X\le B,H_f\le Y\le(H/2)}=0 \tag{3.102a}$$

$$V|_{Z=0,(B-B_c)\le X\le B,H_f\le Y\le(H/2)}=0 \tag{3.102b}$$

$$W\big|_{Z=0,(B-B_c)\le X\le B,H_f\le Y\le(H/2)} = 0 \tag{3.102c}$$

$$\overline{P}\big|_{Z=L,(B-B_c)\le X\le B,H_f\le Y\le(H/2)} = 0 \tag{3.103}$$

$$U\big|_{X=(B-B_c),H_f\le Y\le(H/2),0\le Z\le L} = 0 \tag{3.104a}$$

$$V\big|_{X=(B-B_c),H_f\le Y\le(H/2),0\le Z\le L} = 0 \tag{3.104b}$$

$$W\big|_{X=(B-B_c),H_f\le Y\le(H/2),0\le Z\le L} = 0 \tag{3.104c}$$

$$U\big|_{Y=H_f,(B-B_c)\le X\le B,0\le Z\le L} = 0 \tag{3.105a}$$

$$V\big|_{Y=H_f,(B-B_c)\le X\le B,0\le Z\le L} = 0 \tag{3.105b}$$

$$W\big|_{Y=H_f,(B-B_c)\le X\le B,0\le Z\le L} = 0 \tag{3.105c}$$

$$U\big|_{Y=(H/2),(B-B_c)\le X\le B,0\le Z\le L} = 0 \tag{3.106a}$$

$$V\big|_{Y=(H/2),(B-B_c)\le X\le B,0\le Z\le L} = 0 \tag{3.106b}$$

$$W\big|_{Y=(H/2),(B-B_c)\le X\le B,0\le Z\le L} = 0 \tag{3.106c}$$

$$U\big|_{X=B,H_f\le Y\le(H/2),0\le Z\le L} = 0 \tag{3.107a}$$

$$\left.\frac{\partial V}{\partial X}\right|_{X=B,H_f\le Y\le(H/2),0\le Z\le L} = 0 \tag{3.107b}$$

$$\left.\frac{\partial W}{\partial X}\right|_{X=B,H_f\le Y\le(H/2),0\le Z\le L} = 0 \tag{3.107c}$$

It should be noted that W_{in} here has the same value as it did for the counter-flow and parallel-flow arrangements.

For the channel, for the single channel (small) arrangement, the thermal boundary conditions are

$$T_f\big|_{Z=0,(B-B_c)\le X\le B,H_f\le Y\le(H/2)} = T_{in} \tag{3.108}$$

$$\left.\frac{\partial T_f}{\partial Z}\right|_{Z=L,(B-B_c)\le X\le B,H_f\le Y\le(H/2)} = 0 \tag{3.109}$$

$$\left.\frac{\partial T_f}{\partial X}\right|_{X=B,H_f\le Y\le(H/2),0\le Z\le L}=0 \tag{3.110}$$

$$\left.\frac{\partial T_f}{\partial Y}\right|_{Y=(H/2),(B-B_c)\le X\le B,0\le Z\le L}=0 \tag{3.111}$$

The mathematical expressions ensuring continuity of temperature and heat flux at the solid-fluid interfaces between the solid region and the channel for the single channel (small) arrangement are as follows:

$$T_f\Big|_{X=(B-B_c),H_f\le Y\le(H/2),0\le Z\le L}=T_s\Big|_{X=(B-B_c),H_f\le Y\le(H/2),0\le Z\le L} \tag{3.112}$$

$$k_f\left.\frac{\partial T_f}{\partial X}\right|_{X=(B-B_c),H_f\le Y\le(H/2),0\le Z\le L}=k_s\left.\frac{\partial T_s}{\partial X}\right|_{X=(B-B_c),H_f\le Y\le(H/2),0\le Z\le L} \tag{3.113}$$

$$T_f\Big|_{Y=H_f,(B-B_c)\le X\le B,0\le Z\le L}=T_s\Big|_{Y=H_f,(B-B_c)\le X\le B,0\le Z\le L} \tag{3.114}$$

$$k_f\left.\frac{\partial T_f}{\partial Y}\right|_{Y=H_f,(B-B_c)\le X\le B,0\le Z\le L}=k_s\left.\frac{\partial T_s}{\partial Y}\right|_{Y=H_f,(B-B_c)\le X\le B,0\le Z\le L} \tag{3.115}$$

Thus, the governing equations expressed by Eqs. (3.1) - (3.4), solved on the appropriate regions (identified above), subject to the boundary conditions and interface conditions expressed by Eqs. (3.96) - (3.115), comprise the complete mathematical formulation for the single channel (small) arrangement.

It should be noted that, in the above formulations for the boundary conditions, the equations were written for the cases of the uniform inlet velocity profile assumption. For the fully-developed case(s), one would need to replace W_{in} or $W_{in,\,large}$ by the appropriate fully-developed inlet velocity profiles. An analytical expression, in terms of a converging infinite series, giving the fully-developed velocity profile for rectangular channels can be found in Shah and London (1978). It is not quoted here, since, in this work, a different technique was employed to obtain the fully-developed velocity profile. This technique is discussed in more detail later.

The governing equations presented above for the four arrangements were not solved analytically. Instead, they were solved numerically, making use of a proprietary code. This is described later in Section 3.5.

3.4 Non-Dimensionalization

The mathematical problems presented in the previous section, as well as the solutions, can be non-dimensionalized. This is the purpose of this section.

Before non-dimensionalizing the governing equations and boundary conditions, a few definitions are required. The coordinate directions can be non-dimensionalized as

$$x = \frac{X}{B} \tag{3.116a}$$

$$y = \frac{Y}{B} \tag{3.116b}$$

$$z = \frac{Z}{B} \tag{3.116c}$$

where x, y and z are the non-dimensional coordinate directions. The various length parameters can be non-dimensionalized as follows, by dividing the dimensional values by B. Thus,

$$h = \frac{H}{B} \tag{3.117a}$$

$$h_f = \frac{H_f}{B} \tag{3.117b}$$

$$h_c = \frac{H_c}{B} \tag{3.117c}$$

$$b_c = \frac{B_c}{B} \tag{3.117d}$$

$$l = \frac{L}{B} \tag{3.117e}$$

It should be noted that, in Eqs. (3.115) and (3.116), the choice of dividing the lengths and coordinated directions by B is somewhat arbitrary. The dimensional velocity components can be non-dimensionalized by dividing them by W_{in}, as follows

$$u = \frac{U}{W_{in}} \tag{3.118a}$$

$$v = \frac{V}{W_{in}} \tag{3.118b}$$

$$w = \frac{W}{W_{in}} \tag{3.118c}$$

where u, v and w are the dimensionless velocity components in the x-, y- and z-directions, respectively. The velocity $W_{in\ large}$ can be non-dimensionalized by expressing it as a fraction of W_{in}, as follows

$$w_{in\ large} = \frac{W_{in\ large}}{W_{in}} \tag{3.119}$$

Because of the way the single channel (large) arrangement was defined, the following relation must hold

$$\dot{m}_{large} = \dot{m}_{top} + \dot{m}_{bottom} \tag{3.120}$$

where $\dot{m}_{bottom}$ is the mass flowrate of fluid flowing in the bottom channel for the parallel-flow arrangement, $\dot{m}_{top}$ is the mass flowrate of fluid flowing in the top channel for this same arrangement, and $\dot{m}_{large}$ is the mass flowrate of fluid flowing in the single large channel. Thus, by applying basic relations and simplifying, it can be shown that $w_{in\ large}$ can be expressed as

$$w_{in\ large} = \frac{2h_c}{2h_c + h_f} \tag{3.121}$$

The dimensionless pressure, p, is given by

$$p = \frac{P}{\frac{1}{2}\rho_f W_{in}^2} \tag{3.122}$$

It should be noted that, even when considering dimensionless pressures in the single channel (large) arrangement, the definition given by Eq. (3.121) still uses W_{in}, not $W_{in,\ large}$, in the denominator. However, the appropriate W_{in}, corresponding to the correct Reynolds number, must still be used. The Prandtl number of the fluid, Pr_f, which is a dimensionless property representing the ratio of the viscous diffusion rate to the thermal diffusion rate, is defined as

$$Pr_f = \frac{C_{p,f}\mu_f}{k_f} \tag{3.123}$$

The hydraulic diameter, D_h, which is used as a length scale for the Reynolds number,

defined below, is defined as

$$D_h \equiv 4\frac{A_{ch}}{P_{wetted}} \tag{3.124}$$

where A_{ch} is the cross-sectional area of a channel, and P_{wetted} is the wetted perimeter of a channel. For the counter-flow, parallel-flow and single channel (small) arrangements, the hydraulic diameter becomes

$$D_h = \frac{4B_c H_c}{2B_c + H_c} \tag{3.125a}$$

and, for the single channel (large) arrangement, the hydraulic diameter becomes

$$D_h = \frac{4B_c\left(2H_c + H_f\right)}{2B_c + \left(2H_c + H_f\right)} \tag{3.125b}$$

It should be noted that, in arriving at Eqs. (3.125), one must be careful to do one of the following: 1) remember that the portion of the channel(s) within the respective repeat-units is only half the width of the actual channels, due to symmetry; that is, take the area of the *whole* channel (not just the portion in the repeat-unit) and take the perimeter of the whole channel when applying Eq. (3.125a); or 2) consider only the portion of the channel(s) that are within the repeat-units; that is, for A_{ch}, take only the area of the channel within the repeat-unit (which will be half of the total area), but, for the wetted perimeter, ignore the side at the right-most of the domain (the symmetry side), since, it is not part of the *wetted* perimeter. Using either of these approaches will yield the correct, "standard" value for the hydraulic diameter. However, Vafai and Zhu (1999) used a different definition for the hydraulic diameter, which, when it is translated into the notation used in this work, becomes:

$$D_h\big|_{Vafai\ and\ Zhu} = \frac{4B_c H_c}{B_c + H_c} \tag{3.125c}$$

Thus, they only considered half of the domain when calculating the area, but, they neglected to realize that the wetted perimeter does not include the side of the half-channel that falls on the symmetry line. In this work, care was taken to use the proper, normal definition for the hydraulic diameter, as found, for example, in Fox and McDonald (1998).

The Reynolds number, which represents the ratio of inertial forces to viscous

forces, is defined as

$$Re_{D_h} = \frac{\rho_f W_{in} D_h}{\mu_f} \tag{3.126a}$$

for the counter-flow, parallel-flow and single channel (small) arrangements, and

$$Re_{D_h} = \frac{\rho_f W_{in\,large} D_h}{\mu_f} \tag{3.126b}$$

for the single channel (large) arrangement. The hydraulic diameter is different in the single channel (large) arrangement, and so, for this arrangement, it is necessary for the inlet velocity to be different in order to maintain the same Reynolds numbers as the other arrangements.

It should be noted that the above definitions use W_{in} (or $W_{in\,large}$) as a velocity scale. In cases where the uniform inlet profile assumption is made, this choice is easy to interpret. In cases where the fully-developed inlet profile assumption is made, however, the value of W_{in} can be thought of as either the value of the uniform inlet velocity of the corresponding uniform case, or, the *average* velocity of the fully-developed profile that is supplied as boundary condition.

The non-dimensional temperatures in the solid and fluid, θ_s and θ_f, respectively, are defined as

$$\theta_s = \frac{\left(T_s - T_{in}\right)}{\frac{q''B}{k_f}} \tag{3.127a}$$

and

$$\theta_f = \frac{\left(T_f - T_{in}\right)}{\frac{q''B}{k_f}} \tag{3.127b}$$

With these definitions in place, it is possible to non-dimensionalize the governing equations and the boundary and interface conditions. The non-dimensional counter-parts to Eq. (3.1) - (3.4) become, respectively

$$\frac{\partial u}{\partial x} + \frac{\partial v}{\partial y} + \frac{\partial w}{\partial z} = 0 \tag{3.128}$$

$$u\frac{\partial u}{\partial x}+v\frac{\partial u}{\partial y}+w\frac{\partial u}{\partial z}=-\frac{1}{2}\frac{\partial p}{\partial x}+\frac{1}{Re_{D_h}}\left(\frac{\partial^2 u}{\partial x^2}+\frac{\partial^2 u}{\partial y^2}+\frac{\partial^2 u}{\partial z^2}\right) \tag{3.129a}$$

$$u\frac{\partial v}{\partial x}+v\frac{\partial v}{\partial y}+w\frac{\partial v}{\partial z}=-\frac{1}{2}\frac{\partial p}{\partial y}+\frac{1}{Re_{D_h}}\left(\frac{\partial^2 v}{\partial x^2}+\frac{\partial^2 v}{\partial y^2}+\frac{\partial^2 v}{\partial z^2}\right) \tag{3.129b}$$

$$u\frac{\partial w}{\partial x}+v\frac{\partial w}{\partial y}+w\frac{\partial w}{\partial z}=-\frac{1}{2}\frac{\partial p}{\partial z}+\frac{1}{Re_{D_h}}\left(\frac{\partial^2 w}{\partial x^2}+\frac{\partial^2 w}{\partial y^2}+\frac{\partial^2 w}{\partial z^2}\right) \tag{3.129c}$$

$$\frac{\partial^2 \theta_s}{\partial x^2}+\frac{\partial^2 \theta_s}{\partial y^2}+\frac{\partial^2 \theta_s}{\partial z^2}=0 \tag{3.130}$$

$$u\frac{\partial \theta_f}{\partial x}+v\frac{\partial \theta_f}{\partial y}+w\frac{\partial \theta_f}{\partial z}=\frac{D_h}{B}\frac{1}{Pr_f Re_{D_h}}\left(\frac{\partial^2 \theta_f}{\partial x^2}+\frac{\partial^2 \theta_f}{\partial y^2}+\frac{\partial^2 \theta_f}{\partial z^2}\right) \tag{3.131}$$

It should be noted in passing that Eq. (3.131) contains the ratio $\frac{D_h}{B}$, which is not the same for every arrangement (it has the same value for the counter-flow, parallel-flow and single channel (small) arrangements, but, this value is different from that in the single channel (large) arrangement). Thus, Eq. (3.131) expresses a different equation for the single channel (large) arrangement as it does for the remaining arrangements. This would appear to suggest that, by non-dimensionalizing Eq. (3.4), which is identical for every arrangement, obtained Eq. (3.131) was obtained, which differs for some arrangements. It might appear, then, that the mere act of non-dimensionalizing the governing equations has somehow resulted in the undesirable outcome that the different arrangements obey different physical laws (since the governing equations are different for the various arrangements). This is not the case, however. It should be remembered that the complete formulation of a problem consists of the governing equations, the regions(s) on which the governing equations are to be solved, and the boundary conditions (and possibly also the interface conditions). The problem is not merely the governing equation itself. Thus, even in the dimensional cases, the problem formulations do differ for the different arrangements, even though the governing equations themselves are identical. Nonetheless, the various arrangements are all subject to the same physical "laws". This is easier to see in the dimensional formulations, since, the differences in the physical problems can be seen only in the ranges in which the equations are to be solved, and in

the boundary conditions. It is unfortunate that, in the dimensionless formulation, the differences in the problem formulation is not confined to the boundary conditions and ranges, but also in the governing equation itself. But, it would be a fallacy to think that the mere act of non-dimensionalising the equations has somehow changed the fact that all arrangements follow the same basic physical principles.

What follows is, for each arrangement, a list the regions(s) over which the equations are to be solved and the boundary conditions and interface conditions that apply.

For the counter-flow arrangement, Eqs. (3.128), (3.129) and (3.131) are to be solved on the following two ranges: the bottom channel, which is located in $(1-b_c)\le x\le 1$, $h_f \le y\le (h_f+h_c)$, $0\le z\le l$, and the top channel, which is located in $(1-b_c)\le x\le 1$, $(2h_f+h_c)\le y\le h$, $0\le z\le l$. Eq. (3.130) is to be solved on the solid region, which is given as the sum of the following three sub-regions: the sub-region $0\le x\le(1-b_c)$, $0\le y\le h, 0\le z\le l$, the sub-region $(1-b_c)\le x\le 1$, $0\le y\le h_f$, $0\le z\le l$ and the sub-region $(1-b_c)\le x\le 1$, $(h_f+h_c)\le y\le(2h_f+h_c)$, $0\le z\le l$.

For the solid region, for the counter-flow arrangement, the dimensionless boundary conditions are as follows

$$\left.\frac{\partial\theta_s}{\partial z}\right|_{z=0}=0 \tag{3.132}$$

$$\left.\frac{\partial\theta_s}{\partial z}\right|_{z=l}=0 \tag{3.133}$$

$$\left.\frac{\partial\theta_s}{\partial x}\right|_{x=0}=0 \tag{3.134}$$

$$\left.\frac{\partial\theta_s}{\partial x}\right|_{x=1}=0 \tag{3.135}$$

$$\left.\frac{\partial\theta_s}{\partial y}\right|_{y=h}=0 \tag{3.136}$$

$$\left.\frac{\partial\theta_s}{\partial y}\right|_{y=0}=-\frac{k_f}{k_s} \tag{3.137}$$

It should be noted that, for simplicity, the boundary conditions in Eqs. (3.132) - (3.137) are expressed in a somewhat simpler form than the form used above when presenting their dimensional counterparts. For example, Eq. (3.132), instead of being written out in full as $\left.\frac{\partial \theta_s}{\partial z}\right|_{\substack{z=0,0\le x\le(1-b_c),0\le y\le h;\\ z=0,(1-b_c)\le x\le b,0\le y\le h_f;\\ z=0,(1-b_c)\le x\le b,(h_f+h_c)\le y\le(2h_f+h_c)}} = 0$, it is simply written as $\left.\frac{\partial \theta_s}{\partial z}\right|_{z=0} = 0$. That is, it is simply stated that the derivative $\frac{\partial \theta_s}{\partial z}$ has value of zero at $z = 0$, without mentioning explicitly the regions, within the $z = 0$ plane, to which the boundary condition applies. This is done for the sake of avoiding overly cumbersome notation, and because a complete formulation has already been presented above. Furthermore, there should be no ambiguity as to which regions in the $z = 0$ plane are being referred to, as it was already specified that the boundary condition applies to the solid region. This simplified notation will be used in the remainder of this section.

For the bottom channel, for the counter-flow arrangement, the dimensionless hydrodynamic boundary conditions are as follows:

$$u\big|_{z=l} = 0 \tag{3.138a}$$

$$v\big|_{z=l} = 0 \tag{3.138b}$$

$$w\big|_{z=l} = -1 \tag{3.138c}$$

$$\overline{p}\big|_{z=0} = 0 \tag{3.139}$$

$$u\big|_{x=(1-b_c)} = 0 \tag{3.140a}$$

$$v\big|_{x=(1-b_c)} = 0 \tag{3.140b}$$

$$w\big|_{x=(1-b_c)} = 0 \tag{3.140c}$$

$$u\big|_{y=h_f} = 0 \tag{3.141a}$$

$$v\big|_{y=h_f} = 0 \tag{3.141b}$$

$$w\big|_{y=h_f} = 0 \tag{3.141c}$$

$$u\big|_{y=(h_f+h_c)} = 0 \tag{3.142a}$$

$$v\big|_{y=(h_f+h_c)} = 0 \tag{3.142b}$$

$$w\big|_{y=(h_f+h_c)} = 0 \tag{3.142c}$$

$$u\big|_{x=1} = 0 \tag{3.143a}$$

$$\left.\frac{\partial v}{\partial x}\right|_{x=1} = 0 \tag{3.143b}$$

$$\left.\frac{\partial w}{\partial x}\right|_{x=1} = 0 \tag{3.143c}$$

where $\overline{p}\big|_{z=0}$ is the average dimensionless pressure at the bottom channel outlet.

For the bottom channel, for the counter-flow arrangement, the non-dimensional thermal boundary conditions are

$$\theta_f\big|_{z=l} = 0 \tag{3.144}$$

$$\left.\frac{\partial \theta_f}{\partial z}\right|_{z=0} = 0 \tag{3.145}$$

$$\left.\frac{\partial \theta_f}{\partial x}\right|_{x=1} = 0 \tag{3.146}$$

The conditions that relate the bottom channel to the solid region are, in dimensionless form for the counter-flow case

$$\theta_f\big|_{x=(1-b_c)} = \theta_s\big|_{x=(1-b_c)} \tag{3.147}$$

$$\left.\frac{k_f}{k_s}\frac{\partial \theta_f}{\partial x}\right|_{x=(1-b_c)} = \left.\frac{\partial \theta_s}{\partial x}\right|_{x=(1-b_c)} \tag{3.148}$$

$$\theta_f\big|_{y=h_f} = \theta_s\big|_{y=h_f} \tag{3.149}$$

$$\left.\frac{k_f}{k_s}\frac{\partial \theta_f}{\partial y}\right|_{y=h_f} = \left.\frac{\partial \theta_s}{\partial y}\right|_{y=h_f} \tag{3.150}$$

$$\theta_f\big|_{y=(h_f+h_c)} = \theta_s\big|_{y=(h_f+h_c)} \tag{3.151}$$

$$\left.\frac{k_f}{k_s}\frac{\partial \theta_f}{\partial y}\right|_{y=(h_f+h_c)} = \left.\frac{\partial \theta_s}{\partial y}\right|_{y=(h_f+h_c)} \tag{3.152}$$

For the top channel, for the counter-flow arrangement, the dimensionless hydrodynamic boundary conditions are

$$u\big|_{z=0} = 0 \tag{3.153a}$$

$$v\big|_{z=0} = 0 \tag{3.153b}$$

$$w\big|_{z=0} = 1 \tag{3.153c}$$

$$\bar{p}\big|_{z=l} = 0 \tag{3.154}$$

$$u\big|_{x=(1-b_c)} = 0 \tag{3.155a}$$

$$v\big|_{x=(1-b_c)} = 0 \tag{3.155b}$$

$$w\big|_{x=(1-b_c)} = 0 \tag{3.155c}$$

$$u\big|_{y=(2h_f+h_c)} = 0 \tag{3.156a}$$

$$v\big|_{y=(2h_f+h_c)} = 0 \tag{3.156b}$$

$$w\big|_{y=(2h_f+h_c)} = 0 \tag{3.156c}$$

$$u\big|_{y=h} = 0 \tag{3.157a}$$

$$v\big|_{y=h} = 0 \tag{3.157b}$$

$$w\big|_{y=h} = 0 \tag{3.157c}$$

$$u\big|_{x=1} = 0 \tag{3.158a}$$

$$\left.\frac{\partial v}{\partial x}\right|_{x=1,} = 0 \tag{3.158b}$$

$$\left.\frac{\partial w}{\partial x}\right|_{x=1} = 0 \tag{3.158c}$$

and the thermal boundary conditions are

$$\theta_f\big|_{z=0} = 0 \tag{3.159}$$

$$\left.\frac{\partial \theta_f}{\partial z}\right|_{z=l} = 0 \tag{3.160}$$

$$\left.\frac{\partial \theta_f}{\partial x}\right|_{x=1} = 0 \tag{3.161}$$

$$\left.\frac{\partial \theta_f}{\partial y}\right|_{y=h} = 0 \tag{3.162}$$

The conditions that relate the top channel to the solid region are, in dimensionless form for the counter-flow case

$$\theta_f\big|_{x=(1-b_c)} = \theta_s\big|_{x=(1-b_c)} \tag{3.163}$$

$$\frac{k_f}{k_s}\left.\frac{\partial \theta_f}{\partial x}\right|_{x=(1-b_c)} = \left.\frac{\partial \theta_s}{\partial x}\right|_{x=(1-b_c)} \tag{3.164}$$

$$\theta_f\big|_{y=(2h_f+h_c)} = \theta_s\big|_{y=(2h_f+h_c)} \tag{3.165}$$

$$\frac{k_f}{k_s}\left.\frac{\partial \theta_f}{\partial y}\right|_{y=(2h_f+h_c)} = \left.\frac{\partial \theta_s}{\partial y}\right|_{y=(2h_f+h_c)} \tag{3.166}$$

Thus, the dimensionless governing equations expressed by Eqs. (3.128) - (3.131), solved on the appropriate regions (identified above), subject to the dimensionless boundary conditions and interface conditions expressed by Eqs. (3.132) - (3.166), comprise the complete dimensionless mathematical formulation for the counter-flow arrangement.

For the parallel-flow arrangement, Eqs. (3.128), (3.129) and (3.131) are to be solved on the following two ranges: the bottom channel, which is located in $(1-b_c) \le x \le 1$, $h_f \le y \le (h_f + h_c)$, $0 \le z \le l$, and the top channel, which is located in $(1-b_c) \le x \le 1$, $(2h_f + h_c) \le y \le h$, $0 \le z \le l$. Eq. (3.130) is to be solved on the solid region, which is given as the sum of the following three sub-regions: the sub-region $0 \le x \le (1-b_c)$, $0 \le y \le h, 0 \le z \le l$, the sub-region $(1-b_c) \le x \le 1$, $0 \le y \le h_f$, $0 \le z \le l$ and the sub-region $(1-b_c) \le x \le 1$, $(h_f + h_c) \le y \le (2h_f + h_c)$, $0 \le z \le l$.

For the solid region, for the parallel-flow arrangement, the dimensionless boundary conditions are as follows

$$\left.\frac{\partial \theta_s}{\partial z}\right|_{z=0} = 0 \tag{3.167}$$

$$\left.\frac{\partial \theta_s}{\partial z}\right|_{z=l} = 0 \tag{3.168}$$

$$\left.\frac{\partial \theta_s}{\partial x}\right|_{x=0} = 0 \tag{3.169}$$

$$\left.\frac{\partial \theta_s}{\partial x}\right|_{x=1} = 0 \tag{3.170}$$

$$\left.\frac{\partial \theta_s}{\partial y}\right|_{y=h} = 0 \tag{3.171}$$

$$\left.\frac{\partial \theta_s}{\partial y}\right|_{y=0} = -\frac{k_f}{k_s} \tag{3.172}$$

For the bottom channel, for the parallel-flow arrangement, the dimensionless hydrodynamic boundary conditions are as follows

$$u|_{z=0} = 0 \tag{3.173a}$$

$$v|_{z=0} = 0 \tag{3.173b}$$

$$w|_{z=0} = 1 \tag{3.173c}$$

$$\overline{p}|_{z=l} = 0 \tag{3.174}$$

$$u|_{x=(1-b_c)} = 0 \tag{3.175a}$$

$$v|_{x=(1-b_c)} = 0 \tag{3.175b}$$

$$w|_{x=(1-b_c)} = 0 \tag{3.175c}$$

$$u|_{y=h_f} = 0 \tag{3.176a}$$

$$v|_{y=h_f} = 0 \tag{3.176b}$$

$$w|_{y=h_f} = 0 \tag{3.176c}$$

$$u|_{y=(h_f+h_c)} = 0 \tag{3.177a}$$

$$v|_{y=(h_f+h_c)} = 0 \tag{3.177b}$$

$$w|_{y=(h_f+h_c)} = 0 \tag{3.177c}$$

$$u\big|_{x=1} = 0 \tag{3.178a}$$

$$\left.\frac{\partial v}{\partial x}\right|_{x=1} = 0 \tag{3.178b}$$

$$\left.\frac{\partial w}{\partial x}\right|_{x=1} = 0 \tag{3.178c}$$

and the non-dimensional thermal boundary conditions are

$$\theta_f\big|_{z=0} = 0 \tag{3.179}$$

$$\left.\frac{\partial \theta_f}{\partial z}\right|_{z=l} = 0 \tag{3.180}$$

$$\left.\frac{\partial \theta_f}{\partial x}\right|_{x=1} = 0 \tag{3.181}$$

The conditions that relate the bottom channel to the solid region are, in dimensionless form for the parallel-flow case

$$\theta_f\big|_{x=(1-b_c)} = \theta_s\big|_{x=(1-b_c)} \tag{3.182}$$

$$\left.\frac{k_f}{k_s}\frac{\partial \theta_f}{\partial x}\right|_{x=(1-b_c)} = \left.\frac{\partial \theta_s}{\partial x}\right|_{x=(1-b_c)} \tag{3.183}$$

$$\theta_f\big|_{y=h_f} = \theta_s\big|_{y=h_f} \tag{3.184}$$

$$\left.\frac{k_f}{k_s}\frac{\partial \theta_f}{\partial y}\right|_{y=h_f} = \left.\frac{\partial \theta_s}{\partial y}\right|_{y=h_f} \tag{3.185}$$

$$\theta_f\big|_{y=(h_f+h_c)} = \theta_s\big|_{y=(h_f+h_c)} \tag{3.186}$$

$$\left.\frac{k_f}{k_s}\frac{\partial \theta_f}{\partial y}\right|_{y=(h_f+h_c)} = \left.\frac{\partial \theta_s}{\partial y}\right|_{y=(h_f+h_c)} \tag{3.187}$$

For the top channel, for the parallel-flow arrangement, the dimensionless hydrodynamic boundary conditions are

$$u\big|_{z=0} = 0 \tag{3.188a}$$

$$v\big|_{z=0} = 0 \tag{3.188b}$$

$$w\big|_{z=0} = 1 \tag{3.188c}$$

$$\bar{p}\big|_{z=l} = 0 \tag{3.189}$$

$$u\big|_{x=(1-b_c)} = 0 \tag{3.190a}$$

$$v\big|_{x=(1-b_c)} = 0 \tag{3.190b}$$

$$w\big|_{x=(1-b_c)} = 0 \tag{3.190c}$$

$$u\big|_{y=(2h_f+h_c)} = 0 \tag{3.191a}$$

$$v\big|_{y=(2h_f+h_c)} = 0 \tag{3.191b}$$

$$w\big|_{y=(2h_f+h_c)} = 0 \tag{3.191c}$$

$$u\big|_{y=h} = 0 \tag{3.192a}$$

$$v\big|_{y=h} = 0 \tag{3.192b}$$

$$w\big|_{y=h} = 0 \tag{3.192c}$$

$$u\big|_{x=1} = 0 \tag{3.193a}$$

$$\left.\frac{\partial v}{\partial x}\right|_{x=1} = 0 \tag{3.193b}$$

$$\left.\frac{\partial w}{\partial x}\right|_{x=1} = 0 \tag{3.193c}$$

and the thermal boundary conditions are

$$\theta_f\big|_{z=0} = 0 \tag{3.194}$$

$$\left.\frac{\partial \theta_f}{\partial z}\right|_{z=l} = 0 \tag{3.195}$$

$$\left.\frac{\partial \theta_f}{\partial x}\right|_{x=1} = 0 \tag{3.196}$$

$$\left.\frac{\partial \theta_f}{\partial y}\right|_{y=h} = 0 \tag{3.197}$$

The conditions that relate the top channel to the solid region are, in dimensionless form for the parallel-flow case

$$\theta_f\Big|_{x=(1-b_c)} = \theta_s\Big|_{x=(1-b_c)} \tag{3.198}$$

$$\frac{k_f}{k_s}\frac{\partial\theta_f}{\partial x}\bigg|_{x=(1-b_c)} = \frac{\partial\theta_s}{\partial x}\bigg|_{x=(1-b_c)} \tag{3.199}$$

$$\theta_f\Big|_{y=(2h_f+h_c)} = \theta_s\Big|_{y=(2h_f+h_c)} \tag{3.200}$$

$$\frac{k_f}{k_s}\frac{\partial\theta_f}{\partial y}\bigg|_{y=(2h_f+h_c)} = \frac{\partial\theta_s}{\partial y}\bigg|_{y=(2h_f+h_c)} \tag{3.201}$$

Thus, the dimensionless governing equations expressed by Eqs. (3.128) - (3.131), solved on the appropriate regions (identified above), subject to the dimensionless boundary conditions and interface conditions expressed by Eqs. (3.167) - (3.201), comprise the complete dimensionless mathematical formulation for the parallel-flow arrangement.

Attention is now focused on the single channel (large) arrangement. In this arrangement, for the solid, the dimensionless boundary conditions are

$$\frac{\partial\theta_s}{\partial z}\bigg|_{z=0} = 0 \tag{3.202}$$

$$\frac{\partial\theta_s}{\partial z}\bigg|_{z=l} = 0 \tag{3.203}$$

$$\frac{\partial\theta_s}{\partial x}\bigg|_{x=0} = 0 \tag{3.204}$$

$$\frac{\partial\theta_s}{\partial x}\bigg|_{x=1} = 0 \tag{3.205}$$

$$\frac{\partial\theta_s}{\partial y}\bigg|_{y=h} = 0 \tag{3.206}$$

$$\frac{\partial\theta_s}{\partial y}\bigg|_{y=0} = -\frac{k_f}{k_s} \tag{3.207}$$

For the channel region, for the single channel (large) arrangement, the dimensionless hydrodynamic boundary conditions are

$$u\Big|_{z=0} = 0 \tag{3.208a}$$

$$v\big|_{z=0} = 0 \tag{3.208b}$$

$$w\big|_{z=0} = w_{in\ large} \tag{3.208c}$$

$$\overline{p}\big|_{z=l} = 0 \tag{3.209}$$

$$u\big|_{x=(1-b_c)} = 0 \tag{3.210a}$$

$$v\big|_{x=(1-b_c)} = 0 \tag{3.210b}$$

$$w\big|_{x=(1-b_c)} = 0 \tag{3.210c}$$

$$u\big|_{y=h_f} = 0 \tag{3.211a}$$

$$v\big|_{y=h_f} = 0 \tag{3.211b}$$

$$w\big|_{y=h_f} = 0 \tag{3.211c}$$

$$u\big|_{y=h} = 0 \tag{3.212a}$$

$$v\big|_{y=h} = 0 \tag{3.212b}$$

$$w\big|_{y=h} = 0 \tag{3.212c}$$

$$u\big|_{x=1} = 0 \tag{3.213a}$$

$$\left.\frac{\partial v}{\partial x}\right|_{x=1} = 0 \tag{3.213b}$$

$$\left.\frac{\partial w}{\partial x}\right|_{x=1} = 0 \tag{3.213c}$$

and the thermal boundary conditions are

$$\theta_f\big|_{z=0} = 0 \tag{3.214}$$

$$\left.\frac{\partial \theta_f}{\partial z}\right|_{z=l} = 0 \tag{3.215}$$

$$\left.\frac{\partial \theta_f}{\partial x}\right|_{x=1} = 0 \tag{3.216}$$

$$\left.\frac{\partial \theta_f}{\partial y}\right|_{y=h} = 0 \tag{3.217}$$

The conditions that relate the channel region to the solid region are, in dimensionless form for the single channel (large) arrangement

$$\theta_f\Big|_{x=(1-b_c)} = \theta_s\Big|_{x=(1-b_c)} \tag{3.218}$$

$$\frac{k_f}{k_s}\frac{\partial\theta_f}{\partial x}\bigg|_{x=(1-b_c)} = \frac{\partial\theta_s}{\partial x}\bigg|_{x=(1-b_c)} \tag{3.219}$$

$$\theta_f\Big|_{y=h_f} = \theta_s\Big|_{y=h_f} \tag{3.220}$$

$$\frac{k_f}{k_s}\frac{\partial\theta_f}{\partial y}\bigg|_{y=h_f} = \frac{\partial\theta_s}{\partial y}\bigg|_{y=h_f} \tag{3.221}$$

Thus, the dimensionless governing equations expressed by Eqs. (3.128) - (3.131), solved on the appropriate regions (identified above), subject to the dimensionless boundary conditions and interface conditions expressed by Eqs. (3.202) - (3.221), comprise the complete dimensionless mathematical formulation for the single channel (large) arrangement.

Finally, the single channel (small) arrangement is considered. In this arrangement, for the solid, the dimensionless boundary conditions are

$$\frac{\partial\theta_s}{\partial z}\bigg|_{z=0} = 0 \tag{3.222}$$

$$\frac{\partial\theta_s}{\partial z}\bigg|_{z=l} = 0 \tag{3.223}$$

$$\frac{\partial\theta_s}{\partial x}\bigg|_{x=0} = 0 \tag{3.224}$$

$$\frac{\partial\theta_s}{\partial x}\bigg|_{x=1} = 0 \tag{3.225}$$

$$\frac{\partial\theta_s}{\partial y}\bigg|_{y=h/2} = 0 \tag{3.226}$$

$$\frac{\partial\theta_s}{\partial y}\bigg|_{y=0} = -\frac{k_f}{k_s} \tag{3.227}$$

For the channel region, for the single channel (small) arrangement, the dimensionless hydrodynamic boundary conditions are

$$u\big|_{z=0} = 0 \tag{3.228a}$$

$$v\big|_{z=0} = 0 \tag{3.228b}$$

$$w\big|_{z=0} = 1 \tag{3.228c}$$

$$\overline{p}\big|_{z=l} = 0 \tag{3.229}$$

$$u\big|_{x=(1-b_c)} = 0 \tag{3.230a}$$

$$v\big|_{x=(1-b_c)} = 0 \tag{3.230b}$$

$$w\big|_{x=(1-b_c)} = 0 \tag{3.230c}$$

$$u\big|_{y=h_f} = 0 \tag{3.231a}$$

$$v\big|_{y=h_f} = 0 \tag{3.231b}$$

$$w\big|_{y=h_f} = 0 \tag{3.231c}$$

$$u\big|_{y=h/2} = 0 \tag{3.232a}$$

$$v\big|_{y=h/2} = 0 \tag{3.232b}$$

$$w\big|_{y=h/2} = 0 \tag{3.232c}$$

$$u\big|_{x=1} = 0 \tag{3.233a}$$

$$\left.\frac{\partial v}{\partial x}\right|_{x=1} = 0 \tag{3.233b}$$

$$\left.\frac{\partial w}{\partial x}\right|_{x=1} = 0 \tag{3.233c}$$

and the thermal boundary conditions are

$$\theta_f\big|_{z=0} = 0 \tag{3.234}$$

$$\left.\frac{\partial \theta_f}{\partial z}\right|_{z=l} = 0 \tag{3.235}$$

$$\left.\frac{\partial \theta_f}{\partial x}\right|_{x=1} = 0 \tag{3.236}$$

$$\left.\frac{\partial \theta_f}{\partial y}\right|_{y=h/2} = 0 \tag{3.237}$$

The conditions that relate the channel region to the solid region are, in dimensionless form for the single channel (small) arrangement

$$\theta_f\big|_{x=(1-b_c)} = \theta_s\big|_{x=(1-b_c)} \tag{3.238}$$

$$\frac{k_f}{k_s}\left.\frac{\partial \theta_f}{\partial x}\right|_{x=(1-b_c)} = \left.\frac{\partial \theta_s}{\partial x}\right|_{x=(1-b_c)} \tag{3.239}$$

$$\theta_f\big|_{y=h_f} = \theta_s\big|_{y=h_f} \tag{3.240}$$

$$\frac{k_f}{k_s}\left.\frac{\partial \theta_f}{\partial y}\right|_{y=h_f} = \left.\frac{\partial \theta_s}{\partial y}\right|_{y=h_f} \tag{3.241}$$

Thus, the dimensionless governing equations expressed by Eqs. (3.128) - (3.131), solved on the appropriate regions (identified above), subject to the dimensionless boundary conditions and interface conditions expressed by Eqs. (3.222) - (3.241), comprise the complete dimensionless mathematical formulation for the single channel (small) arrangement.

A close examination of the dimensionless governing equations, the dimensionless ranges on which these dimensionless governing equations are to be solved, the dimensionless boundary conditions, and the dimensionless interface conditions (in short, the entire dimensionless mathematical formulation) for the four arrangements reveals that the problems for u, v, w, p, θ_s and θ_f can be formulated entirely in terms of: the dimensionless co-ordinate directions (x, y and z), h, h_c, h_f, l, b_c, Re_{D_h}, Pr_f, $\frac{D_h}{B}$ and the ratio $\frac{k_f}{k_s}$ (it should be noted that $w_{in\ large}$ is not included, since, it can be expressed in terms of other parameters). Thus, it can be said that the dimensionless problems depend on geometry, Reynolds number, Prandtl number, and on the ratio of thermal conductivities $\frac{k_f}{k_s}$.

3.5 Software Used

The mathematical formulations shown in the previous section, whether in dimensional or dimensionless forms, are quite complex. Thus, in order to solve them, it was decided to make use of a few CFD (computational fluid dynamics) software packages. The two software packages used are called ANSYS ICEM CFD version 10.0 and ANSYS CFX version 10.0. Over the course of this work, ANSYS released version 11.0 of these software packages. Thus, some of the work in this thesis used version 10.0, while later parts used version 11.0.

Running a case consisted of the following steps:

- Using ANSYS ICEM CFD, generate the meshes for the solid region, as well as the channel region(s) for the case being run. These meshes were saved in separate files.
- Open ANSYS CFX-pre (one of three sub-programs of ANSYS CFX), and, one-by-one, load the meshes generated earlier in ANSYS ICEM CFD.
- Define two or three (as the case may be) domains: one for the solid region, and one for each channel region. This step occurred once again in ANSYS CFX-pre.
- Create what ANSYS CFX-pre calls "Domain Interfaces" at every two-dimensional region where the solid is in contact with the channel (or one of the channels). For all cases in this thesis, the "1:1" option was selected as the way that ANSYS CFX would connect the nodes at the interfaces. This required that the meshes generated in ANSYS ICEM CFD has matching nodes at corresponding interfaces in the solid and the channel(s).
- Specify the boundary conditions on any solid and channel surfaces not already part of the above-defined Domain Interfaces. These boundary conditions did not need to be expressed mathematically. Instead, the software allowed the user to select from among a set of possible boundary condition types (inlet, outlet, wall, symmetry, opening). Then, depending on the type, a few necessary parameters were specified. For example, for an inlet, it was necessary to specify the inlet velocity (or the profile) and the inlet temperature.
- Specify a few numerical parameters (such as convergence criteria), and, write the definition file. The definition file (or a .def file) is a file, written by ANSYS

CFX-pre, which is read by ANSYS CFX-solver. It contains all the information needed by ANSYS CFX-solver to actually run the simulation.

- Start ANSYS CFX-solver and ask it to run the simulation. While running, it is possible to monitor the progress of the simulation, and to stop the run, or modify the run in progress. When ANSYS CFX-solver finishes the simulation, it writes out the results to the results file (a .res file).
- Open the results file in ANSYS CFX-post. This program is a utility that allows one to post-process the results file. This program allow the generation of plots, the calculation various quantities, and the exporting of certain data for further plotting or calculations (in other software).

These steps were performed for every case presented in this thesis.

All of the runs were performed on SPARC-based Solaris machines, or on a Linux-based machine.

When running a simulation, it is necessary to specify a *convergence criterion*, which is the criterion that determines when the iterations performed by ANSYS CFX will stop. The convergence criterion is based on the *residuals*, which represent the imbalance in the algebraic analogues of the governing equations at a node. These residuals are calculated at every node. The exact definition of the residuals used by ANSYS CFX is not known to the general public. However, it is known that the residuals are somehow normalized. One can specify that ANSYS CFX stop the calculations when the root mean square (RMS) of the residuals, for every equation, drops below a certain value, or when the maximum residual, for every equation, drops below a certain value. In this work, unless otherwise specified, the convergence criterion was to stop when the maximum value of the residuals of all equations dropped below 10^{-5}. This is considerably more conservative than the default behavior of ANSYS CFX, which stops the simulation as soon as the RMS of the residuals drops below 10^{-4} (at which point, some nodes will have residuals larger than this value, except in the unlikely event that all residuals for every equation are *exactly* equal to 10^{-4} at *every* node).

It should be noted that for fully-developed inlet conditions, the problems are greatly simplified. The mass conservation equation, and the momentum equations, do not need to be solved. This removes all the complexity of the pressure-velocity coupling,

that must be resolved in order to solve the problem. With the velocity field specified, there remains only to solve the temperature equations in the solid and channel(s). This is substantially more straightforward than solving all the equations. That is, if one were to write one's own code, making the fully-developed inlet assumption reduces the programming effort greatly.

However, in this work, with the use of ANSYS CFX, making the fully-developed inlet flow assumption does not simplify the calculations, and, in fact, adds extra steps in the process. To run a case with fully-developed inlet flow conditions, the following procedure was employed. First, the corresponding case with uniform inlet assumption was run. In all cases, the length of the channels (L) was sufficiently long so that the fully-developed region was attained before the outlet of the channels. Then, the outlet profile for the channel(s) in these cases was exported, and, was imported into another simulation and specified as the inlet hydrodynamic boundary condition. If the channel length would not have been long enough to attain fully-developed hydrodynamics, it would have been necessary to execute several passes of the above procedure, until the total length of all the simulations combined was long enough to attain fully-developed conditions. However, this was not necessary. It should be noted that the procedure used does not involve any simplification or reduction in the number of steps to run a fully-developed inlet assumption case. Furthermore, the run-time of the program was not reduced. Thus, the fully-developed inlet assumption cases were run strictly to see what effect this assumption has on the solution's accuracy.

CHAPTER 4
VALIDATION

As mentioned in the preceding chapter, the simulations performed in this work were solved with the use of CFD packages distributed by ANSYS. Even though these programs were not written by the author, it was still necessary to be sure that the results were valid. Therefore, it was necessary to make sure that these programs were working as expected, and that no errors arose because of errors within the programs, or because, in some way, the simulations were not being set up correctly.

Furthermore, in any CFD work, it is necessary to ensure that the results obtained are mesh-independent. That is, the results obtained must not depend significantly on the choice of mesh. This means that the mesh must be fine enough, so that every physical feature of the problem is captured, and that no non-physical features are introduced solely because the mesh is too coarse. Even assuming that no errors were present in the software, and that the simulations were correctly implemented, the results cannot be expected to be correct if the mesh used was inadequate.

Thus, this chapter consists of a series of checks, designed to make sure that the results are mesh-independent and physically correct. These checks come in two varieties. The first is the standard grid refinement studies, where, starting with a coarse grid, grid refinements are made until there is no significant difference in the solution between two successive refinements. The second is the comparisons of obtained results with known results. These known results can either be exact analytical results for simplified geometries, other numerical studies, experimental results, or combinations thereof.

Rather than tackling the exact geometries under consideration in this work right from the start, it was decided to first consider just a case of simple channel flow, considering only the hydrodynamics. The reason for this choice was that channel flow is a simple, well-understood problem, and so, comparisons with known results are possible. Then, channel flow with heat transfer was studied. Finally, grid refinement tests were performed on the problems under study in this thesis, particularly the counter-flow arrangement (which is the most difficult problem), and, where possible, comparisons were made to the results of Vafai and Zhu (1999).

4.1 Channel Flow: Hydrodynamics

The problem under consideration in this section is shown in Figure 4.1. A channel of length L has, at one end, flow entering with a uniform velocity W_{in}. The fluid flows through the channel and eventually achieves fully-developed conditions. The

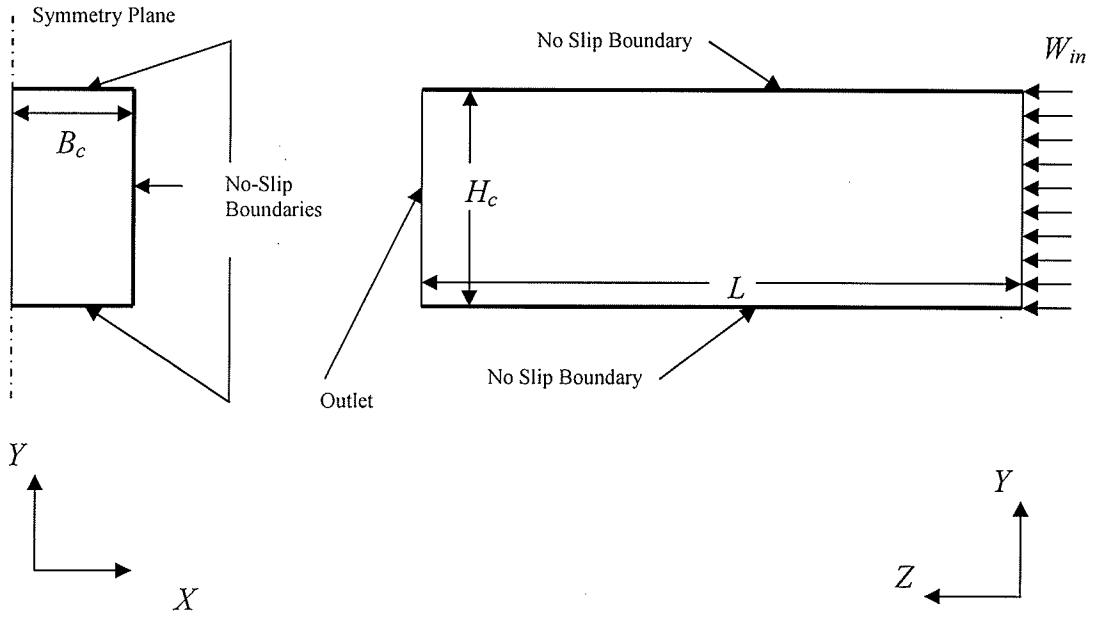

Figure 4.1: Schematic of the Fluid-Flow Channel-Only Problem

cross-sectional dimensions of the channel are $2B_c$ (in the x-direction) and H_c (in the y-direction). Because of symmetry, only one half the flow domain is solved. While it would have been possible to further reduce the problem by considering only one quarter of the channel, it was decided to consider half the problem, since, in the microchannel heat sink arrangements, the channels have only one symmetry plane.

In this section, the following values were used: $B_c = 0.5$ [mm], $H_c = 2.0$ [mm], $L = 80.0$ [mm], $W_{in} = 0.0334717$ [m/s]. The abnormal number of decimal places in W_{in} is explained by the fact that its value was chosen so that a Reynolds number of exactly 50.0 was obtained. This choice was somewhat arbitrary, but, a low Reynolds number was desired, so as to start out with a problem that is as simple as possible. The Reynolds

number chosen by Vafai and Zhu (1999) is greater than this value, by a factor slightly greater than 2. The fluid that was used is water, with properties taken at 25 °C.

The nomenclature used for the various grids studied in this section is illustrated in Figures 4.2a (for a cross-section) and 4.2b (in the *Z*-direction). The grids were orthogonal and non-uniform. In the *X*-direction, a small spacing, ΔX_1 was placed near the wall, and, the *X*-spacings expanded geometrically, up until the last spacing, ΔX_{nx}, which was located adjacent to the plane of symmetry. A geometric expansion of the spacings means that the ratio of successive spacings is a constant, as follows

$$\frac{\Delta X_2}{\Delta X_1} = \frac{\Delta X_3}{\Delta X_2} = \frac{\Delta X_4}{\Delta X_3} = \cdots = \frac{\Delta X_{nx}}{\Delta X_{nx-1}} = r_X \tag{4.1}$$

where r_X is the *X*-direction expansion factor and *nx* is the number of *X*-direction spacings. Additionally, the sum of all the spacings equals the half-width of the channel:

$$\Delta X_1 + \Delta X_2 + \Delta X_3 + \cdots + \Delta X_{nx-1} + \Delta X_{nx} = B_c \tag{4.2}$$

In the *Y*-direction, the spacings again followed a geometric progression, except that here, there were two geometric progressions. Starting at the bottom, with a spacing of ΔY_1, the spacings increased geometrically until the spacing just below the vertical mid-plane, which had a length of $\Delta Y_{ny/2}$, where *ny* (which must be an even number) is the total number of *Y*-direction spacings including those above and below the vertical mid-plane. Then, the spacings above the vertical mid-plane were a mirror image of those below it. The following relations must hold

$$r_Y = \frac{\Delta Y_2}{\Delta Y_1} = \frac{\Delta Y_3}{\Delta Y_2} = \frac{\Delta Y_4}{\Delta Y_3} = \cdots = \frac{\Delta Y_{ny/2}}{\Delta Y_{ny/2-1}} \tag{4.3}$$

$$\Delta Y_1 + \Delta Y_2 + \Delta Y_3 + \cdots + \Delta Y_{ny/2-1} + \Delta Y_{ny/2} = \frac{H_c}{2} \tag{4.4}$$

where r_Y is the *Y*-direction expansion factor. In the *Z*-direction, a fine spacing (ΔZ_1) was placed near the inlet, and, along the Z-axis, the spacings increased geometrically in length by a ratio of r_Z, defined as

$$r_Z = \frac{\Delta Z_2}{\Delta Z_1} = \frac{\Delta Z_3}{\Delta Z_2} = \frac{\Delta Z_4}{\Delta Z_3} = \cdots = \frac{\Delta Z_{nz}}{\Delta Z_{nz-1}} \tag{4.5}$$

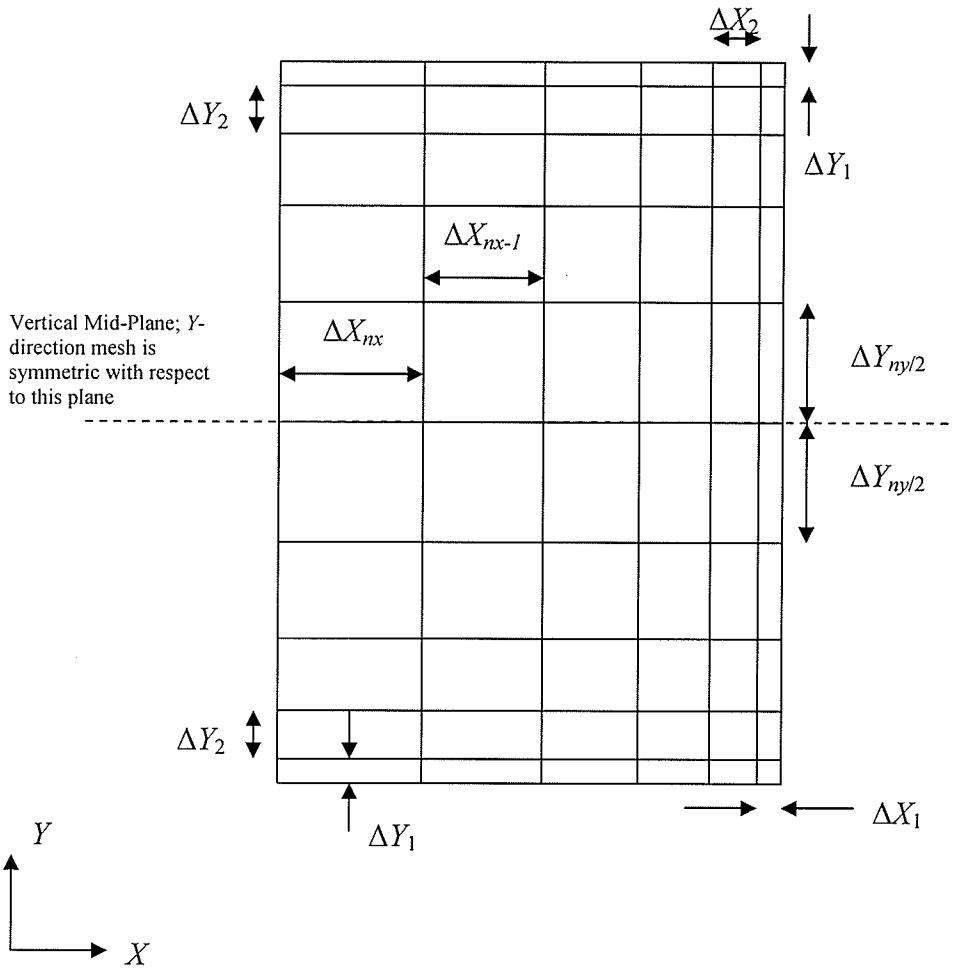

Figure 4.2a: Grid Nomenclature Used for Channel-Only Problem: Cross-Section

where *nz* is the number of *Z*-direction spacings. The following relation must hold in the *Z*-direction:

$$\Delta Z_1 + \Delta Z_2 + \Delta Z_3 + \cdots + \Delta Z_{nz} = L \tag{4.6}$$

It should be noted that the *nodes* at which the solution variables were solved are located at the *intersections* of all the lines that define the various spacings mentioned above. That is, the nodes are vertex-centered, not cell-centered. More discussion on this terminology can be found in Patankar (1980).

The reason for these choices regarding the non-uniform spacings in the *X*- and *Y*-directions is that, in a cross-section, a fine mesh is desired near the walls, where gradients of the solution variables are known to be high, and, near symmetry planes, where gradients are known to be small, there is no need for extra refinements. The reason for

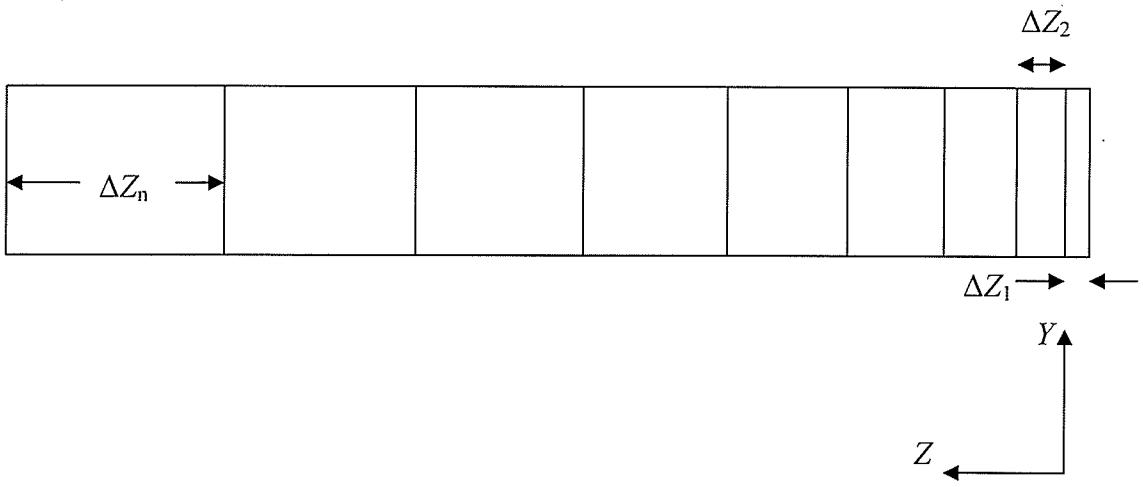

Figure 4.2b: Grid Nomenclature Used for Channel-Only Problem: Axial Spacings

the refinement in the *Z*-direction is as follows. Near the inlet, it is known that the velocity field is developing. Thus, in order to accurately capture the fluid flow phenomena occurring in the developing region, it is necessary to have a finer mesh in that region. In the fully-developed region, axial variations are known to be non-existent. Thus, the axial spacings can be, theoretically, arbitrarily large, since, nothing is changing in the Z-direction, and the problem becomes two-dimensional. Thus, in summary, the strategy employed here was that more nodes were placed in regions of the flow where it was known that a finer mesh was desired, at the expense of placing less nodes in regions where they were not needed.

Three meshes were examined in solving the problem of this section (more grids were looked at, but only three are presented here). They are denoted the *coarse*, *medium* and *fine* meshes. Their definitions are presented in Table 4.1. It should be noted that, given the number of spacings along a given axis, and the first spacing, the corresponding expansion factor is automatically specified, as is the final spacing. In this case, as shown in Table 4.1, all of the "initial" spacings (ΔX_1, ΔY_1, and ΔZ_1) had the same value, namely 0.01 [mm]. This choice was somewhat arbitrary, and was made based on experience and some simple calculations, as a starting point.

Table 4.1: Definitions of the Various Grids Used in Solving the Hydrodynamic Problem

Mesh	*nx*	*ny*	*nz*	ΔX_1 [mm]	ΔY_1 [mm]	ΔZ_1 [mm]
Coarse	10	20	100	0.01	0.01	0.01
Medium	15	30	200	0.01	0.01	0.01
Fine	20	40	400	0.01	0.01	0.01

In determining the success or failure of the grid refinement study, the following definitions, from Shah and London (1978), were relevant

$$Z^+ = \frac{Z}{ReD_h} \tag{4.7}$$

$$f(Z) = \frac{d\overline{P}(Z)}{dZ}\frac{1}{\frac{1}{2}\rho_f W_{in}^2}\frac{D_h}{4} = \frac{d\overline{P}(Z)}{dZ}\frac{D_h}{2\rho_f W_{in}^2} \tag{4.8}$$

$$f_{app}(Z) = \frac{D_h}{4}\frac{\overline{P}(Z)-\overline{P}(0)}{Z}\frac{1}{\frac{1}{2}\rho_f W_{in}^2} = \frac{D_h\left(\overline{P}(Z)-\overline{P}(0)\right)}{2Z\rho_f W_{in}^2} \tag{4.9}$$

where D_h and Re (previously denoted Re_{D_h}; the subscript D_h is dropped for convenience) are the hydraulic diameter and the Reynolds number based on this hydraulic diameter, respectively, as defined earlier, Z^+ is a non-dimensional coordinate, $\overline{P}(Z)$ is the cross-section average pressure, which is a function of only Z, and $\overline{P}(0)$ is the average pressure in the inlet (that is, at $Z = 0$). The non-dimensional Z coordinate given by Eq. (4.7) is different from the one used earlier when non-dimensionalizing the governing equations. It is used here only because it will serve to compare with data in Shah and London (1978), and because, later on, it will be used to set a criteria for calculating ΔZ_1.

In order to perform the grid-refinement tests, three comparisons were made. The first was to compare, for the various meshes, the values of $f_{app}Re$, which are plotted against Z^+ in Figure 4.3. The second was to compare the values of fRe, which are plotted,

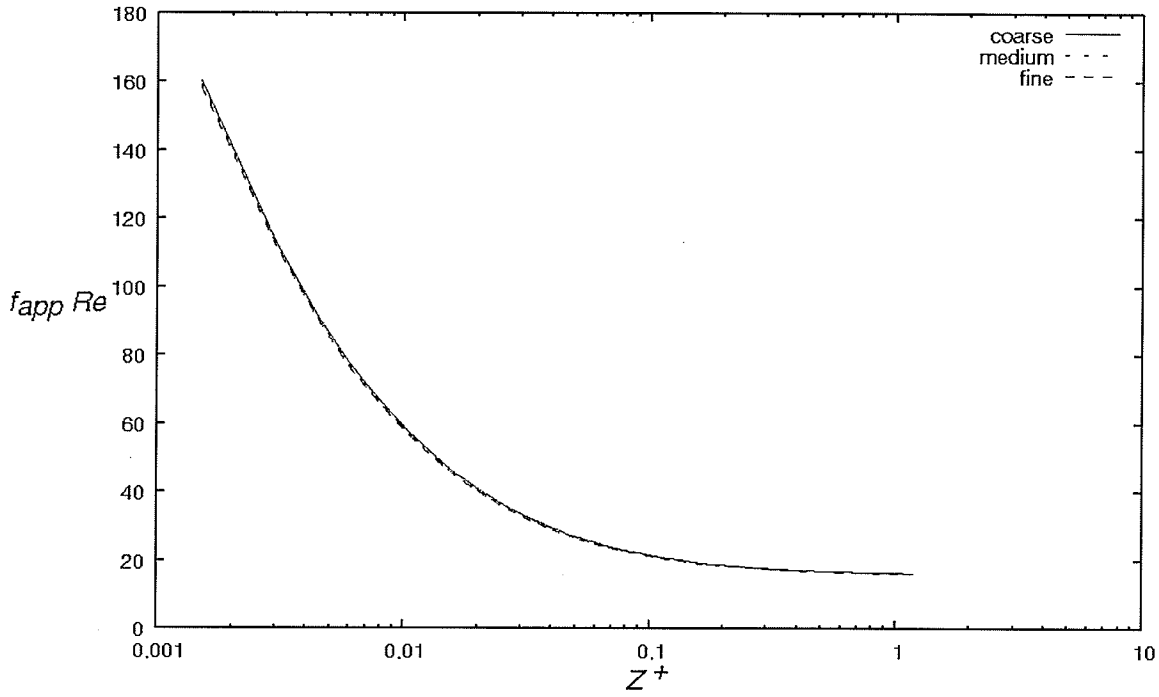

Figure 4.3: Channel-Only Hydrodynamic Problem Grid Refinement for $f_{app}Re$

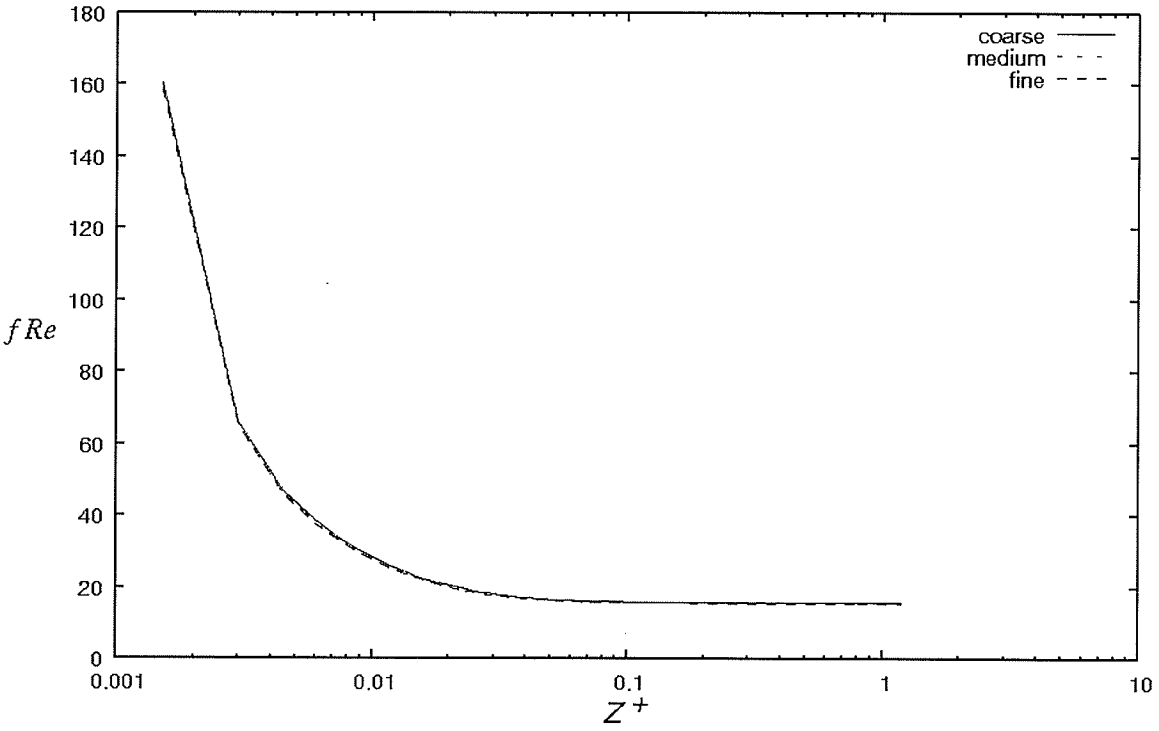

Figure 4.4: Channel-Only Hydrodynamic Problem Grid Refinement for fRe

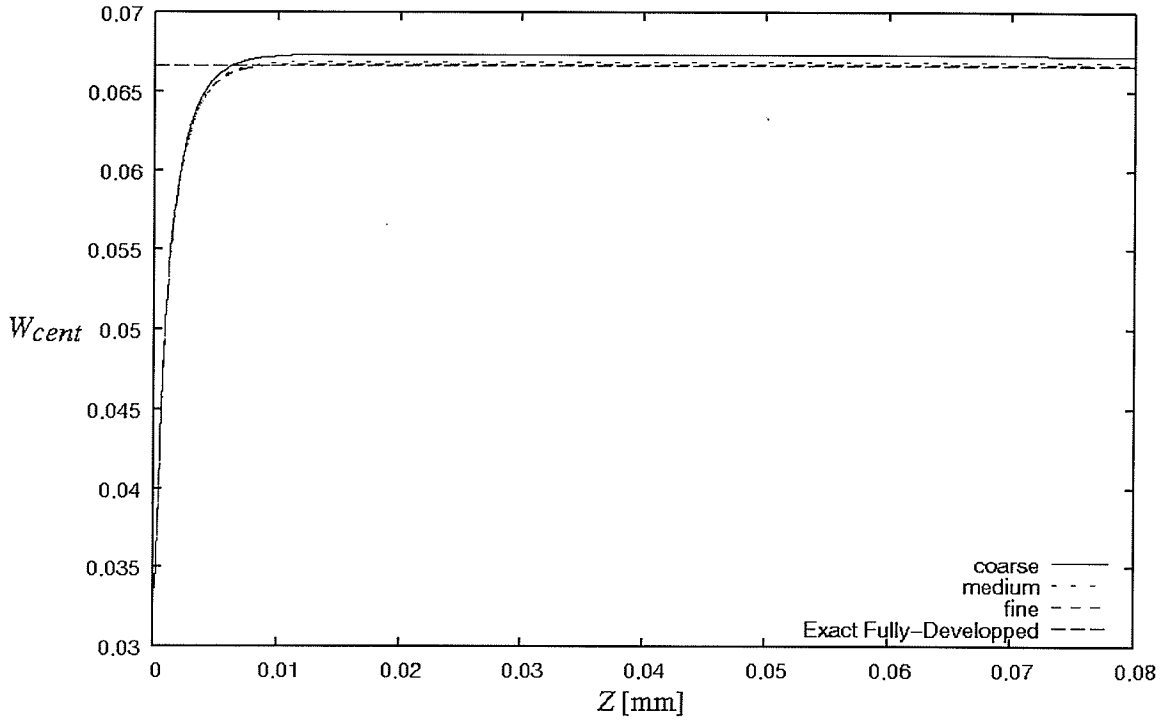

Figure 4.5: Channel-Only Hydrodynamic Problem Grid Refinement for W_{cent}

again against Z^+, in Figure 4.4. The third means was to compare the centerline velocity profiles (W_{cent}) for the various meshes. The velocity comparisons are made in Figure 4.5.

By a visual inspection of Figure 4.3, it appears that the coarse, medium and fine meshes give close predictions for $f_{app}Re$, since all three curves appear to more or less overlap. The values of $f_{app}Re$ predicted using the coarse and medium meshes are always within 1.56 % of each other, while those predicted by the medium and fine meshes are always within 0.46 % of each other. Thus, based on this information as well as the plot in Figure 4.3, it appears that grid-independent results have been obtained, as far as predicting $f_{app}Re$ is concerned. That is, refining the mesh from the coarse to the medium mesh produced a significant change, but refining from the medium to the fine did not improve the solution considerably (less than 0.5 %), as far as $f_{app}Re$ is concerned. The 0.46 % discrepancy between the medium and fine meshes may seem large, but, since it is only desired, in this section, to obtain general ideas about what is needed in a mesh, and to see that the problem was correctly setup, the 0.46 % discrepancy is small enough for the purposes of this section.

Looking at the fRe predictions, now, the plot in Figure 4.4 shows that visually, the curves for the coarse, medium and fine meshes appear to more or less overlap. The fRe curve generated by the coarse mesh and that generated by the medium mesh are always within 2.25 % of each other, while the fRe curve generated by the medium mesh is always within 0.64 % of the fRe curve generated from the solution using the fine mesh.

It should be kept in mind that both $f_{app}Re$ and fRe, while they are important quantities with which to compare the current solutions to known results from the literature, are cross-section averaged quantities. As such, it is possible, theoretically, that they somehow "smear-out" differences that exist within a cross-section. That is, the value of fRe in a given cross-section may be the same for two different meshes, even though the meshes have different pressure distributions within the cross-section. Therefore, it is also desired to base the grid-independence test on non-averaged quantities. This was accomplished by looking at the centerline velocity, denoted as W_{cent}. Because the problem was solved by making use of symmetry, and hence only half the domain was modeled, the centerline velocity is the velocity on the line located at the left of the domain, at a vertical (Y) height of $H_c/2$, going from $Z = 0$ to $Z = L$.

Figure 4.5 shows the prediction of W_{cent} for the coarse, medium and fine meshes. It should be noted that, at $Z = 0$, all three curves start at the value of W_{in}, which for this case is 0.0334717 [m/s]. The W_{cent} solution obtained from the coarse mesh and the one obtained from the medium mesh are within 0.71 % of each other, while the W_{cent} solutions from the medium mesh and the one from the fine mesh are within 0.20 % of each other. This indicated that the solution is mesh-independent as far as W_{cent} is concerned.

So, since grid-independent behavior was obtained for $f_{app}Re$, fRe and W_{cent}, confidence was gained that the current solutions are, indeed, grid independent. That is, the medium mesh should be good enough, since refining the mesh further produced only small changes $f_{app}Re$, fRe and W_{cent}.

In addition to performing grid-independence tests, it was desired to assess the quality of the solution by making comparisons to known results. Here, Shah and London (1978) provided data that enables such comparisons to be made. In particular, they

provided data that can be used to check $f_{app}Re$ in the developing region, as well as fRe and W_{cent} in the fully-developed region.

Shah and London (1978) provided an analytical solution that can be used to calculate the fully-developed velocity at any value of X and Y. This solution, which involves the evaluation of two infinite series, was applied by truncating the infinite series after a sufficient number of terms. In every case when an infinite series was evaluated in applying this solution, the series was truncated after no less than 801 terms (of which at least 400 were non-zero). While this choice was somewhat arbitrary, it ensured that the truncation error was well below a reasonable cutoff value. Applying this solution with the relevant parameter values for this case, the fully-developed value of the centerline velocity, $W_{cent,fd}$, was calculated to be 0.06666874 [m/s]. The coarse, medium and fine meshes predicted this value with absolute relative percent errors of 1.0 %, 0.32 % and 0.13 %, respectively. Thus, it can be said that the current velocity predictions are not only grid-independent; they are also in agreement with known values.

The fully-developed value of fRe given in Shan and London (1978), for the aspect ratio used in this case, is 15.54806. The coarse, medium and fine meshes predicted this value with absolute relative percent errors of 0.96 %, 0.29 % and 0.084 %, respectively. Thus, the prediction of fRe was grid-independent, and the predicted fully-developed value of fRe compared well with the known value.

It should be kept in mind that, while encouraging, the preceding tests only test for the correctness of fully-developed values. Obtaining good predictions in the fully-developed region is an indication that the grid within a cross-section is adequate. However, in order to ensure that the axial grid is also adequate, it is necessary to compare the solution against known values in the developing region. Fortunately, Shah and London (1978) also provided values of $f_{app}Re$ in the developing region.

The $f_{app}Re$ values provided by Shan and London (1978), along with the values predicted by the fine mesh, are plotted in Figure 4.6. It is clear from this figure that the values predicted by the fine mesh are not in agreement with the values provided by Shah and London (1978). The disagreement is greater for lower values of Z^+. At the smallest Z^+ value for which Shah and London (1978) report a value of $f_{app}Re$, namely $Z^+ = 0.001$, the discrepancy is greater than 50 %. At the highest value of Z^+ for which Shah and

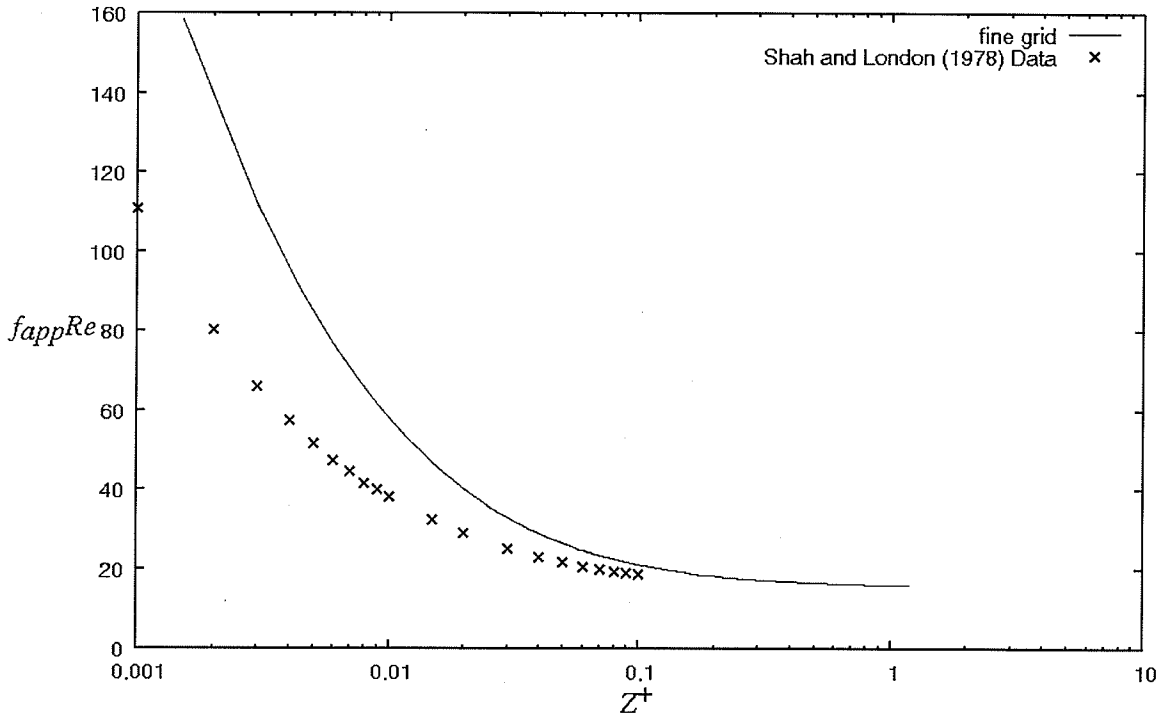

Figure 4.6: Channel-Only Hydrodynamic Problem Comparisons with Known Results for $f_{app}Re$

London (1978) report a value of $f_{app}Re$, namely $Z^+ = 0.1$, the discrepancy is approximately 13 %. This non-agreement definitely needed to be addressed before proceeding.

In an attempt to resolve this discrepancy, it was decided to re-run the current case with what another mesh, termed the *very fine* mesh, to see if, in spite of earlier, apparently-successful grid-refinement tests, the results were still somehow not mesh-independent. The specifications of the very fine mesh are as follows: $nx = 40$, $ny = 80$, nz = 400; $\Delta X_I = 0.01$ [mm], $\Delta Y_I = 0.01$ [mm], $\Delta Z_I = 5\text{x}10^{-5}$ [mm]. The most significant difference between the fine and very fine meshes is that the value of ΔZ_I is $5\text{x}10^{-5}$ [mm] in the very fine mesh, and 0.01 [mm] in the fine mesh. Thus, ΔZ_I has been reduced by a factor of 200. The choice for the value of ΔZ_I for the very fine mesh was made by selecting ΔZ_I such that $\Delta Z_1^+ < 10^{-6}$. It was hoped that this refinement in ΔZ_I would solve the problem of the large errors in predicting $f_{app}Re$, particularly at near the inlet.

Figure 4.7 shows the predictions of the fine and very fine meshes, along with the data presented in Shah and London (1978). It is clear from this figure that the very fine

mesh does not change the $f_{app}Re$ prediction materially, except at lower values of Z^+, where slight discrepancies between the fine and very fine meshes are observed. This

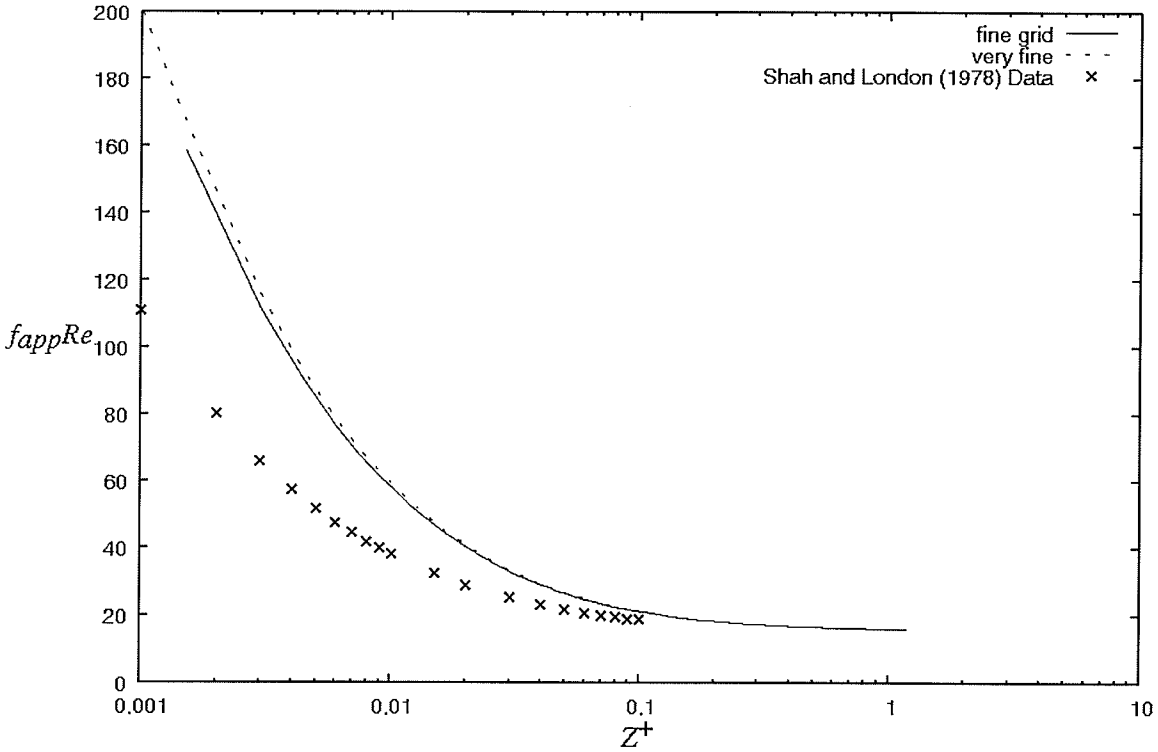

Figure 4.7: Channel-Only Hydrodynamic Problem Comparisons with Known Results for $f_{app}Re$: Second Pass

suggests that earlier results were indeed mesh independent. However, the problem remains: none of the meshes produced results agreeing with known results.

Therefore, it was attempted to determine the cause of this non-agreement between the present model and known results. This required much thought, a careful review of the procedure being used, a re-reading of the ANSYS CFX and ANSYS ICEM CFD documentation, and a re-reading of the relevant sections of Shah and London (1978). It was during this re-reading of Shah and London (1978) that the cause of the problem was discovered. It turns out that the data presented in Shah and London (1978) were obtained by a *marching* technique, one which must therefore ignore certain terms in the governing equations. This was done because, at the time when these data were generated, the limited computing resources would have rendered the solution to the full governing equations infeasible. It can be reasoned on physical and mathematical grounds that

employing the marching technique will produce greater error for lower Reynolds numbers, in the developing region. At higher Reynolds numbers, the error introduced by the marching procedure becomes smaller. Thus, even though there is no explicit mention in Shah and London (1978) of any Reynolds number dependence of the $f_{app}Re$ results presented, it can be reasoned that these results are valid only for certain Reynolds numbers. The Reynolds number must be large enough to avoid the errors associated with the marching technique, but small enough so that the flow is still laminar. This provides a plausible explanation as to why none of the simulations produced good predictions of $f_{app}Re$: at the currently chosen Reynolds number of 50, the terms neglected in arriving at the data in Shah and London (1978) are large in the developing region, and, because ANSYS CFX does not ignore these terms, the current results differ significantly from the "known" results.

Thus, to obtain agreement with the $f_{app}Re$ data in Shah and London (1978), it would be necessary to either repeat the calculations by omitting the terms that were neglected (which is not possible in ANSYS CFX, to the best knowledge of the author), or, repeat the calculations with a greater Reynolds number. Figure 4.8 shows the predictions of $f_{app}Re$ obtained, for various Reynolds numbers, using the very fine mesh for all cases (the value of ΔZ_1 was modified in each case, to give the same ΔZ_1^+ as was used in the $Re = 50$ case). From a visual inspection of this figure, it is clear that, for low Reynolds number, the data in Shah and London (1978) agrees poorly with the data generated in this work, but, as the Reynolds number increases, agreement between the data of Shah and London (1978) and the results of the present computations using ANSYS CFX improves. For Reynolds numbers of $Re = 500$, $Re = 1000$ and $Re = 2000$ (the "D_h" subscript on the Reynolds number is again omitted for convenience), the maximum absolute relative percent differences to the Shah and London (1978) data are, 13.2 %, 8.62 %, and 3.71 %, respectively. Even though the 3.71 % discrepancy for the $Re = 2000$ case is not as small as would have been desired, the progressive reduction of errors as the Reynolds number is increased is undeniable. It is suspected that running a case with a higher Reynolds number, and instructing ANSYS CFX to use laminar flow correlations even the flow would be known to be turbulent (or in the laminar-turbulent transition), would yield an even smaller discrepancy in the $f_{app}Re$ values in the developing

region. However, this was not done, since, this would not be "correct" (using laminar governing equations to a non-laminar problem) and because it was felt that there was

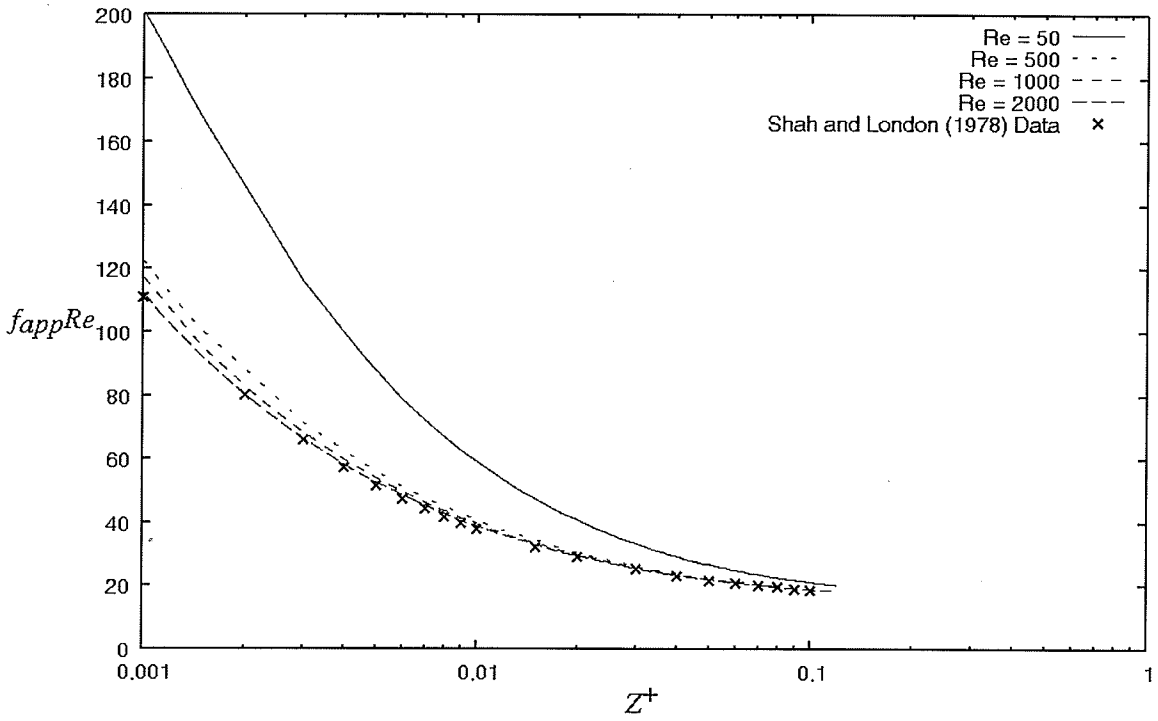

Figure 4.8: Channel-Only Hydrodynamic Problem Comparisons with Known Results for $f_{app}Re$: Effect of Reynolds Number

sufficient evidence to confirm that the available data was being matched, when the assumptions made to obtain this data were preserved. It should be mentioned in passing that, since the purpose of this section is simply to confirm that everything was being done correctly in setting up the simulations, and to obtain *some idea* of the grid necessary to solve the microchannel problems of this thesis, grid-refinement tests were not repeated on the higher Reynolds number cases.

Thus, having obtained grid-independent behavior, and having obtained solutions that match available data in the developing and fully-developed regions, it is possible to proceed to further comparisons. Before examining the complete microchannel problems, the analysis presented in this section will be extended to include heat transfer. This is the subject of the following section.

4.2 Channel Flow: Heat Transfer

The problem under consideration in this section is shown schematically in Figure 4.9. Flow enters at $Z = 0$ with a uniform velocity and uniform temperature of W_{in} and T_{in}, respectively. The channel has a width of $2B_c$, a height of H_c and a length L. Unlike the

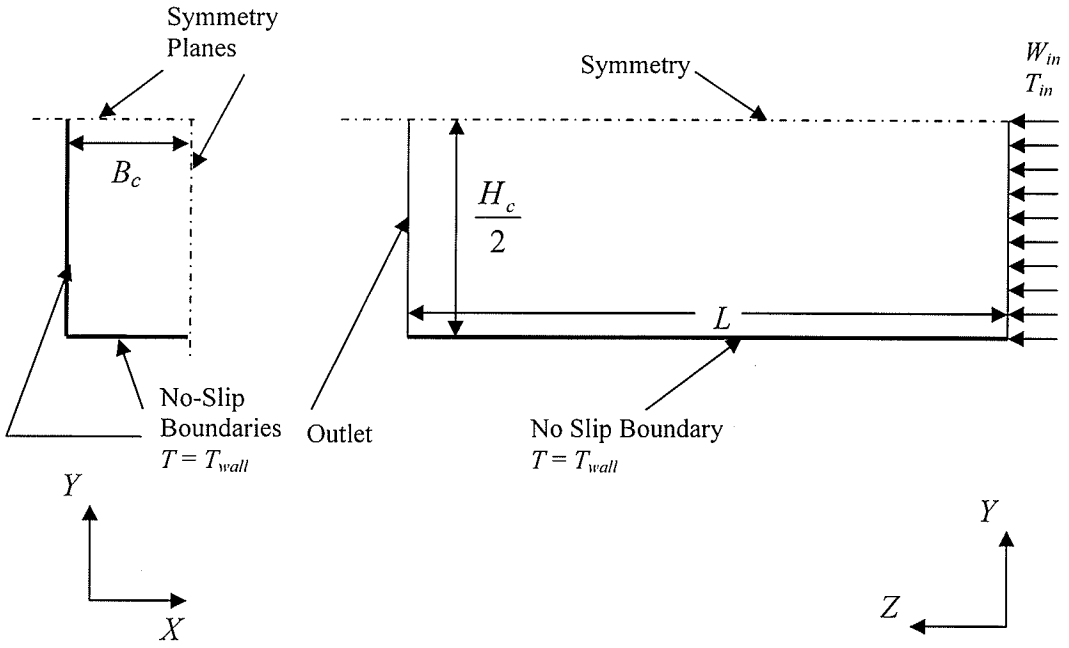

Figure 4.9: Schematic of the Heat Transfer Channel-Only Problem

hydrodynamic problem of the previous section, where only one plane of symmetry was used, here two planes of symmetry are used. Thus, the width and height of the solution domain are B_c and $\frac{H_c}{2}$, respectively. The sides of the channel are held at a uniform temperature T_{wall}. Because of symmetry, only two sides (the left and bottom sides of a cross-section of the solution domain, when viewed towards the negative Z direction) have a uniform-temperature boundary condition, while the remaining two sides of the solution domain have a symmetry boundary condition. At the channel outlet, ANSYS CFX imposes a zero-axial-gradient boundary condition. While this boundary condition is not strictly speaking correct, it is expected that the impact of making this approximation is

negligible (if this is not correct, it will be seen later in the comparisons with known results).

The grid used for this problem is similar to that used in the previous section. It is identical in the X and Z directions, and almost identical in the Y direction. The only difference in the Y direction is that, since there is now a vertical symmetry plane, the spacings continually expand with height, unlike in the preceding section, where they expanded and then contracted. The Y-direction grid is illustrated in Figure 4.10. The

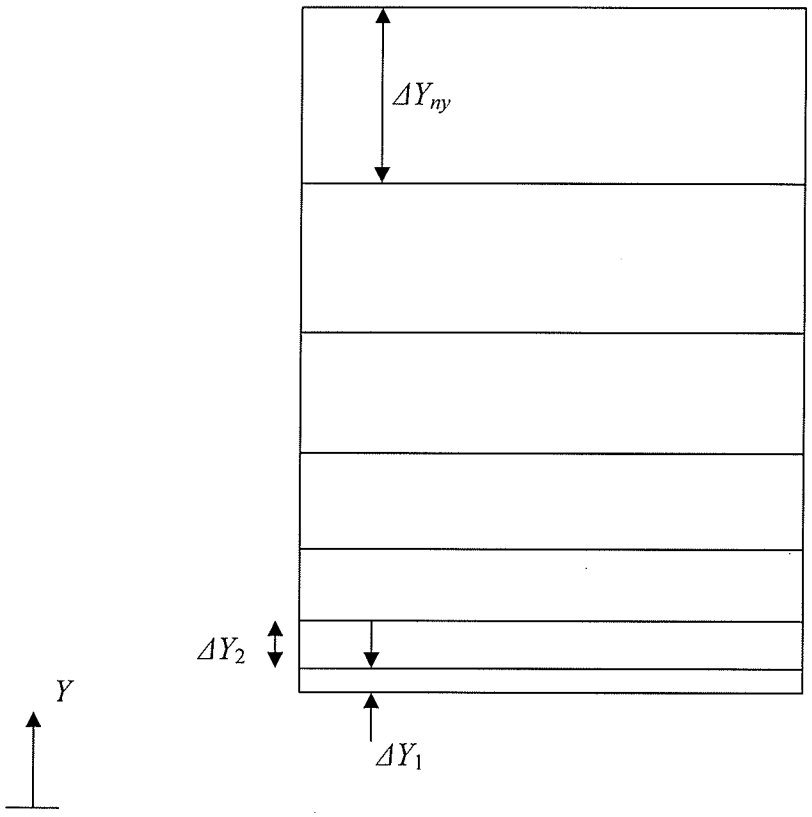

Figure 4.10: Schematic of Y-Direction Grid for the Heat Transfer Channel-Only Problem

mathematical relations given in Eqs. (4.1) - (4.2), as well as Eqs. (4.5) - (4.6) are still valid in this section. However, the relations given by Eqs. (4.4) - (4.5) no longer apply. Their counterparts in the problem being solved in this section are:

$$r_Y = \frac{\Delta Y_2}{\Delta Y_1} = \frac{\Delta Y_3}{\Delta Y_2} = \frac{\Delta Y_4}{\Delta Y_3} = \cdots = \frac{\Delta Y_{ny}}{\Delta Y_{ny-1}} \tag{4.10}$$

$$\Delta Y_1 + \Delta Y_2 + \Delta Y_3 + \cdots + \Delta Y_{ny-1} + \Delta Y_{ny} = \frac{H_c}{2} \tag{4.11}$$

Three different grids were considered in this section, and their definitions are presented in Table 4.2. It should be remembered that the nodes are at the *intersections* of the lines that delimit the various *spacings*. The values of ΔZ_1 were chosen to ensure that $\Delta Z_1^+ < 10^{-6}$.

The values of the various parameters defining the problem of this section are as follows: $B_c = 0.5$ [mm], $H_c = 2.0$ [mm], $L = 300$ [mm], $W_{in} = 23.1772$ [m/s], $T_{in} = 300$ [K], $T_{wall} = 400$ [K]. The fluid was constant-property air, but where the value of the thermal conductivity has been modified, slightly, to the value needed to yield a Prandtl number of exactly 0.72. This was done because the results available in Shah and London (1978) are for a Prandtl number of 0.72. The value of W_{in} was chosen to give a Reynolds number of 2000.

Table 4.2: Definitions of the Various Grids Used in Solving the Heat Transfer Problem

Mesh	*nx*	*ny*	*nz*	ΔX_1 [mm]	ΔY_1 [mm]	ΔZ_1 [mm]
Coarse	10	20	100	0.01	0.01	0.002
Medium	20	40	200	0.01	0.01	0.002
Fine	40	80	400	0.001	0.001	0.002

In order the perform both the grid refinement test and the comparisons to known results, it is necessary to define a variable that characterizes the heat transfer problem. First, the *local Nusselt number* is defined as follows:

$$Nu(Z) = \frac{h_Z D_h}{k_f} \tag{4.12}$$

where h_Z is the axially local (but averaged over the perimeter of the channel) heat transfer coefficient, given by

$$h_Z = \frac{q''_Z}{T_{wall} - T_{bulk}(Z)} \tag{4.13}$$

where q''_Z is axially local (but averaged over the perimeter of the channel) heat flux, and $T_{bulk}(Z)$ is the bulk temperature in the channel at the given Z coordinate. This bulk temperature represents some sort of "average" temperature, except that, in the averaging process, the temperature is weighted with the mass flow rate. It should be noted that, from the solution field, it is possible to have ANSYS CFX calculate q''_Z and $T_{bulk}(Z)$ at any desired Z location. Once the local Nusselt number has been calculated for a variety of values of Z, the "mean" Nusselt number can be calculated from

$$Nu_m = \frac{1}{Z}\int_0^Z Nu(Z)dZ \tag{4.14}$$

Thus, the mean Nusselt number is a quantity that varies with Z, and represents an axial averaging of the local Nusselt number from the inlet, up to the Z location where the mean Nusselt number is to be determined.

It should be noted that the determination of the mean Nusselt number involves the evaluation of an integral. This was done, in the present work, by applying the trapezoidal rule between each successive values of the local Nusselt number. Thus, the accuracy of the mean Nusselt number depends on the choice of sampling points at which values of the local Nusselt number are calculated. If the sampling of points is not adequate, particularly at low values of Z, where the values of $Nu(Z)$ are larger and the absolute value of its axial gradient is largest, then poor predictions of Nu_m will result. This will be the case *even if* the solution fields obtained by ANSYS CFX are arbitrarily close to the "exact" answer. Through a series of tests that are not presented here, it was found that using a sampling distribution that consisted of evaluating the local number at each Z location where nodes are located was sufficient.

To allow comparisons of the mean Nusselt number data obtained in this work with that presented in Shah and London (1978), it is necessary to define a new dimensionless Z coordinate, called Z^*, since Shah and London (1978) presented the variation of Nu_m with this variable. The definition of Z^* is

$$Z^* = \frac{Z}{D_h RePr_f} \tag{4.15}$$

where once again the subscript D_h is dropped on Re for convenience, and where Pr_f is the Prandtl number of the fluid.

A Reynolds number of 2000 was chosen in the current case because the mean Nusselt data in Shah and London (1978) is only valid at higher Reynolds number within the laminar flow regime. This is because the model used to generate the data in Shah and London (1978) neglected the effect of axial momentum diffusion. Furthermore, this model was based on the assumption that the transverse components of velocity (U and V) were zero. This is only true in the fully-developed region. Thus, even if the current solution is completely correct, agreement between the predicted mean Nusselt numbers and those presented by Shah and London (1978) is only expected in the fully-developed region. It is further expected that the discrepancy should be largest near the inlet, and monotonically decrease with Z^*.

The following point should be mentioned in passing. ANSYS CFX uses a solution procedure whereby two values are calculated at each node that is located on the boundaries of the domain. One value is termed the "conservative" value, which comes from the solution of the conservation equation at the control volume around the boundary node. The other is called the "hybrid" value, which is the value at the boundary node when the value is specified as a boundary condition. More details on this can be found in the ANSYS CFX documentation (2007). ANSYS CFX gives the user the choice, when determining various values, such as $T_{bulk}(Z)$, to use either conservative values or hybrid values. It was discovered through tests not documented here that the proper values to use are the conservative values. By default, if the user does nothing explicit, hybrid values will be used by ANSYS CFX.

Figure 4.11 shows the Nu_m profiles obtained using the coarse, medium and fine grids, along with the data from Shah and London (1978). From a visual inspection of the profiles generated using the three different meshes, it is clear that grid-independent behavior was obtained. Qualitatively, the predictions given by the coarse and medium meshes in Fig. 4.11 were within 0.85 % of each other, while those given by the medium and fine meshes were within 0.32 % of each other. Thus, grid independent behavior was observed. As expected, none of the grids closely predict the data presented in Shah and London (1978), except for higher values of Z^*. At the highest Z^* value for which Shah and London (1978) report a value for Nu_m, namely $Z^* = 0.1$, the coarse, medium and fine meshes predict the value of Nu_m within absolute relative percent errors of 1.2 %, 0.37 %

and 0.36 %, respectively. At the lowest value for which Shah and London (1978) report a value, namely $Z^* = 1/220$, the discrepancy between the data presented in Shah and London (1978) and the data obtained here, for all three grids, are approximately 22 %. Thus, even in the worst case scenario, the present data matched that of Shah and London (1978) to within *engineering* accuracy. This is surprising, given that the current model does not neglect transverse velocity components, while that used in arriving at the data presented in Shah and London (1978) does.

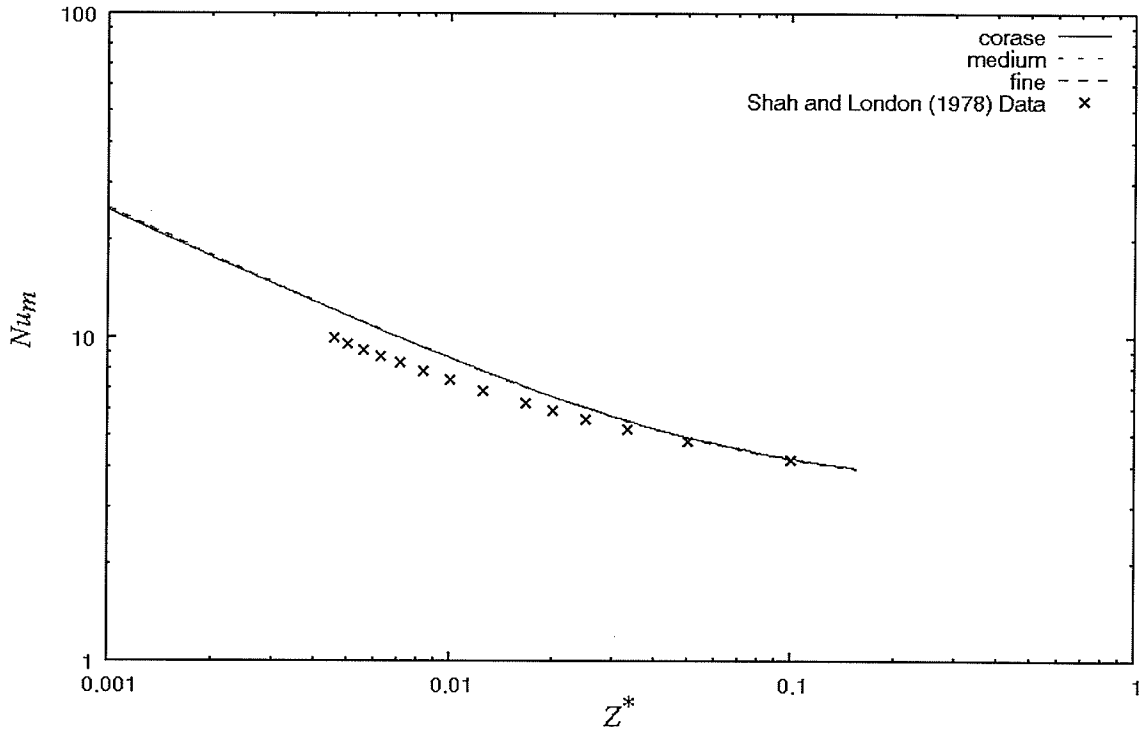

Figure 4.11: Mean Nusselt Number Predictions for the Heat Transfer Problem

Thus, having performed a number of tests on a single-channel hydrodynamic and a single-channel thermodynamic problem, it is possible to proceed with the examination of full microchannel problems. This is considered in the next section.

4.3 Counter-Flow: First Pass

The tests that have been performed in the previous two sections, on both the hydrodynamics and thermodynamics of channel flow, have been done as an intermediate

step before analyzing a full microchannel problem. The purpose of this section is to apply the knowledge and experience gained in the process to solve a microchannel problem. The problem examined in this section is the counter-flow arrangement, with a low Reynolds number assuming developing flow. The choice of the counter-flow arrangement was made because it matched the case run by Vafai and Zhu (1999) and because it was thought that this would be the toughest case (where, by the "toughest case", it is meant that this case would be the most demanding on the grid, such that a grid that solves this arrangement will also solve the other arrangements, but the converse is not necessarily true).

Using the experience gained in the preceding two sections, it was decided to make a first attempt at a grid on the counter-flow arrangement. The nomenclature for this grid is shown in Figs. 4.12a and 4.12b. It should be noted that, while for convenience, Fig. 4.12a contains the cross-sectional grids for the upper channel, the lower channel and the solid region all on the same sketch, the cross-sections in which there are nodes in the three regions are not the same (except at the faces $Z = 0$ and $Z = L$). In a cross-section, the node spacings in the X direction in both channels followed a geometric progression, with the finest spacing, $\Delta X_{c,1}$, located next to the solid region, and the spacings increased geometrically by a ratio r_{Xc}. Thus, the following must hold:

$$\frac{\Delta X_{c,2}}{\Delta X_{c,1}} = \frac{\Delta X_{c,3}}{\Delta X_{c,2}} = \frac{\Delta X_{c,4}}{\Delta X_{c,3}} = \cdots = \frac{\Delta X_{c,nxc}}{\Delta X_{c,nxc-1}} = r_{Xc} \tag{4.16}$$

where r_{Xc} is the X-direction expansion factor in the channels and nxc is the number of X-direction spacings in the channels. Additionally,

$$\Delta X_{c,1} + \Delta X_{c,2} + \Delta X_{c,3} + \cdots + \Delta X_{c,nxc-1} + \Delta X_{c,nxc} = B_c \tag{4.17}$$

In a cross-section in the channels, the Y-direction spacings followed two geometric progressions: the finest Y-spacing, $\Delta Y_{c,1}$ was located at the bottom of the channel; from there, the spacings increased geometrically with increasing height in the channel, up to the channel's middle height, directly below which there was a spacing of $\Delta Y_{c,nyc/2}$. Then,

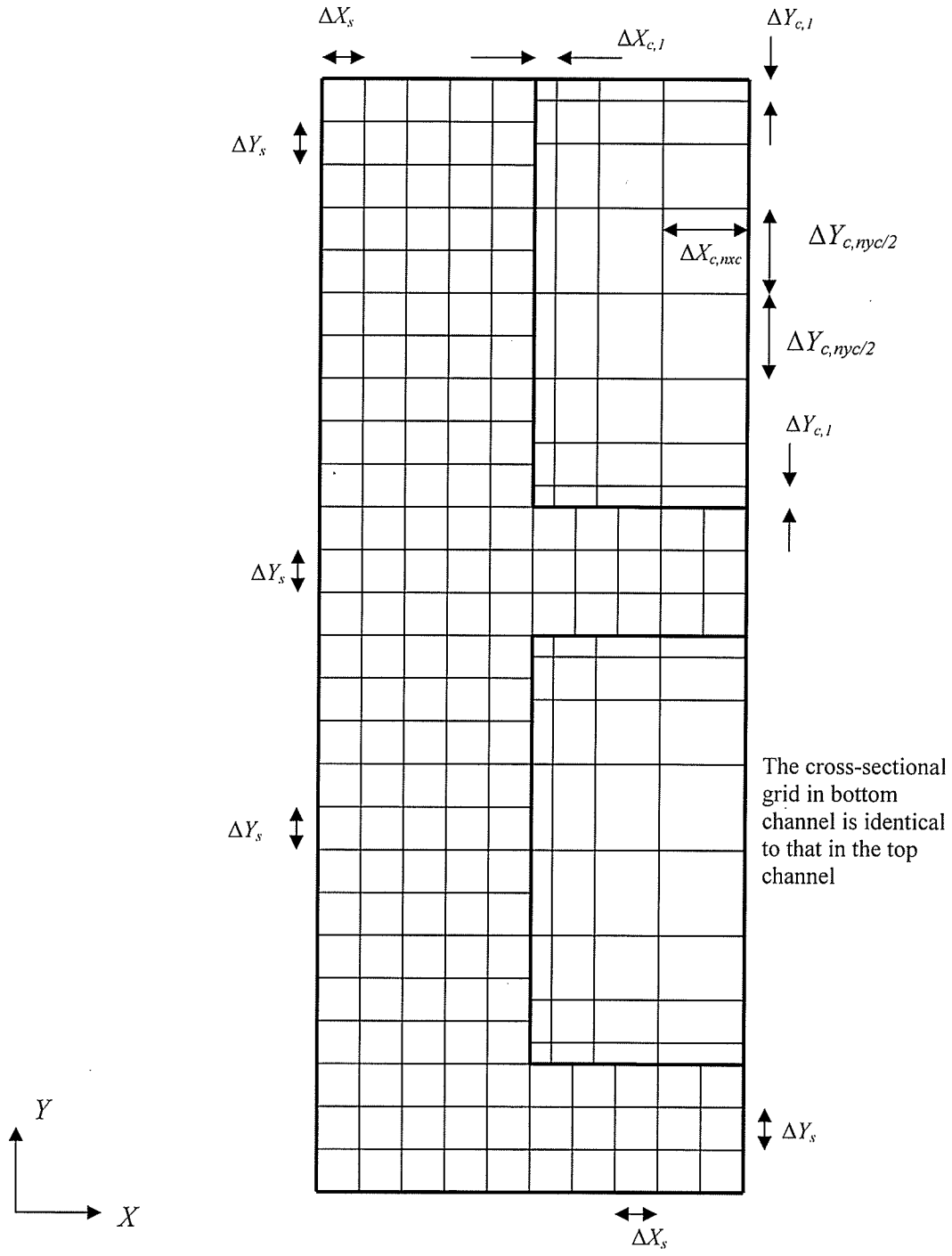

Figure 4.12a: Cross-Sectional Grid Nomenclature for the First Attempt at the Counter-Flow Arrangement Problem

the top half of each of the channels was a mirror image of its lower half. The following must hold:

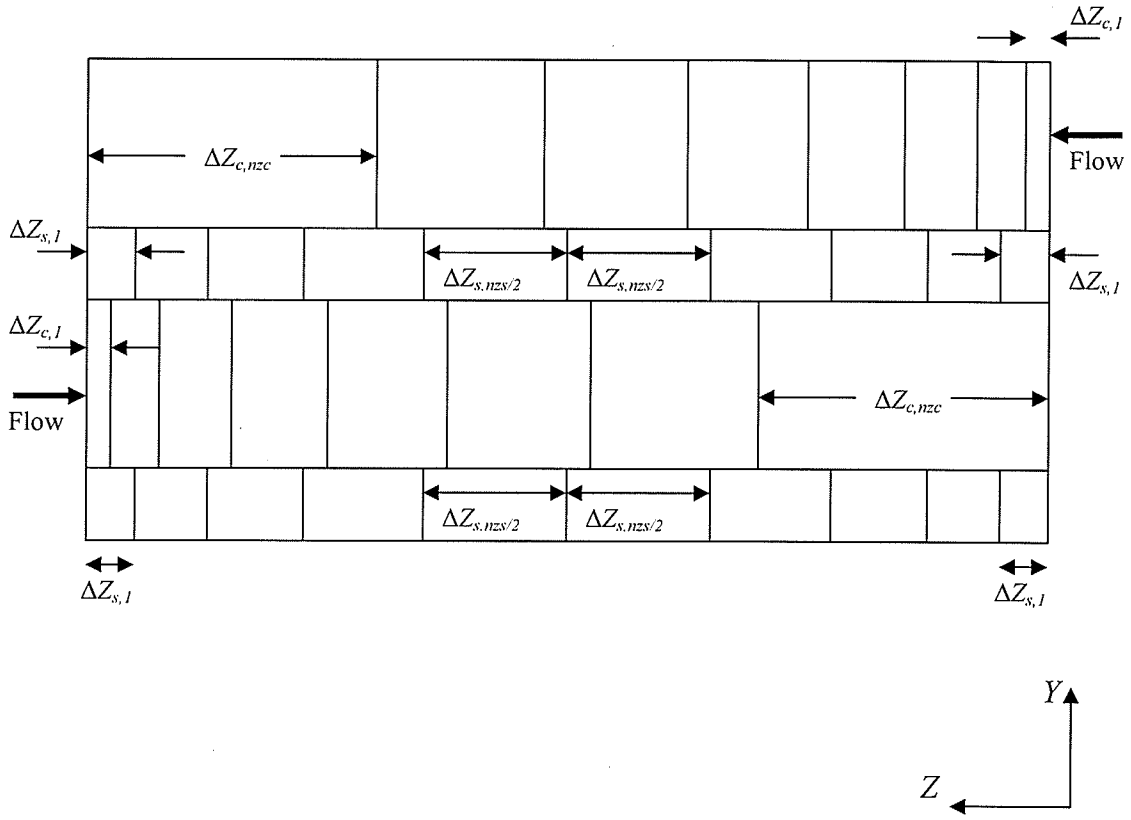

Figure 4.12b: Axial Grid Nomenclature for the First Attempt at the Counter-Flow Arrangement Problem

$$\frac{\Delta Y_{c,2}}{\Delta Y_{c,1}} = \frac{\Delta Y_{c,3}}{\Delta Y_{c,2}} = \frac{\Delta Y_{c,4}}{\Delta Y_{c,3}} = \cdots = \frac{\Delta Y_{c,nyc/2}}{\Delta Y_{c,nyc/2-1}} = r_{Yc} \tag{4.18}$$

where r_{Yc} is the Y-direction expansion factor in the channels and nyc is the number of Y-direction spacings in the channels. Additionally, the sum of all the spacings equals the half-width of the channel:

$$\Delta Y_{c,1} + \Delta Y_{c,2} + \Delta Y_{c,3} + \cdots + \Delta Y_{c,nyc-1} + \Delta Y_{c,nyc} = \frac{H_c}{2} \tag{4.19}$$

where nyc is the number of Y-direction spacings. The X-direction spacing was chosen such that there was an integral number of spacings in the "fin" regions, and an integral number of spacings in the region to the left of the channels. In the Y-direction, there was an integral number of spacings in each of the following regions: in the area below the

bottom channel, in the area to the left of the lower channel, the area in between the two channels, and in the area to the left of the upper channel.

Axially, the Z-direction spacings were as shown in Fig. 4.12b. It should be remembered that, in this view, which looks towards the negative X-direction, there was some solid material "behind" each of the two channels. In the channels, there was a geometric progression, with the smallest spacing of $\Delta Z_{c,1}$, located at each channel's respective inlet, and, the spacings increased geometrically with ratio r_{Zc} along each channel's direction of flow. Because the direction of flow was different, each channel had its smallest spacing at opposite ends. Mathematically, it can be written that

$$\frac{\Delta Z_{c,2}}{\Delta Z_{c,1}} = \frac{\Delta Z_{c,3}}{\Delta Z_{c,2}} = \frac{\Delta Z_{c,4}}{\Delta Z_{c,3}} = \cdots = \frac{\Delta Z_{c,nzc}}{\Delta Z_{c,nzc-1}} = r_{Zc} \tag{4.22}$$

and

$$\Delta Z_{c,1} + \Delta Z_{c,2} + \Delta Z_{c,3} + \cdots + \Delta Z_{c,nzc-1} + \Delta Z_{c,nzc} = L \tag{4.23}$$

In the solid, in the Z-direction, the spacings followed two geometric progressions: starting from one end, the spacings increased from $\Delta Z_{s,1}$ by a ratio r_{Zs}, up to the middle, at which point the spacings decreased towards the other end, by the same ratio, such that the second half was a mirror image of the first. Here, the following relations were applicable:

$$\frac{\Delta Z_{s,2}}{\Delta Z_{s,1}} = \frac{\Delta Z_{s,3}}{\Delta Z_{s,2}} = \frac{\Delta Z_{s,4}}{\Delta Z_{s,3}} = \cdots = \frac{\Delta Z_{s,nzs/2}}{\Delta Z_{s,nzs/2-1}} = r_{Zs} \tag{4.24}$$

and

$$\Delta Z_{s,1} + \Delta Z_{s,2} + \Delta Z_{s,3} + \cdots + \Delta Z_{s,nzs/2-1} + \Delta Z_{s,nzs/2} = \frac{L}{2} \tag{4.23}$$

The values of the parameters that specify the grid were as follows (parameters not listed can be calculated from listed values): $\Delta X_s = 2.0$ [μm], $\Delta Y_s = 2.0$ [μm], $\Delta Z_{s,1} = 1.0$ [μm], $nzs = 400$, $\Delta X_{c,1} = 0.5$ [μm], $\Delta Y_{c,1} = 0.5$ [μm], $nxc = 20$, $nyc = 40$, $\Delta Z_{c,1} = 0.05$ [μm], $nzc = 400$.

However, this grid did not yield realistic results. This is shown in Fig. 4.13, where the temperature profiles, at $X = 0$, are plotted against Z for various values of Y. Those fluctuations in the temperature profile are not realistic, and furthermore, Vafai and

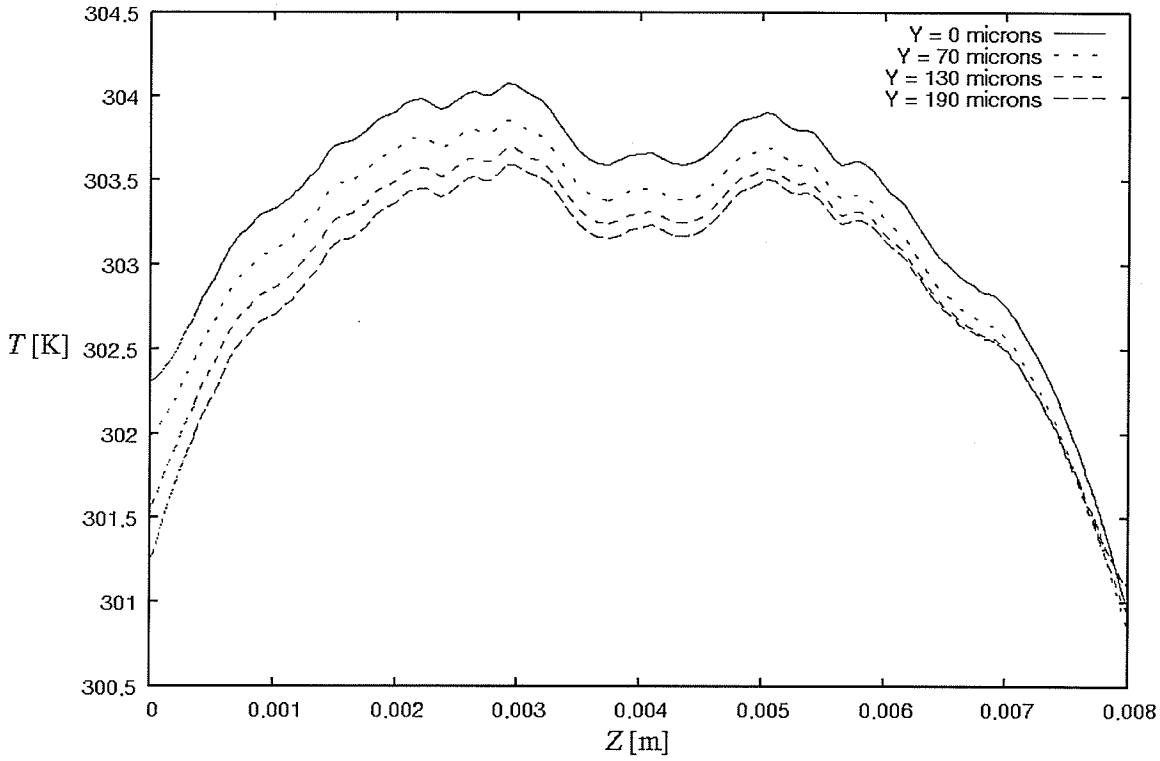

Figure 4.13: Temperature Profiles Along Z, for Various Y Values, at $X = 0$, for the Grid Used in Section 4.3

Zhu (1999) obtained no oscillations when drawing these profiles. Thus, the current attempt at a grid is not adequate. It was suspected that, while ANSYS CFX can theoretically handle grids where the nodes do not line up 1:1 at the interfaces, the interpolation scheme used was causing problems, perhaps exacerbated by other factors such as the aspect ratio of the control volumes. Thus, it was decided to avoid the non-matching nodes at the interface, by using only 1:1 nodal connections at interfaces, and, as a first step, using only uniform spacings. This is explored in the next section.

4.4 Counter-Flow: Uniform Grids

In order to solve the problem of the nonphysical results obtained in the previous section, it was decided to perform the calculations using uniform grids. This would eliminate the effect of the non-1:1 nodal connections at the interfaces, and hopefully, produce physically realistic results. The problem examined in this section is that of the counter-flow arrangement, with a low Reynolds number, and using the uniform inlet velocity assumption (Case 1).

The nomenclature of the grids used in this section is shown in Fig. 4.14a for a cross-section and in Fig. 4.14b for the axial distribution. In a cross-section, the nodes were spaced a length of ΔX, in the X-direction, and a length of ΔY in the Y-direction. The X- and Y-spacings were chosen such that there was an integral number of X-spacings in each of B_c and $(B - B_c)$, and an integral number of Y-spacings in each of H_c and H_f. This ensured that every "control volume" was located entirely within one of the following three regions: the bottom channel, the top channel, the solid region. Axially, the nodes were spaced a distance ΔZ. With *nx*, *ny* and *nz* being, respectively, the number of X-, Y- and Z-direction spacings, the following relations must hold:

$$nx\Delta X = B \tag{4.24}$$

$$ny\Delta Y = H \tag{4.25}$$

$$nz\Delta Z = L \tag{4.26}$$

Once again, it should be kept in mind that the *nodes* were located at the intersections of the lines that define the various *spacings*.

Table 4.3 summarizes the parameters of the grids used in this section. The corresponding values of ΔX, ΔY, ΔZ can be calculated from Eqs. (4.24) - (4.26), and are hence not listed.

Table 4.3: Definitions of the Various Uniform Grids Used in Solving the Counter-Flow Problem

Mesh	*nx*	*ny*	*nz*
Coarse	10	36	100
Medium	20	60	200
Fine	40	120	400

While solving the counter-flow arrangement problem using these grids, convergence problems were encountered. After searching to determine the cause of this problem, it was discovered that, for the values of the parameters used in Vafai and Zhu (1999), it was necessary to use double precision in the solution. The reason for this is that, with the relatively small heat flux supplied, the temperature field, particularly in the solid, contained gradients that were too small to capture with single precision (while this

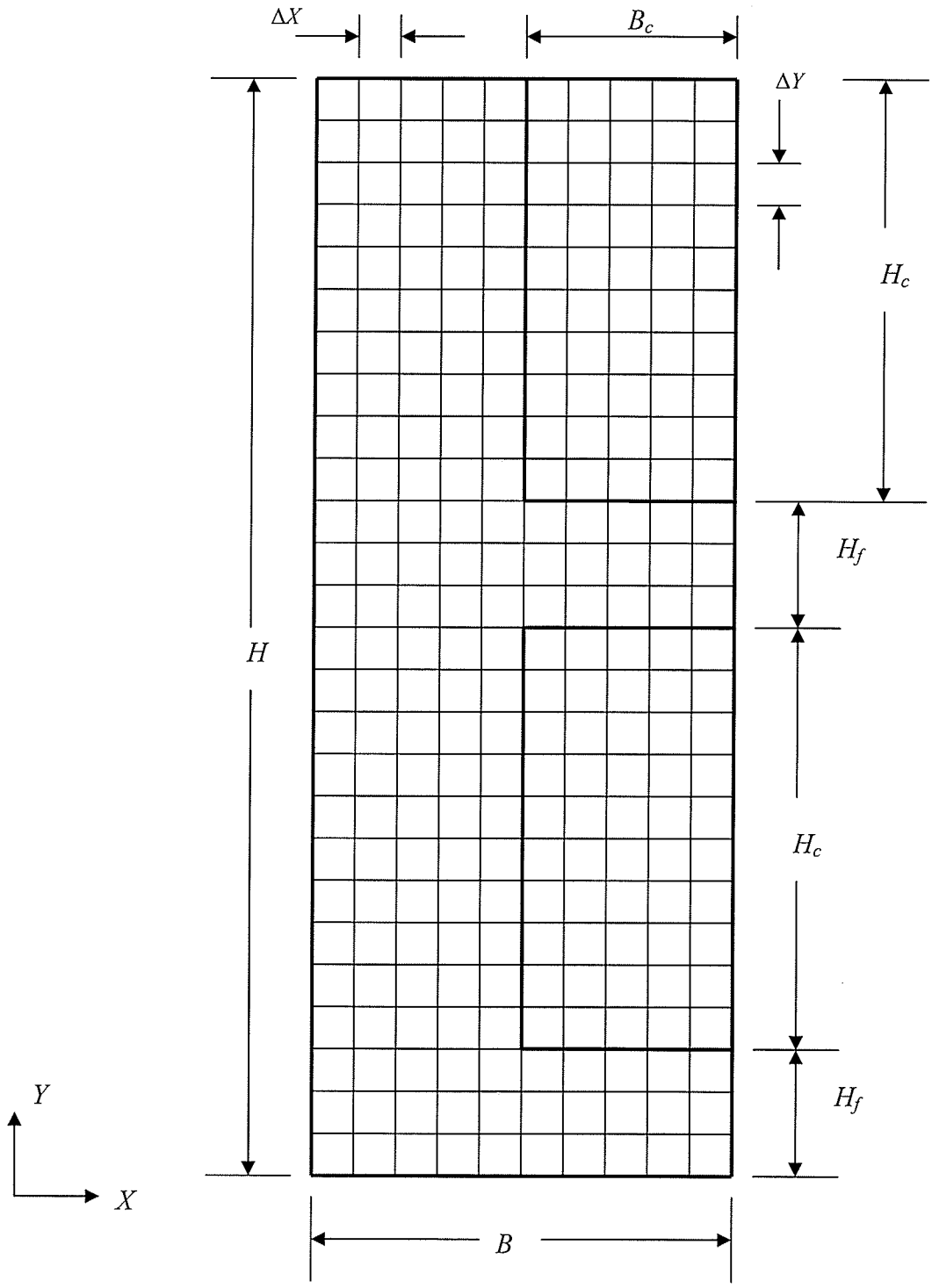

Figure 4.14a: Cross-Sectional Grid Nomenclature for the Counter-Flow Arrangement Problem Using Uniform Grids

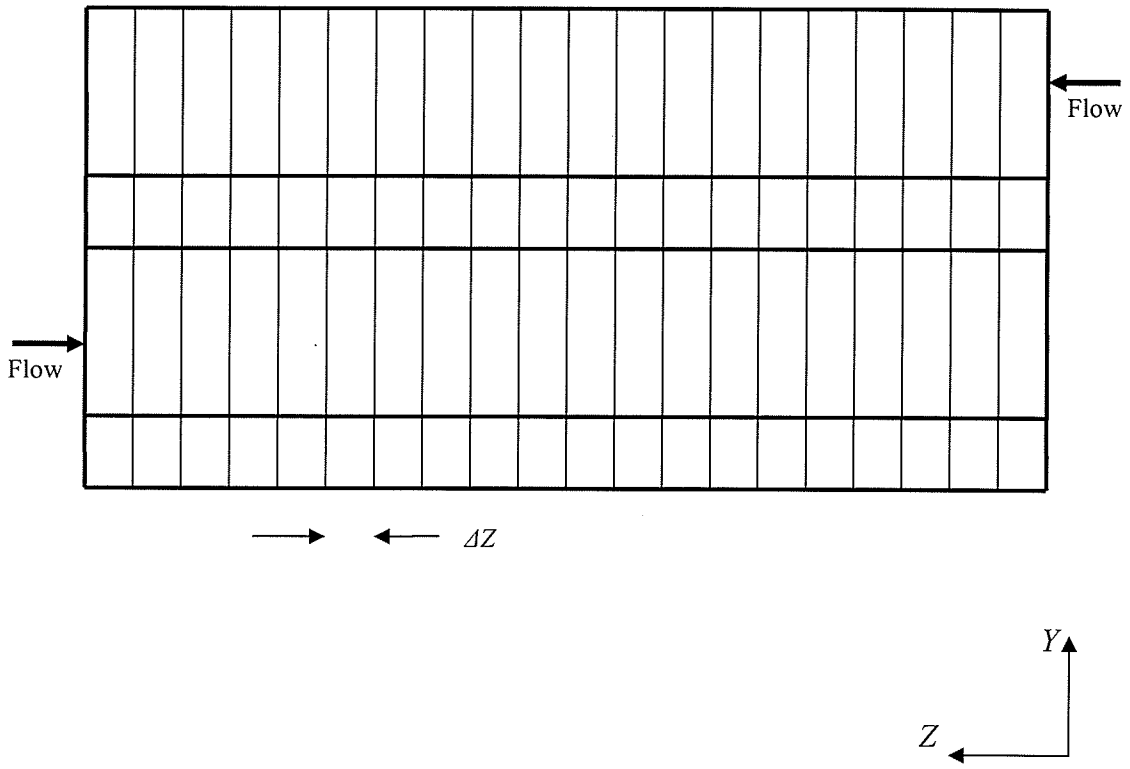

Figure 4.14b: Axial Grid Nomenclature for the Counter-Flow Arrangement Problem Using Uniform Grids

may seem to suggest that the problem studied is not of practical importance, it should be remembered that the results can be non-dimensionalized, and, when scaled up, the results have practical significance).

In order to assess the grid-independence of the solution, and to later compare the current solutions with those of Vafai and Zhu (1999), it is necessary to define a few lines at this point, along which the temperature will be plotted. Figure 4.15 shows the various lines, defined in a cross-section. These lines are valid for the counter-flow and parallel-flow arrangements (for the other arrangements, other definitions, presented later, are defined). As shown, there are four vertical lines and four horizontal lines in a cross-section, whose descriptions are as follows:

- Line "a": vertical line passing along the left hand side of the domain ($X = 0$; from $Y = 0$ to $Y = H$)

- Line "b": vertical line passing along the vertical interface planes between the channels and the solid ($X = B - B_c$; from $Y = 0$ to $Y = H$)
- Line "c": vertical line passing one quarter of the channels' width (or one half of the portion of the channels' width located within one repeat unit) to the right of the vertical channel-solid interfaces ($X = B - \frac{B_c}{2}$; from $Y = 0$ to $Y = H$)
- Line "d": vertical line passing along the symmetry planes of both channels, which is at the right side of the repeat unit ($X = B$; from $Y = 0$ to $Y = H$)
- Line "A": horizontal line passing along the bottom of the domain ($Y = 0$; from $X = 0$ to $X = B$)
- Line "B": horizontal line passing along the vertical middle of the bottom channel ($Y = H_f + \frac{H_c}{2}$; from $X = 0$ to $X = B$)
- Line "C": horizontal line passing midway between the top of the bottom channel, and the bottom of the top channel ($Y = \frac{3}{2} H_f + H_c$; from $X = 0$ to $X = B$)
- Line "D": horizontal line passing along the vertical middle of the top channel ($Y = 2H_f + \frac{3}{2} H_c$; from $X = 0$ to $X = B$)

In order to completely specify the above-described lines, it is necessary to specify in which axial cross-section they are located. Five axial cross-sections were considered in this work. They are:

- Cross-section "1": cross-section in which are located the inlet of the top channel, and the outlet of the bottom channel ($Z = 0$)
- Cross-section "2": cross-section located 5 % of the channels' length away from the top channel inlet, or 95 % of the channels' length away from the bottom channel inlet ($Z = 0.05\ L$)
- Cross-section "3": cross-section passing along the axial middle
- Cross-section "4": cross-section located 95 % of the channels' length away from the top channel inlet, or 5 % of the channels' length away from the bottom channel inlet ($Z = 0.95\ L$)

- Cross-section "5": cross-section in which are located the outlet of the top channel, and the inlet of the bottom channel ($Z = L$)

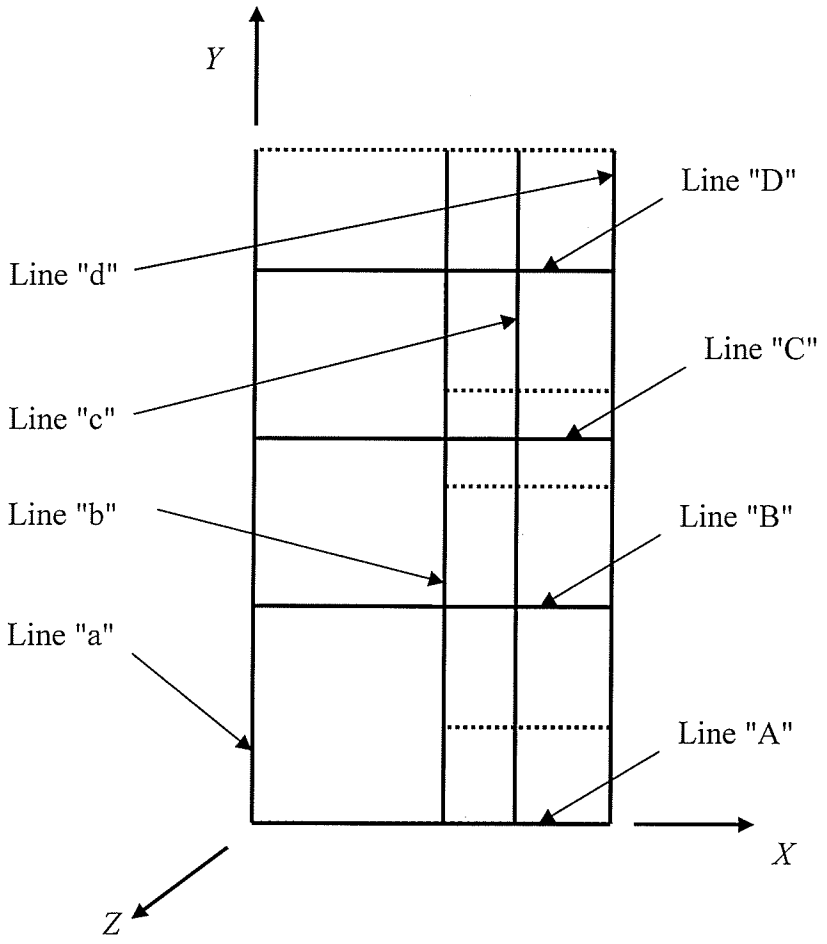

Figure 4.15: Schematic Representation of the Various Cross-Sectional Lines Along Which Solution Fields can be Plotted

Thus, a line is completely specified by giving its letter designation, along with the number corresponding the cross-section in which it is located. For example, line "c", in cross-section "4" would be designated as "line c4" (without the quotes), or simply "c4" (without the quotes), and it would have as its extremities the points ($X = B - \frac{B_c}{2}$, $Y = 0$, $Z = 0.95\ L$) and ($X = B - \frac{B_c}{2}$, $Y = H$, $Z = 0.95\ L$). With the 8 lines within a cross-section, and the 5 cross-sections, a total of 40 lines have been defined thus far.

In addition to the 40 lines defined so far, the following 4 lines are also defined:

- Line "AX": a line parallel to the direction of flow in the channels, having as its extremities the points ($X = 0$, $Y = 0$, $Z = 0$) and ($X = 0$, $Y = 0$, $Z = L$)
- Line "BX": a line parallel to the direction of flow in the channels, having as its extremities the points ($X = 0$, $Y = H_f + \frac{H_c}{2}$, $Z = 0$) and ($X = 0$, $Y = H_f + \frac{H_c}{2}$, $Z = L$)
- Line "CX": a line parallel to the direction of flow in the channels, having as its extremities the points ($X = 0$, $Y = \frac{3}{2}H_f + H_c$, $Z = 0$) and ($X = 0$, $Y = \frac{3}{2}H_f + H_c$, $Z = L$)
- Line "DX": a line parallel to the direction of flow in the channels, having as its extremities the points ($X = 0$, $Y = 2H_f + \frac{3}{2}H_c$, $Z = 0$) and ($X = 0$, $Y = 2H_f + \frac{3}{2}H_c$, $Z = L$)

A word of caution is in order for readers who might be comparing this work to that of Vafai and Zhu (1999). As much as possible, the current work used the same nomenclature as that used by Vafai and Zhu (1999) in defining the lines above. The eight letter-designations of lines in a cross-section are the same as Vafai and Zhu (1999) used. However, they did not employ a numbering scheme; instead, they simply quoted the Z value where the line was located. Furthermore, they only studied temperature profiles at three axial cross-sections, instead of five. The most significant difference is that their Z axis is in the opposite direction as the one used in this work. Thus, what they refer to as "$Z = L$", is referred to as "$Z = 0$" in this work. This choice was made to avoid the use a left-handed coordinate system. Furthermore, what is referred to as "AX" in this work, they refer to as "A". Here, the deviation from their notation was done to avoid ambiguous notation.

Figure 4.16 shows the temperature profiles along the various axial lines, using the results obtained from the coarse mesh. It is analogous to Figure 4.13 in the previous section, except that the coarse uniform mesh of this section is used. It is encouraging to note that oscillatory, non-physical temperature profiles are no longer obtained. Instead,

physically realistic results, which qualitatively agree with the results of Vafai and Zhu (1999), are obtained. Furthermore, while not documented here, similar plots using the medium and fine meshes produce the same result. Therefore, a grid-refinement test of the grids used in this section can now be performed.

Figure 4.17 shows the temperature profiles along line AX, using the coarse, medium and fine grids. A visual examination of this plot shows that the three grids give temperature predictions, along line AX, that are close together, with the maximum deviations occurring at the two extremities, namely $Z = 0$ and $Z = L$. Qualitatively, the temperature predictions of the coarse and medium grids are within 0.052 % of each other, while the predictions of the medium and fine grids are within 0.020 % of each other. In both cases, the maximum discrepancies occur at $Z = L$.

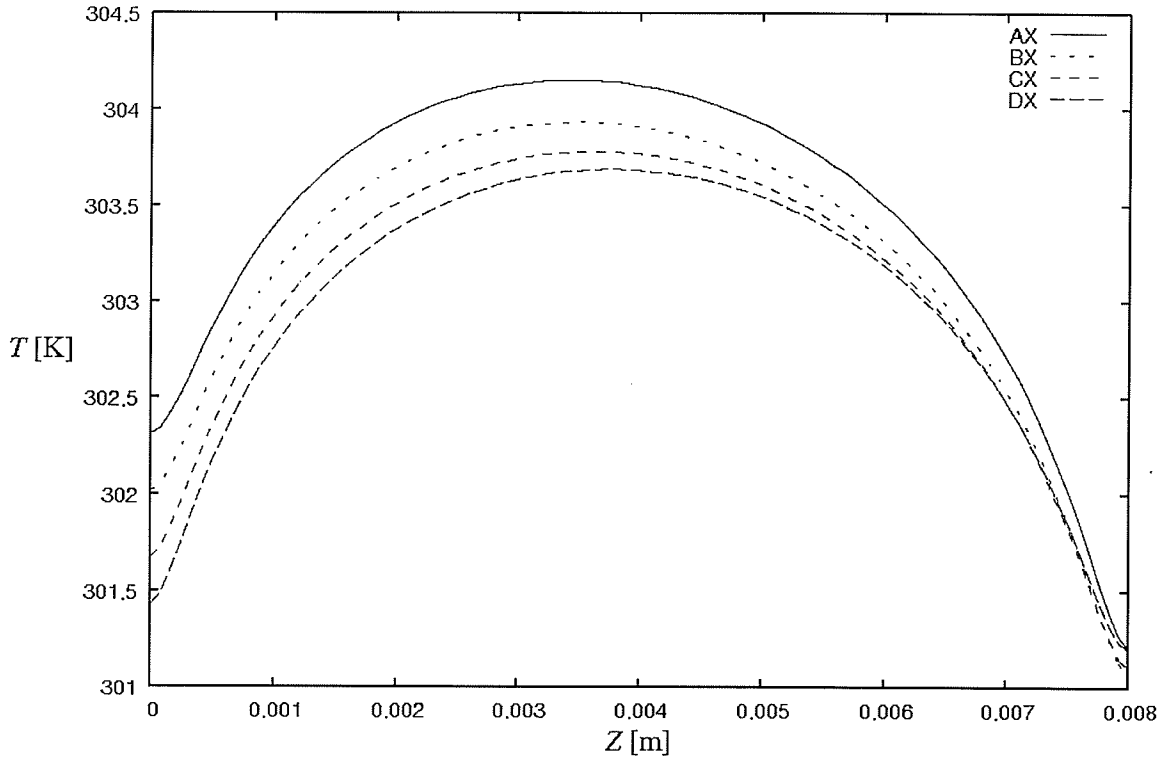

Figure 4.16: Temperature Profiles Along Axial Lines Using Coarse Uniform Grid for the Case 1 Problem

While the results shown in Figure 4.17 are encouraging, it should be remembered that the temperature profiles therein are taken along a line located entirely within the

solid. It was decided, then, to also perform a grid-refinement test on a line that passes through the fluid regions. The reason for this is that the heat transfer phenomenon in the

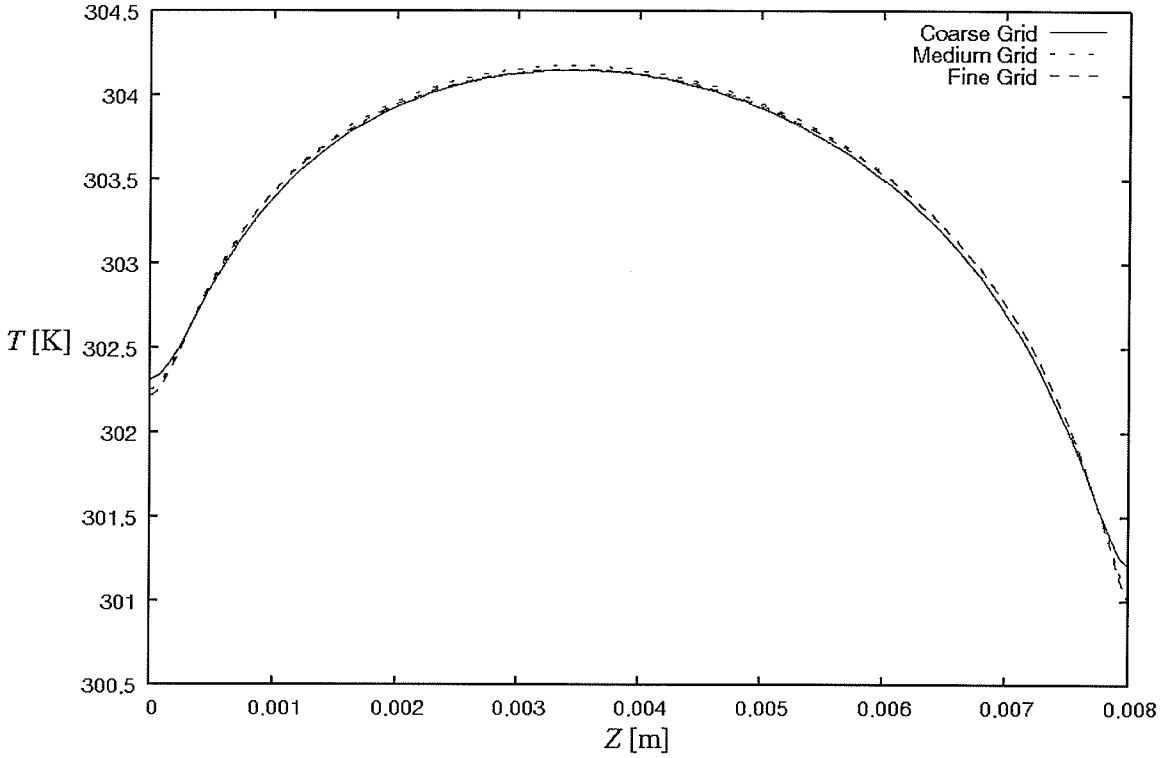

Figure 4.17: Temperature Profiles Along Line AX Using the Various Uniform Grids for the Case 1 Problem

fluid is more complicated than that in the solid, and, it is quite possible that the temperature profiles obtained by the three meshes differ more significantly from each other in other regions of the domain, particularly in the fluid. Thus, it was decided to perform a grid-refinement test along line c2. This is shown in Figure 4.18. This figure reveals a near overlap of the temperature predictions for the coarse, medium and fine grids, except in a few locations, such as $Y = H$. Quantitatively, the predictions of the temperature along line c2 of the coarse and medium grids are within 0.043 % of each other, while those of the medium and fine grids are within 0.018 % of each other. In both cases, the maximum discrepancy occurs in the region of steep gradient, located near $Y = 0.00015$ [m], which corresponds to a location within the top channel, close to the bottom of this upper channel.

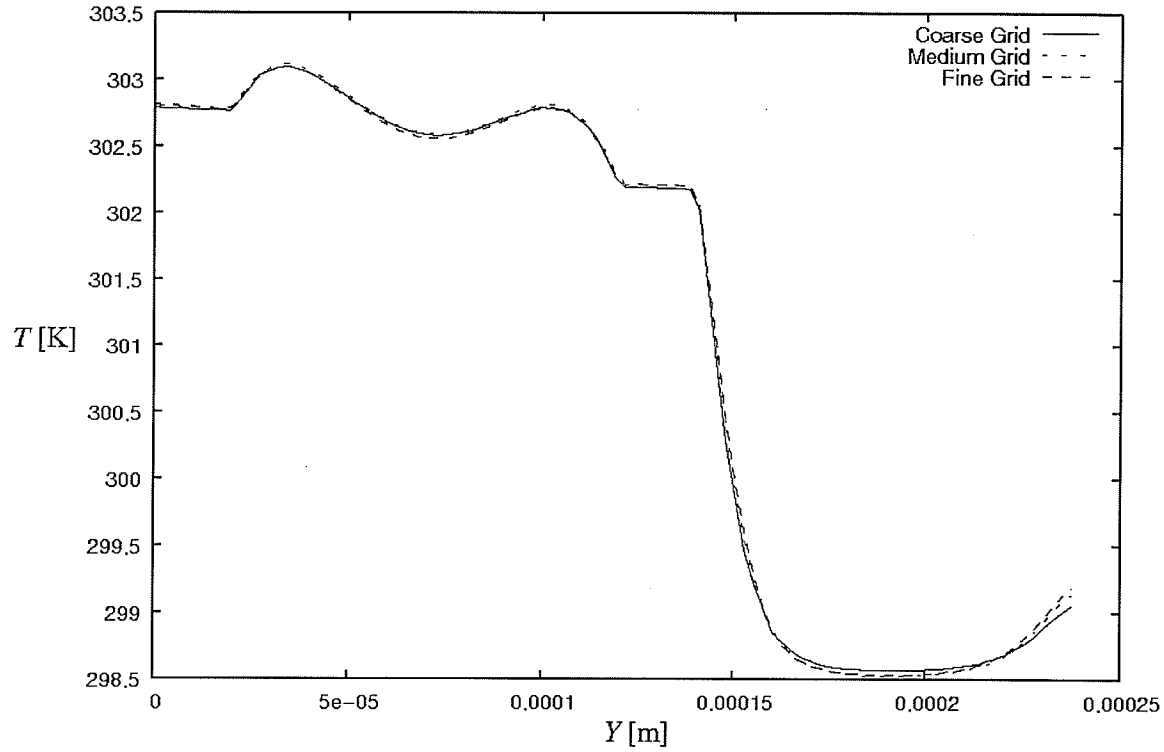

Figure 4.18: Temperature Profile Along Line c2 Using the Various Uniform Grids for the Case 1 Problem

The following point should be kept in mind. Along line AX, the temperature predictions of the medium and fine grids were within 0.020 % of each other, and, along line c2, they were within 0.018 % of each other. While this is indeed what is desired in a grid-refinement study, since it shows that the refinement from the medium grid to the fine grid has produced no noticeable change in the solution, the amount by which the grid-refinement test is successful can appear, at first glance, more than it is in reality. The temperatures in Figures 4.17 and 4.18 hover near 300 [K]. Thus, a difference as large 1.5 [K] still corresponds to only about 0.5 %. However, given that the range of temperature values in Figures 4.17 and 4.18 is less than 5 [K], a discrepancy of 1.5 [K] would be quite considerable, even though it would only correspond to a 0.5 % discrepancy between two temperature profiles. Thus, the relatively high magnitudes of the temperatures, combined with the comparatively small range of temperatures in the solutions, gives the impression that the grid-refinement test is more successful than it is. It is still successful, but not *as much as* one might believe judging only from the low discrepancies between the medium and fine meshes.

The problem under consideration so far in this section is the counter-flow problem, with a low Reynolds number, using the uniform inlet assumption. That is, Case 1 (Table 3.1 contains the definitions of this case, as well as the other cases examined in this work). Even though the grids of this section passed the grid-refinement test, when used on Case 1, it was decided to test the grids on the corresponding high Reynolds number case, namely Case 3. This is done because, with the higher mass flow rates, the grids of this section may not be adequate on Case 3, particularly in regions of steep gradients, even though the grid-refinement of Case 1 was successful. Since the goal is ultimately to find of a grid that will work for all problems considered in this thesis, it is necessary to achieve grid-independent behavior for Case 3 as well. In theory, Case 3 could have been examined directly, without worrying about Case 1, but, since Case 1 corresponds to the same Reynolds number as used by Vafai and Zhu (1999), it was decided to first consider Case 1. It should be mentioned in passing that, since the supplied heat flux is greater in Case 3 than it is in Case 1, by a factor of 10, the temperature field in Case 3 will span a larger range, which will partially alleviate the problem described in the preceding paragraph.

Figure 4.19 shows the temperature predictions along line AX for Case 3, for the uniform grids examined in this section. Here, it cannot be said that the curves nearly overlap. The typical grid-refinement pattern is observed: the difference between the predictions of the coarse mesh and the medium mesh is relatively large, and the difference between the medium mesh and the fine mesh is comparatively smaller. Nonetheless, none of the temperature profiles is visually identical to another. Quantitatively, the temperature profiles obtained using the coarse and medium grids are within 0.96 % of each other, while those using the medium and fine mesh are within 0.53 % of each other. Thus, while the correct trend is observed with successive grid refinements, the discrepancy between the predictions of the medium and fine meshes is still too great (especially, as discussed earlier, that the range of temperature data is small compared to the magnitude of the temperatures). Thus, the solution to Case 3 cannot be considered mesh-independent.

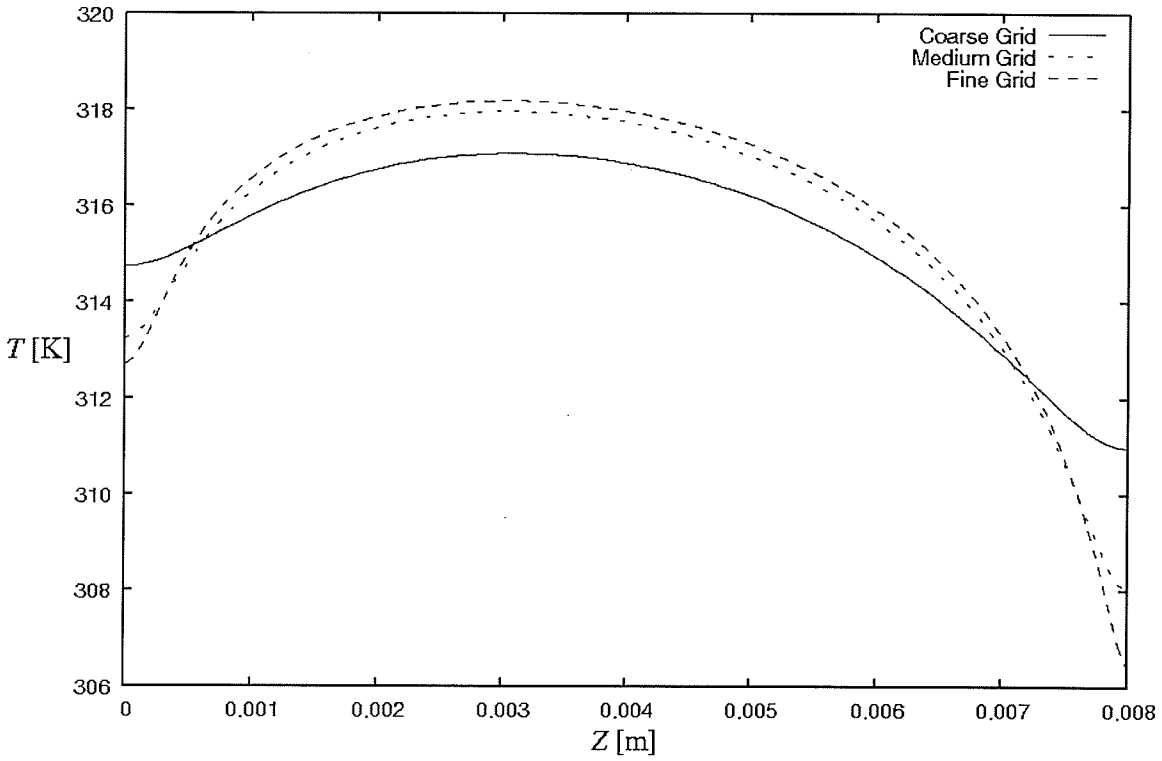

Figure 4.19: Temperature Profiles Along Line AX Using the Various Uniform Grids for the Case 3 Problem

The temperature profiles along line c2, for the uniform grids of this section, are shown in Figure 4.20. The temperature predictions of the coarse and medium meshes are within 0.74 % of each other, while those of the medium and fine meshes are within 0.25 % of each other. Even though the maximum discrepancies occur in the solid, it becomes apparent upon further reasoning that it is not the grid in the solid that is inadequate. Every grid predicts the same basic trend (slope) of the temperature profile in the solid. The only difference is at what height the temperature in the solid is placed. This actually depends on how well the gradient is captured in the fluids. If the gradient is not correct, it skews the location of the solid temperature profile, but, the "shape" of the profiles are nevertheless correct. Thus, what is missing is refinement in the fluids, near the walls.

Thus, some success was encountered in this section, particularly in the Case 1 problem. For Case 3, however, it turns out that the results are not mesh-independent. However, since it was not feasible, due to computing resource issues, to further refine

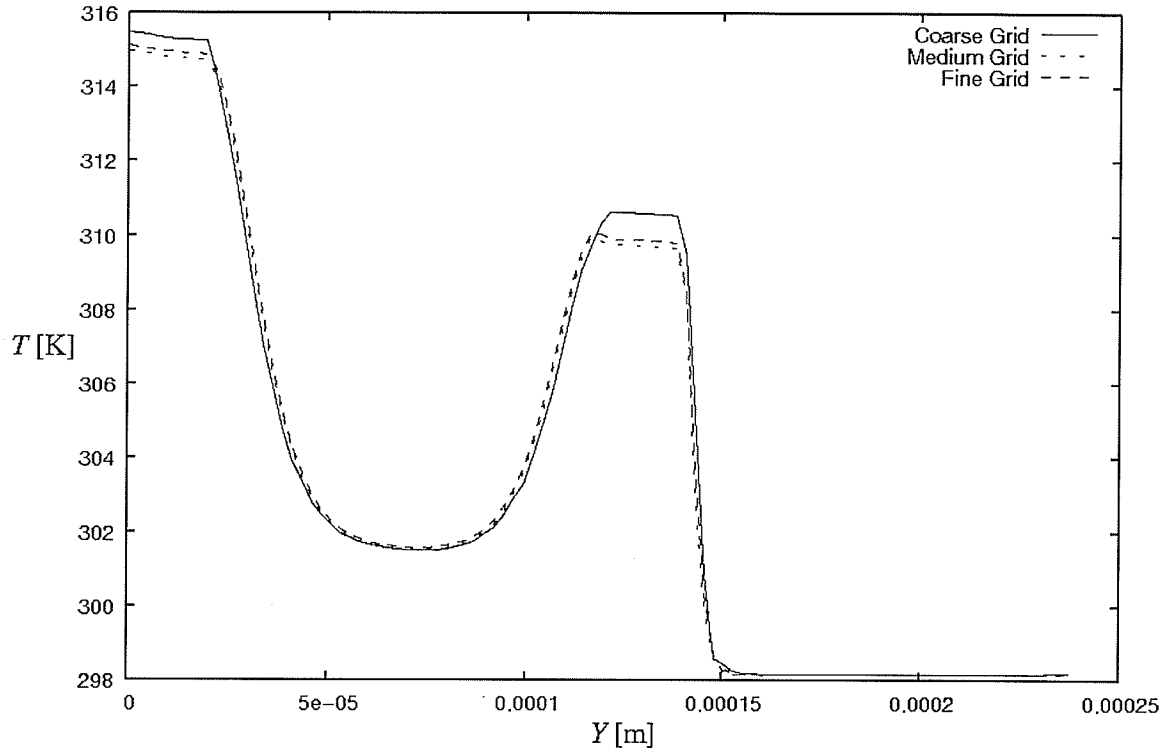

Figure 4.20: Temperature Profiles Along Line c2 Using the Various Uniform Grids for the Case 3 Problem

the grids, it was necessary to keep the same number of nodes, and redistribute them, placing more nodes where they are most needed, namely in regions of high gradients. Thus, the next section will re-explore non-uniform grids. Nodes will be packed more densely in regions near walls, and at the axial extremities of the domain. However, the lessons learned from the Section 4.3 will be followed, and it will be ensured that there is a 1:1 matching of nodes at the interfaces between the fluid regions and the solid.

4.5 Counter-Flow: Final Pass

The nomenclature for the grid spacings of the grids to be examined in this section is illustrated schematically in Figures 4.21a (in a cross-section) and 4.21b (axially). In a cross-section, the grid spacings were as follows. Inside the channels, as well as in the portions of the solid that are below the bottom channel, and in between the top and bottom channel, in the X-direction, a spacing of $\Delta X_{cs,1}$ was located next to the solid-channel interface, and the spacings increased geometrically, by a factor of r_{Xcs}, up to the channels' symmetry plane, next to which the X-spacing was $\Delta X_{cs,nxcs}$. The subscript "cs"

denotes that the value applies in both the channel and solid regions. Mathematically, it can be written

$$\frac{\Delta X_{cs,2}}{\Delta X_{cs,1}} = \frac{\Delta X_{cs,3}}{\Delta X_{cs,2}} = \frac{\Delta X_{cs,4}}{\Delta X_{cs,3}} = \cdots = \frac{\Delta X_{cs,nxcs}}{\Delta X_{cs,nxcs-1}} = r_{Xcs} \tag{4.27}$$

and

$$\Delta X_{cs,1} + \Delta X_{cs,2} + \Delta X_{cs,3} + \cdots + \Delta X_{cs,nxcs-1} + \Delta X_{cs,nxcs} = B_c \tag{4.28}$$

In the X-direction, in the portion located entirely to the left of the channels, the spacings were simply uniform, with a width of ΔX_s. Thus

$$nxs\Delta X_s = B - B_c \tag{4.29}$$

where nxs is the number of X-direction spacings in the region of the solid located entirely to the left of the channels. The spacing size ΔX_s was chosen so that nxs is an integer. The total number of X-direction spacings was thus $nxs + nxcs$.

In the Y-direction, the spacings were as follows. Inside the top channel, the top-most spacing had a length of $\Delta Y_{cs,1}$. Then, proceeding downwards, the spacings increased geometrically, by a ratio r_{Ycs}, such that the spacing whose bottom node was exactly on the top channel's vertical mid-plane has a length of $\Delta Y_{cs,nycs/2}$. Then, in the bottom half of the top channel, the spacings were a mirror image of the top half. The Y-direction spacings in the bottom channel were the same as they are in the top channel: that is, the spacing adjacent to its top and bottom were $\Delta Y_{cs,1}$, and the spacings increased in length by a ratio of r_{Ycs}, such that the spacings directly above and below the channel's vertical mid-plane had a length of $\Delta Y_{cs,nycs/2}$. In the portion of the solid region directly to the left of the channels, the Y-direction spacings were the same as they were inside the channels themselves. The following relations were applicable:

$$\frac{\Delta Y_{cs,2}}{\Delta Y_{cs,1}} = \frac{\Delta Y_{cs,3}}{\Delta Y_{cs,2}} = \frac{\Delta Y_{cs,4}}{\Delta Y_{cs,3}} = \cdots = \frac{\Delta Y_{cs,nycs/2}}{\Delta Y_{cs,nycs/2-1}} = r_{Ycs} \tag{4.30}$$

and

$$\Delta Y_{cs,1} + \Delta Y_{cs,2} + \Delta Y_{cs,3} + \cdots + \Delta Y_{cs,nycs/2-1} + \Delta Y_{cs,nycs/2} = \frac{H_c}{2} \tag{4.31}$$

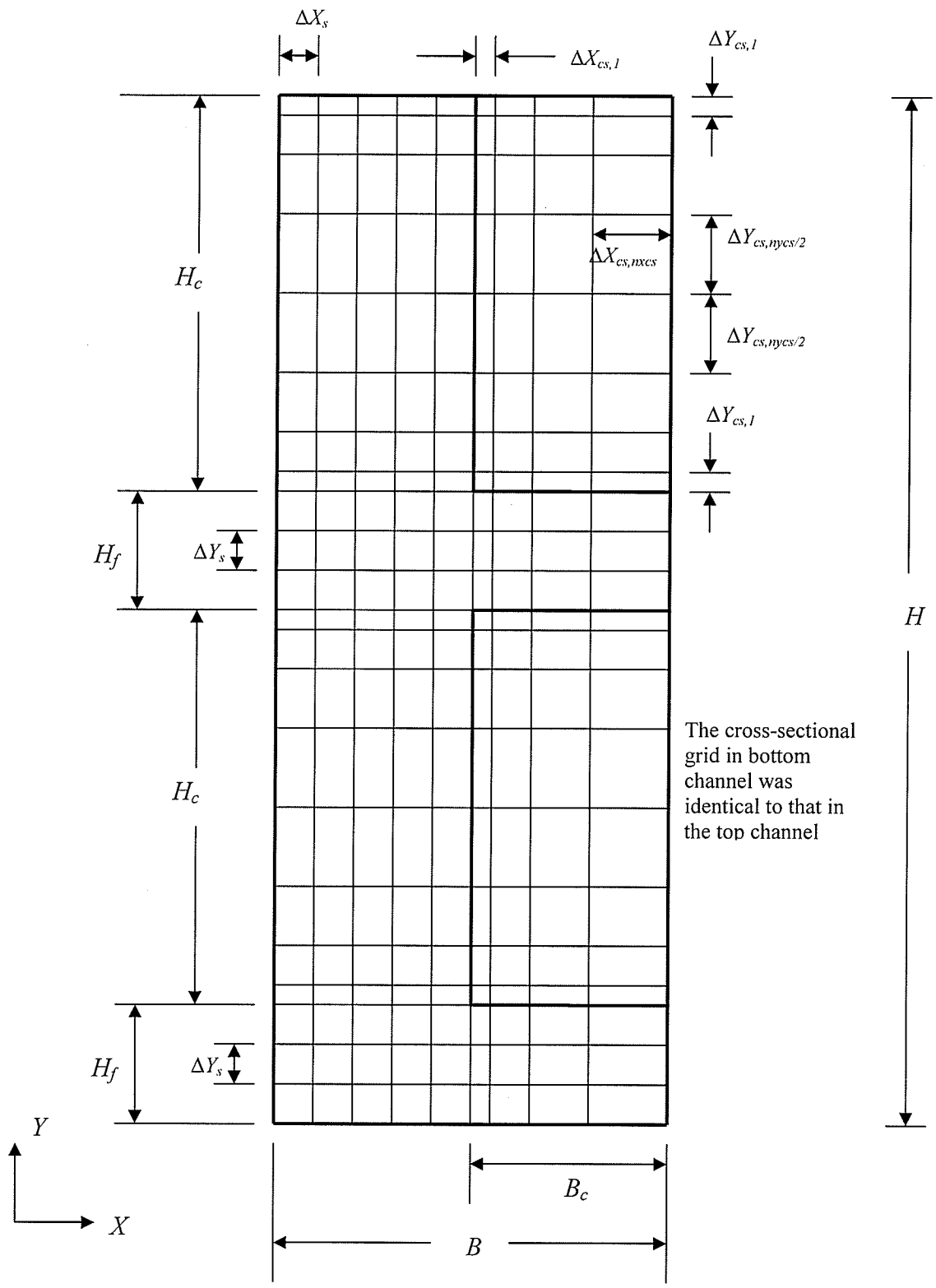

Figure 4.21a: Schematic Representation of the Cross-Sectional Grid Nomenclature Used in the Final Pass of the Grid-Refinement Studies

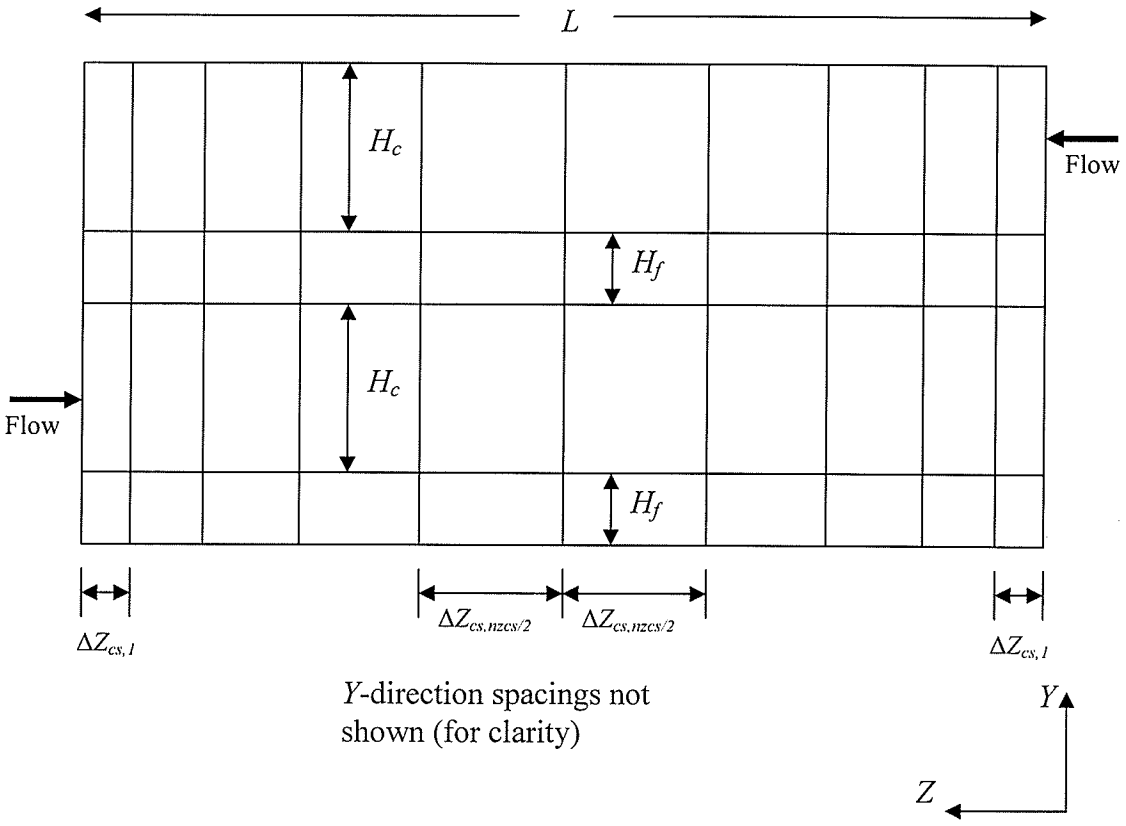

Figure 4.21b: Schematic Representation of the Axial Grid Nomenclature Used in the Final Pass of the Grid-Refinement Studies

In the *Y*-direction ranges $0 \le Y \le H_f$ and $(H_f + H_c) \le Y \le (2H_f + H_c)$, the spacings in the *Y*-direction were simply uniform, with a length of ΔY_s, as shown in Figure 4.21a. Thus,

$$nys\Delta Y_s = H_f \tag{4.31}$$

where *nys* represents the number of *Y*-direction spacings in each of the ranges $0 \le Y \le H_f$ and $(H_f + H_c) \le Y \le (2H_f + H_c)$. Thus, the total number of *Y*-direction spacings was then 2(*nys* + *nycs*).

As shown in Figure 4.21b, the *Z*-spacings in the solid, the top channel and the bottom channel are all identical. The spacing adjacent to Z = 0 had a length of $\Delta Z_{cs,1}$. Then, with increasing *Z*, the spacings increased in length by a ratio r_{Zcs}, up to the middle

of the length of the heat sink (that is, up to $Z = L/2$). Then, the spacings in the range $L/2 \le Z \le L$ were a mirror image of the spacings in the range $0 \le Z \le L/2$. Thus, mathematically,

$$\frac{\Delta Z_{cs,2}}{\Delta Z_{cs,1}} = \frac{\Delta Z_{cs,3}}{\Delta Z_{cs,2}} = \frac{\Delta Z_{cs,4}}{\Delta Z_{cs,3}} = \cdots = \frac{\Delta Z_{cs,nzcs/2}}{\Delta Z_{cs,nzcs/2-1}} = r_{Zcs} \tag{4.32}$$

and

$$\Delta Z_{cs,1} + \Delta Z_{cs,2} + \Delta Z_{cs,3} + \cdots + \Delta Z_{cs,nzcs/2-1} + \Delta Z_{cs,nzcs/2} = \frac{L}{2} \tag{4.33}$$

where *nzcs* is the number of *Z*-direction spacings in half the length of the heat sink. The total number of *Z*-direction spacings was thus $2nzcs$.

Once again, it should be kept in mind that the *nodes* (that is, the points at which ANSYS CFX applied the relevant, discretized versions of the governing equations) were located at the *intersections* of the lines that define the various *grid spacings*.

While trying to set up the simulations using the grids of this section, it was discovered that ANSYS CFX has a limitation, whereby the value of r_{Zcs} cannot be too large. It was found that, when the value of r_{Zcs} was too large (or, equivalently, when $\Delta Z_{cs,1}$ was too small), ANSYS CFX could not start the simulation, complaining of an error having to do with a "[f]atal overflow in linear solver". It is not known whether this was the result of a bug in ANSYS CFX, or an inherent flaw with the current grid with values of r_{Zcs} that are too large. Numerous tests, not documented here, were performed to investigate this issue, and find a possible workaround. It was found in the course of these tests that the problem lies in having fine grid spacings (or a contraction that is too pronounced) near $Z = L$. That is, there is no problem having a fine spacing near $Z = 0$, nor with a relatively quick expansion away from this face. However, since counter-flow was being investigated, and since it was desired to have a 1:1 matching of nodes at the domain interfaces, it was necessary to limit the value of r_{Zcs}; that is, it was not possible, given these constraints, to have one value in the first half of each channel, and a different one in the second. It was desired to meet the criterion $\Delta Z^+_{cs,1} < 10^{-6}$ (recall the definition given by Eq. (4.7)). However, the limitation found with ANSYS CFX required that a compromise be made, whereby a value of $\Delta Z^+_{cs,1} \approx 2x10^{-4}$ had to be accepted.

The definitions of the various grids used in this section are presented in Table 4.4. The grid parameters not presented in this table can be determined from the values given in the table, the problem parameters, as well as the various relations presented above when describing the grid nomenclature.

Table 4.4: Definitions of the Various Grids Used in the Final Pass of the Counter-Flow Arrangement Grid-Refinement Test

Mesh	*nxcs*	*nycs*	*nzcs*	*nxs*	*nys*	r_{Xcs}	r_{Ycs}	$\Delta Z_{cs,1}$ [μm]
Coarse	5	14	50	5	3	1.2	1.2	1.55387
Medium	10	26	100	10	5	1.2	1.2	1.55387
Fine	20	50	200	20	10	1.2	1.2	1.55387

In the process of analyzing the results obtained by solving the Case 1 problem (Case definitions are presented in Table 3.1) using the grids listed in Table 4.4, anomalous results were obtained (for all grids) whereby, when asked to generate temperature profiles along lines in cross-section 5, ANSYS CFX-post produced temperature profiles that contained non-physical spikes. As an example, the temperature profiles along the horizontal lines in cross-section 5, using the results of the medium grid, are plotted in Figure 4.22. The plot was generated by asking ANSYS CFX-post to generate plots along the appropriate lines, and, the data of this plot were exported, and the plot was generated using other software, to allow for greater customization of the plot, and because of a personal preference of the author. Clearly, the temperature profiles, as shown, are not correct. The spikes are definitely non-physical. It appears that, when the spikes are removed, the resulting temperature profiles are otherwise plausible. Normally, when plots were taken right at domain boundaries, the ANSYS CFX documentation suggested that, if necessary, the line definitions be moved slightly inward, to avoid problems with interpolations near boundaries. For example, rather than defining the Z coordinate of the lines to be $Z = L$, the lines should be defined with a Z coordinate of, say, $Z = 0.9999\ L$. However, in this case, even when this trick was used, non-physical spikes still occurred.

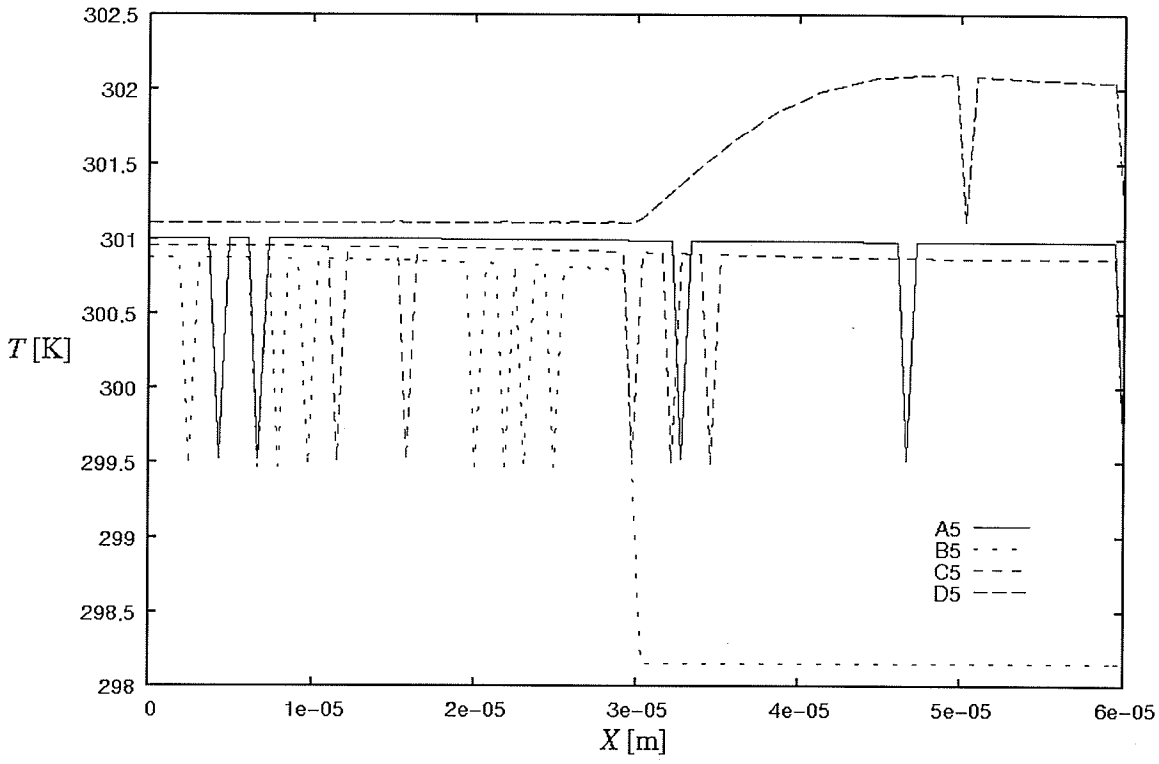

Figure 4.22: Example of Non-Physical Spikes in the $Z = L$ Cross-Section

It was suspected that it was probably the grid-refinement near the $Z = L$ plane that caused these problems with spikes. That the corresponding problem was not observed near $Z = 0$ can be explained by the fact that, relative to the current Z coordinate, the spacings are too small near $Z = L$, but this is not the case near $Z = 0$. To confirm this, the following test was performed. Using a case of *parallel-flow*, the problem was solved using two distinct grids. The first, denoted here as the *original* grid, was the exact grid as defined in Figures 4.21 and Table 4.4, where, for this problem, non-necessary grid refinements occurred in the channels (and the solid) near $Z = L$. The second grid, the *modified* grid, was the same as the original grid, with one modification: in the Z-direction, the same total number of spacings were used, except that, instead of having them expand and contract, they expanded only, with increasing Z. Because this was applied on a parallel-flow problem, no loss in solution accuracy should have resulted, since the coarse Z-spacings were all located in regions known to be in the fully-developed region. It was found that, in all cross-sections except cross-section 5, the temperature predictions of both the original and modified grids were identical. In cross-section 5, the

predictions of the original and modified grids were mostly similar, except for the spikes. That is, in regions where the code did not "predict" a spike, the original grid predicted the same temperature as the modified grid. This revealed that the original grid did not pose a problem in the actual internal solution of the discretized governing equations, when they were solved by ANSYS CFX-solver. That is, the spikes arose in the *post-processing* phase, due to some sort of glitch in the interpolation process. Thus, fortunately, the output given by ANSYS CFX-post when asked for temperature profiles in other cross-section can be trusted. Nevertheless, this bug (or inherent numerical instability) did limit, and in some cases prevented, the analysis of temperature profiles near $Z = L$.

The grid-refinement test was performed next. Since it was found, in the previous section, that the temperature predictions along the various axial lines achieves grid-independent behavior more easily than does the temperature distribution along other lines, particularly those that pass through the channel regions, this section will not focus on demonstrating grid-independent behavior on these lines. Rather, the focus will be on the temperature predictions along line c2.

Figure 4.23 shows the temperature predictions, for the various grids examined in this section, along line c2, for the Case 1 problem (that is, the low Reynolds number, counter-flow problem). Visually, this plot seems to suggest grid-independent behavior. Qualitatively, the temperature predictions given by the coarse and medium grids were within 0.019 % of each other, while those given by the medium and fine grids were within 0.0089 % of each other. Thus, grid-independent behavior was achieved.

Figure 4.24 shows the temperature predictions, for the various grids examined in this section, along line c2, for the Case 3 problem (that is, the high Reynolds number counter-flow problem). Visually, this plot seems to suggest grid-independent behavior. Qualitatively, the temperature predictions given by the coarse and medium grids were within 0.28 % of each other, while those given by the medium and fine grids were within 0.036 % of each other. Thus, grid-independent behavior was obtained.

Thus, since the grid-refinements tests were successful, even on the most "difficult" problem, namely that of counter-flow with the higher Reynolds number, the search for an appropriate grid was over. The grid to be used was the medium grid, as

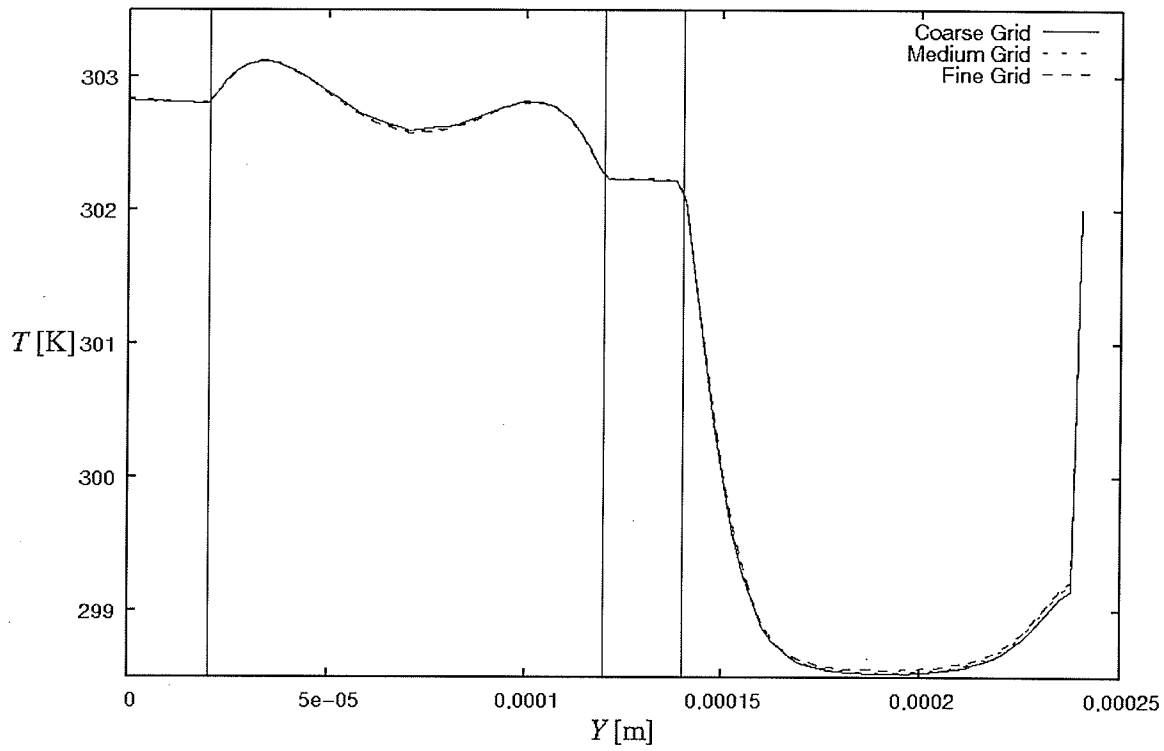

Figure 4.23: Temperature Profiles Along Line c2 Using the Various Non-Uniform Grids for the Case 1 Problem

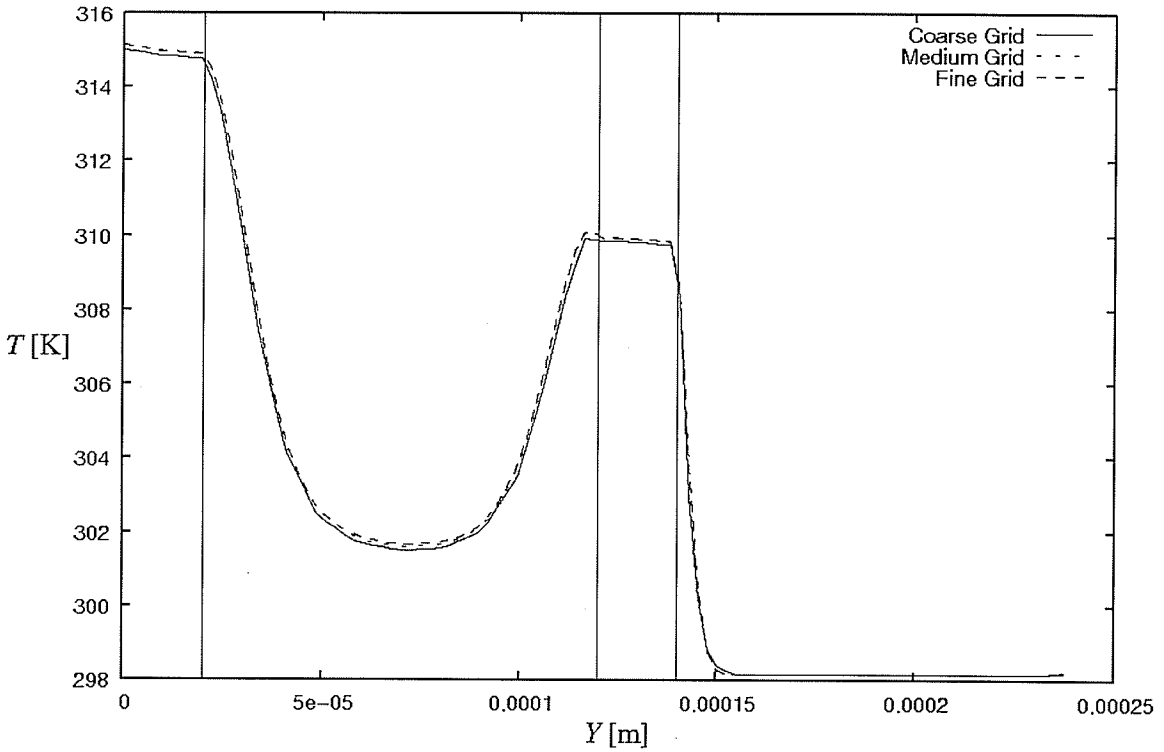

Figure 4.24: Temperature Profiles Along Line c2 Using the Various Non-Uniform Grids for the Case 3 Problem

defined in Table 4.4. The only remaining test was to compare the results obtained with this grid to "known" results, namely those obtained by Vafai and Zhu (1999). Since they only considered the low Reynolds number, counter-flow case using the fully-developed inlet profile assumption, the current comparisons needed to be done on Case 2. This is, among the current cases, the closest match to the exact problem studied by Vafai and Zhu (1999) was used. The only difference was that they included viscous dissipation terms in their analysis, while in this work ANSYS CFX was not asked to include these terms. It should be kept in mind that there were numerous sources of error in these comparisons: the slightly different assumptions used, the exact values used for the properties, errors resulting from the digitization process. Indeed, the paper of Vafai and Zhu (1999) contains relatively small figures, which made it difficult to accurately digitize the curves in these figures. Thus, when making the comparison between the current results and those of Vafai and Zhu (1999), these sources of error need to be kept in mind.

Vafai and Zhu (1999) presented temperature profiles along lines A, B, C, D, a, b, c and d, in cross-sections 1, 3 and 5, as well as lines AX, BX, CX and DX. This gave, in theory, 28 curves along which their temperature could be compared to the present results.

However, some of the results presented by Vafai and Zhu (1999) could not be used with confidence in the comparisons to present results. Figure 4.25 shows the temperature profiles along line D1, for the data of Vafai and Zhu (1999) and the present data. Line D1 passes in the solid region, and in the inlet of the top channel. In the inlet, the temperature was set to 25 [°C], or 298.15 [K], as a boundary condition. Thus, the temperature should have been exactly equal to this value at every point along line D1 that corresponds to the channel region (that is, for $X > (B - B_c)$). This behavior was indeed observed from the present data. However, the data of Vafai and Zhu (1999) showed a different trend. The temperature was slightly greater than the specified inlet value near the center of the channel (that is, near $X = B$), and then, proceeding in the negative X-direction towards the channel/solid interface, the temperature increased. This behavior was contrary to both the boundary condition that was applied in the current work (and that Vafai and Zhu (1999) *claimed* to implement), and to the current results. However, this behavior would have made sense if the temperature profile had indeed been along line B, but, in a cross-section slightly inward, in the axial direction, from the top channel

inlet. This is indeed the suspicion of the present author. Thus, if this suspicion is correct, the results that Vafai and Zhu (1999) presented for the $Z = 0$ cross-section actually corresponded to some other cross-section, near $Z = 0$, but not right at $Z = 0$. Thus, their results would not have been incorrect, per se, but they would merely have corresponded to a different position than what was claimed. However, since there was no way for the present author to know where the temperature profiles, claimed to be for the cross-section at $Z = 0$, were actually taken, no comparison between Vafai and Zhu's (1999) data in the $Z = 0$ cross-section could be made with confidence. A similar observation was made when comparing the present results to those of Vafai and Zhu (1999) along line B5 (and when one ignores the non-physical spikes generated by ANSYS CFX in the $Z = L$ cross-section, as discussed earlier). Thus, again, it was suspected that the temperature results shown by Vafai and Zhu (1999), supposedly for the $Z = L$ cross-section, actually corresponded to some other cross-section, slightly axially inward from this cross-section. Therefore, no comparison could be made between the present work and that of Vafai and Zhu (1999) for temperatures in the $Z = L$ cross-section. Thus, of the temperature results presented by Vafai and Zhu (1999), only those presented for lines in the $Z = 0.5\ L$ cross-section, and for lines AX, BX, CX and DX could be compared with confidence to the data obtained in the present work. This gave 12 lines along which comparisons could be made between the present work, and the results of Vafai and Zhu (1999).

It should be noted that the discrepancies between the temperature data of Vafai and Zhu (1999) and the present results in the $Z = 0$ and $Z = L$ cross-sections were **not** due to the fact that Vafai and Zhu (1999) set up the "Z" axis in the opposite direction as was done in the present work. That is, the discrepancy in Figure 4.25 between the present results and the data of Vafai and Zhu (1999) was not a result of the present author having somehow incorrectly labeled the temperatures obtained by Vafai and Zhu (1999) along line B5 as having been obtained along line B1. (Besides which, if the temperature profile from the data of Vafai and Zhu (1999) presented in Figure 4.25 was indeed been intended to correspond to the profile along line B5, this would have been an even greater deviation from both physical expectations, and the current results.) Care was indeed applied, in digitizing the data from Vafai and Zhu (1999), to remember about the left-

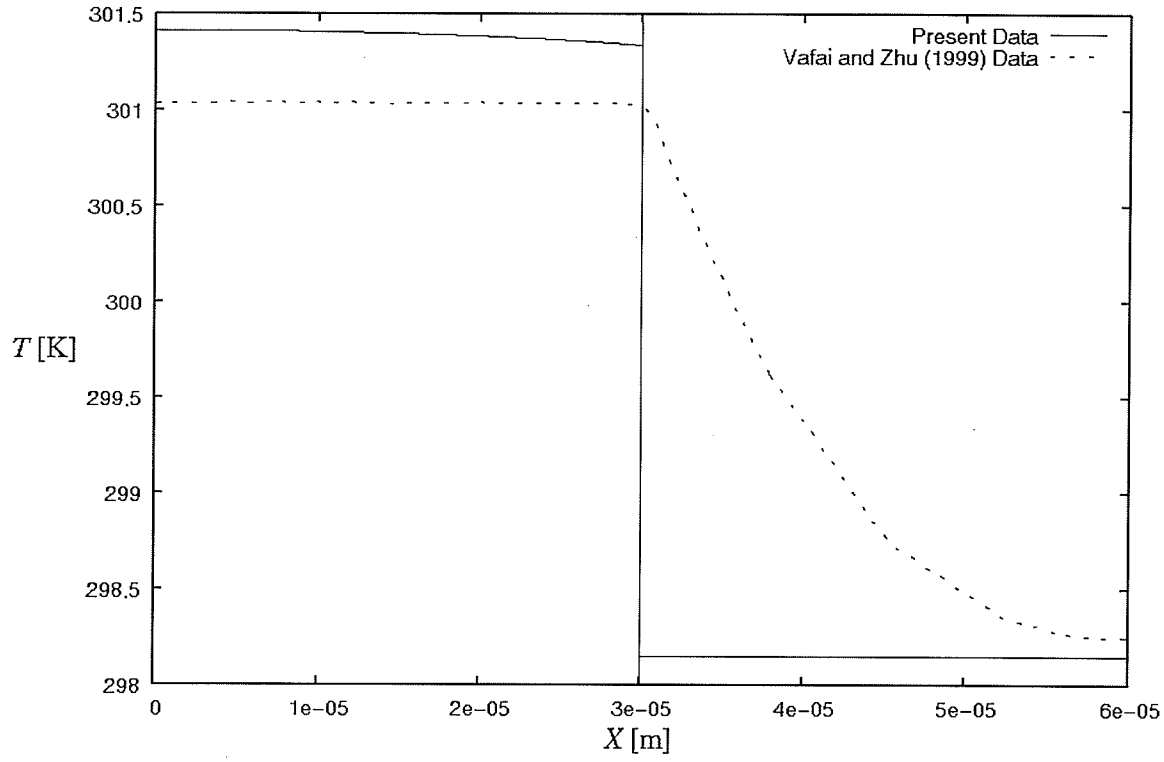

Figure 4.25: Temperature Profiles Along Line D1, Using Vafai and Zhu (1999) Data and Present Data for the Case 2 Problem

handed coordinate system used by Vafai and Zhu (1999), and to process their data accordingly.

So, as mentioned earlier, there were, once the lines in the $Z = 0$ and $Z = L$ cross-sections were excluded, only 12 lines along which the temperature profiles from the data of Vafai and Zhu (1999) and the current data could be compared. Temperature profiles were compared on all of these lines. These comparisons are not all presented here. Instead, a sampling of temperature profile comparisons is shown, so as to present an overview of the outcomes of these comparisons.

Figure 4.26 shows a comparison of Vafai and Zhu's (1999) results and the current results for the temperature along line CX. Clearly, the two curves do not overlap. There is a region, in the middle, where both curves are close to one another, and are separated by an approximately constant, and relatively small, difference. At both extremities, however, the curves deviate more significantly from one another. As shown in the two inserts in Figure 4.26, which zoom into the temperature profile obtained from the present

calculations near $Z = 0$ and $Z = L$, the gradient of temperature profile with respect to Z along line CX at both ends is zero (the inserts are included because these zero-gradients

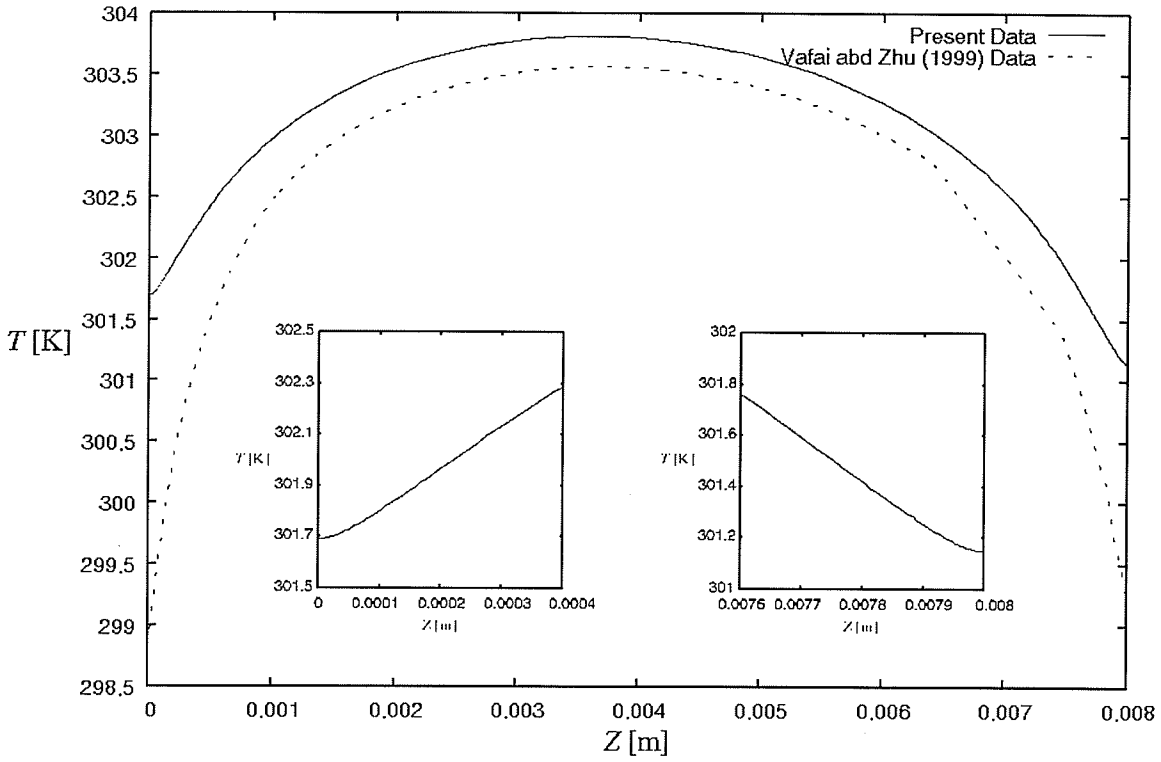

Figure 4.26: Temperature Profiles Along Line CX, Using Vafai and Zhu (1999) Data and Present Data for the Case 2 Problem

are indiscernible on the full-scale plot). This is due to the boundary condition that was used in this work. However, because the data from Vafai and Zhu was digitized from a paper graph, it was not possible to "zoom-in" beyond a certain magnification, and either confirm or deny the existence of zero-gradients at $Z = 0$ and $Z = L$. Attempting to do so simply resulted in blurry lines/points that yielded no more information than was known from the regular size of the graph. Furthermore, the paper of Vafai and Zhu (1999) was re-examined carefully at this point. This careful examination revealed that Vafai and Zhu (1999) did not explicitly state what boundary condition was used on the solid faces at $Z = 0$ and $Z = L$. One possibility that seems plausible, from Figure 4.26, is that they set the temperature to T_{in}. While this is not seen directly, it is possible that, if extrapolated ever-so slightly towards $Z = 0$ and $Z = L$, the steep gradients in their temperature profiles could be leading to T_{in} at these extremities. While plausible, there was no way to confirm

this. Thus, it is possible that Vafai and Zhu (1999) used a different boundary condition on the solid surfaces at $Z = 0$ and $Z = L$. This would mean, in fact, that, even for the current case that most closely resembled the problem examined by Vafai and Zhu (1999), the problem formulation was different. But, without a precise knowledge of how they set up their numerical computations, it was not possible to replicate their results for the sake of comparison. It was suspected that Vafai and Zhu (1999) did in fact formulate the problem differently from how it was formulated in this work, particularly in the boundary condition specification at the $Z = 0$ and $Z = L$ planes in the solid. This explains the great discrepancy at these extremities. The temperature profiles near the middle were more in agreement, because the effect of the boundary conditions was less significant in that region. Similar observations were made when comparing the temperature profiles along the other "axial" lines: AX, BX and DX.

In other comparisons, it appeared that, while maybe not "incorrect", the data of Vafai and Zhu (1999) was in some cases mislabeled. Figure 4.27 shows the temperature profiles along line C3, for both the present data and the data of Vafai and Zhu (1999). Clearly, the two curves are not in agreement. For X values below about $3\text{x}10^{-5}$ [m], corresponding to the value of $(B - B_c)$, the behaviors in the temperature data from the present results and the data of Vafai and Zhu (1999) were qualitatively the same. Furthermore, the differences in temperatures in this region could reasonably be explained by various factors such as the use of different values for the properties, setting up the problem formulation slightly differently, and so on. But, for X values above $3\text{x}10^{-5}$ [m], the present results showed the expected trend (temperature staying nearly constant), but the data from Vafai and Zhu (1999) showed a drastic reduction in temperatures, which would imply high temperature gradients in the solid. Because of the high thermal conductivity of the solid, such large temperature gradients would mean that there were unrealistically high heat fluxes occurring in the solid, well beyond any physically realistic value for the heat flux. However, this dip in temperature would be qualitatively consistent with the behavior expected on horizontal lines that cross through the channels (such as lines B or D). Thus, the portion of the curve for $X > 3\text{x}10^{-5}$ [m] is suspected to be the correct temperature profile, but for a different location. Thus, the results of Vafai and Zhu (1999) could still possibly have been correct, but simply mislabeled.

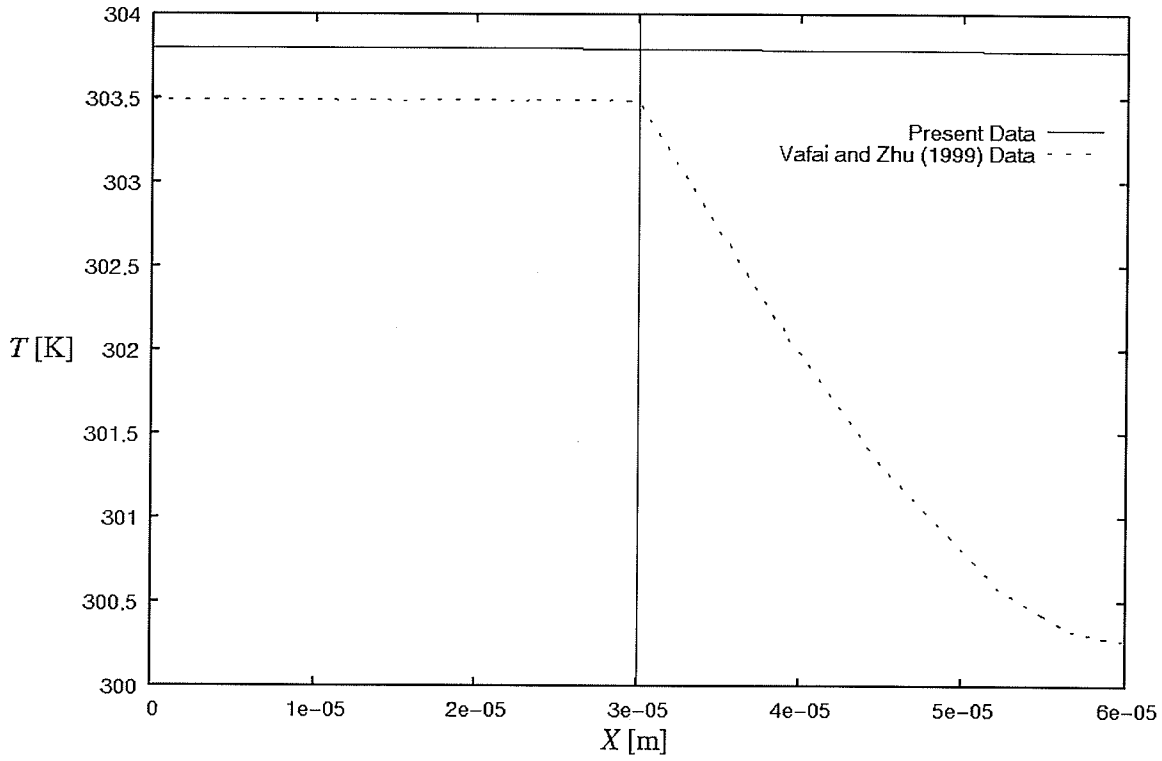

Figure 4.27: Temperature Profiles Along Line C3, Using Vafai and Zhu (1999) Data and Present Data for the Case 2 Problem

Another example of suspected mislabeling on the part of Vafai and Zhu (1999) is shown in Figure 4.28, where the temperature profiles for the current results and the data of Vafai and Zhu (1999) are compared along line D3. For $X < (B - B_c)$, no mislabeling was suspected, since both curves were qualitatively identical, and the magnitude of the discrepancy could be explained by other factors. For the $X > (B - B_c)$ region, both the present data and the data of Vafai and Zhu (1999) exhibited the correct qualitative behavior. However, the two temperature profiles crossed each other, and the discrepancy at $X = B$ was rather large. Since, in every other case where there was no mislabeling suspected, the data of Vafai and Zhu (1999) never gave a higher temperature prediction than the present data, it is suspected that their temperature prediction for $X > (B - B_c)$ was correct, but mislabeled, and instead corresponded to the temperature at some other location. Furthermore, if the portion of the temperature profile along line D3 which appeared to correspond to another location had been replaced with the portion of the temperature profile along line C3 (shown in Figure 4.27) which was mislabeled, it would

have yielded a good comparison between the present data and the data of Vafai and Zhu (1999).

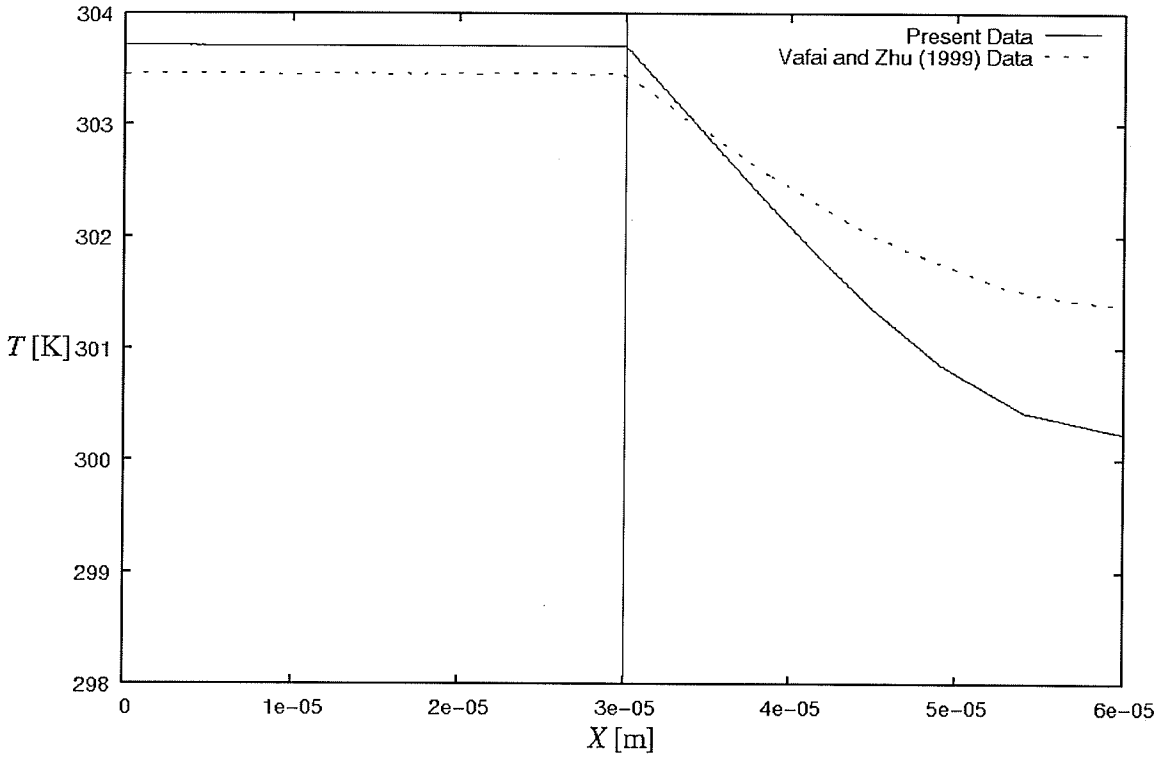

Figure 4.28: Temperature Profiles Along Line D3, Using Vafai and Zhu (1999) Data and Present Data for the Case 2 Problem

In some cases, the comparison of temperature data was successful. Figure 4.29 shows the temperature profiles along line B3, for the present data and that of Vafai and Zhu (1999). The two profiles were qualitatively similar, and reasonably quantitatively similar as well. The maximum discrepancy was 0.10 %. An example of a successful comparison is shown in Figure 4.30, where the temperature profiles are compared along line d3. Here again, the same qualitative trends were observed for the present data and the data of Vafai and Zhu (1999). The data on both curves were always within 0.10 % of each other. It should be noted that lines B3 and d3 contained points in the solid region, and in at least one channel region. Since higher temperature gradients can be expected in the fluid regions, it is important to compare the results in these regions, which has been done.

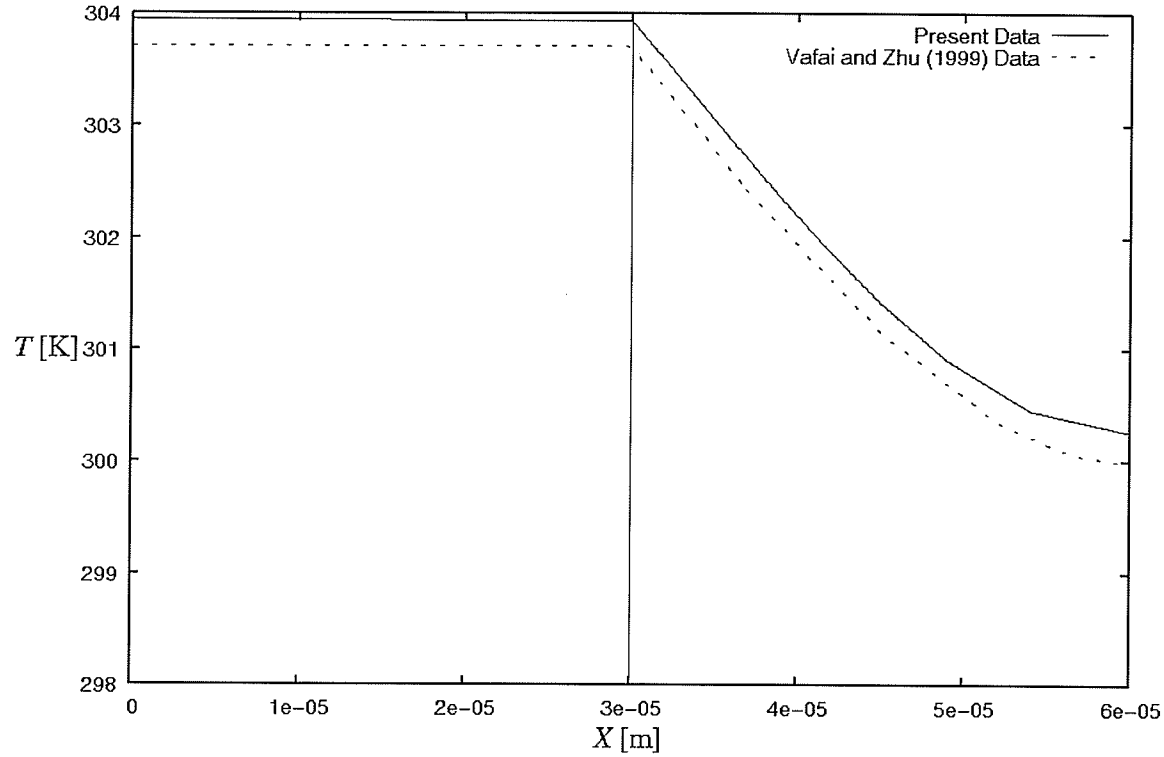

Figure 4.29: Temperature Profiles Along Line B3, Using Vafai and Zhu (1999) Data and Present Data for the Case 2 Problem

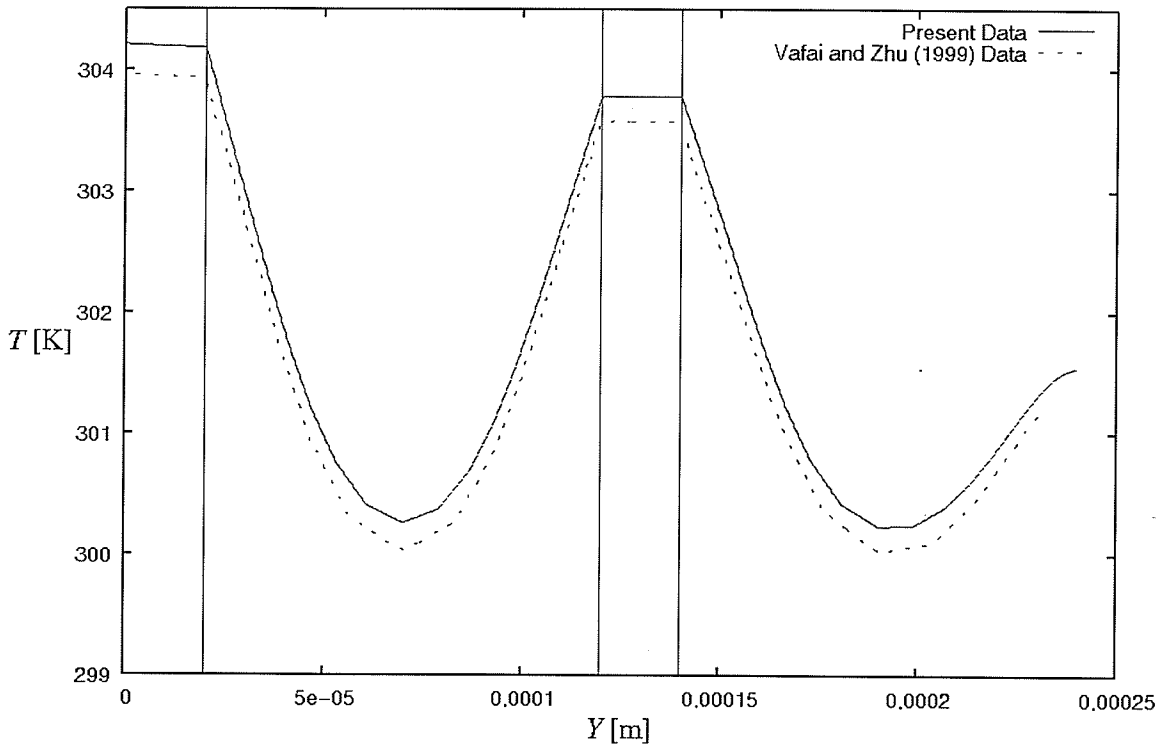

Figure 4.30: Temperature Profiles Along Line d3, Using Vafai and Zhu (1999) Data and Present Data for the Case 2 Problem

It should be noted that even in the cases where the comparison with Vafai and Zhu (1999) yielded good agreement, the data of Vafai and Zhu (1999) was always below the present data, and always by approximately the same amount. This is an interesting observation. It could be, and it is suspected, that there was some difference in the way Vafai and Zhu (1999) set up and/or solved the problem that accounts for this. For example, if they had set up their problem by choosing a value of T_{in} equal to 298 [K], which they would have done by wanting to use a value of 25 [°C] but used the rounded conversion factor of 273, but then, when re-converting their data back into [°C], they had used the un-rounded conversion factor of 273.15, they would have, in effect, used an inlet temperature of 24.85 [°C]. Because of the nature of the temperature equation, if the inlet temperatures are reduced by a certain value, it can be shown that the entire solution field is also reduced by this same constant value. Thus, if they had indeed performed the calculations by effectively using an inlet temperature of 24.85 [°C], one would only need to add 0.15 [K] to all of their temperatures, to compare them with the present data. This was indeed done, as a check (not documented here). As expected, the resulting agreements were better. There is no way to be certain whether the explanation provided above was indeed the reason behind the near-constant discrepancy between the temperature profiles in every case where the comparison was successful. However, with all due respect, it is certainly *plausible* that such an error (using a rounded conversion factor in a conversion, then attempting to re-convert with an un-rounded conversion factor) could have been made.

Thus, in summary, a detailed comparison with Vafai and Zhu's (1999) data has been performed. It was found that the present data and the data of Vafai and Zhu (1999) agreed reasonably well with one another, except in cases where obvious mislabeling of data had occurred in the work of Vafai and Zhu (1999). It was also discovered in this comparison that Vafai and Zhu (1999) may have employed a slightly different problem formulation than was used here, meaning that close agreement could not be expected.

So, since agreement was obtained between the present data and the data of Vafai and Zhu (1999), and plausible explanations could be provided to explain all the cases where agreement was not obtained, both the grid-refinement tests and the comparison

with known data were successful. Thus, since the counter-flow problem is the most "difficult", it can be stated with confidence that an adequate grid has been found.

4.6 Limitations Found With Software

Throughout the work that has been performed in this chapter, a number of limitations and drawbacks of the software used have been found. These are described next.

- ANSYS CFX uses two values at every node located on a boundary: one which is termed the hybrid value, and the other termed the conservative value. This represents a conceptual difficulty in interpreting the results. Furthermore, it creates difficulty in cases where ANSYS CFX asks the user to choose which value to use in a computation or plot. It also seems that the default choice is not always the correct one.
- The initial, non-1:1 grid, which was chosen based on the experience gained with the channel-only problems, did not work. It appears that, even though ANSYS CFX can theoretically handle multiple domains where the nodes do not match-up 1:1 at the interfaces, and even though ANSYS CFX did not complain when an attempt was made to use such a grid, the results thus-obtained were obviously incorrect.
- For reasons that are not known, there was a limit on the value of the contraction ratio that could be placed near an outlet. If the contraction ratio was too large, ANSYS CFX would simply not be able to start the run, displaying instead a message that complained about some fatal overflow. It is not known whether this is merely a bug in ANSYS CFX, or some inherent limitation in the methods used. In either case, though, it was necessary to make concessions on the value of the axial contraction ratio used.
- Furthermore, while it does not appear that the contraction near the outlet causes the results themselves to be incorrect, it does pose problems when ANSYS CFX is asked for temperature profiles near the outlet. When this is done, bizarre, definitely non-physical "spikes", that oscillate above and below the correct solution, are obtained. No way around this problem has been found. The result is

that temperature profiles along any lines in cross-section 5 (and sometimes even cross-section 4) cannot be shown.

- While not documented in this chapter, it was found that ANSYS CFX does not allow the plotting of heat flux along any user-defined locations (planes, line, and so on). What ANSYS CFX called the "Wall Heat Flux" could be used on user-defined locations, but, this is only expected to give correct results along walls. Thus, no simple way of obtaining heat fluxes at arbitrary locations was found.

The comments about the various shortcomings of ANSYS CFX are not an attempt to diminish the value of this program. Nor is it claimed, by any means, that the use of another CFD package would have resulted in a total absence of such issues. ANSYS CFX is a high quality program, which embodies countless hours of programming and debugging by skilled professional programmers, and its technical merits are hereby acknowledged. It is important to appreciate that, like any other program, it is not perfect, and it cannot be treated as a magical black box, which necessarily gives the correct answer in all cases. Care must be exercised when using, and interpreting the results of, any CFD program.

4.7 Closing Remarks

A suitable grid has been found for the problems under consideration in this thesis. For the counter-flow and parallel-flow geometries, the grid listed in Table 4.4 as the *medium* grid is the one that was used in this thesis. A cross-section of this grid, as output from ANSYS CFX-pre, is shown in Figure 4.31. There, one can see the complexity of the mesh, and see how it really looks. The solid region is shown in a different shade than the fluid regions for clarity.

For the single channel arrangements, the mesh had to be modified slightly. For the single channel (small) arrangement, the grid is simply the bottom half of the grid used for the two-row arrangements, as shown in Figure 4.32. For the single channel (large) arrangement, however, the grid is as follows. The X- and Z-direction spacings are the same as those of the grid for the two-row designs. In the Y-direction, the spacings below the channel are identical to those of the two-row design grids. Inside the channel region, the Y-spacings follow two geometric progressions, with the smallest spacings located

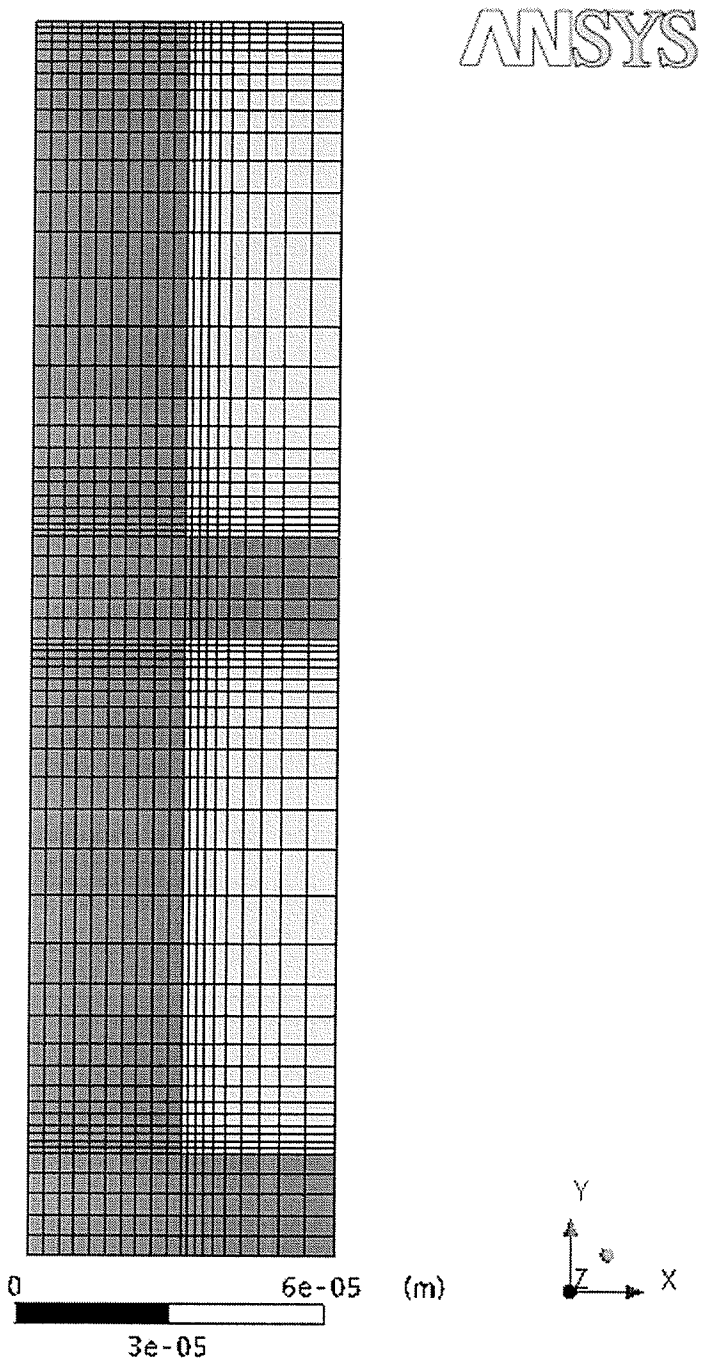

Figure 4.31: Cross-Sectional Grid for the Two-Row Arrangements

adjacent to the top and bottom of the channel. The contraction (or expansion) ratio is the same as for the two-row grid, namely 1.2. However, this channel has a number of *Y*-spacings that is equal to the sum of the number of *Y*-spacings in the bottom channel, the "fin" in between the top and bottom channel, and the top channel of the two-row grid, in

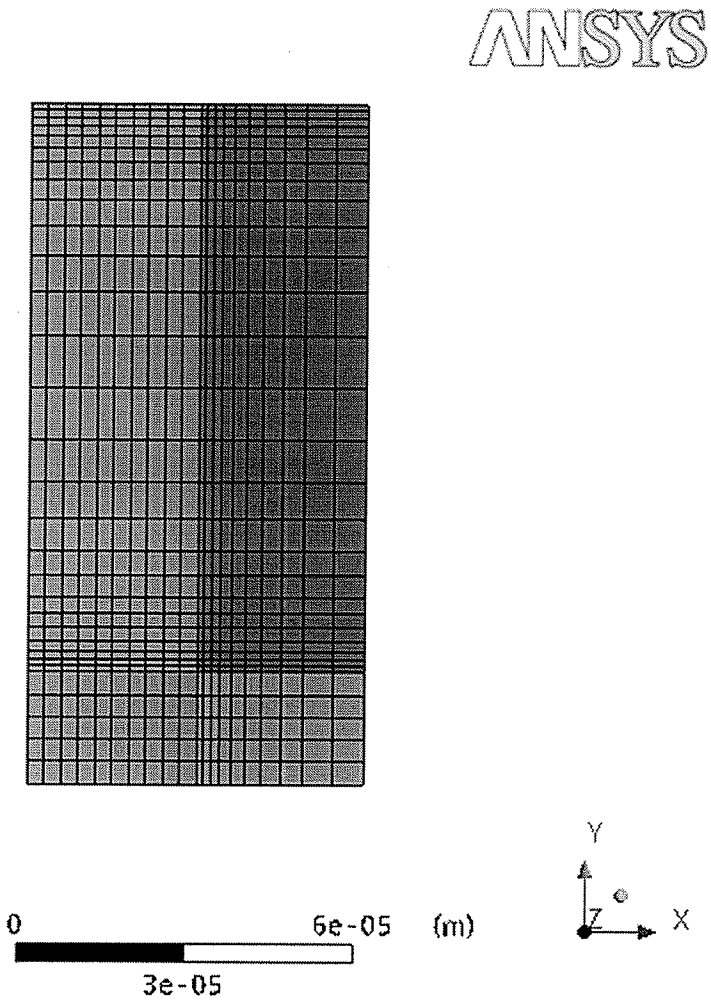

Figure 4.32: Cross-Sectional Grid for the Single Channel (Small) Arrangement

such a way that the total number of *Y*-spacings is the same as it is in the two-row grid. This grid is shown, in cross-section, in Figure 4.33. Mathematically, with the grid defined in this manner, it works out that the *Y*-spacings near the top and bottom of the channel for the single channel (large) arrangement are smaller than the spacings near the top and bottom of the channels for the two-row arrangements. Hence, the horizontal lines in Figure 4.33 near the top and bottom of the channel are so close together, that individual lines and spacings are indistinguishable in these regions.

It should be mentioned in passing that all the grids are identical in the axial direction.

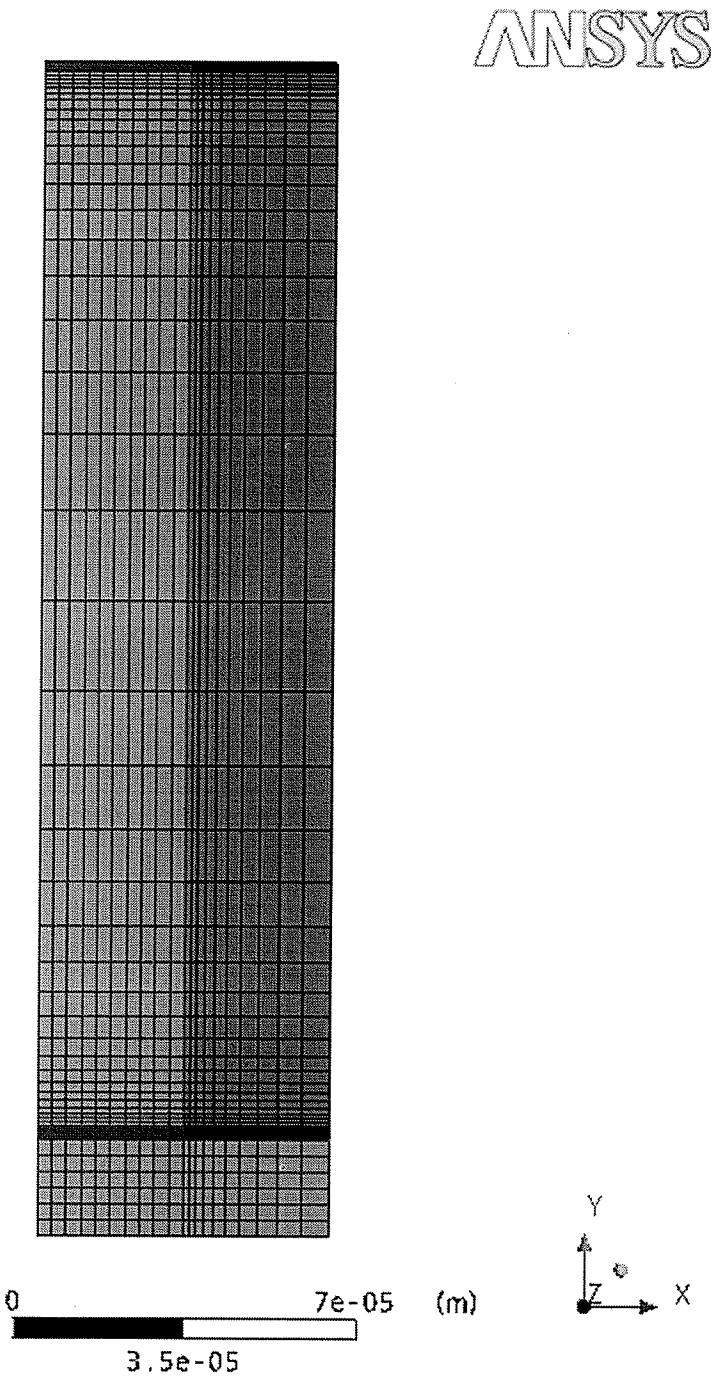

Figure 4.33: Cross-Sectional Grid for the Single Channel (Large) Arrangement

Various tests have been performed in this chapter. Having performed all of these tests, it is now possible to proceed to the specific geometries under consideration in this thesis, and to do so with confidence that the grids found are adequate, and that the simulations are being correctly implemented.

CHAPTER 5
RESULTS AND DISCUSSION

With a suitable grid having been found in the previous chapter, the cases in the test matrix presented in Table 3.1 can now be solved. This chapter will present a summary of these results, discuss their significance, and present a detailed description of the heat transfer phenomena taking place within the heat exchanger.

5.1 Assessment Parameters

In order to assess the relative merits of the various designs considered in this work, three distinct parameters are used as the basis for the evaluation. These parameters are the overall thermal resistance, the pumping power, and the maximum temperature difference on the heated surface. The overall thermal resistance, R_{th}, is defined as

$$R_{th} = \left(\frac{T_{\max} - T_{in}}{2BLq''} \right) \tag{5.1}$$

where T_{max} is the maximum temperature occurring in the entire microchannel heat sink arrangement. On physical grounds, it is known that this temperature occurs somewhere along the heated surface ($Y = 0$). The denominator corresponds to the heat supplied per channel (or, for the two-row designs, per *pair* of channels). Equation (5.1) can be non-dimensionalized to give

$$r_{th} = R_{th} B k_f = \frac{\theta_{\max}}{2l} \tag{5.2}$$

where r_{th} is the dimensionless thermal resistance and $\theta_{\max}$ is the maximum dimensionless temperature occurring in the heat sink, obtained by applying Eq. (3.126a), and omitting the subscript "s" for convenience. The dimensionless x-, y- and z-coordinates where $\theta_{\max}$ occurs are denoted x_{max}, y_{max} and z_{max}, respectively.

The thermal resistance is a measure of how well the heat sink dissipates heat. A low value, corresponding to a low maximum temperature, is desirable. This is because the maximum temperature in the heat sink is related to the maximum temperature in the component that is being cooled (typically a computer chip). Being able to dissipate the

heat generated by the component, while maintaining this component at the lowest possible temperature, is desirable. This is reflected in the thermal resistance.

The pumping power for a given channel, PP_c, is defined as

$$PP_c = \frac{\dot{m}_c \Delta P_c}{\rho_f} \tag{5.3}$$

where $\dot{m}_c$ is the mass flowrate flowing in this channel, and ΔP_c is the channel's pressure drop, given by

$$\Delta P_c = \overline{P}_{in} - \overline{P}_{out} \tag{5.4}$$

where $\overline{P}_{in}$ is the cross-sectional area-averaged pressure taken over the channel's inlet area, and $\overline{P}_{out}$ is the cross-sectional area-averaged pressure taken over the channel's outlet area. ANSYS CFX gives the value of ΔP_c directly. To obtain the total pumping power for a given case, the per-channel pumping power is multiplied by the number of channels. Rather than dealing with total pumping powers, the following approach will be used. When comparing the different designs, the pumping power per two "repeat units" will be considered, and will be denoted *PP*. Thus, for single-row designs, the pumping power *PP* will simply be the pumping power in one channel. For the two-row designs, the pumping power will be the sum of the pumping power in one full lower channel, plus that in one full upper channel. Thus, it can be written that

$$PP = \frac{\dot{m} \Delta P}{\rho_f} \tag{5.5}$$

where it is understood that $\dot{m}$ refers to the mass flowrate in one full channel for the single channel arrangements, and that $\dot{m}$ refers to the sum of the mass flowrate in one full top channel and the mass flowrate in one full bottom channel, and that, for the two-row cases, ΔP is the same in both channels. When Eq. (5.5) is non-dimensionalized, and the appropriate relations for $\dot{m}$ are used, the dimensionless pumping power, *pp*, can be shown to be

$$pp = \frac{PP}{\rho_f B^2 W_{in}^3} = 2 b_c h_c \Delta p \tag{5.6a}$$

for the two-row arrangements and the single channel (large) arrangement, and

$$pp = \frac{PP}{\rho_f B^2 W_{in}^3} = b_c h_c \Delta p \tag{5.6b}$$

for the single channel (small) arrangement.

The pumping power is a measure of how much energy is required to pump the fluid through the heat exchanger. This is an important design parameter because it is directly related to one of the costs associated with operating the heat sink. The lower the pumping power, the better. It should be noted that the pumping power, as presented above, only accounts for the channels themselves. It does not account for the power required to pump the fluid into the channels (from the inlet plenum to the inlet planes of the channels) and out of the channels (from the outlet planes of the channels to the outlet plenum). However, there is still meaning to the component of the overall pumping power that comes from pumping the fluid within just the channels. The only way that this component of the pumping power would not matter is if it were insignificant compared to the other components of the pumping power. Simple calculations were performed to estimate the pumping powers to pump the fluid into and out of the channels. It was found from these calculations that the pumping power to pump the flow into and out of the channels is always either of the order of the pumping power in the channels themselves, or, of lower order. Thus, in no case was the pumping power, as calculated above, merely an insignificant component of the overall pumping power.

The final parameter used in assessing the relative merits of the various designs is the difference between the maximum and minimum temperatures on the surface along which the heat flux is applied (that is, $Y = 0$). This parameter is denoted by ΔT_{heated}, and the equation that gives its definition is

$$\Delta T_{heated} = T_{\max,Y=0} - T_{\min,Y=0} \tag{5.7}$$

where $T_{\max,Y=0}$ is the maximum temperature on the heated surface, and $T_{\min,Y=0}$ is the minimum temperature along this same surface. In dimensionless form, this becomes

$$\Delta\theta_{heated} = \frac{\Delta T_{heated}}{\frac{q''B}{k_f}} = \theta_{max,y=0} - \theta_{min,y=0} \tag{5.8}$$

where $\theta_{max,y=0}$ is the maximum dimensionless temperature along the heated surface, and $\theta_{min,y=0}$ is the minimum dimensionless temperature along the heated surface.

This parameter is important because it is desirable, ideally, that the temperature along the surface of heat application be as uniform as possible. This is because the chip (or whichever other device is being cooled by the heat sink) is typically made of more than one material, each of which having a different coefficient of thermal expansion. Thus, some portions of the chip will expand more than others. If the temperature variation is too large, then the extent of this mis-match in expansion due to heat will be so great that severe stresses will be induced within the chip, possibly leading to cracking. Thus, it is desired to keep the chip's temperature as uniform as possible, to avoid these *thermal stresses* due to coefficient of thermal expansion mismatches. The difference between the maximum and minimum temperatures along the heated surface is one measure of how uniform the temperature along this surface (and hence the temperature of the chip) is. The lower the value of this parameter, the more uniform the temperature is, and hence the better the design. It should be noted that there are other possible parameters that could have been used to measure how "uniform" the temperature is. For example, the maximum temperature gradient in the X- and Z-directions along the $Y = 0$ surface could also have served as a measure of uniformity. Alternatively, it would have been possible to calculate the mean temperature on this surface, and calculated the root-mean-square deviation from this temperature for every node on the heated surface. However, it was deemed that these more elaborate measures of uniformity were not necessary in this work.

In cases where the thermal resistance and the pumping power give conflicting conclusions when comparing two designs, (one design is better in terms of pumping power, while the other is better in terms of thermal resistance), it is useful to have a way to determine which is the better design. One way to do this is to consider the heat that can be dissipated through the heat sink, per unit pumping power, for the same mass flowrate and for the same maximum difference in temperature across the heat exchanger. This new parameter, which is denoted β, can be expressed as

$$\beta = \frac{q''}{PP} \tag{5.9}$$

where q'' represents the maximum heat flux that will be dissipated through the heat sink for a fixed maximum temperature difference across the heat exchanger. While β is a good parameter, it is not directly possible to compute it, since, it would require that all cases had been performed for the same maximum temperature difference across the heat exchanger. This was not the case. Instead, for the two two-row arrangements and the single channel (large) arrangement, within each of the high and low Reynolds number cases, the heat flux was fixed, and the corresponding temperature difference was determined. However, multiplying the definition for β by $\frac{2BL}{T_{\max} - T_{in}}$ gives

$$\frac{2BL\beta}{T_{\max} - T_{in}} = \frac{2BL}{T_{\max} - T_{in}} \frac{q''}{PP} = \frac{1}{R_{th} PP} \tag{5.10}$$

Now, because of the way the non-dimensionalization was carried out, it can be shown that $\frac{q''}{T_{\max} - T_{in}}$ is a constant for fixed geometry and mass flow rate. Thus, even though q'' was fixed and $(T_{\max} - T_{in})$ varied, their *ratio* is the same as would have been obtained if the temperature difference was fixed and the heat flux was calculated. Thus, the product of the parameters R_{th} and PP, which is proportional to the inverse of β, as calculated from the present results, has the same value for a given geometry as would have been obtained if the test was indeed performed by keeping the temperature difference fixed. So, the parameter $R_{th}\,PP$ is an indication of the heat flux that can be dissipated per unit pumping power for fixed mass flow rate. The lower the value of $R_{th}\,PP$, the more heat that can be dissipated per unit pumping power. This can thus serve as a tie-breaker in cases where the best "compromise" between pumping power and thermal resistance is desired.

5.2 Summary of Parameters

This section presents and discusses the values of the parameters for the 14 cases considered in this work. Table 5.1 presents, in dimensional form, the thermal resistance, pumping power and ΔT_{heated} data. As a reminder, the applicable supplied heat fluxes and mass flowrates are presented as well. The mass flowrates in Table 5.1 are for two "repeat

units", or, in other words, for one full channel (for single row cases), or for one full pair of channels (for two-row cases). Also presented are the values of (R_{th} PP) for every case. The data in Table 5.1 are presented as a compact summary, and for the sake of presenting all parameters dimensionally, for the sake of completeness. Each of the three assessment parameters are presented in later tables, and their discussion accompanies those tables. The discussion of thermal resistance times pumping power is presented later, following discussion of individual parameters.

Table 5.1: Dimensional Summary of all Assessment Parameters

Case Number	R_{th} [K/W]	PP [W]	ΔT_{heated} [K]	R_{th} PP [K]	q'' [W/m^2]	$\dot{m}$ [kg/s]
1	21.2	$9.08\text{x}10^{-4}$	3.27	0.0192	$3.00\text{x}10^{5}$	$1.65\text{x}10^{-5}$
2	21.1	$8.66\text{x}10^{-4}$	3.00	0.0183	$3.00\text{x}10^{5}$	$1.65\text{x}10^{-5}$
3	7.16	0.111	12.8	0.797	$3.00\text{x}10^{6}$	$1.65\text{x}10^{-4}$
4	7.15	0.0867	10.7	0.620	$3.00\text{x}10^{6}$	$1.65\text{x}10^{-4}$
5	21.9	$9.08\text{x}10^{-4}$	5.05	0.0199	$3.00\text{x}10^{5}$	$1.65\text{x}10^{-5}$
6	22.0	$8.66\text{x}10^{-4}$	4.93	0.0190	$3.00\text{x}10^{5}$	$1.65\text{x}10^{-5}$
7	7.65	0.111	16.9	0.852	$3.00\text{x}10^{6}$	$1.65\text{x}10^{-4}$
8	7.68	0.0867	15.6	0.666	$3.00\text{x}10^{6}$	$1.65\text{x}10^{-4}$
9	22.3	$6.39\text{x}10^{-4}$	5.03	0.0143	$3.00\text{x}10^{5}$	$1.65\text{x}10^{-5}$
10	22.4	$5.94\text{x}10^{-4}$	4.90	0.0133	$3.00\text{x}10^{5}$	$1.65\text{x}10^{-5}$
11	8.27	0.0789	18.2	0.652	$3.00\text{x}10^{6}$	$1.65\text{x}10^{-4}$
12	8.30	0.0596	16.6	0.495	$3.00\text{x}10^{6}$	$1.65\text{x}10^{-4}$
13	42.7	$4.54\text{x}10^{-4}$	10.0	0.0194	$3.00\text{x}10^{5}$	$8.26\text{x}10^{-6}$
14	14.3	0.0556	33.6	0.795	$3.00\text{x}10^{6}$	$8.26\text{x}10^{-5}$

The cases that used the fully-developed inlet flow assumption were studied to examine the effect of making this assumption on the results. This section therefore focuses only on those cases that used the uniform inlet assumption. It is the goal of the following section to discuss how the fully-developed assumption impacts the solution as compared to the solutions of the cases using the uniform profile assumption (which is

deemed more "correct"; while the exact inlet velocity distribution cannot be known without knowing the header arrangement leading to the inlet of the channels, it is deemed on physical and intuitive grounds that the uniform inlet assumption is "closer" to the actual inlet velocity distribution than the fully-developed velocity profile).

In making the comparison, it is necessary to determine which of the single-row designs is the standard against which the two-row designs are to be compared. It was decided that the single channel (large) arrangement was the appropriate choice, since it occupies the same overall dimensions as the two-row designs, required roughly the same amount of heat sink material, and used the same amount of coolant flow as did the two two-row designs. The single channel (small) arrangement, on the other hand, was only considered so as to determine the effect of adding an identical layer on top of the original layer. Clearly, this should result in better heat transfer characteristics, but, to what extent?

The thermal resistance data are shown in Table 5.2. (This section only discusses the values of the parameters; the locations where maximum and minimum dimensionless temperatures occur are discussed in later sections.) The details of the various cases are listed in Table 3.1. In all cases, for a given Reynolds number, the two-row designs offer better (lower) thermal resistance properties than either of the single row designs, with the counter-flow arrangement proving slightly superior to the parallel-flow arrangement. For the low Reynolds number cases, the counter-flow arrangement (Case 1) offers a 5.0 % decrease in thermal resistance as compared to the single channel (large) arrangement (Case 9), and the parallel-flow arrangement (Case 5) has a thermal resistance that is 1.8 % lower than that of the single channel (large) arrangement. For the high Reynolds number cases, the same trend is observed, but, to a greater extent. The counter-flow arrangement (Case 3) has a thermal resistance that is 13 % lower than the single channel (large) arrangement (Case 11), and the parallel-flow arrangement (Case 7) has a thermal resistance that is 7.3 % lower than that of the single channel (large) arrangement. Thus, the advantages, from a thermal resistance perspective, of making the change from a single-row design to a two-row design are greater at higher Reynolds number.

Table 5.2: Summary of Dimensionless Thermal Resistance Data

Case Number	Location of θ_{max}			θ_{max}	r_{th}
	x_{max}	$\frac{y_{max}}{h}$	$\frac{z_{max}}{l}$		
1	1.00	0.00	0.432	0.206	7.72×10^{-04}
2	1.00	0.00	0.432	0.205	7.70×10^{-04}
3	1.00	0.00	0.373	0.0695	2.61×10^{-04}
4	1.00	0.00	0.373	0.0694	2.60×10^{-04}
5	1.00	0.00	1.00	0.213	7.98×10^{-04}
6	1.00	0.00	1.00	0.213	8.00×10^{-04}
7	1.00	0.00	1.00	0.0743	2.79×10^{-04}
8	1.00	0.00	1.00	0.0746	2.80×10^{-04}
9	1.00	0.00	1.00	0.217	8.13×10^{-04}
10	1.00	0.00	1.00	0.217	8.15×10^{-04}
11	1.00	0.00	1.00	0.0803	3.01×10^{-04}
12	1.00	0.00	1.00	0.0806	3.02×10^{-04}
13	1.00	0.00	1.00	0.415	1.56×10^{-03}
14	1.00	0.00	1.00	0.139	5.20×10^{-04}

For the low Reynolds number, making the switch from the single channel (small) arrangement (Case 13) to the parallel-flow arrangement results in a 48.8 % decrease in thermal resistance. Furthermore, for the high Reynolds number, making the switch from the single channel (small) arrangement (Case 14) to the parallel-flow arrangement results in a 46.3 % decrease in thermal resistance. Thus, adding another identical row on top of the initial one will reduce the thermal resistance, by about 50 %.

If the same comparison is repeated, but this time considering the effect of adding a second layer on top of the first one, with the flow in the opposite direction (that is, comparing the switch from the single channel (small) arrangement to the counter-flow arrangement), the following is observed. For the high Reynolds number, the reduction in thermal resistance is 49.8 %, and, for the low Reynolds number, the reduction is 50.5 %.

It is interesting that this last value is greater than 50 %. It is not known whether this is simply some anomaly, resulting from the sources of error in the computations, and hence there is a theoretical limit of 50 % on the reduction in thermal resistance, or whether this actually represents that it is conceptually possible to reduce the thermal resistance by more than 50 % by adding a second identical layer on top of an existing layer, and having the flow go in the opposite direction. At any rate, it has been demonstrated, *at a minimum*, that, when adding a second identical layer on top of an existing layer, and having the flow go in the opposite direction, it is possible to approach a 50 % reduction in thermal resistance.

The pumping power data are shown in Table 5.3. The parallel-flow and counter-flow arrangements require the same pumping power (in dimensionless and dimensional form). This is true for both the high and low Reynolds number scenarios. This result is supported by theory, since, the pumping power does not depend on the direction of the flow. The single channel (small) arrangement, for the respective high or low Reynolds number being considered, has a pressure drop equal to those of the individual channels in the two-row designs (as they should, since the hydrodynamics of one channel is in no way influenced by the presence of another channel), and a pumping power of half of the two-row designs (because this design has half as many channels in total). Comparing the single channel (large) arrangement to the two-row designs, it is found that the single channel (large) arrangement has a pumping power that is roughly 30 % lower than the two-row designs. This is true for both the high and low Reynolds numbers, and can be explained by the reduction in the surface area per unit mass flowrate in the single channel (large) arrangement as compared to the two-row arrangements.

Thus, in short, the effect of adding a second identical layer on top of an original layer is to simply double the pumping power. The effect of merging two rows of channels into one bigger row is to reduce the pumping power.

It should be noted that Table 5.3 may appear to contain an unintuitive result, namely that, all other parameters being equal, it appears that the pumping powers are greater for the low Reynolds number cases as they are for the corresponding high Reynolds number cases. However, in dimensional form, as shown in Table 5.1, it is indeed the case that the high Reynolds number cases have higher pumping powers than

Table 5.3: Summary of Dimensionless Pumping Power Data

Case Number	Δp	pp
1	57.8	96.3
2	55.1	91.8
3	7.08	11.8
4	5.52	9.19
5	57.8	96.3
6	55.1	91.8
7	7.08	11.8
8	5.52	9.19
9	40.6	67.7
10	37.8	63.0
11	5.02	8.37
12	3.79	6.32
13	57.7	48.1
14	7.08	5.90

low Reynolds number cases. However, in the non-dimensionalization process, this characteristic is lost, owing to the fact that the pressures are normalized by a different velocity for the high and low Reynolds number cases, in such a way that, dimensionlessly, the pumping powers are lower for the high Reynolds number cases.

The temperature variation along the heated surface data is presented in Table 5.4. For the low Reynolds number, the value of $\Delta\theta_{heated}$ is nearly identical for the single channel (large) arrangement and the parallel-flow arrangement. The value for the counter-flow is lower, by approximately 35 %. For the high Reynolds number, the parallel-flow arrangement offers a 7 % reduction in $\Delta\theta_{heated}$ compared to the single channel (large) arrangement, and the counter-flow arrangement offers a 30 % reduction in $\Delta\theta_{heated}$ compared to the single channel (large) arrangement. Thus, the superiority of

the counter-flow arrangement over the parallel-flow arrangement, as far as keeping the temperature on the heated surface as uniform as possible is concerned, is undeniable.

Table 5.4: Summary of Dimensionless Temperature Variation Along Heated Surface Data

Case Number	Location of $\theta_{max,y=0}$		Location of $\theta_{min,y=0}$		$\Delta\theta_{heated}$
	$x_{max,y=0}$	$\frac{z_{max,y=0}}{l}$	$x_{min,y=0}$	$\frac{z_{min,y=0}}{l}$	
1	1.00	0.432	1.00	133	0.110
2	1.00	0.432	1.00	133	0.101
3	1.00	0.373	0.350	133	0.0431
4	1.00	0.373	0.00	133	0.0360
5	1.00	1.00	0.00	0.00	0.170
6	1.00	1.00	0.00	0.00	0.166
7	1.00	1.00	0.00	0.00	0.0570
8	1.00	1.00	0.00	0.00	0.0525
9	1.00	1.00	0.00	0.00	0.169
10	1.00	1.00	0.00	0.00	0.165
11	1.00	1.00	0.00	0.00	0.0615
12	1.00	1.00	0.00	0.00	0.0560
13	1.00	1.00	0.643	0.00	0.337
14	1.00	1.00	0.200	0.00	0.113

Comparing the single channel (small) arrangements to the counter-flow arrangements reveals that, adding an identical second row of channels on top of an initial row, with the flow in the top row being in the opposite direction, decreases $\Delta\theta_{heated}$ by 67 % for the low Reynolds number, and 62 % for the high Reynolds number.

Considering now the data for the product of R_{th} and PP presented in Table 5.1, it can be seen that the counter-flow arrangement has a lower R_{th} PP value than the parallel-flow arrangement (by 3.6 % for the low Reynolds number cases and 6.9 % for the high Reynolds number case). However, the single channel (large) arrangement is better than

either of the two-row arrangement in terms of $R_{th}\,PP$. For the low Reynolds number, the product $R_{th}\,PP$ for the single channel (large) arrangement is 25 % lower than for the counter-flow arrangement, while for the high Reynolds number, the product $R_{th}\,PP$ for the single channel (large) arrangement is 18 % lower than for the counter-flow arrangement. Thus, it can be said that, for fixed mass flowrate and overall temperature difference, the single channel (large) geometry dissipates more heat per unit pumping power than the counter-flow arrangement, which in turn dissipates more heat per unit pumping power than the parallel-flow arrangement. The single channel (small) arrangement cannot be included in this comparison because it was run, in this work, with half of the mass flow than the other arrangements.

5.3 Effect of Fully-Developed Inlet Profile Assumption

This section examines the effect of making the fully-developed flow assumption in the inlet on the predictions of the three assessment parameters. A discussion of the effect of this assumption on other values, such as the locations of maximum and minimum temperatures, is deferred until the relevant sections where the detailed physical analyses are presented.

Looking first at the thermal resistance data presented in Table 5.2, it is apparent even at first glance that the r_{th} predictions given by making the fully-developed inlet profile assumption are remarkably close to the values obtained using the uniform inlet flow assumption. The greatest discrepancy observed is for the parallel flow arrangement with high Reynolds number, where making the fully-developed inlet assumption results in an overprediction of r_{th} by 0.38 % (this value was arrived at by using the full precision available, not by using the rounded r_{th} values appearing in Table 5.2). For all of the parallel flow and single channel (large) arrangement cases, making the fully-developed flow assumption results in an overprediction of the thermal resistance, with the magnitude of this discrepancy (in relative percentage terms) being greater for the high Reynolds number cases than for the corresponding low Reynolds number cases. This makes sense, since, the length of the developing region is greater in the higher Reynolds number cases, and hence, the impact of neglecting this region, and replacing it by a fully-developed flow, is greater for higher Reynolds number cases. Furthermore, that the

difference in thermal resistance given by the fully-developed inlet flow assumption and the uniform inlet assumption is small can be explained as follows, for the parallel flow and single channel (large) arrangements. For these arrangements, the maximum temperature (which is the only non-input parameter on which the thermal resistance depends) occurs in the cross-section $z = l$, which is the outlet planes in these cases. Thus, this maximum temperature occurs in a plane where, even when using the uniform inlet velocity assumption, the flow has already reached fully-developed velocity conditions. It can also be reasoned that, if the length of the channel(s) is long enough, in theory, fully-developed *thermal* conditions should also be achieved by this cross-section. Fully-developed thermal conditions would imply that the temperature field for every xy point, in the solid and in the channel(s), varies with z by a constant slope. Thus, in any cross-section that is in this thermally fully-developed region, the difference between the maximum temperature, and the bulk temperature of the channel (or of either channel for the parallel flow case) is a constant. Furthermore, the difference between the inlet and outlet bulk temperature(s) can be determined from overall energy balances on the fluid. Thus, if thermal fully-developed conditions occur, the complete temperature field in the region where these conditions occur (including everywhere in the $z = l$ cross-section) should be identical, regardless of which inlet velocity assumption was used, as long as the *bulk* temperature(s) in the inlet(s) are the same, which will be the case for a uniform inlet temperature, regardless of the inlet velocity distribution (for uniform inlet temperature, the bulk temperature will simply equal this uniform value). So, if, as suspected, fully-developed thermal conditions were indeed reached before the $z = l$ cross-section, for the parallel flow and single channel (large) arrangements, the maximum temperature in the domain, and hence the thermal resistance, should be identical, regardless of the inlet velocity distribution used. The slight difference in thermal resistance between cases of uniform inlet velocity and the corresponding fully-developed inlet velocity cases could be explained by the fact that, due to the zero-gradient of temperature with respect to z imposed by ANSYS CFX at $z = l$, *true* fully-developed thermal conditions were never actually obtained, but these conditions were, rather, only approached.

However, for the counter-flow arrangement, while the thermal resistances for the uniform inlet velocity cases were indeed close to those of the corresponding fully-

developed inlet velocity cases, no simple physical argument can be made to explain this. Fully-developed thermal conditions can definitely not be obtained for the counter-flow arrangement. Furthermore, in contrast to the parallel flow and the single channel (large) arrangements, making the fully-developed inlet flow assumption resulted, for the counter flow arrangement, in an underprediction of the thermal resistance, and the magnitude of the discrepancy (expressed as a percentage of the respective uniform-flow inlet assumption value) was greater for low Reynolds number. That the "error" is greater at low Reynolds number is contrary to what is expected on physical grounds.

In spite of these unresolved issues, it is quite clear that, as far as predicting the thermal resistance is concerned, there is no practical difference between using the uniform inlet assumption and using the fully-developed inlet assumption. That is, if one were interested *only* in predicting the thermal resistance, the analysis that uses the fully-developed inlet flow assumption (that is, the simplified analysis) is quite adequate.

For the dimensionless pumping power, it is seen in Table 5.3 that making the fully-developed inlet flow assumption always results in the pumping power being underpredicted. This can be explained by the fact that, for developing flow, there is some energy needed to change the shape of the temperature profile with axial position, which is not needed for fully-developed flow. For the two-row designs (both the counter-flow and parallel flow arrangements), making the fully-developed assumption results in an underprediction of the dimensionless pumping power by 4.7 % for the low Reynolds number, and 22 % for the high Reynolds number. For the single channel (large) arrangement, making the fully-developed assumption results in an underprediction of the dimensionless pumping power by 7.0 % for the low Reynolds number, and 24 % for the high Reynolds number. Thus, as would be expected on physical grounds, it is indeed found that the error introduced by making the fully-developed inlet flow assumption is greater for larger Reynolds number, since the length of the developing region being neglected is greater in those cases.

For the prediction of $\Delta\theta_{heated}$, it is found from Table 5.4 that the cases corresponding to the fully-developed inlet assumption always underpredict this value, compared to the corresponding uniform inlet velocity case. No simple physical argument is known that can be made to support this observation. It is also observed that the

magnitude of the discrepancies between the values of $\Delta\theta_{heated}$ predicted by the uniform and fully-developed inlet assumptions is always greater for the high Reynolds number cases than for the corresponding low Reynolds number cases. Furthermore, the discrepancies are greater for the counter-flow arrangement than for the other arrangements. For the counter-flow arrangement, the magnitude of the difference in $\Delta\theta_{heated}$ obtained by making the fully-developed inlet flow assumption is 8.2 % for low Reynolds number, and 17 % for high Reynolds number. The corresponding values for the parallel-flow arrangement are 2.4 % for low Reynolds number, and 7.8 % for high Reynolds number, and, for the single channel (large) arrangement, the corresponding values are 2.5 % for low Reynolds number, and 9.0 % for high Reynolds number.

5.4 Detailed Investigation: Single Channel (Large)

This section contains a detailed investigation of the fluid flow and heat transfer phenomena occurring within the microchannel heat sink for the single channel (large) arrangement. Because the fluid flow problem is decoupled from the heat transfer problem (that is, the fluid flow problem is independent of the heat transfer problem), the fluid flow problem is relatively well understood, and the fluid flow problem is qualitatively the same for every channel regardless of which arrangement is being considered, a detailed investigation of the fluid flow problem is only performed in this section, and will be omitted when discussing other arrangements.

Since the cases that use the fully-developed inlet flow assumption were studied only to see the impact of this assumption on the quality of solutions and have no importance in themselves, they will not be examined explicitly. Furthermore, this section will only examine the high Reynolds case, except when and to the extent that the low Reynolds number case is qualitatively different. Thus, this section contains, more or less, a detailed examination of Case 11 (case definitions are in Table 3.1).

The hydrodynamics are examined first. In analyzing the hydrodynamics, the velocities will be plotted along various lines to understand the flow. While the lines defined in Section 4.4 could be used, it is preferred instead to define another set of lines, that will only be used for this section (and, in this section, only for the hydrodynamics). This is done because the geometry is slightly different, and, it is desired to have more

horizontal and vertical lines within the channel itself, since the hydrodynamics occur in the channel only, not in the solid. The same basic approach as that used in section 4.4 will be used here: a series of vertical and horizontal lines are defined which, when combined with the specification of the cross-section, specify the exact line segment in three-dimensional space. The various vertical and horizontal lines (or, more precisely, line segments) are shown schematically in Figure 5.1. They can be described as follows:

- Line "v0": Vertical line segment passing along the left hand side of the channel region ($X = B - B_c$), from the bottom of this larger channel ($Y = H_f$) to the mid-height of this larger channel ($Y = H_c + \frac{3}{2}H_f$).
- Line "v1": Vertical line segment passing one sixth of the channel's *total* width from the channel's left boundary ($X = B - \frac{2}{3}B_c$), from the bottom of this larger channel ($Y = H_f$) to the mid-height of this larger channel ($Y = H_c + \frac{3}{2}H_f$).
- Line "v2": Vertical line segment passing one third of the channel's *total* width from the channel's left boundary ($X = B - \frac{1}{3}B_c$), from the bottom of this larger channel ($Y = H_f$) to the mid-height of this larger channel ($Y = H_c + \frac{3}{2}H_f$).
- Line "v3": Vertical line segment passing one half of the channel's *total* width from the channel's left boundary ($X = B$), from the bottom of this larger channel ($Y = H_f$) to the mid-height of this larger channel ($Y = H_c + \frac{3}{2}H_f$).
- Line "h0": Horizontal line segment passing along the bottom of the large channel ($Y = H_f$), from the left boundary of the channel ($X = B - B_c$), to the channel's vertical symmetry plane ($X = B$).
- Line "h1": Horizontal line segment passing one eighth of the channel's height from its bottom ($Y = \frac{9}{8}H_f + \frac{1}{4}H_c$),from the left boundary of the channel ($X = B - B_c$), to the channel's vertical symmetry plane ($X = B$).

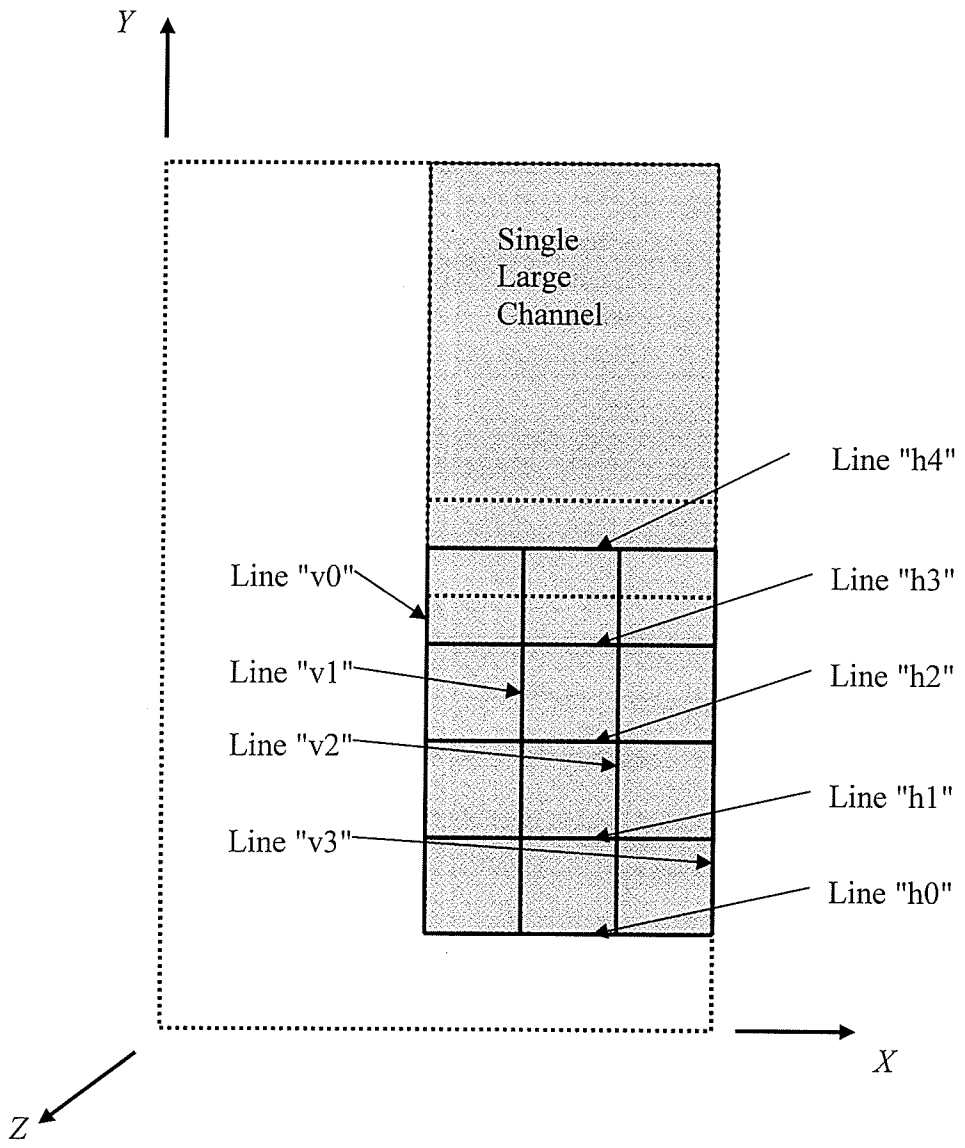

Figure 5.1: Schematic Representation of the Nomenclature Specifying the Various Lines Used to Analyze the Hydrodynamics of the Single Channel (Large) Arrangement

- Line "h2": Horizontal line segment passing one quarter of the channel's height from its bottom ($Y = \frac{5}{4}H_f + \frac{1}{2}H_c$),from the left boundary of the channel ($X = B - B_c$), to the channel's vertical symmetry plane ($X = B$).

- Line "h3": Horizontal line segment passing three eights of the channel's height from its bottom ($Y = \frac{11}{8} H_f + \frac{3}{4} H_c$),from the left boundary of the channel ($X = B - B_c$), to the channel's vertical symmetry plane ($X = B$).
- Line "h4": Horizontal line segment passing one half of the channel's height from its bottom ($Y = \frac{3}{2} H_f + H_c$), from the left boundary of the channel from the left boundary of the channel ($X = B - B_c$), to the channel's vertical symmetry plane ($X = B$).

The various cross-sections considered are as follows:

- "CS0": Cross-section located at $Z = 0$
- "CS1": Cross-section located at $Z = 0.05L$
- "CS2": Cross-section located at $Z = 0.10L$
- "CS3": Cross-section located at $Z = 0.15L$
- "CS4": Cross-section located at $Z = 0.20L$
- "CS5": Cross-section located at $Z = 0.25L$
- "CS6": Cross-section located at $Z = 0.50L$
- "CS7": Cross-section located at $Z = 0.75L$
- "CS8": Cross-section located at $Z = 0.95L$

There is nothing to gain by defining a cross-section located exactly at $Z = L$, because of the problem with non-physical spikes in this cross-section discussed in Section 4.5, and because the flow is fully-developed near the outlet in any case.

The complete definition of a line segment is denoted by first specifying the line, and giving the cross-section, and adjoining the two with a hyphen. For example, the line denoted by h2-CS6 would represent the line h2, in cross-section CS6. Once again, this nomenclature is used only in this section, and only for the purposes of analyzing the hydrodynamics. It should be noted in passing that the various lines defined above are presented in dimensional terms; they can also be expressed in dimensionless terms by applying the relevant definitions.

A subtle but important point should be made at this point. The single channel (large) arrangement is, in a sense, "derived" from the parallel-flow arrangement. Indeed, the geometry of the single channel (large) arrangement is obtained by removing the solid space above the lower channel and below the upper channel from the parallel-flow geometry. The inlet velocity of the single channel (large) arrangement is "derived" from the parallel-flow arrangement as follows: set the velocity of the single channel (large) arrangement to the value necessary so that, in the larger channel of this arrangement, the mass flow rate is equal to the sum of the mass flow rates flowing in the two channels of the parallel-flow arrangement. In mathematical terms, $W_{in\ large}$ can be determined from W_{in} according to Eqs. (3.120) and (3.118). Thus, even though W_{in} does not appear, at first glance, to have a meaning in the single channel (large) arrangement, it does have meaning, in the sense that it represents the inlet velocity of the *corresponding* parallel-flow arrangement case used to generate the single channel (large) case. So, because of this, it was decided to perform the non-dimensionalization of the velocities by dividing each of the velocity components by W_{in} (even for the single channel (large) arrangement). Thus, in the inlet cross-section, the dimensionless velocity w is indeed uniform, but does not have a value of unity (the value is slightly below unity). This is because of how the dimensionless velocities are defined, and not the result of some error. If the dimensionless velocities for this case were defined by dividing the dimensional values by $W_{in\ large}$, then the z-direction dimensionless velocity, w, would indeed have a value of unity in the inlet. This is not done, however, so that there may be a consistent definition of dimensionless velocity across all arrangements.

Figure 5.2 shows the dimensionless axial velocity, w, along the various horizontal lines in cross-section CS1 (the corresponding plot in cross-section CS0 is not shown, as it only reveals that the velocities along all lines are the uniform inlet value). It can be seen that at the left of the channel ($x = 0.5$), the velocity on every curve is zero. This is because of the no-slip velocity condition at the walls. Because line h0 passes along the bottom of the channel, the velocity along this line is zero, again because of the no-slip velocity condition at the walls. Along the other horizontal lines, the following trend is observed. Starting from a zero-velocity at the left wall at $x = 0.5$, the velocity increases monotonically with downward concavity, until such a point (in this case, approximately

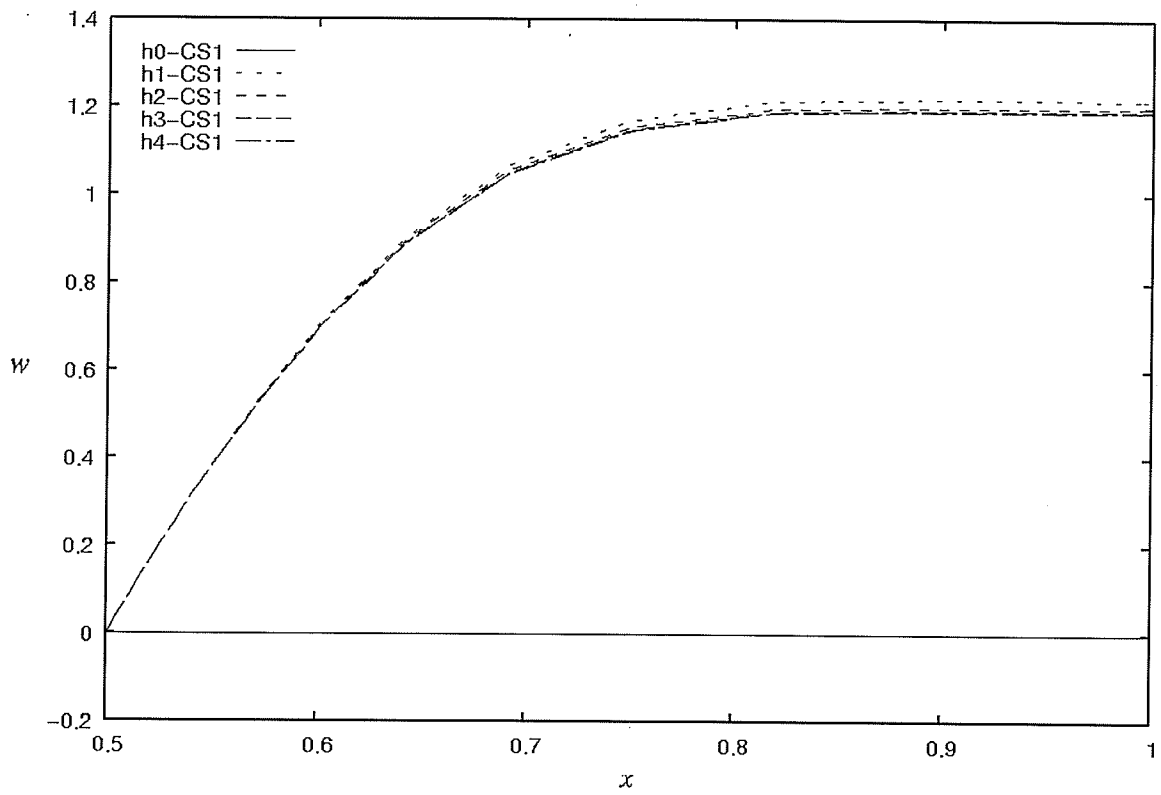

Figure 5.2: Dimensionless Axial Velocity for Various Horizontal Lines in the $z = 0.05\ l$ Cross-Section (CS1) for the Case 11 Problem

$x = 0.8$) where the velocity levels off to a nearly uniform value. This can be explained as follows. The velocity at the left wall is "pinned" at zero because of the no-slip condition. In the region where x is greater than approximately 0.8, the velocity is nearly uniform because, in this region, viscous effects are negligible. That the viscous effects are negligible is explained as follows. The flow enters with a uniform velocity into the inlet of the channel from a source where viscous effects are essentially negligible, since there is no surface near enough to the flow to offer any impedance to flow. But, with increasing axial distance, the flow at the walls becomes zero, and a thin region surrounding the walls develops, in which the viscous effects are significant. This is sometimes termed the boundary layer. But, outside of this thin region, viscous effects are negligible. This region is sometimes termed the *inviscid core*. As one progresses axially away from the inlet, the thickness of the boundary layer increases, and the inviscid core decreases, until such a point where the inviscid core has disappeared, and the viscous effects are felt throughout the entire cross-section. So, in this case, viscous effects are negligible for x values greater than 0.8 because, for the cross-section under consideration

(CS1), values of x above this value are still in the inviscid core. So, the velocity is pinned at zero at the left wall, and there is a viscous-free region of uniform velocity in the center (it should be recalled that the velocity plot shown is only for the left half of the channel; the velocity is symmetric about the line $x = 1.0$). In the boundary layer region, the velocity distribution is shaped subject to the condition that it must join the zero-velocity at the left wall, and must join the uniform velocity near the channel's middle, in a continuous and smooth fashion (that is, with no discontinuities in either the values of the velocity w, nor in its first derivative with respect to x, respectively).

While the velocity profiles along all the horizontal profiles aside from h0 are close to one another, the velocity along line h1 is greater than those along h2, h3 and h4, even though h1 is closer to the bottom wall than the other horizontal lines. This is not an error, even though it may be counter-intuitive. This can be explained by what are termed *velocity overshoots*, discussed below.

It should be noted that it is incorrect to say that the velocity in the inviscid core is *unaffected* by the walls, or that it has not felt the presence of the walls. The velocity everywhere in the channel is affected by the walls. If the velocity were to be truly unaffected by the walls, the uniform value of the velocity within the inviscid core would be equal to the inlet value. But, this is not the case. The magnitude of the near-uniform velocity is in fact greater than the inlet value. This is because, with the velocity at the wall being zero, and the velocity dropping sharply as the wall is approached, it is necessary for the velocity in the inviscid core to have "shot up" in order to maintain the same mass flowrate in the entire cross-section. Thus, even in the inviscid core, the velocity is influenced by the wall. It is only the viscous effects that are not felt in the inviscid core.

Figures that are analogous to Figure 5.2, but for the remaining cross-sections, were generated. For the sake of brevity, they are not all presented here. Instead, here is a summary of the observations made from such figures. As one proceeds axially in the direction of flow, the length of the inviscid core region decreases, and the magnitude of the velocity in this inviscid core region increases. This is seen in the w profiles along h1, h2, h3 and h4. Along h0, the dimensionless axial velocity, w, remains at zero in every cross-section. Furthermore, with increasing z, the w-profiles along the various horizontal

lines become more and more separated from each other. This is more noticeable for the horizontal lines closest to the bottom, and less noticeable for the profiles closer to the center of the channel. Figure 5.3 shows the velocity along the horizontal lines in cross-section CS8, which is in the fully-developed region. It can be seen that the inviscid core region has disappeared, and that the profiles have separated from each other compared to the corresponding profiles in Figure 5.2. Furthermore, in Figure 5.3, in the fully-developed region, the dimensionless velocity w is always greater, for a given x, the further away from the bottom of the channel. (The exception is at the left wall, at $x = 0.5$, where $w = 0$ on every horizontal line.) Of course, if other horizontal lines had been defined above the channel mid-height, then the reverse trend would be observed in the top half of the channel.

The trends mentioned above can be seen in Figure 5.4, which shows how the velocity w varies along line h1, for various cross-sections (for clarity, the cross-sections

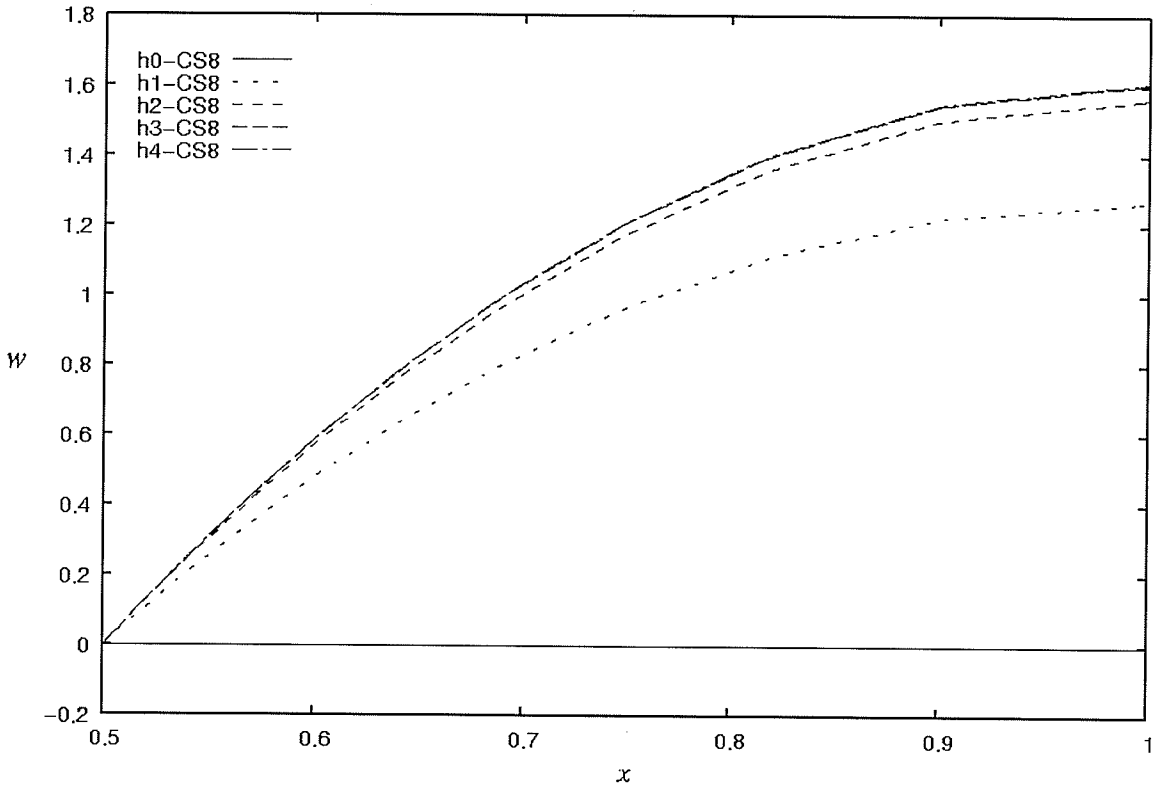

Figure 5.3: Dimensionless Axial Velocity for Various Horizontal Lines in the $z = 0.95\ l$ Cross-Section (CS8) for the Case 11 Problem

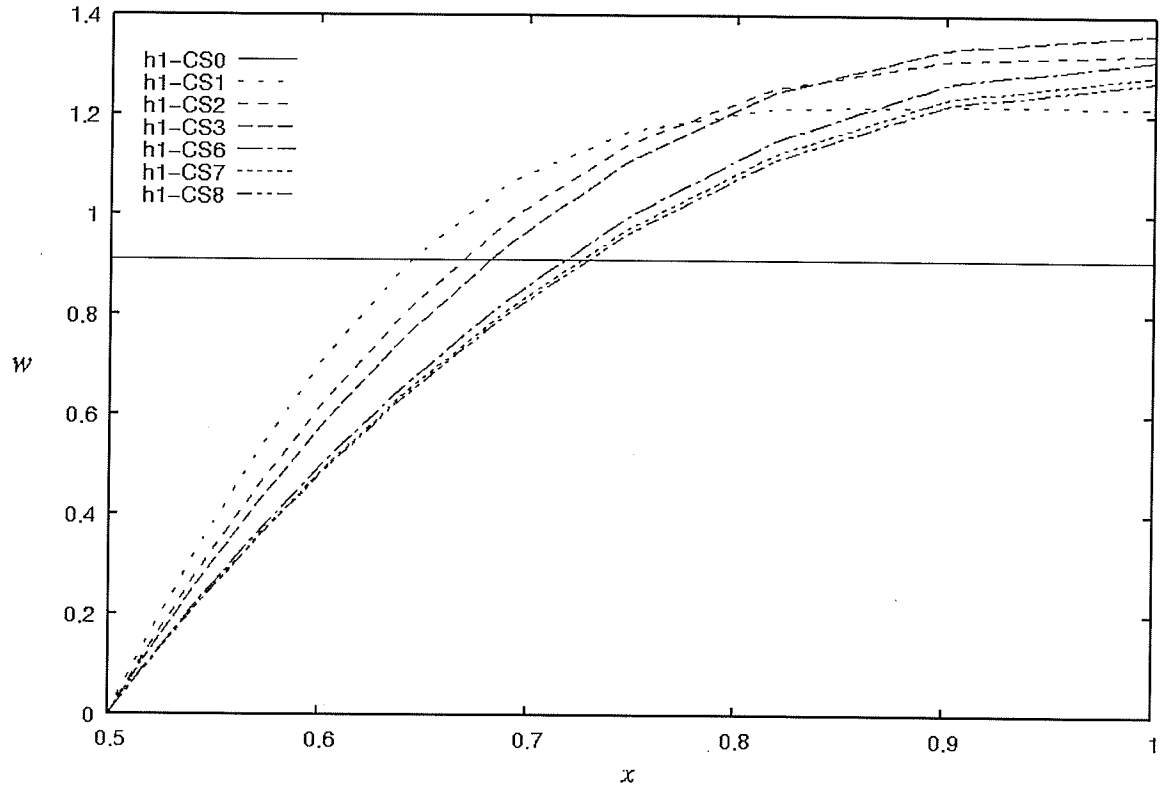

Figure 5.4: Dimensionless Axial Velocity Along Lines h1 for Various Cross-Sections for the Case 11 Problem

CS4 and CS5 are omitted, as their presence adds too much clutter to the graph, yet makes no qualitative difference). Furthermore, the achievement of fully-developed conditions with increasing z can be observed by noticing that the w-profiles change less and less the deeper one proceeds into the flow. The velocity profile along line h1 in cross-section CS7 is nearly overlapping that in cross-section CS8, despite the fact that these cross-sections are spaced 20 % of the channel's length apart.

Figure 5.5 presents the velocity w along various vertical lines in cross-section CS1. It should be noted that the region in which the axial velocity along line v1 is relatively constant does not correspond to the inviscid core. Rather, it is simply a region in which the velocity varies little with y, and more with x. This is not surprising, given that the channel is stretched in the y-direction more than in the x-direction. The notable feature, however, in Figure 5.5, is that there are velocities along lines v2 and v3 that are greater than the velocity in the inviscid core. Starting from a value of zero at the left wall and proceeding in the direction of increasing x, it is found that w increases to a local

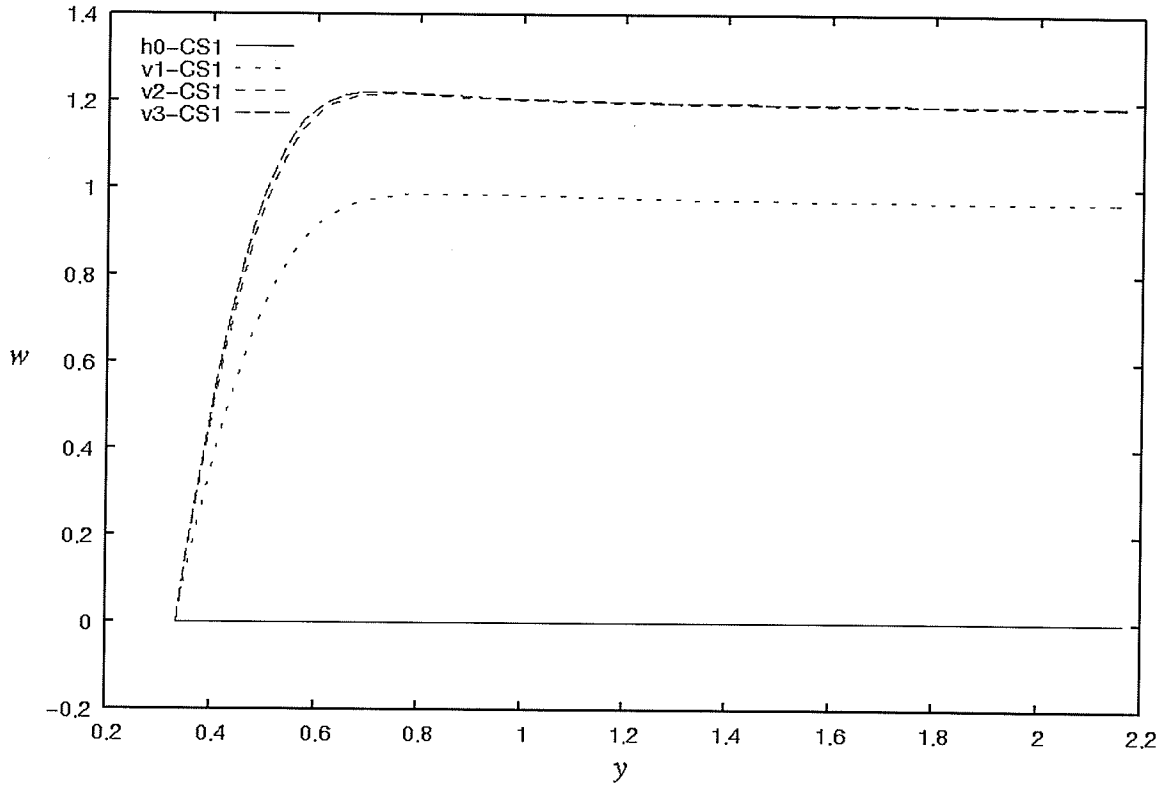

Figure 5.5: Dimensionless Axial Velocity for Various Vertical Lines in the $z = 0.05\ l$ Cross-Section (CS1) for the Case 11 Problem

maximum, which is greater than the value w in the inviscid core, then decreases towards the inviscid core. This phenomenon, sometimes termed *velocity overshoots*, has already been observed by other researchers. It is documented in Shah and London (1978). Explaining this phenomenon in detail is beyond the scope of this section, especially given that it is documented elsewhere. It was merely desired to point out that this phenomenon was observed.

Figure 5.6 shows the variation of the magnitude of the dimensionless pressure gradient, $\frac{dp}{dz}$ (which would strictly be written $\left|\frac{d\bar{p}}{dz}\right|$, but the overbar, which denotes cross-sectional averaging, and the absolute values signs, are omitted for convenience; furthermore, again for convenience, the "magnitude of the dimensionless pressure gradient" is referred to henceforth simply as the "pressure gradient"), along the axial

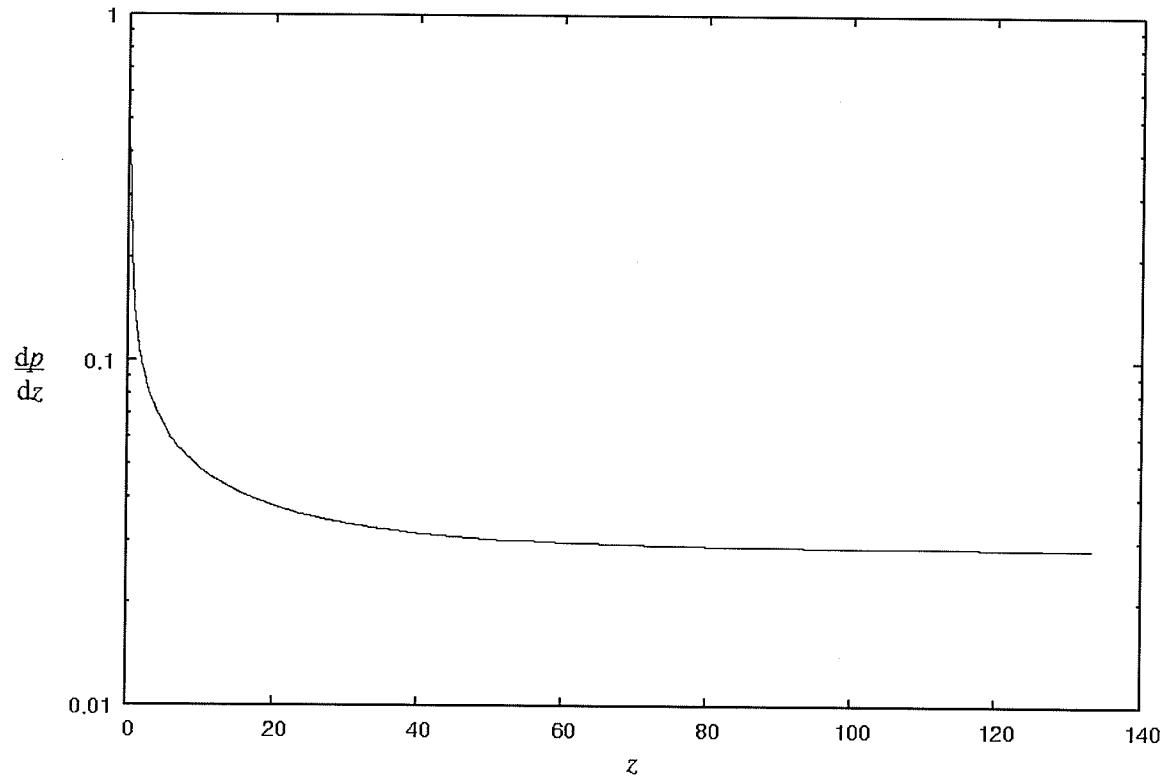

Figure 5.6: Axial Variation of Dimensionless Pressure Gradient for the Case 11 Problem

direction. Right at the inlet, the pressure gradient has an infinite value. This arises because of the discontinuity of the velocity profile at the inlet. Right at the inlet, the velocity is uniform, yet, even a small infinitesimal distance into the channel, the flow at the walls has been brought to zero, and the velocity everywhere in the cross-section has felt the presence of the wall (even, as discussed earlier, in the inviscid core). Thus, there is a theoretically-explained infinite pressure gradient at the inlet. Then, with increasing z, the pressure gradient decreases, and eventually levels off to a uniform value as the flow becomes fully-developed. The pressure gradient (and hence the pumping power required) is greater in the developing region because, in addition to overcoming friction, it is necessary, in the developing region, to change the shape of the velocity profile, which requires more energy to be supplied. As one proceeds axially towards the fully-developed region, the degree to which the velocity changes with axial variations becomes less pronounced, which is why the pressure gradient decreases.

Now, with a detailed examination of the fluid flow phenomena having been done, the heat transfer phenomena can be examined more closely.

It is useful to define the area fraction, AF, as

$$AF = \frac{A_{surface}}{A_{total}} \tag{5.11}$$

where $A_{surface}$ is the area of the surface of which the AF is being calculated, and A_{total} is the total area of all solid/fluid interfaces, in a given repeat-unit, along which heat passes from the solid to the fluid. For this arrangement, A_{total} is the sum of the areas of the channel's side and half of its bottom. It is also useful to define the heat fraction HF, as

$$HF = \frac{q_{surface}}{q_{total}} \tag{5.12}$$

where $q_{surface}$ is the heat exchanged between the solid and the fluid along the surface in question, and q_{total} is the total of all heat exchanged along all solid/fluid interfaces in a repeat-unit. By applying the principal of the conservation of energy on the solid heat sink material, this q_{total} must equal the amount of heat supplied at the bottom of the heat exchanger for one repeat-unit.

Table 5.5 shows the values of AF for this arrangement, and the values of HF, for the cases of uniform inlet velocity, for both the low and high Reynolds number cases. It should be noted that AF is a function of geometry only. For both the low and high Reynolds number, the value of HF is greater for the channel's side surface than for its bottom. This is not surprising, given that the bottom surface accounts for only 12 % of the area over which the heat sink transfers heat to the channel. Furthermore, the value of HF for the side surface for both the low and high Reynolds number cases is greater than the value of AF for this surface. This means that the side of the channel "pulls" a greater proportion of the supplied heat than its fraction of heat transfer area. This can be explained as follows. Within the solid, the thermal resistance between any two points is relatively small, owing to the large thermal conductivity of silicon. Thus, the determining factor that dictates where the heat will flow is the thermal resistance across the fluid. Because of the channel's elongated height compared to its width, there is less thermal resistance, on average, between points on the channel's side and the center of the channel (where, for a given cross-section, the temperature is the lowest), than there is between points on the channel's bottom and the center. Thus, since heat will

preferentially flow in the direction of least thermal resistance, the side will attract more heat than its area fraction.

Table 5.5: Area Fraction and Heat Fraction Data for the Single Channel (Large) Arrangement

Surface	*AF* (%)	*HF* (%)	
		Low Reynolds Number (Case 9)	High Reynolds Number (Case 11)
Side of channel	88	93.0	89.6
Bottom of channel	12	7.0	10.4

It is interesting that, for the high Reynolds number case, while it is indeed observed that heat preferentially exits through the side of the channel, the magnitude of this preference is less than it is in the low Reynolds number case. In fact, for the high Reynolds number case, the values of *HF* for the two solid/fluid interfaces are nearly equal to the corresponding *AF* values. This means that, with increasing Reynolds number, the heat being transfer from the solid to the fluid is transferred more uniformly across the solid/fluid interfaces.

It should be remembered, in the following discussions, that because the geometry is different in this arrangement than in the two-row arrangements, the interpretations of the various horizontal lines are also different. Most notably, the lines "C" in the various cross-sections pass through the channel, at its mid-height, and not in the solid only.

Figure 5.7 shows the dimensionless temperature along the lines C in the various cross-sections. For some unknown reason, the non-physical spikes in the $z = l$ cross-section described earlier were not observed along line C, even though they were observed for the other horizontal lines, and for the vertical lines. As expected, the value of θ_f (henceforth, the subscripts f and s on θ are omitted for convenience) is constant, at a value of 0, throughout the channel region in the $z = 0$ cross-section. In the $z = 0.05\ l$ cross-section, θ still has a value of zero near $x = 1$, but, proceeding away towards the channel/solid interface, the temperature increases. In cross-section 3, there is again a region where θ is for all practical purposes zero, but, it is much smaller. Thus, it is confirmed that, contrarily to the trend observed in the velocities, for the temperature,

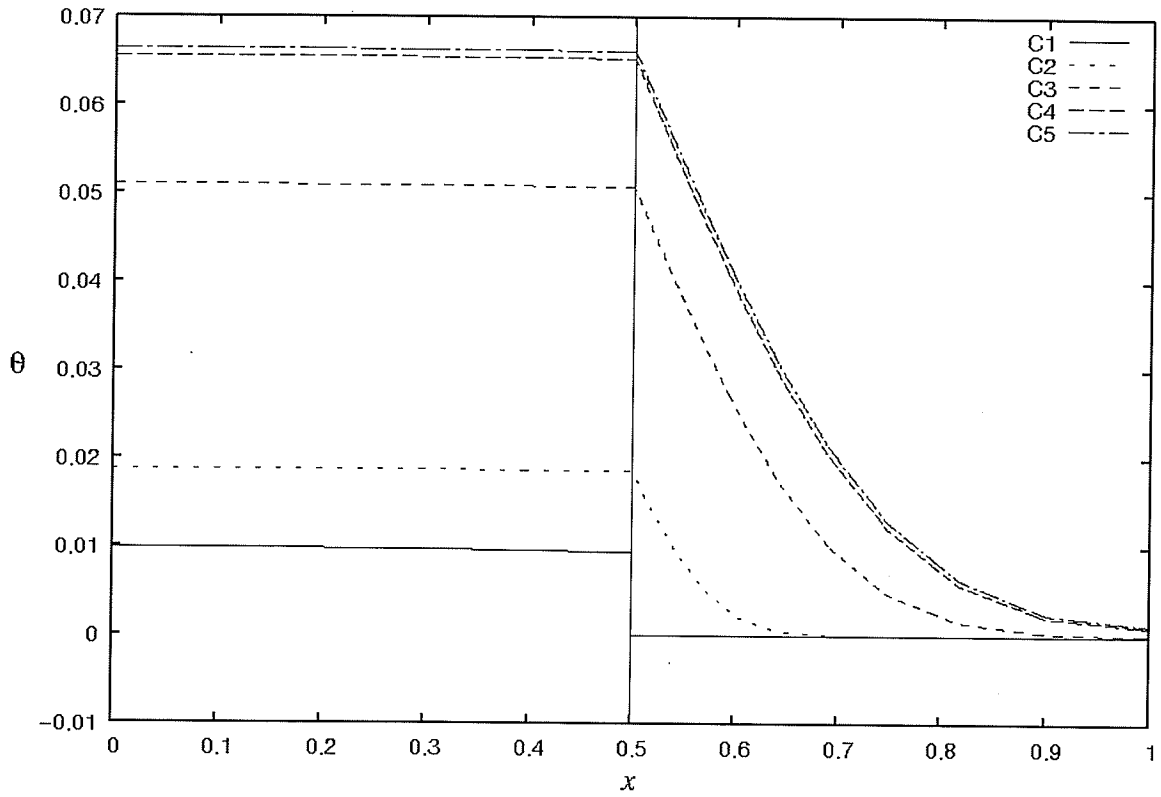

Figure 5.7: Dimensionless Temperatures Along Line C in Various Cross-Sections for the Case 11 Problem

there is indeed a region in the center of the channel in which the temperature is *unaffected* by the presence of the wall. This region gets smaller and smaller for increasing depth into the channel, until it disappears.

Figure 5.8 shows the temperature profiles along the various horizontal lines in cross-section 1 (that is, in the $z = 0$ cross-section). The temperature along all of these lines has zero-gradients at $x = 0$ and $x = 1$, because these locations are symmetry planes. The temperature along line A1, which passes entirely below the channel, increases for increasing x, though the magnitude of this increase is small, because of the solid material's high thermal conductivity. Because this line is entirely within the solid, there is no abrupt change in the derivative of temperature along it. Along the lines B1, C1 and D1, the temperature decreases in the solid region, $x < 0.5$, but, once again, the variation of temperature is slight, since the solid has a high thermal conductivity. For points on lines

B1, C1 and D1 that lie within the channel, (that is, for $x > 0.5$), the temperature is uniform, and equal to the inlet value. The derivative of θ with respect to x is undefined

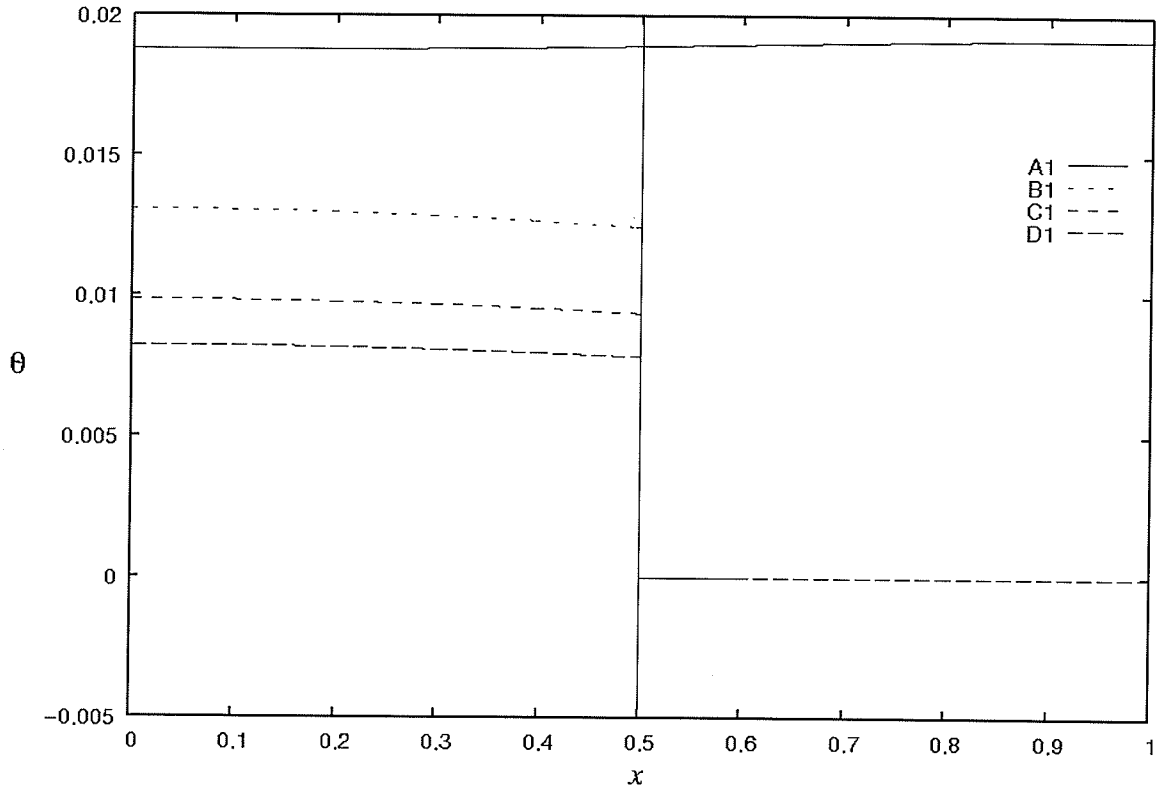

Figure 5.8 Dimensionless Temperatures Along Various Horizontal Lines in Cross-Section 1 ($z = 0$) for the Case 11 Problem

right at $x = 0.5$, which is the interface between the solid and the fluid. The temperatures increase (or, in some cases stay the same) for increasing vertical distance from the heat source. That is, the temperature profile along line A1 is greater than that along line B1, which in turn is greater (or equal to) that along line C1, and so on. All of these observations can be explained as follows. Heat is supplied at the bottom surface. Then, some of that heat flows directly into the bottom of the channel. But, as observed in earlier discussion, the left side of the channel absorbs a greater fraction of the supplied heat than its area fraction. Given that the side is also larger than the portion of the bottom within the repeat-unit, the side absorbs more heat than the bottom. Clearly, then, since half of the heat is supplied in the area directly below the channel (that is for $x > 0.5$), some of this heat must travel towards the negative x direction to wind up entering the

channel through its side. This flow of heat results in the temperature along line A1 needing to increase with increasing x. Then, once this heat has reached the region beside the channel, it combines with the heat supplied directly in the $x < 0.5$ region of the bottom plane. Some of this heat proceeds towards the side wall of the channel, while the remaining heat proceeds upwards, to eventually reach the side wall of the channel at a higher (greater y) location. Thus, in the region to the left of the channel, the heat flows upwards and to the right. This explains why the temperature along lines B1, C1 and D1 decreases towards the channel in the $x < 0.5$ region. It also explains why the temperature profile is greater along line A1 as it is along line B1, greater along line B1 as along line C1, and so on. All of these heat flows occur as result of the heat wanting to flow in the path of least thermal resistance, as expressed more formally in the governing equations given by Eqs. (3.3) and (3.4). Right in the channels, θ is equal to zero along lines B1, C1 and D1, because this is the inlet boundary condition for temperature. The discontinuity in derivative of temperature with respect to x at $x = 0.5$ for lines B1, C1 and D1 is explained by the different thermal conductivities of the solid and the fluid.

Figure 5.9 shows the temperature profiles along the various vertical lines in cross-section 1 ($z = 0$). The line a1 passes entirely in the solid domain, and so, no discontinuity of derivative of temperature is observed along this line. The derivative of temperature along this line is negative, and its absolute value decreases with decreasing y. This is because, as y increased, as the heat exits through the side of the channel, there is less and less heat remaining that flows upwards. Right at the top surface, the derivative is zero because of the insulated boundary condition. Along lines b1, c1 and d1, the temperature is equal to the specified inlet value for points that lie within the channel region. Right at $y = 0$, all curves have the same non-zero slope. The slope is non-zero because the bottom surface is not insulated. Rather, it has as a boundary condition the specified heat flux. Because the heat flux is the same, and because the thermal conductivity of the solid is uniform, the gradient of temperature with respect to y at $y = 0$ has the same value along all of the vertical lines in Figure 5.9.

It should be mentioned that, in the inlet plane, it is not possible to exactly satisfy the conditions across the interfaces. The conditions across the interfaces are that continuities of temperature and heat flux are preserved. In the inlet, however, the

temperature is set to a uniform value, meaning that the gradient, and hence the heat flux, are zero. Thus, it would be necessary for the temperature in the solid to have zero-gradients at the solid/fluid interfaces as well. This would be problematic in two ways.

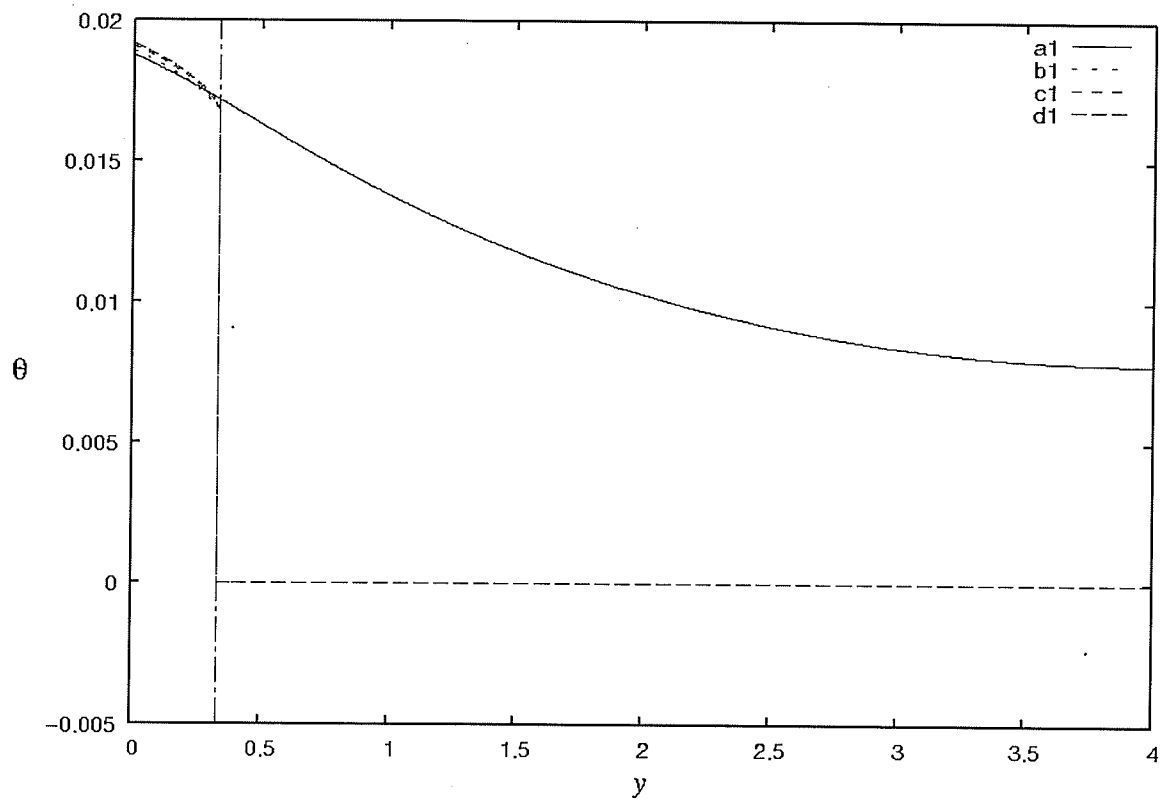

Figure 5.9: Dimensionless Temperatures Along Various Vertical Lines in Cross-Section 1 ($z = 0$) for the Case 11 Problem

First, it would imply that no heat is transfer from the solid to the fluid in this plane, and, second, it would require the discontinuity of temperature at the interface. Thus, the exact conditions cannot be satisfied exactly. This explains why, in cross-section 1, there does not appear to be a continuity of temperature at the solid/fluid interfaces.

With the temperature profiles in the inlet having been observed, it is insightful to observe similar graphs in other cross-sections. Figure 5.10 shows the variation of temperature along the horizontal lines in cross-section 2 ($z = 0.05\ l$). Many of the same trends observed in the $z = 0$ cross-section are observed here as well. One noteworthy difference is that here, the continuity of temperature at the solid/fluid interface can be observed. Also, the temperature is no longer constant within the channel region. Instead,

along lines B2, C2 and D2, starting with a slope that can be determined by ensuring the continuity of heat flux at the interface, the temperature decreases for increasing x in the channel region ($x > 0.5$). The magnitude of the derivative decreases, until it reaches a value of zero in the center of the channel, at which point the temperature is still not

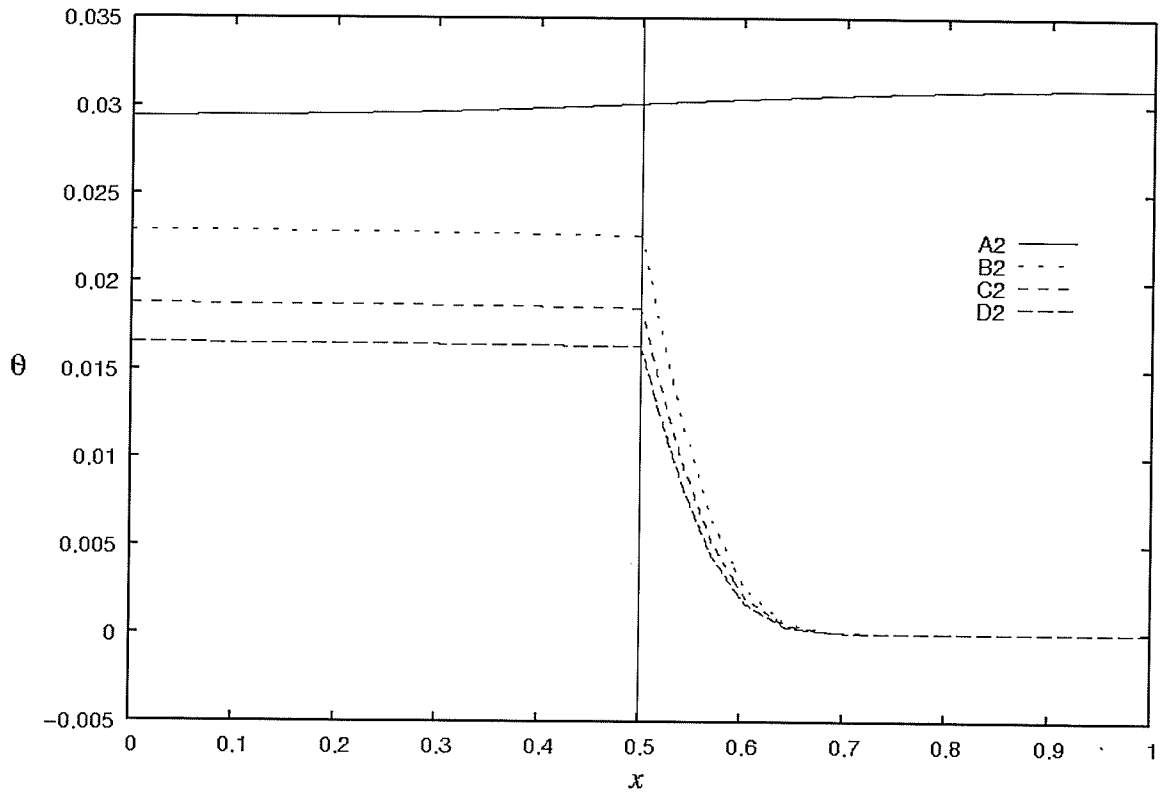

Figure 5.10: Dimensionless Temperatures Along Various Horizontal Lines in Cross-Section 2 ($z = 0.05\ l$) for the Case 11 Problem

affected by the presence of the heat transferred at the wall. With increasing distance from the inlet plane (that is, with increasing z), the temperature profiles for a given horizontal line increase. Furthermore, the size of the region where temperature is the same as the inlet value decreases. However, no other qualitative noteworthy differences are observed when looking at horizontal temperature profiles in other cross-sections. So, these graphs are not presented here.

It should be noted that the trend observed in Figure 5.10, whereby the temperature in the channel region is always lowest for lines with greater y value, is not always

observed. It happens here because of the specific choice of which horizontal lines are used to plot temperatures on.

Figure 5.11 shows the temperature profiles along the various vertical lines in cross-section 3 ($z = 0.5\ l$). Unlike the corresponding graph for cross-section 1, the continuity of temperature at the solid/fluid interface can be seen. Because line b3 passes directly along the solid fluid interface, and is hence separated from line a3 by solid

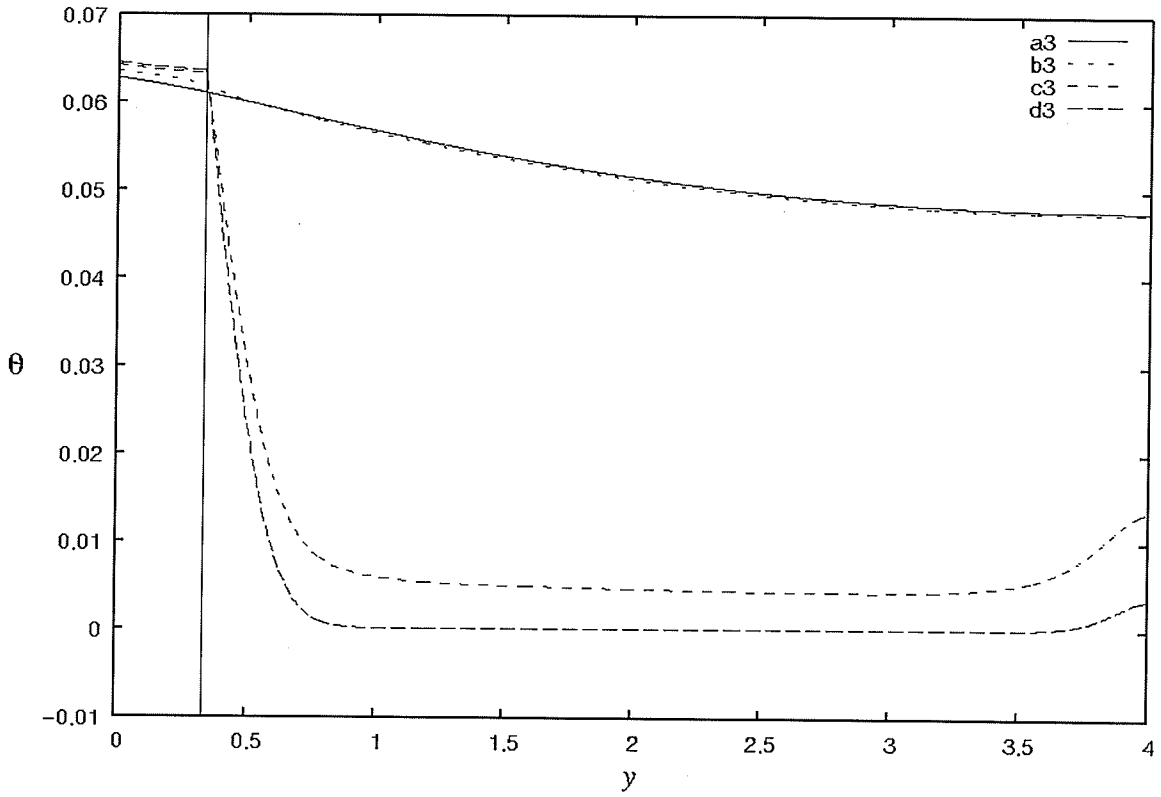

Figure 5.11: Dimensionless Temperatures Along Various Vertical Lines in Cross-Section 3 ($z = 0.5\ l$) for the Case 11 Problem

material only, the temperature profiles along line a3 and b3 are close together, owing to the high thermal conductivity of the solid material. This was not observed in Figure 5.9, because there, for values of y corresponding to the channel region, the temperature on line b1 is set to the inlet temperature boundary condition. At the solid/fluid interface, the temperature profiles along line c3 and d3 are continuous, but, the derivatives of temperature are discontinuous, in a manner that ensures the continuity of heat flux. Then, the temperatures decrease with increasing y, with the magnitude of the derivative

decreasing as well, until the temperatures achieve a uniform value. However, as the top wall of the channel is approached, the temperature once again increases, and then it levels off to a zero-gradient at the top wall. The zero-gradient at the top wall makes sense; it can be explained by the fact that the top wall is assumed to be insulated. However, the rise in temperature that occurs following the zero-gradient region in the middle of the channels seems incorrect at first glance. It appears at first glance that heat is magically created. This is not the case, and, this behavior can be explained. First, though, it is necessary to explain a few other facts.

While the preceding discussions of where the heat is flowing made no explicit mention of this fact, since it was not necessary to qualitatively explain most heat transfer processes discussed thus far, the heat transfer processes are in fact three-dimensional. That is, in both the solid and the fluid, heat flows in the axial direction, as well as within a given cross-section. The following trend is observed. For a given set of xy coordinates, whether in the solid or in the fluid, the temperature rises with increasing z (that is, for increasing axial distance from the inlet). In some cases, the temperature rises with upward concavity, in other cases, with downward concavity, and in some cases, there is a point of inflection somewhere along the z direction. But, in all cases, the temperature increases with increasing z. This is due to the fact that, for increasing axial distance from the inlet, more heat is being "carried along" by the fluid than is the case for cross-sections closer to the inlet.

Within the solid, heat transfer occurs by one mechanism only, namely conduction. This implies, given the observation that temperatures increase with increasing axial distance, that heat flows in the direction of decreasing z within the solid (in addition to the "transverse" heat flows described earlier). This may seem counter-intuitive, at first, but is nevertheless correct.

Within the fluid region, the heat transfer process is more complicated. Here, there are two mechanisms of heat flow. The first mechanism is the heat transfer that occurs by conduction. As in the solid, the axial component of conduction occurs in the negative z direction, meaning in the direction opposite to the fluid flow. The other mechanism of heat transfer is heat flow by advection, which is, simply put, the transfer of heat that takes place when the moving fluid "carries away", or advects, the heat that is contained in the

fluid at a given location. On the whole, more heat is transferred by advection than by conduction. However, there are regions of the flow where this is not the case. Indeed, close the walls of the channel, where the velocities are relatively small (and, right at the walls, where the velocities are by definition zero, because of the no-slip boundary condition), conduction (axially, and within a cross-section) dominates over advection. But, further away from the walls, the advection dominates. Because the flow is essentially uni-directional, even in the developing region, advection carries heat in the direction of fluid flow.

Thus, an overall picture of the heat transfer is as follows. Heat is supplied at the bottom surface. Heat is then conducted through the solid, axially, in the direction opposite the direction of fluid flow, and in transversally, in the manners discussed previously. All of the heat that enters the solid through the bottom surface makes its way, through axial and transverse conduction, to the solid/fluid interfaces. Once there, the heat is absorbed by the fluid. There is a thin region near the channel walls where conduction effects dominate. In this region, heat is actually carried backwards, by conduction, towards the channel inlet. At the same time, however, there is a component of conduction that carries the heat "radially" (that is, in the x- and/or y-directions) inwards towards the center of the channel. So, as the heat is carried "backwards" and towards the center of the channel by conduction, it eventually reaches a radial position where the axial velocity is great enough, and, it starts to flow predominantly "forward" by advection, and is ultimately carried out of the channel outlet by advection. It should be emphasized that conduction, whether axial or "radial", occurs everywhere, even near the center of the channel where the velocities are great. However, in such regions, it is insignificant compared to advection. At the top of the channel, there is indeed a wall, but this wall is not a solid/fluid interface. It is instead an insulated wall. Even though no heat "originates" from this wall, there is, in the thin region near this wall, axial conduction of heat. A small distance away from this wall, heat that has been so-conducted is also conducted radially, until such a point where advection becomes significant, and the heat is carried along with the fluid flow.

It would have been desired at this point to carefully study the flow of heat, and to demonstrate the phenomena described above. It would have been to show how the heat

flow in the regions near the walls of the channel are in the direction opposite to the direction of flow. However, ANSYS CFX does not seem to be able to give heat flux values at arbitrary, user-defined planes. When asked to produce such heat flux values, it gives an error message to the effect that heat flows are not defined on such surface. Furthermore, attempting to work around this limitation by defining a user-specified variable is not fruitful, because, in order to do so, it is necessary to evaluate spatial derivatives of temperature, and, to the best knowledge of the authors, after attempting to do so, this is not possible. Thus, there is no reasonably-convenient way to obtain the "heat flux field". (It was possible, in earlier sections, to generate Nusselt numbers, which depend on heat flux, by making use of the fact that the desired heat flows were all along walls, and so it was possible to use the variable that ANSYS CFX calls "Wall Heat Flux".)

Thus, it is now possible to explain the apparently non-physical behavior observed in Figure 5.11. At the top of the channel, no heat is supplied from the wall. However, along the wall, where the velocity is zero because of the no-slip boundary condition, axial conduction occurs, because of the axial increase in temperature discussed previously. Then, once this heat gets conducted into cross-section 3, some of it continues to be conducted towards the inlet plane, but some of it gets conducted "radially" towards the center of the channel. For this to happen, the temperature along lines c3 and d3 near the top of the channel ($y = 6$) must be as shown in Figure 5.11. Thus, in short, the heat that appears to originate out of "nowhere" originates in fact from a downstream cross-section. It is unfortunate that this cannot be demonstrated or explored further, because of the limitation discussed in the previous paragraph.

The discussions of heat flows presented above imply that the maximum temperature occurs in the outlet plane (because the temperature rises along the z axis), on the bottom surface (the surface of heat application), and directly below the channel's symmetry plane. In other words, at the dimensionless point ($x = 1, y = 0, z = l$). This is confirmed by the data presented in Table 5.2. Because this maximum temperature for the whole domain is located along the plane of heat flux application ($y = 0$), it follows that the maximum temperature on this surface, $\theta_{max,y=0}$, is the same as the overall maximum temperature, and of course its location is the same. As for $\theta_{min,y=0}$, its location is known

to be in the inlet plane ($z = 0$) because of the fact that temperatures always rise for increasing z. Furthermore, because it was shown that, for low y, the heat flows along the negative x direction, the x-coordinate of $\theta_{min,y=0}$ is expected to be $x = 0$. Thus, the minimum temperature along the surface of heat application is expected to be located at $x = 0$ and $z = 0$. This is indeed observed to be the case in Table 5.4.

While the heat flow discussions for the single channel (large) arrangement have focused on the high Reynolds number case using the uniform inlet velocity profile (that is, Case 11), it should be mentioned that no qualitative difference is observed in the low Reynolds number case. Also, when making the fully-developed inlet velocity assumption, while the temperatures are different from those obtained using the inlet velocity profile, no qualitative difference in the heat flow patterns is observed. The locations of the maximum temperature overall, as well as the maximum and minimum temperatures along the heated surface, are identical for all cases using the single channel (large) arrangement. This is one symptom of the similar qualitative heat flow patterns obtained for these cases.

An interesting observation was made while comparing temperature profiles of the uniform inlet velocity profile cases to the corresponding fully-developed inlet velocity profile cases. Figure 5.12 shows the variations of temperature along line DX, using the low Reynolds number, for both the uniform inlet velocity and fully-developed inlet velocity cases. Also shown in Figure 5.12 is a vertical line at the z coordinate that corresponds to the theoretically calculated entrance length for this problem, by applying the correlation for laminar flow presented in Incropera and DeWitt (2002). As a check, the centerline velocity at this axial location for the uniform inlet velocity case was compared against the centerline velocity near the outlet for this same case, and it is confirmed that the centerline velocity is within 96 % of its fully-developed value. It appears from Figure 5.12 that, for axial positions greater than the hydrodynamic entrance length, the temperature predictions along line DX using the uniform inlet velocity and the fully-developed inlet velocity are nearly identical. In fact, for z values greater than the hydrodynamic entrance length, the predictions of temperature (on a dimensionless basis) along line DX given by the uniform inlet velocity case and the fully-developed velocity profile case are within 1.80 % of each other. Other tests not presented here confirm that

similar observations are made when comparing the temperature profiles along any line that runs parallel to the z axis. So, using the uniform inlet velocity assumption, in cross-sections where the velocity is fully-developed, the temperature field obtained is nearly identical to that obtained using the fully-developed assumption. So, if only temperatures in the region where the flow is known to be fully-developed are desired, it is possible to

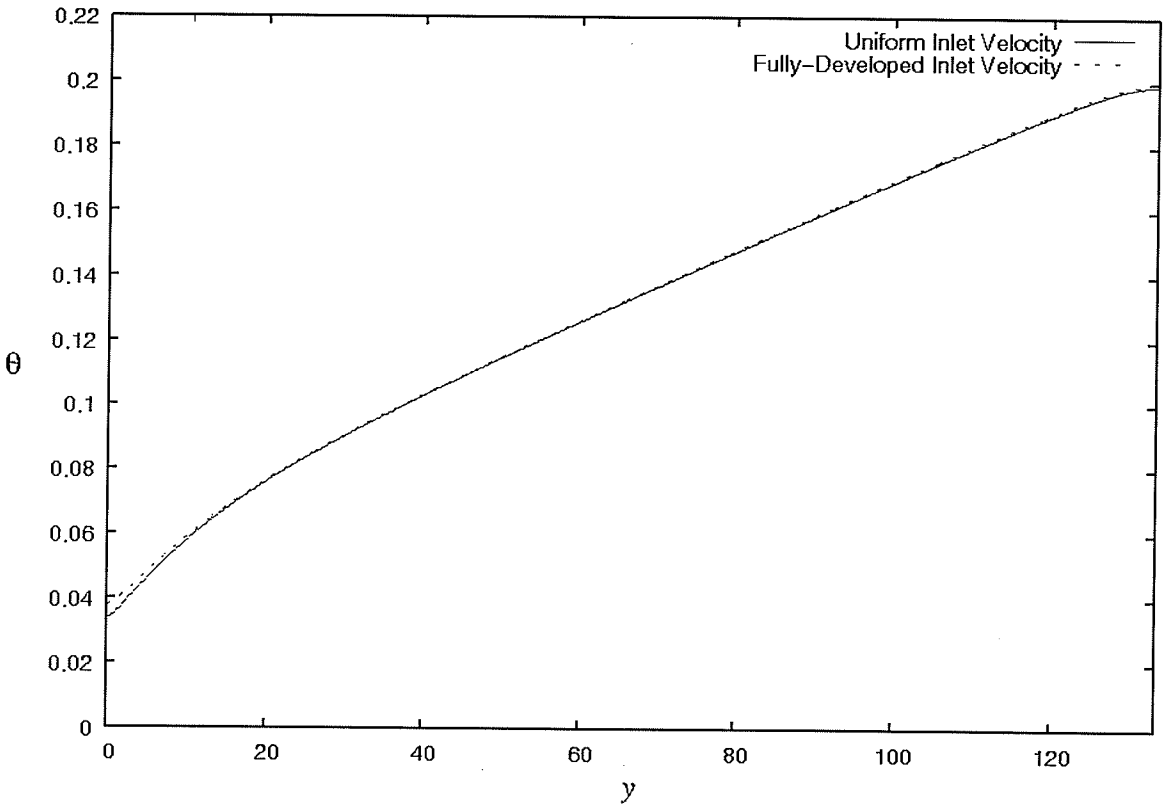

Figure 5.12: Dimensionless Temperatures Along Line DX for Different Inlet Velocity Assumptions

make the fully-developed assumption in the inlet, with negligible loss in accuracy. Expressed another way, it is only necessary to use the uniform inlet velocity assumption when the temperatures in cross-sections where the flow is developing need to be determined with accuracy. This can be explained as follows. It should be recalled that the velocity field is determined separately from, and then used as input in the equations to determine, the temperature field. For cross-sections where the velocity field of the uniform inlet velocity case has reached fully-developed conditions, the velocity fields of both inlet assumptions are identical. Additionally, it was found earlier that, for the solid

regions and a thin layer surrounding the walls of the channel, the heat flow in the axial direction occurs in the negative z direction. Thus, the region where the velocity profiles of the two different assumptions differ is, so to speak, for any z value greater than the hydrodynamic entrance length, "downstream" along the heat flow lines. Thus, the difference in velocity fields for z values smaller than the hydrodynamic entrance length has negligible effect on the temperature field for greater z values.

Thus, in addition to the earlier argument that the achievement of fully-developed thermal conditions could account for why making the fully-developed inlet velocity assumption results in such a good approximation to the thermal resistance, another argument, that does not rely on this presumption, can be made based on the observation made in the previous paragraph. Because the thermal resistance depends only on input parameters to the problem and the maximum temperature in the domain, and because for the single channel (large) arrangement, it is known that the maximum temperature will occur in the outlet plane, where the temperature predictions obtained using either inlet profile assumption are nearly identical, it follows that the thermal resistances predicted using either inlet velocity profile assumptions will be nearly the same. However, because the lowest temperature in the domain is known to occur in the $z = 0$ plane, where the velocity fields for the two different inlet profile assumptions are known to differ significantly, the minimum temperature obtained using the fully-developed inlet assumption differs significantly from the "correct" value obtained using the uniform inlet assumption. Thus, when determining $\Delta\theta_{heated}$, it is necessary to use the inlet velocity profile; making the fully-developed inlet profile assumption will not yield great accuracy.

5.5 Detailed Investigation: Parallel-Flow

Because a detailed presentation of the fluid flow phenomena has been presented in the previous section, and because the fluid flow does not depend on the heat transfer and is hence qualitatively the same for every arrangement, this section only presents a detailed investigation of the heat transfer.

Table 5.6 shows heat fraction and area fraction data for the parallel-flow arrangement, for the uniform cases of both low and high Reynolds number (Case 5 and Case 7, respectively). In some cases, entries in this table that should add up to 100 % do

not do so, because of rounding error. Because the top channel has no solid heat sink material above it, while the bottom channel does, the area fractions of the channels are not 50 %. Instead, $AF = 55.1$ % for the bottom channel, while $AF = 44.8$ % for the top channel. If one looks at the heat fractions of both channels overall, without regard for individual sides, for the low Reynolds number case, the bottom channel has a smaller heat fraction than area fraction and the top channel has a larger heat fraction that its area fraction, meaning that the upper channel has a "stronger pull" on the heat than the bottom channel. The opposite trend is observed in the high Reynolds number case, where the

Table 5.6: Area Fraction and Heat Fraction Data for the Parallel-Flow Arrangement

Surface	*AF* (%)	*HF* (%)	
		Low Reynolds Number (Case 5)	High Reynolds Number (Case 7)
Bottom of lower channel	10.3	8.6	11.0
Side of lower channel	34.5	36.6	37.7
Top of lower channel	10.3	7.2	8.2
Bottom of upper channel	10.3	7.6	8.4
Side of upper channel	34.5	40.0	34.6
Lower Channel Total	55.1	52.4	56.9
Upper Channel Total	44.8	47.6	43

bottom channel has a stronger pull of heat. However, in both cases, the difference in the overall heat fractions for the channels and their respective area fractions is not significant.

For both channels, for both Reynolds numbers considered, the respective sides have greater heat fractions than their respective area fraction. This mean that the sides tend to pull more heat than other solid/fluid interfaces. The reason for this is the same as in the single channel (large) arrangement. Because the channels are elongated in the y-direction, the thermal resistance between the heated surface and the cooler middle regions of the channels is smaller for heat that enters the channels from the side than for heat that

enters through the top and bottom. This is the case simply because there is less distance (and hence less thermal resistance) between the sides of the channels and the cooler inner regions of the channels, than there is between the bottom and/or top of the channels, and the cooler inner regions. Thus, heat tends to preferentially exit the solid through the sides of the channels.

Of the remaining three solid/fluid interfaces, which are horizontal and have the same area (and area fraction), the bottom of the bottom channel attracts more heat than the other two. This is to be expected, since it is located much closer to the heat source than the other two, and the advantage the distances to the channels' cooler inner regions are expected to be similar for all three surfaces. In fact, for the high Reynolds number, the heat fraction is $HF = 11.0$ %, which is higher than the area fraction for this interface. This is the only case of a horizontal surface having a greater value of HF than its AF for the parallel-flow arrangement. It occurs here because, with the higher Reynolds number and hence the smaller distance required to reach the cooler inner regions of the bottom channel from this surface, and with the smaller distance that heat needs to travel in the solid to reach this surface, the thermal resistance to heat flow for heat that follows a path that exits from this surface is low enough to allow this surface to have a greater heat fraction than area fraction.

The other two horizontal surfaces are the top of the lower channel, and the bottom of the top channel. For both the high and low Reynolds number cases, the heat fractions of these surfaces are less than their corresponding area fractions. Of the two surfaces, the bottom of the upper channel attracts more heat than the top of the bottom channel. However, the difference is nearly insignificant. For example, for the low Reynolds number case, the heat fraction of the top of the bottom channel is $HF = 7.2$ %, while that for the bottom of the top channel is 7.6 %. For the high Reynolds number case, the difference is even less significant, with the top of the bottom channel have $HF = 8.2$ %, and the bottom of the top channel having $HF = 8.4$ %. The slight difference is due to the fact that the top channel is expected to be cooler, on average, than the bottom channel, because it is further away from the heat source. Thus, the bottom of the top channel can absorb more heat than the top of the bottom channel.

Attention is now focused to temperature plots, in dimensionless form, along various lines. Unless otherwise noted, all temperature profiles are for the high Reynolds number case using the uniform inlet velocity assumption (Case 7).

Figure 5.13 shows the temperature profiles along the various horizontal lines in cross-section 2 ($z = 0.05\ l$). At $x = 0$ and $x = 1$, the temperature profiles along all lines in this figure has a slope of 0, because the surfaces at these ends are symmetry planes. Because they are both located entirely within the solid, there is no discontinuity in the slope of the temperature profiles at any point along lines A2 and C2. Along lines B2 and D2 there are discontinuities in the slope at $x = 0.5$, which is where these lines cross solid/fluid interfaces (from the solid into the bottom and top channels, respectively). The abrupt change in slope is due to the difference in thermal conductivities between the solid and the fluid. Along line A2, the temperature increases in the direction of increasing x. This can be explained by the fact that half of the heat that enters the solid from the bottom surface does so directly below the bottom of the bottom channel, while this surface absorbs only 11 % of the heat, as shown in Table 5.6. Thus, some of the heat that enters the heat sink directly below the bottom channel must flow in the direction of decreasing x, in order to travel along paths leading to other solid/fluid interfaces. This flow of heat in the negative x-direction is reflected in the temperature profile along line A2. Then, in the region to the left of the channels ($x < 0.5$), heat that has originated below the channels but moved towards the left, and heat that originated directly below the region to the left of the channels, combine, and proceed upwards (in the direction of increasing y). As this heat is proceeding upwards, some of it gets absorbed into the side of the bottom channel, while the remainder continues upwards. This upwards flow of heat, therefore, is not truly moving only upwards: it has a component towards the right as well (otherwise, the heat could not actually flow towards either channel). Heat thus proceeds upwards, with some losses along the way. These losses occur as heat flows into the side of the bottom channel, into the solid region above the bottom channel but below the top channel, and into the side of the top channel. The upward flow of heat in the region $x < 0.5$ is reflected in Figure 5.13 by the fact that, in this region, the temperatures along line A2 are greater than those along line B2, which are greater than those along line C2, which are in turn greater than those along D2. Thus, temperatures in this region

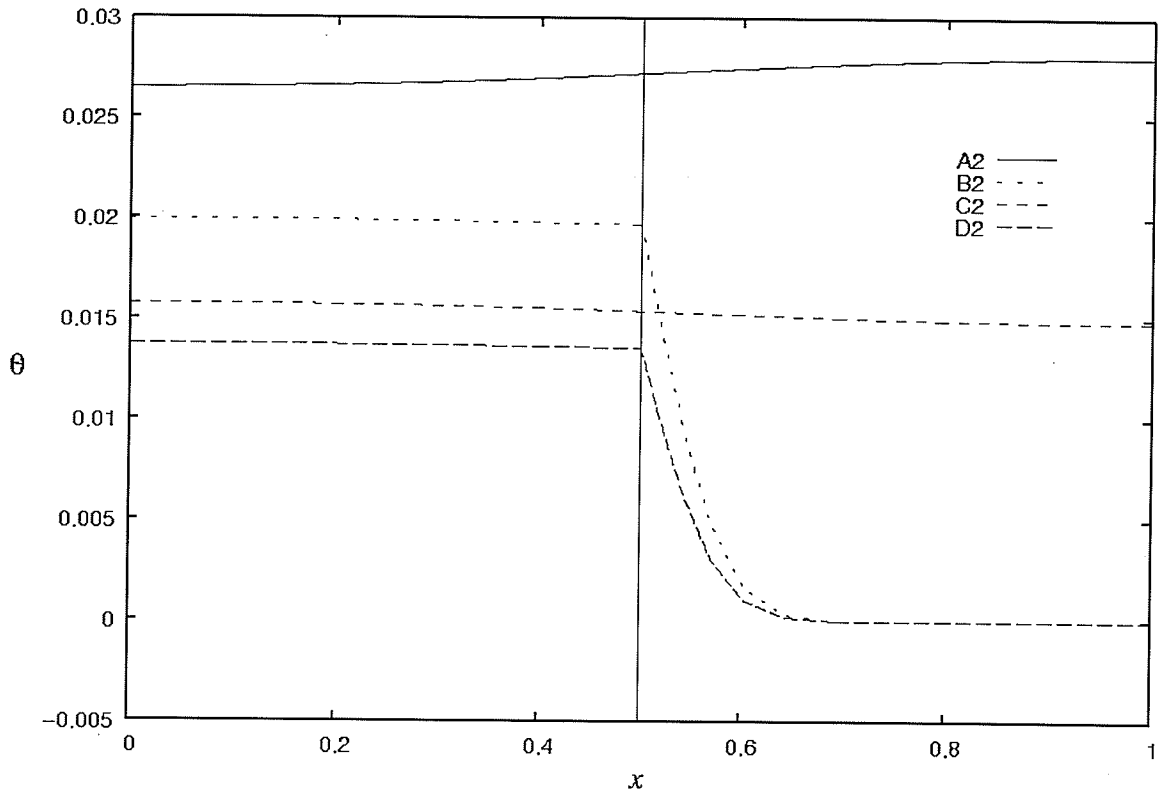

Figure 5.13: Dimensionless Temperatures Along the Various Horizontal Lines in Cross-Section 2 ($z = 0.05\ l$) for the Case 7 Problem

decrease for increasing y, which indicates an upward flow of heat. Furthermore, the rightward component of heat can be seen, in Figure 5.13, by the fact that, for $x < 0.5$, the temperature profiles along lines B2, C2 and D2 have a slight negative slope. Along lines B2 and D2, after the abrupt discontinuities in slopes at $x = 0.5$, the temperature profiles drop off sharply, as heat is being absorbed and carried by the fluid, and continue to drop until they level off at some point. Towards the center of the channels (that is, for x values close $x = 1$) the temperatures along line B2 and D2 both approach the channel inlet temperature, which is the same in both channels. This is because the region where the temperature is unaffected by the heat transfer from the solid/fluid interfaces is approached. The region where the temperature in the channels still equal the inlet value is relatively large, because this is the high Reynolds number case, and because the cross-section under consideration is close to the inlet plane. In the region above the bottom channel and below the top channel, the heat flows from left to right, and, as it does so, some of it gets absorbed into the top and bottom channels. This flow of heat from left to

right is shown by the negative slope of the temperature profile along line C2. As the heat gets absorbed by either channel, the heat that continues to flow towards the right diminishes. This is seen by the decrease in the absolute value of the slope of the temperature profile along line C2 for increasing x in $x > 0.5$.

Figure 5.14 shows the temperature profiles along the various vertical lines in cross-section 2 ($z = 0.05\ l$). The slope of the temperature profiles at $y = 0$ are non-zero. This is true for all lines. The negative slope at $y = 0$, which is the same along all vertical lines, can in fact be determined by applying the boundary condition (the specified heat flux) at this boundary. The temperature profiles along lines c2 and d2, in the regions corresponding to the channels, reveal that the region of the channels where the temperature is equal to the inlet value is relatively large (occupying most of the channel regions' axial cross-sections). The temperature profiles along lines a2 and b2 always decrease with increasing y, which signifies that the heat is flowing upwards along these lines. Furthermore, the magnitude of the slopes of the temperature profiles along these lines decreases with increasing y. This is because, as y increases, there is less and less heat flowing upwards, because some of this heat is lost along the way (it is lost to the side of the bottom channel, the solid space above the bottom channel but below the top channel, and the side of the top channel). In the y range corresponding to the region below both channels ($y < 0.333$), the temperature profile along line d2 is greater than that along line c2, which in turn is greater than that along line b2, which in turn is greater than that along line a2. This is because, as discussed, the heat in this region is flowing in the direction of decreasing x, and hence the temperature increases with increasing x. The reverse is observed in the region above the bottom channel and below the top channel ($2 \le y \le 2.333$). Here, the heat is flowing in the direction of increasing x, meaning that the temperatures are decreasing with increasing x. The profiles along line a2, b2, c2 and d2 in the region $2 \le y \le 2.333$ confirm this trend.

The only significant axial effect is that temperatures increase along the direction of flow. Thus, analogues to Figures 5.13 and 5.14 in other cross-sections look qualitatively similar (except in the inlet, where the temperatures are exactly equal to the specified inlet values, and hence "square" profiles result). Since temperatures rise with increasing z, which is true in the solid and in the fluid, axial conduction occurs in the

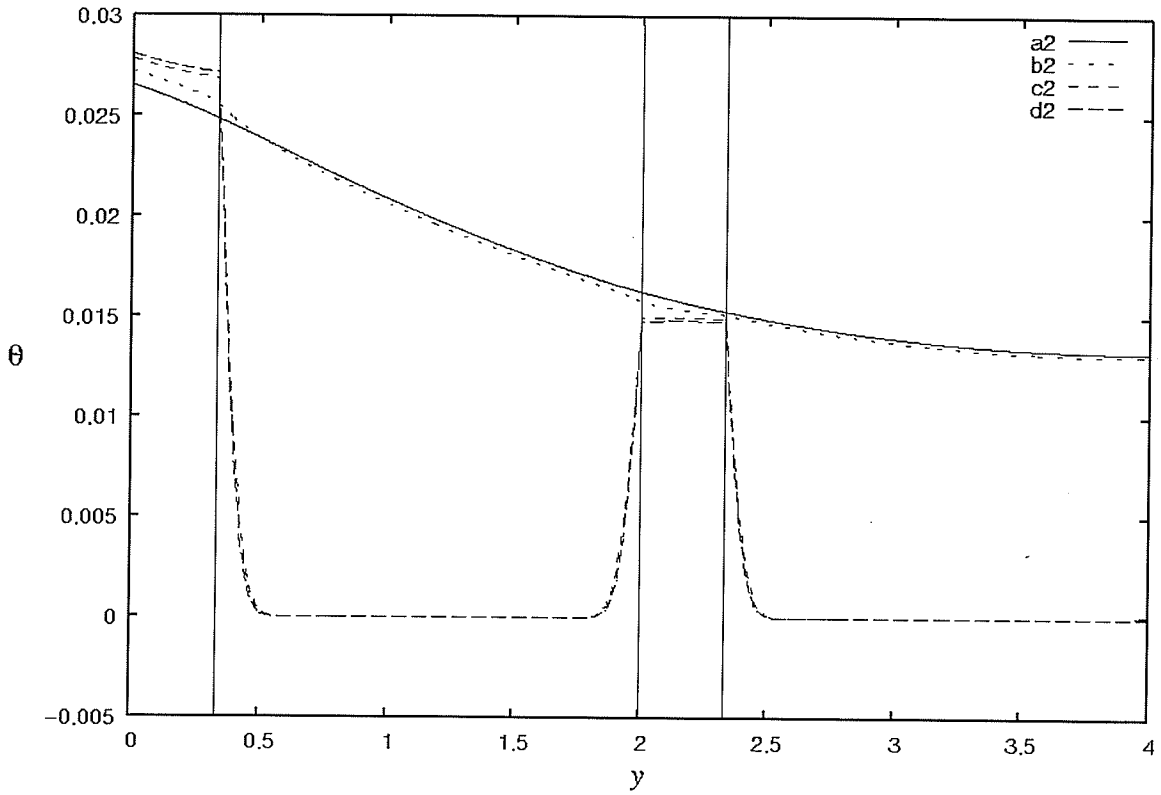

Figure 5.14: Dimensionless Temperatures Along the Various Vertical Lines in Cross-Section 2 ($z = 0.05\ l$) for the Case 7 Problem

direction of decreasing z. This is true everywhere in the solid and fluid. However, it is only in the solid and in a thin region surrounding the wall of the channels (where the velocities are small) that conduction is significant. In the central regions of the channels, conduction is negligible, and advection is the dominant mode of heat transfer.

Thus, an overall picture of the heat flow patterns is as follows. Heat enters the bottom surface of the solid, according to the boundary condition on this surface. Within the solid, heat flows in the negative z-direction, axially, and at the same time flows within a cross-section in the manners specified above. Then, when heat crosses into one of the channels, it flows towards the center of the respective channel, and is conducted axially in the negative z-direction. As it proceeds towards the channel's center, it eventually reaches a point where the velocities are great enough, and the heat is advected, into the positive z-direction, by the fluid. When the fluid exits through the outlet, it carries the heat with it.

Comparisons were made between this case (Case 7), and the other parallel-flow cases. No qualitative differences in temperature profiles were observed among any of these four cases.

5.6 Detailed Investigation: Counter-Flow

Table 5.7 shows the area fraction and heat fraction data for the counter-flow arrangement cases using the uniform inlet velocity assumption. It can be seen from these data that the sides of the channels have greater heat fractions than their area fractions. This can be seen in every case except for the side of the top channel in the high Reynolds number case, where the heat fraction ($HF = 34.3$ %) is ever-so-slightly less than the area

Table 5.7: Area Fraction and Heat Fraction Data for the Counter-Flow Arrangement

Surface	AF (%)	HF (%)	
		Low Reynolds Number (Case 1)	High Reynolds Number (Case 3)
Bottom of lower channel	10.3	8.5	11.2
Side of lower channel	34.5	37.5	38.3
Top of lower channel	10.3	6.9	8.2
Bottom of upper channel	10.3	6.9	8.0
Side of upper channel	34.5	40.1	34.3
Lower Channel Total	55.1	52.9	57.7
Upper Channel Total	44.8	47.0	42.3

fraction ($AF = 34.5$ %). As was the case in the parallel-flow arrangement, this observation can ultimately be traced to the fact that the channels are elongated in the y-direction.

Among each of the remaining solid/fluid interfaces, all of which are horizontal and all of which have the same area (and hence the same area fraction),the one through which most heat gets transferred is the bottom of the bottom channel. In fact, for the high

Reynolds number case, the heat fraction for this surface ($HF = 11.2$ %) is greater than the area fraction of this surface ($AF = 10.3$ %). This is the case because, as was the case in the parallel-flow case, with the higher Reynolds number and hence the smaller distance required to reach the cooler inner regions of the bottom channel from this surface, and with the smaller distance that heat needs to travel in the solid to reach this surface, it ends up being the case that heat is "pulled" towards this surface in a greater proportion than this surface's proportion of total solid/fluid interface area.

When the heat fraction data for the top of the bottom channel and the bottom of the top channel are considered, the trend observed is different from the trend observed in the parallel-flow arrangement. For the low Reynolds number case, the heat fraction of these two surfaces are identical (to 2 significant digits, they are both $HF = 6.9$ %). For the high Reynolds number case, the heat fraction of the top of the bottom channel is greater than that of the bottom of the top channel (the former is $HF = 8.2$ %, while the latter is $HF = 8.0$ %). This is in contrast to the parallel-flow arrangement, where the heat fraction of the bottom of the top channel was greater than that for the top of the bottom channel. However, the difference in heat fractions, even for the high Reynolds number case where they are not equal, are nearly equal for both surfaces. Thus, it can be said that the heat fractions of the bottom of the top channel and the top of the bottom channel are nearly equal, and are below the area fractions for these surfaces. It is also interesting to note that, for both the parallel-flow arrangement and the arrangement under current consideration (the counter-flow arrangement), the heat fractions of these two surfaces is greater for high Reynolds number. Thus, increasing the Reynolds number resulted in more heat being attracted to these surfaces.

Having examined the heat flows along the various solid/fluid interfaces, attention can now be focused on temperature profiles. Unless otherwise noted, the plots are for the high Reynolds number, uniform inlet velocity case (that is, Case 3). Furthermore, to avoid excessive repetition, the discussions that follow will place emphasis on phenomena that were not already observed when looking at temperature profiles for the previously considered arrangements. As such, certain features, such as zero-slopes at symmetry planes, and the discontinuity in slope across solid/fluid interfaces, will not be pointed out.

Figures 5.15, 5.16 and 5.17 show, respectively, the non-dimensional temperature profiles along the various horizontal lines in cross-section 2 ($z = 0.05\ l$), the non-dimensional temperature profiles along the various horizontal lines in cross-section 3 ($z = 0.5\ l$), and the non-dimensional temperature profiles along the various horizontal lines in cross-section 4 ($z = 0.95\ l$).

In interpreting the temperature profiles shown in Figure 5.15, it must be remembered that they correspond to an axial cross-section that is close to the inlet of the top channel, but, close to the outlet of the bottom channel. Thus, the bottom channel contains fluid that has already picked up most of the heat that it will pick up before exiting the heat exchanger, while the top channel has just begun to pick up some heat. So, in this cross-section, the top channel is cooler, which would tend to make it pull more heat than the bottom channel, but, it is also located further away from the heat source. These two trends tend to have opposite effects; the result is the temperature profiles shown in Figure 5.15. In the region to the left of the channels ($x < 0.5$), the temperatures are greatest along lines closest to the heat source. Thus, in this cross-section, the heat flow proceeds, in the region to the left of the channels, in a mainly upward and rightward fashion. Along line D2, in the top channel region, the temperature to the right of the solid/fluid interface drops relatively suddenly, and then levels off to the specified inlet value. However, along line B2, in the bottom channel region, the temperature also drops of with increasing x, but it does so in a different fashion. Rather than dropping off suddenly, immediately to the right of the solid/fluid interface, it "lingers", so to speak, behind the temperature profile along D2. The temperatures at most x coordinates in the region $x > 0.5$ is substantially greater along line B2 than along line D2. This is because this channel has already undergone a lot of heating by the time it reaches this cross-section. Close to $x = 1.0$, however, the temperature profile along line B2 levels off, and its value at $x = 1.0$ is only slightly greater than that along line D2. This is because, even though the bottom channel has undergone most of its heating, the temperature near its center has risen only slightly. This is due to the high Reynolds number. This is a desirable feature because, even though the temperature of the bottom channel has risen, even near its outlet, there still remains a region of cool fluid, that acts to attract heat to this bottom channel (albeit to a lesser extent than is the case near its inlet).

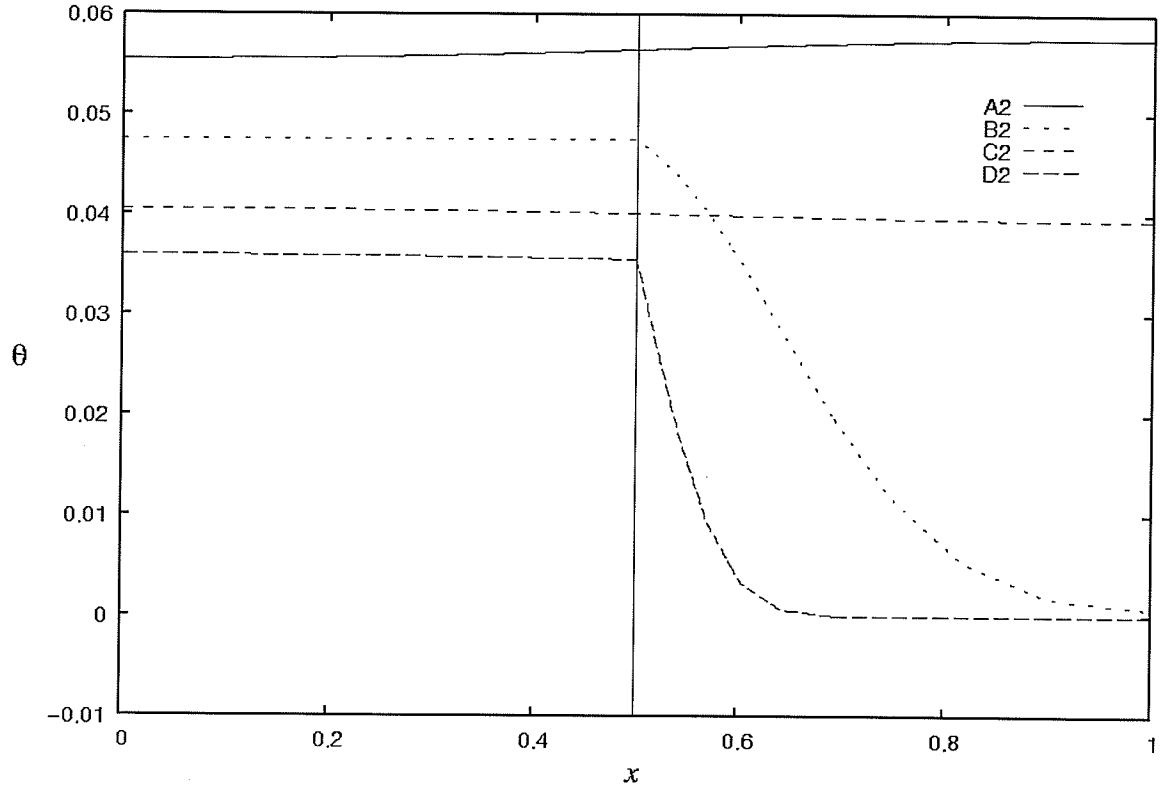

Figure 5.15: Dimensionless Temperatures Along the Various Horizontal Lines in Cross-Section 2 ($z = 0.05\ l$) for the Case 3 Problem

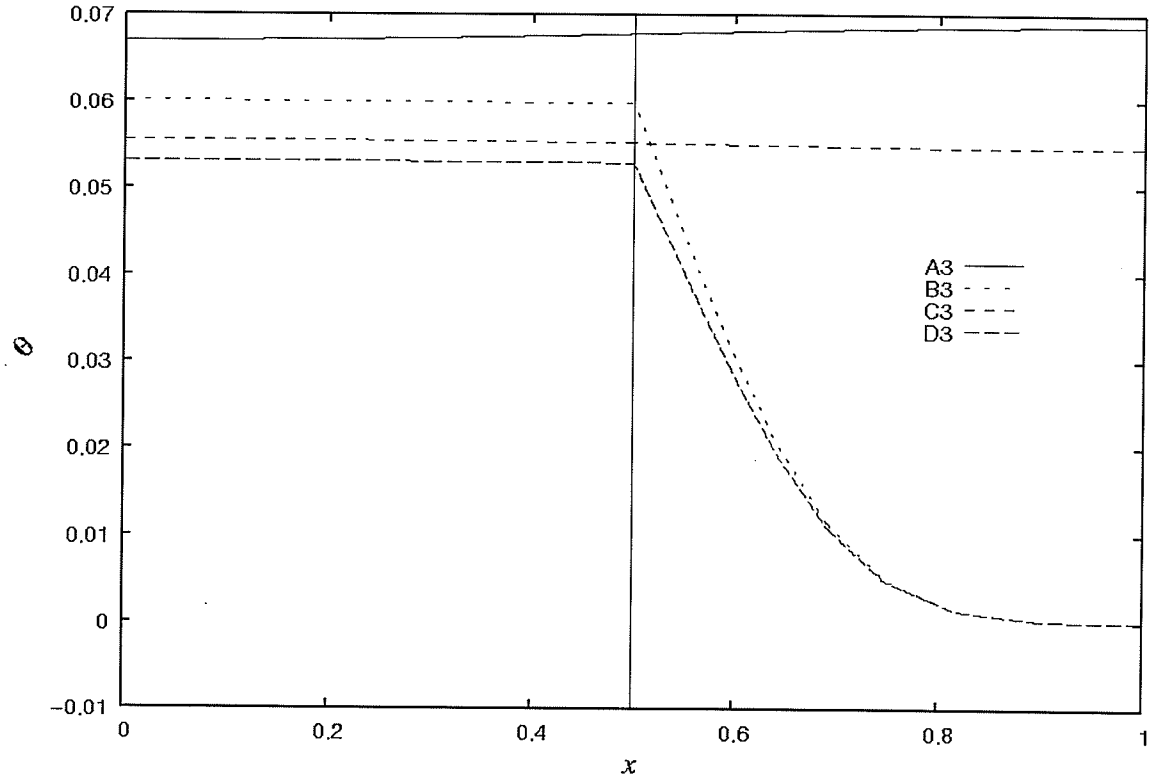

Figure 5.16: Dimensionless Temperatures Along the Various Horizontal Lines in Cross-Section 3 ($z = 0.5\ l$) for the Case 3 Problem

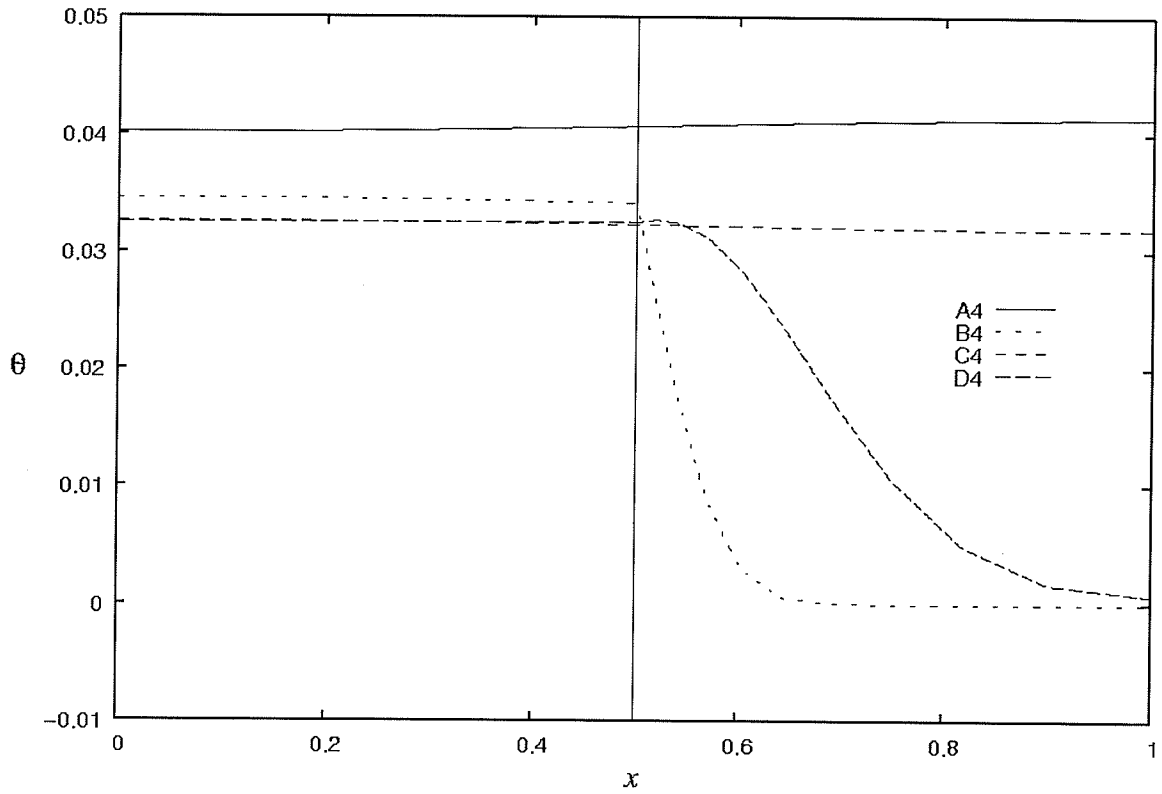

Figure 5.17: Dimensionless Temperatures Along the Various Horizontal Lines in Cross-Section 4 ($z = 0.95\ l$) for the Case 3 Problem

The temperature profiles in Figure 5.16 are for the cross-section $z = 0.5\ l$. This cross-section is sufficiently far away each channels' respective inlets and outlets. Thus, as might be expected intuitively, since each channel has (to a first approximation) undergone the same amount of heating prior to reaching this cross-section, the qualitative behavior of the temperature profiles (and hence the heat flow patterns) in this cross-section is the same as it is in any cross-section for the parallel-flow arrangement.

Figure 5.17 shows the temperature profiles in cross-section 4. In this cross-section, it is the top channel that has undergone more heating upstream, and the bottom channel that is close to its inlet and has thus undergone less heating. Thus, the top channel is warmer than the bottom channel, and it is located father away from the heat source. Both of these factors favor the flow of heat, in this cross-section, to preferentially exit the solid through its interfaces with the bottom channel. Indeed, in the region $x < 0.5$, the temperature profile along line C4 nearly overlaps that along line D4, which suggests that little or no heat is actually flowing upwards from line C4 to eventually enter

the top channel through its side surface. In this cross-section, then, the top channel is only attracting a negligible amount of heat; the rest is flowing axially, and/or towards the bottom channel.

Figure 5.18 shows the temperature profiles along the various vertical lines in cross-section 4. It can be seen from this figure that, not only is there no heat flowing from the solid into the top channel, but, some heat is actually flowing *out of* the top channel, into the solid, and enters the bottom channel. This is indicated by the rise in the temperature profiles along lines c4 and d4 just to the right of $y = 2.333$.

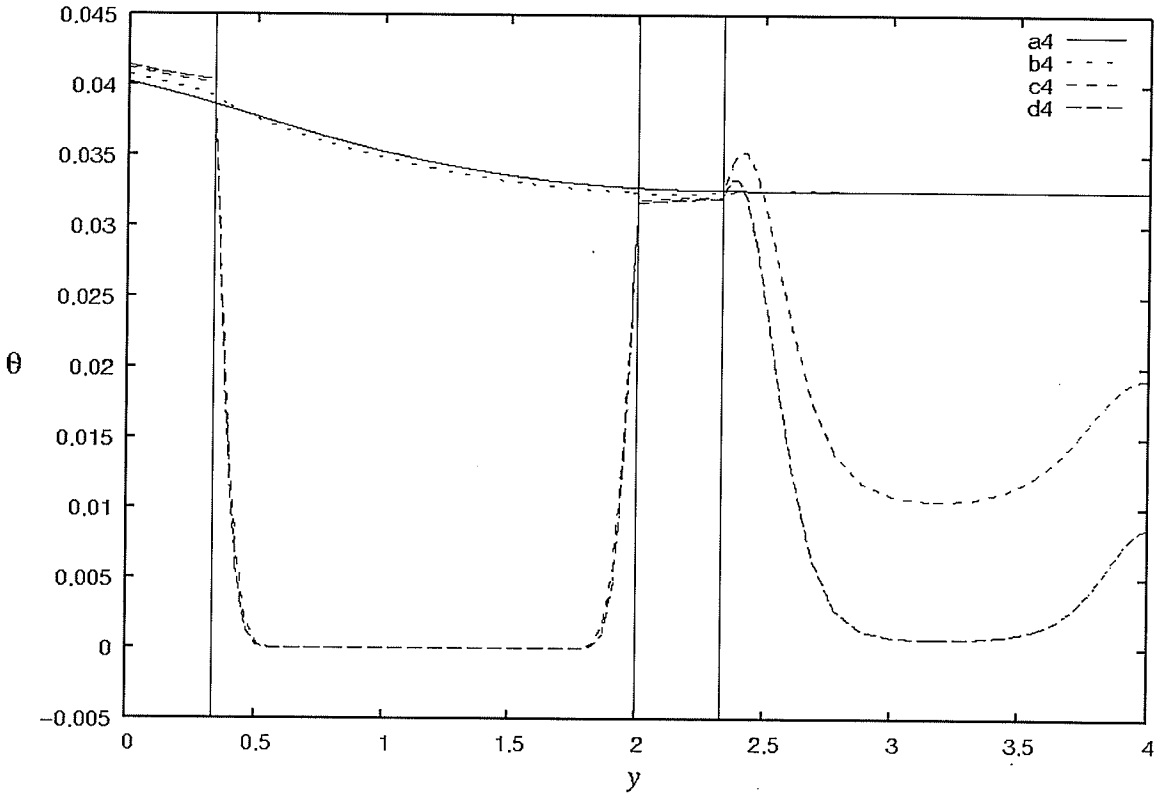

Figure 5.18: Dimensionless Temperatures Along the Various Vertical Lines in Cross-Section 4 ($z = 0.95\ l$) for the Case 3 Problem

Figure 5.19 shows the variation of dimensionless temperature along line AX, using the high Reynolds number, for the counter-flow (Case 3) and parallel-flow (Case 7) arrangements. The significant trend in the axial direction is that, for the counter-flow arrangement, starting from one end ($z = 0$ or $z = l$) the temperature rises to a maximum, and then decreases. The temperatures at both ends may be close to each other, or, one

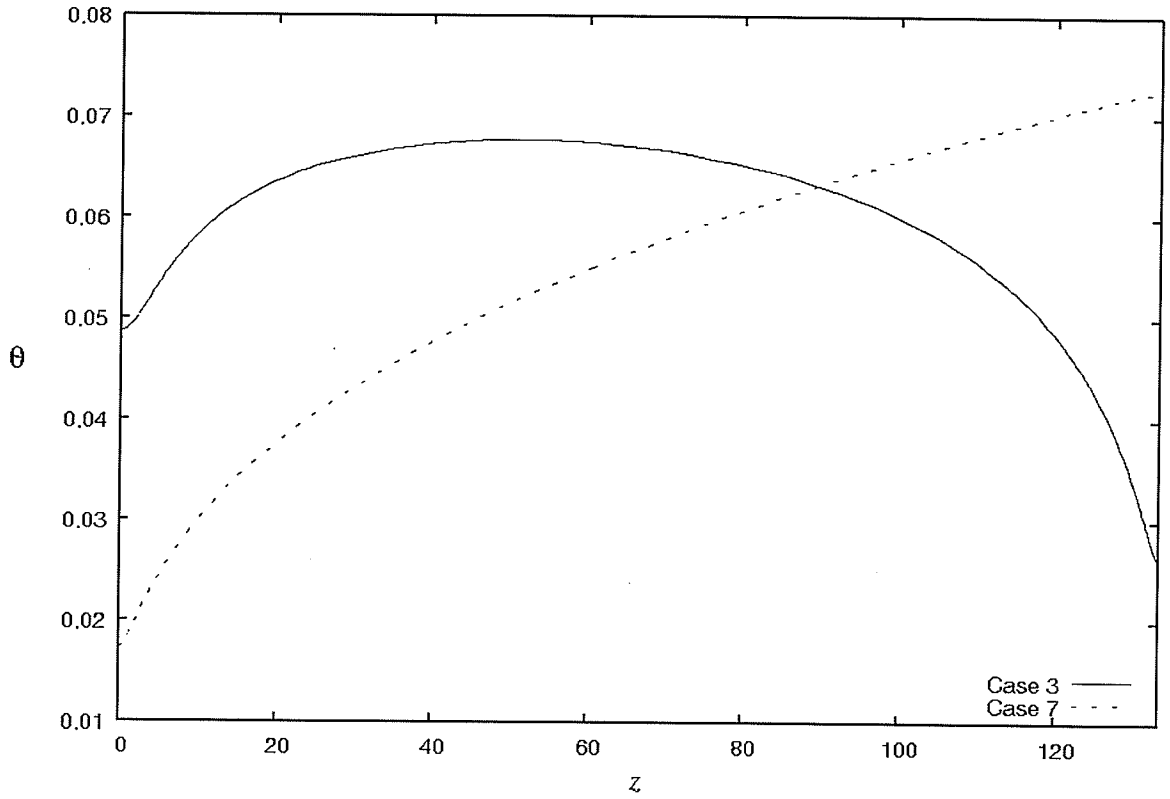

Figure 5.19: Dimensionless Temperature Variation Along Line AX for the Case 3 and Case 7 Problems

may be significantly higher than the other (in all observed cases, the temperature at $z = 0$ was found to be higher than that at $z = l$ for a given axial line). Because of this, compared to the other arrangements, there tends to be less variation of temperatures axially, and less amplitude of temperature along a given axial line. This true everywhere, including on the heated surface ($y = 0$). However, the temperature variation along line AX is monotonic for the parallel-flow case. This simple yet crucial feature explains why the counter-flow arrangement is the best at maintaining the uniformity of temperature along the heat surface. Furthermore, it can be seen that the lowest temperature along line AX for the parallel-flow case is lower than that for the counter-flow case. This is the case because, for the parallel-flow case, both channels have their inlets in the same plane, which can keep temperatures in this cross-section cooler than in the counter-flow case, where the inlet of one channel is in the same cross-section as the outlet of the other.

There are no major qualitative differences between the temperature profiles for the high Reynolds number case using the uniform inlet velocity assumption and the high

Reynolds number case using the fully-developed inlet velocity assumption. Also, there are no major qualitative differences between the temperature profiles for the low Reynolds number case using the uniform inlet velocity assumption and the low Reynolds number case using the fully-developed inlet velocity assumption. However, there is one significant qualitative difference between the high Reynolds number case using the uniform inlet velocity assumption and the low Reynolds number case using the uniform inlet velocity assumption.

Figure 5.20 shows the temperature profiles along the various vertical lines in cross-section 4 ($z = 0.95\ l$) for the low Reynolds number, uniform inlet velocity case (Case 1). This reveals that, in the top channel, even the "innermost" temperature is greater than the temperatures of the surrounding solid material (and hence, in this cross-section, heat flows from this channel, into the solid and into the other channel). This is in sharp contrast to the high Reynolds number case where, in this cross-section, while some heat was indeed flowing from the top channel, into the solid and then into the bottom channel), the temperature at the *innermost* regions of this channel were below the temperatures of the surrounding solid material, and was in fact only slightly higher than the inlet temperature. The three-dimensional effect that was first-demonstrated in Figure 5.11 (and explained in detail in Section 5.4) can also be seen in Figure 5.20.

Figure 5.21 shows a contour plot of the heat flux along the walls of the channels (q''_{wall}) for the counter-flow, low Reynolds number case (Case 1). Only negative values are shown, where a negative value indicates that the heat is *leaving* the channel, and entering the solid. Values are normalized by dividing them by the heat flux supplied at the bottom. It should be noted that the view in Figure 5.21 is not isometric. Instead, it is a view from an angle almost (but not completely) "head-on" to the Z-axis, which is necessary to be able to see the whole heat sink in one view (since the length of the channels is much greater than the cross-sectional dimensions). It can be seen in Figure 5.21 that there are regions near each channel's respective outlet where heat actually flows out of the channels. Figure 5.22 shows a contour plot of the negative heat flux values along the walls of the channels for the counter-flow, high Reynolds number case (Case 3). Clearly, it can be seen that, for the high Reynolds number case, there are again

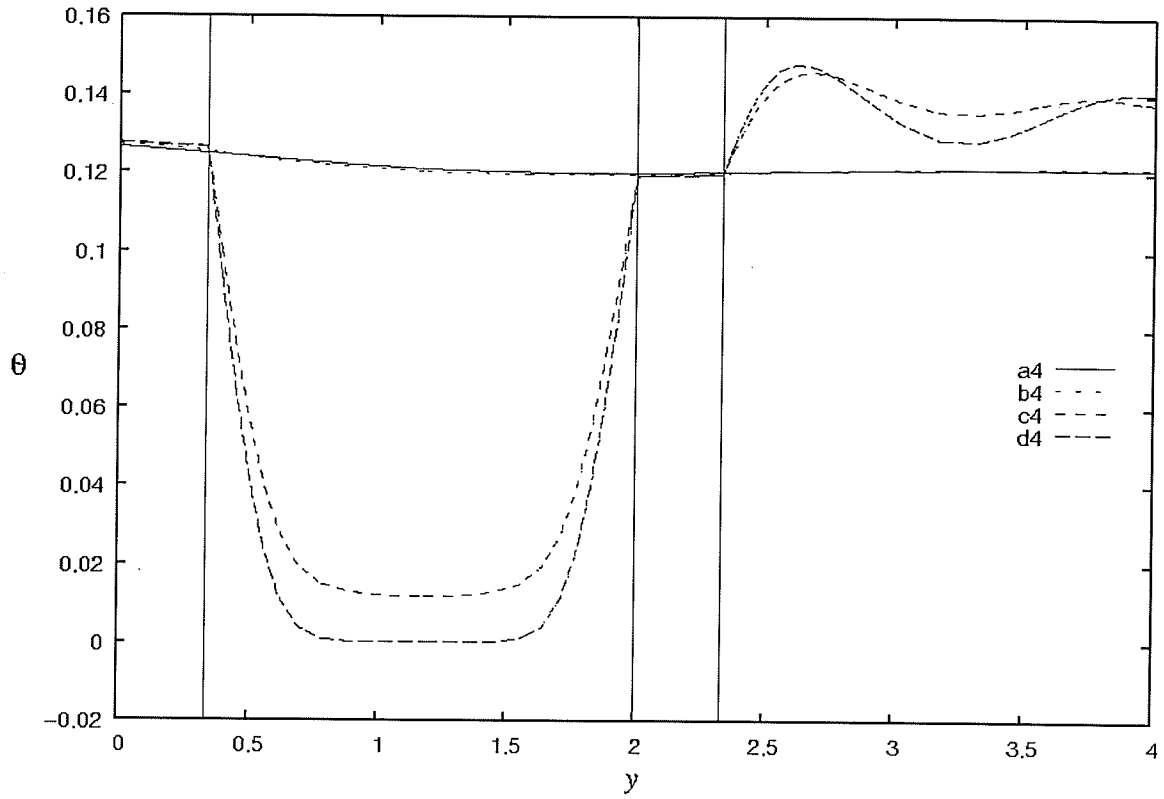

Figure 5.20: Dimensionless Temperatures Along the Various Vertical Lines in Cross-Section 4 ($z = 0.95\ l$) for the Case 1 Problem

regions where heat flows out of the channels into the solid (and absorbed into the other channel), but, these regions are smaller than they are for the low Reynolds number case.

Thus, in summary, the heat transfer processes in this counter-flow arrangement are more complicated than those of the other arrangements (even though the same physical principles, and the same governing equations, apply). Axial conduction does occur, but, unlike earlier arrangements, it does not only occur in one direction. At lower z, axial conduction occurs in the negative z-direction (temperatures increase with z), while at higher z, axial conduction occurs in the positive z-direction (temperatures decrease with z). Axial conduction occurs everywhere, but, it is only significant in the solid and in the thin region in the channels surrounding the walls. Heat flows also occur cross-sectionally, but, these heat flow patterns are not, as was the case for the parallel-flow and single-channel (large) arrangements, qualitatively the same in every axial cross-section. Instead, these heat flow patterns vary with axial cross-section. This is due to the fact that the flow directions in the two channels are opposite to one another, and thus,

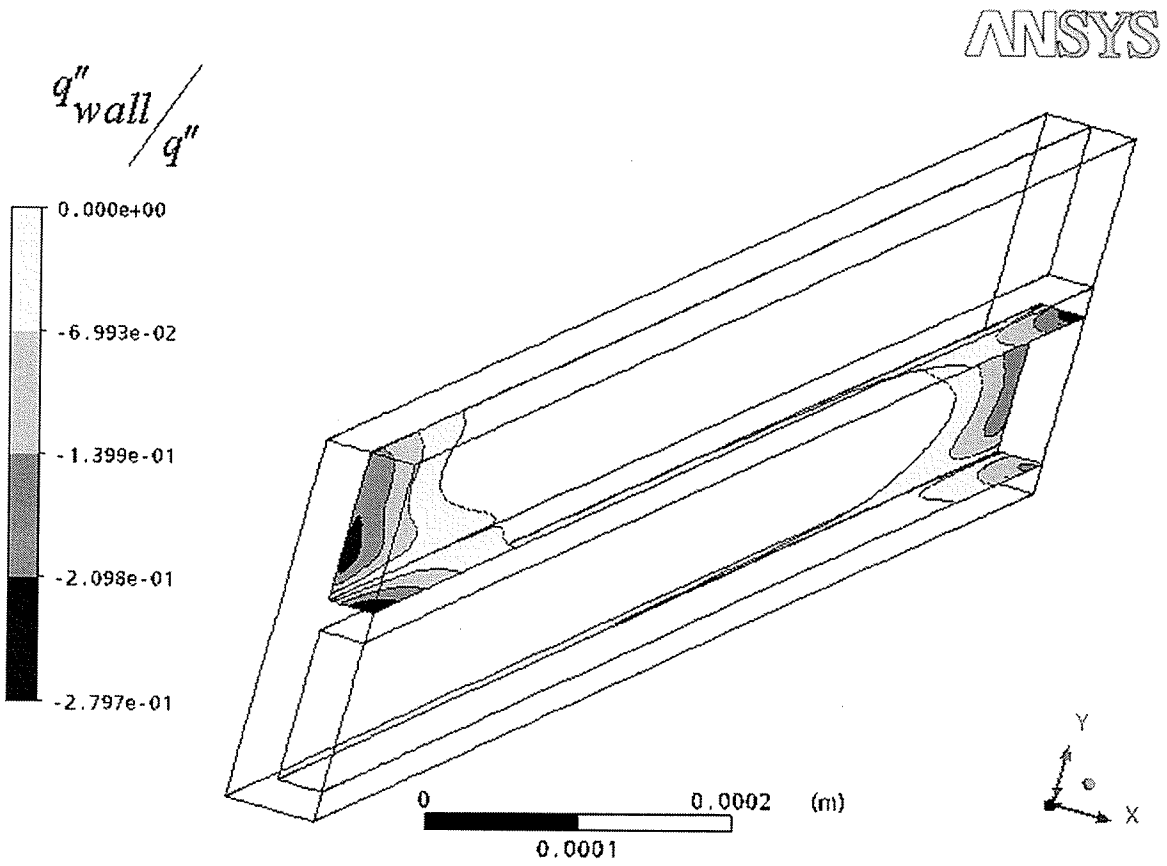

Figure 5.21: Negative Wall Heat Fluxes for the Case 1 Problem

there are cross-sections where one channels has experienced little heated, while the other has experience more. Near each channels' respective outlets, particularly in the low Reynolds number case, heat will actually flow from the channel, into the solid, and be absorbed into the other channel (because this channel is cooler, since it is close to its inlet).

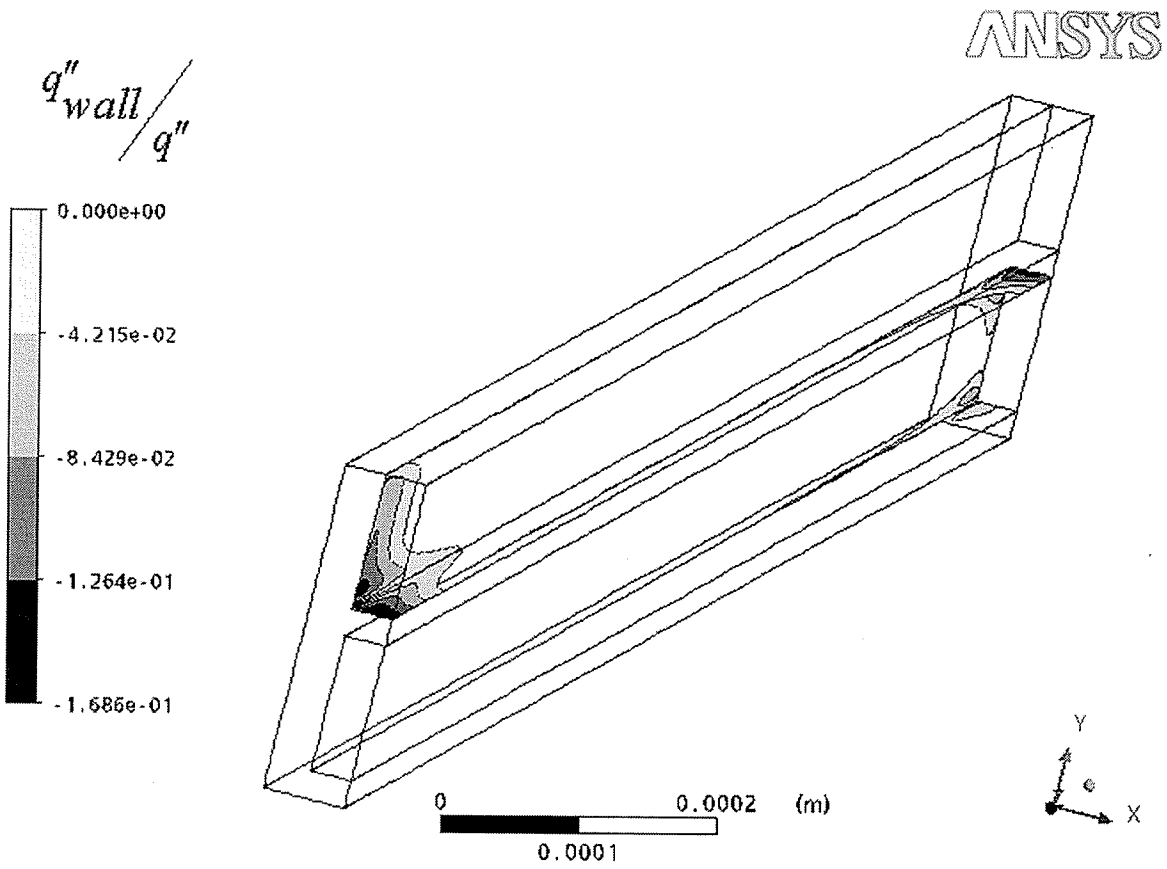

Figure 5.22: Negative Wall Heat Fluxes for the Case 3 Problem

CHAPTER 6
CLOSING REMARKS

6.1 Conclusions

A number of conclusions can be drawn from this work:

- If one is only interested in predicting the value of the thermal resistance of the heat sink, the fully-developed inlet velocity assumption can be made, which simplifies the calculations. However, determining the maximum temperature difference along the heated surface and the pumping power requires using the uniform inlet velocity profile, particularly for high Reynolds number.
- For a given total mass flowrate, the counter-flow arrangement gives the lowest thermal resistance (lower values are desirable). This is followed by the parallel-flow arrangement. The single channel (large) arrangement has the highest thermal resistance. (The single channel (small) arrangement, as examined in this work, did not use the same total mass flowrate as the other arrangements. Hence, it cannot be used in this comparison.)
- The difference in thermal resistance among the two two-row designs is smaller than that between the single channel (large) arrangement and either of the two-row arrangements. Thus, the two-row designs show promise.
- While the counter-flow arrangement has a lower thermal resistance than the parallel-flow arrangement, it is more difficult to construct, because of the complexity of pumping the flow in both rows of channels in opposite directions. Thus, since the difference in thermal resistance between the two two-row designs was not overwhelmingly great, it may be desired to sacrifice some performance in the area of thermal resistance in favor of a simpler (and less expensive to construct) design.
- The pumping power required to pump a given mass flowrate is lowest in the single channel (large) arrangement. The pumping power for the two-row arrangements is higher, and both two-row arrangements considered have the same pumping power for a given mass flowrate to be pumped.
- The single channel (large) arrangement was found to be able to dissipate more heat per unit pumping power than either of the two-row designs, for fixed mass flowrate and

overall temperature difference across the heat sink. Among the two-row designs, the counter-flow arrangement can dissipate more heat per unit pumping power than the parallel-flow arrangement, again for fixed mass flowrate and overall temperature difference across the heat sink.

- Where the counter-flow arrangement demonstrates its superiority over the other arrangements is in cases where a low variation of temperature along the heated surface is the dominant criterion. If this is the key factor in a given application, then it might be necessary to use the counter-flow arrangement, since, achieving the same uniformity of temperature along the heated surface would require comparatively large amounts of pumping power.

6.2 Recommendations for Further Work

The work presented in this thesis could be improved upon in the following ways:

- Cases where the validity of classical fluid mechanics does not apply could be considered.
- A more detailed parametric study could be performed, where various geometric and flow parameters are varied. The effect of varying these parameters on the heat transfer and pumping power data could then be determined.
- Channels of circular cross-section could be examined.
- Multi-row designs with more than two-rows could be studied.
- Turbulent flows could be considered.
- A more detailed examination of the additional complexities (and costs) of the counter-flow arrangement over the parallel-flow arrangement could be made.
- More generally, the costs of the various designs presented in this work could be examined more closely, including the costs to manufacture, operate and maintain the heat sinks.
- Cases of two-row designs where the mass flowrates in both channels are not the same could be explored.
- To improve the exactness of the analysis, the plenum before and after the channels could be modeled.

REFERENCES

T.M. Adams, S.I. Abdel-Khalik, S.M. Jeter, Z.H. Qureshi, An experimental investigation of single-phase forced convection in microchannels, International Journal of Heat and Mass Transfer 41 (1998) 851-857.

ANSYS CFX Documentation, Distributed Along With ANSYS CFX Software Suite, ANSYS, 2007.

Y. J. Cheng, Numerical simulation of stacked microchannel heat sink with mixing-enhanced passive structure, International Communications in Heat and Mass Transfer 34 (2007) 295-303.

S. H. Chong, K. T. Ooi, T. N. Wong, Optimisation of single and double layer counter flow microchannel heat sinks, Applied Thermal Engineering 22 (2002) 1569-1585.

A.G. Fedorov, R. Viskanta, Three-dimensional conjugate heat transfer in the microchannel heat sink for electronic packaging, International Journal of Heat and Mass Transfer 43 (2000) 399-415.

R. W. Fox, A. T. McDonald, Introduction to Fluid Mechanics, 5th Edition, John Wiley, New York, NY, 1998.

F.P. Incropera, D.P. DeWitt, Fundamentals of Heat and Mass Transfer, 5th Edition, John Wiley, New York, NY, 2002.

C.J. Kroeker, H.M. Soliman, S.J. Ormiston, Three-dimensional thermal analysis of heat sinks with circular cooling micro-channels, International Journal of Heat and Mass Transfer 47 (2004) 4733-4744.

J. Li, G. P. Peterson, 3-Dimensional numerical optimisation of silicon-based high performance parallel microchannel heat sink with liquid flow, International Journal of Heat and Mass Transfer 50 (2007) 2895-2904.

E.Y.K. Ng, S.T. Poh, CFD analysis of double-layer microchannel conjugate parallel liquid flows with electric double-layer effects, Numerical Heat Transfer, Part A, 40 (2001) 735-749.

W. Owhaib, B. Palm, Experimental investigation of single-phase convective heat transfer in circular microchannels, Experimental Thermal Fluid Science 28 (2004) 105-110.

S. V. Patankar, Numerical Heat Transfer and Fluid Flow, Hemisphere Publishing Corporation, 1980.

W. Qu, I. Mudawar, Analysis of three-dimensional heat transfer in micro-channel heat sinks, International Journal of Heat and Mass Transfer 45 (2002) 3973-3985.

R.K. Shah, A.L. London, Laminar Flow Forced Convection in Ducts: a Source Book for Compact Heat Exchanger Analytical Data, Academic Press, New York, NY, 1978.

P. Skandakumaran, A. Ortega, T. Jamal-Eddine, R. Vaidyanathan, Multi-layered SiC mircochannel heat sinks - modeling and experiment, Inter Society Conference on Thermal Phenomena (2004).

G. Tunc, Y. Bayazitoglu, Heat transfer in rectangular microchannels, International Journal of Heat and Mass Transfer 45 (2002) 765-773.

K. Vafai, L. Zhu, Analysis of two-layered micro-channel heat sink concept in electronic cooling, International Journal of Heat and Mass Transfer 42 (1999) 2287-2297.

X. Wei, Y. Joshi, Stacked microchannel heat sinks for liquid cooling of microelectronic components, Transactions of the ASME 126 (2004) 60-66.

A. Weisberg, H.H. Bau, J.N. Zemel, Analysis of microchannels for integrated cooling, International Journal of Heat and Mass Transfer 35 (1992) 2465-2474.